INERT REFRACTORY SYSTEMS FOR CASTING OF TITANIUM ALLOYS

by

XU CHENG

A thesis submitted to the

University of Birmingham

for the degree of

DOCTOR OF PHILOSOPHY

School of Metallurgy and Materials
School of Engineering
University of Birmingham
Sep 2012

Abstract:

Research has been undertaken to develop new yttria slurry systems for use in mould face coats for investment casting TiAl alloy, solving the pre-gelation problems of commercial yttria slurry systems to increase slurry life. Meanwhile, the new face coats should also have excellent sintering properties, chemical inertness, surface finish and be easy to prepare.

The processes of developing the new slurry started with the filler powder investigation by adding different sintering additives into the yttria powder to achieve good sintering properties. Then the best filler powder candidates were selected to make the slurry. Finally, the new face coat slurries were used to make the shell face coat and the chemical inertness of those shells were investigated through the sessile drop and investment casting. In the research, the filler powder and face coat sintering properties were quantified through density, dilatometer testing, X-ray diffraction (XRD) and microstructural change at different testing temperatures. The interaction of different face coat systems and the metal were identified using hardness tests, sessile drop contact angle and the microstructural change at the metal/shell interface.

In this research, three water-based binder face coat systems containing YF_3, Y_2O_3+0.5wt% Al_2O_3+ 0.5 wt% ZrO_2 (YAZ), and B_2O_3 additives were found to have similar or even better sintering properties compared to a commercial face coat. Meanwhile, they had long life.

Acknowledgements:

The author also would like to thank Prof. Nick Green and Dr. Chen Yuan for the supervision and provision the facilities in school of metallurgy and materials and the IRC in materials.

The author would like to thank the Rolls-Royce plc for their financial support. Especially thanks to Prof. Paul Withey for carefully and kindly helping to correct the thesis prior to publishing, and the finishing Ph. D.

All the research fellows and technicians in the casting group in school of metallurgy and materials are gratefully acknowledged.

On a personal level, I would like to say thanks to all my family for their unwavering support and encouragement, and my friends in this department.

TABLE OF CONTENTS

LIST OF TABLES

LIST OF FIGURES

LIST OF PUBLISHING

Refractory material mould study for investment casting TiAl alloys
(14th Ti conference, will be published in Dec.2011)

An investment of a refractory face coat system for the investment casting of Ti-Al alloy (Journal of Intermetallics)

The influence of polymer content and sintering temperature on yttria-face coat moulds for TiAl casting (Journal of European ceramic society).

The papers are submitted:

Evaluation of inertness of Investment casting moulds using both sessile drop and centrifugal casting methods
(Journal of Metallurgy and Materials Transaction A, accepted)

The sintering mechanism study of yttria with different additives
(Journal of Ceramic International, revision)

Enhanced sintering properties of yttria face coat by addition of B_2O_3, YF_3, Al_2O_3 and ZrO_2
(Journal of Materials science and technology)

Chapter 1. Introduction:

Titanium aluminide alloys are widely used in automotive application such as valves and turbochargers. Due to their good strength and creep resistance, TiAl alloys are recently used to replace nickel superalloy turbine blades at the working temperature around 600-750 °C. Due to the comparable low density of these alloy, it save nearly 40 % of the turbine weight whilst reducing the cost.

Because of the intrinsic properties of TiAl alloy, such as chemical heterogeneity, brittleness, low room temperature ductility and poor workability [20], wrought methods like rolling and forging are unsuitable for mass production of TiAl components. Kuang *et al*, [22] and Sung *et al* [23] suggested that investment casting, which can give very precise net-shape with extremely smooth component surface, is one of the best economic ways to produce TiAl components.

When investment casting is used to produce TiAl, two main problems arise in industry mould production. Firstly, the poor chemical inertness of the standard mould materials causes extensive interaction take place during casting process, and thus forms a hardened (brittle) layer at the component surface [41]. Secondly, pre-gelation problems of face coat slurry systems limit the life of slurries to one hour after mixing [151].

1.1 Aim:

The aims of this project are to design a water-based binder face coat slurry system for TiAl casting which has long life time, is easy prepare to and of low cost, whilst retaining excellent thermodynamic stability and chemical inertness.

1.2 Thesis layout:

This thesis is divided into nine main chapters. Chapter 1 is the introduction of the thesis includes research aims and layout. Chapter 2, the literature review, will be initially reviewing the background knowledge of the TiAl alloy such as microstructures, properties, production methods and the interaction between the alloy and the mould during the investment casting process. Then the review will first focus on the mould materials‘ research for the investment cast refractory mould since the last century and then the large efforts which have been made to increase the life of the slurry. The last part of the review is concentrated on the new slurry formulation/recipe development.

Chapters 3 to 7 encompass all the experimental work. In those chapters, new slurry recipes were developed starting from the filler powders to the slurries, and the face coat sintering properties and chemical inertness were also analyzed through the experimental process. Chapter 3 looks at the designed filler powder physical properties such as powder particle size and distribution, filler powder particle shape, thermal expansion and the composition change at different isothermal sintering temperatures. The best filler powders were then

selected to make the face coat slurry.

A series of face coat slurries with the designed composition were made and their microstructures, life, viscosity change and sintering properties were reported in Chapter 4. After that, the best slurry with good consistency and sintering properties was chosen to make small shell pieces to test their chemical inertness against the molten TiAl alloys by using the sessile drop test in Chapter 5. Then the metal interfacial energy changes of each face coat shell during interaction were calculated from sessile drop evaluation to predict the thermal inertness of each shell. The cast metal drop metal/shell interface microstructures and interfacial hardened layer thickness were also characterized and reported in this chapter.

The new face coat slurries were then used to make moulds from small scale crucibles to a large scale investment ‗T' shape to test the face coat strength and shell surface finish in Chapter 6. Poor face coat strength is then addressed using sol ‗back penetration' as the new face coat slurry manufacture method. Due to the high reactivity of Si in the backup coat, it will penetrate/diffuse into the face coat layer though high temperature sintering process. Therefore, in this chapter, issues with Si back penetration will be given a detailed introduction.

Chapter 7 mainly reviews the centrifugal investment cast TiAl bar surfaces and metal/shell interfacial microstructures from using the new face coat slurry with the sol ‗back

penetration‘ methods. The metal interface hardened layer thickness and interaction properties by using the new slurries were characterized and compared to the industry standard yttria slurry. The inertness of each face coat is analyzed by the measuring the thickness of the interaction layer and Si penetration distance at the metal/shell interface area of the cast sample. These results were then used to compare with the predicted results in Chapter 5 and 6. Last but not least, Chapter 8 and 9 draws the main discussions, conclusions and proposes future work for further development of the face coat slurry for production TiAl components.

Chapter 2. Literature review:

The literature review is divided into three parts; the first part will focus on reviewing the properties of the gamma titanium aluminide alloy, commercial production methods and the associated production problems. The second part will introduce the reactivity of titanium alloys, the development history of mould refractory materials from last century and the objectives of this project. The third part will concentrate on new slurry formulation development.

2.1 The background of Titanium aluminide

2.1.1 Titanium aluminide and their applications

Titanium alluminide alloys are widely used in automotive applications, such as car engine valves and turbochargers due to its high melting point, good oxidation and creep resistance [1-2]. In the past 10 years, TiAl alloy has been considered as a potential material that can be used for aerospace applications, such as turbine blades due to their superior high temperature properties [3].

Compared to the nickel superalloy used in the turbine blades, TiAl alloys have lower densities between 3.76×10^3 to 4.5×10^3 kg/m^3 [4] than nickel superalloy (8.9×10^3 kg/m^3). Therefore, if titanium aluminide alloys can be used to replace nickel superalloy blades in low temperature

engine parts (Figure 2-1), it will not only save the half weight of the blade, but also reduce stress/force generated during rotating and hence save disk weight.

In 2008, General Electric announced that gamma TiAl low pressure turbine (LPT) blades were going to be used on its GEnx engine, which powered the Boeing 787 and Boeing 747-8 aircraft [5]. This is the first large-scale use of this material on a commercial jet engine and save around 40 % weight of the turbine blades, reducing the two stages of turbine cost. The TiAl LPT blades were cast by Precision Castparts Corp in the same year, and have now entered service.

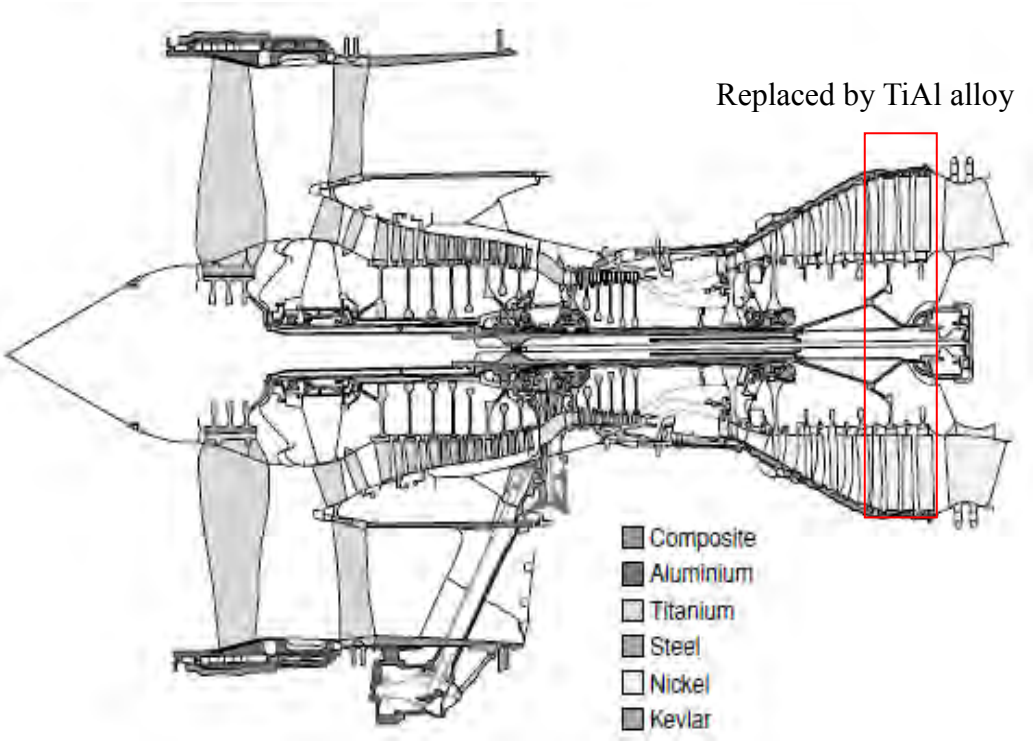

Figure 2-1. llustration of material usage in the Trent 800 engine. Note the extensive use of nickel-based superalloys in the combustor and turbine section (Courtesy of Rolls-Royce). [6]

Also the superior mechanical properties of gamma TiAl are the other reason to attract the world‘s attention on titanium aluminides to replace nickel superalloy at temperatures around 600-750°C. As an engineering material, gamma TiAl alloys have very high rupture strength and specific strength, Figure 2-2.

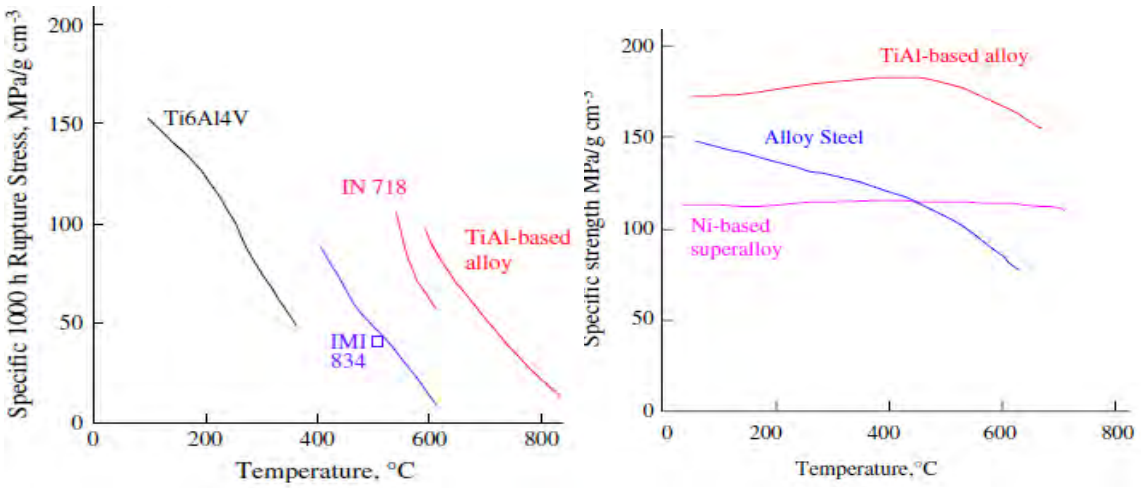

(a) (b)

Figure 2-2. (a) 1000h rapture strength as a function of temperature for a TiAl based alloy compared to nickel and other alloys (b) specific strength as a function with temperature of a TiAl alloy [1].

2.1.2 The composition and microstructure of TiAl alloys

As was known, gamma TiAl, has an Al content of around 40 to 50 at%, which makes the microstructure of these alloy different from other Titanium alloys. The cooling from the beta phase area will prefer to form three types of microstructures, Figure 2-3 and 2-4. i.e, fully lamellar (Ti-(45-47) Al) with grains consisting of an arrangement of α_2 (DO_{19}, ordered hexagonal) and γ (face-centred tetragonal) laminate microstructure, the duplex (Ti-(49-50) Al) alloy, where lamellar grains coexist with equiaxed γ phase [7], and near fully lamellar

(Ti-48Al) structures. Figure 2-4 showed three types of TiAl alloy.

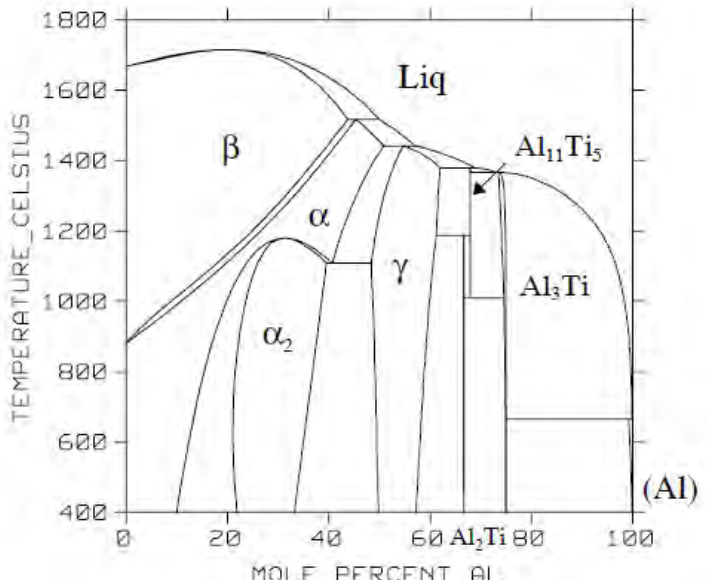

Figure 2-3. A TiAl alloy phase diagram [8]

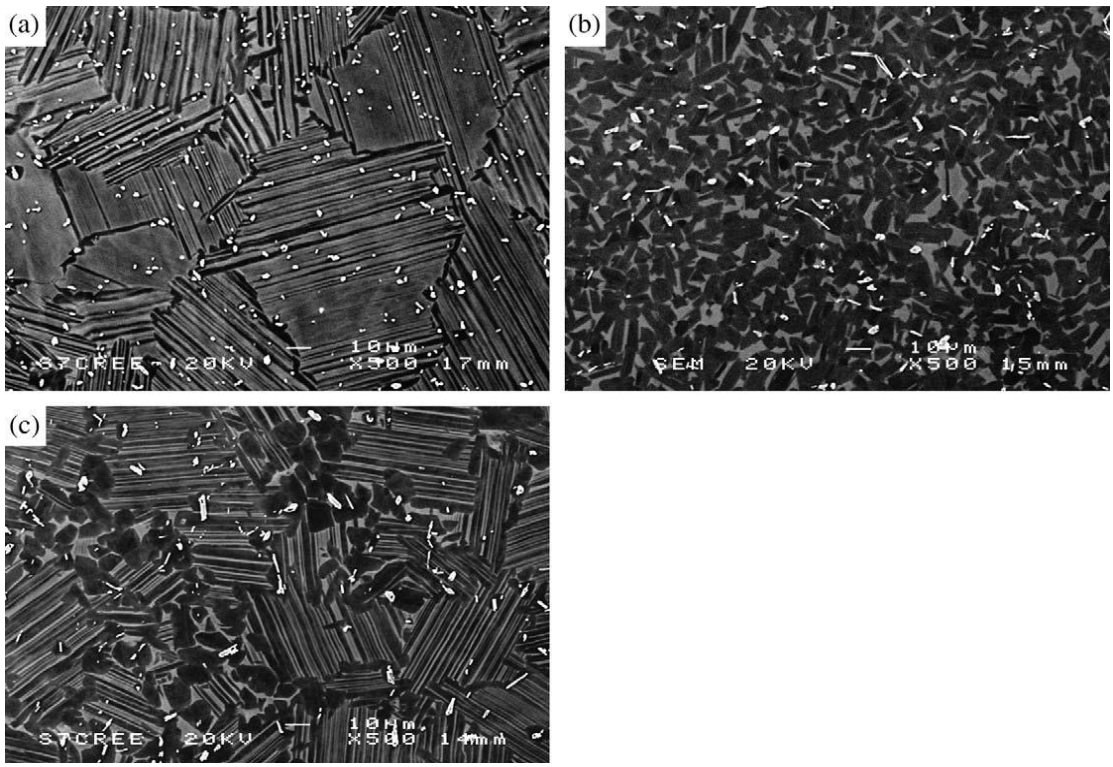

Figure 2-4. Three typical microstructures of TiAl: (a) fully lamellar; (b) duplex and (c) near fully lamellar. The actual composition for those microstructures is Ti-44Al-8Nb-1B. [1]

M. Lamirand [9] reported that the full duplex structure was more ductile at room temperature, and that the fully lamellar structure, while less ductile, has a very good creep resistance at high temperatures. Some properties of gamma-TiAl alloys are shown in Table 2-1.

Table 2-1. Property profiles of γ-TiAl alloys [10]

Properties	**γ-TiAl**
Density	++
Specific tensile strength	+/-
High temperature Young‘s Modulus	++
Rom temperature ductility	-
Formability	-
Creep	++
Room temperature fracture toughness	-
Room temperature crack growth	-
Specific fatigue strength	+/-
Oxidation	++
High temperature embrittlement	+/-

＋: good , ＋＋: very good, - : ok

In order to further improve the specific strength, creep, and oxidation resistance of TiAl alloys, substitutional elements, such as Nb, Cr & Hf [11], Mn & Mo [12], and Ru [13] etc. were added into the alloy for different purposes. These elements change the TiAl alloy properties by substitution in the Al atomic positions and solid-solution hardening the alloy, meanwhile, addition of these elements will increase the melting temperature of TiAl alloy from around 1550 °C for pure Ti to around 1600 °C. The benefits/purpose of the additives

alloy elements are listed in Table 2-2.

Table 2-2. The effects of selected alloying elements in gamma-TiAl alloys [2]

Element	Effect
Nb	Increase oxidation resistance and creep resistance, high temperature strength
P	Decrease oxidation rate
Si	Addition 0.5-1% range increase creep resistance. Silicon also increase oxidation resistance and fluidity and decrease susceptibility to hot cracking
Ta	Increases oxidation and creep resistance and tendency for hot cracking
V	Addition in 1-3% range increases ductility in duplex alloys. Reduces oxidation resistance.
W	Oxidation and creep resistance increased.
C	Increase creep resistance and decreases ductility
Cr	Additions of 1-3% increase ductility of duplex alloys, addition >2% increase workability and super elasticity, and >8% increase oxidation resistance
Mn	Additions of 1-3% increase ductility of duplex alloys
Mo	Increase ductility, strength and oxidation resistance

The development of TiAl alloy has reached the 4th generation since the 1980s, and the improvement of each generation was mainly focused on enhancing alloy creep resistance, strength, ductility, and high temperature oxidation resistance. Table 2-3 shows the TiAl alloy composition and production methods.

Table 2-3. Composition and processing of gamma-TiAl alloy in each generation. [10]

Generation	Composition (at%)	processing
1st	Ti-48Al-1V-0.3C	Exploratory
2nd	Ti-47Al-2(Cr,Mn)-Nb TI-(45-47)Al-2Nb-2Mn-0.8%TiB_2	Cast Cast (XD)
3rd	Ti-47Al-2W-0.5Si Ti-47Al-5(Cr, Nb, Ta) Ti-46.2Al-2Cr-3Nb-0.2W	Cast Cast wrought
4th	Ti-(45-48)Al-(1-2)Cr-(1-5)Nb-(0-2)(W, Ta, Hf, Mo, Zr)- (0-0.2)B-(0.03-0.3)C-(0.03-0.2)Si-(0.15-0.25)O-X	Wrought/cast

In order to refine the grain size, boron has been added into TiAl since the second generation of the alloy [14], see Figure 2-5. There are two hypotheses for the grain refinement mechanism of $TiB_{(1, 2)}$, first is the increase of the under-cooling effect [15], and second is providing the nucleation sites for heterogeneous nucleation of alpha (TiAl) on borides [16, 17]. Two main TiAl alloys, Ti-(45-47)Al-2Mn-2Nb-0.8at%TiB_2 and Ti-48Al-2Cr-2Nb are now widely used in engineering applications [18] due to their special properties.

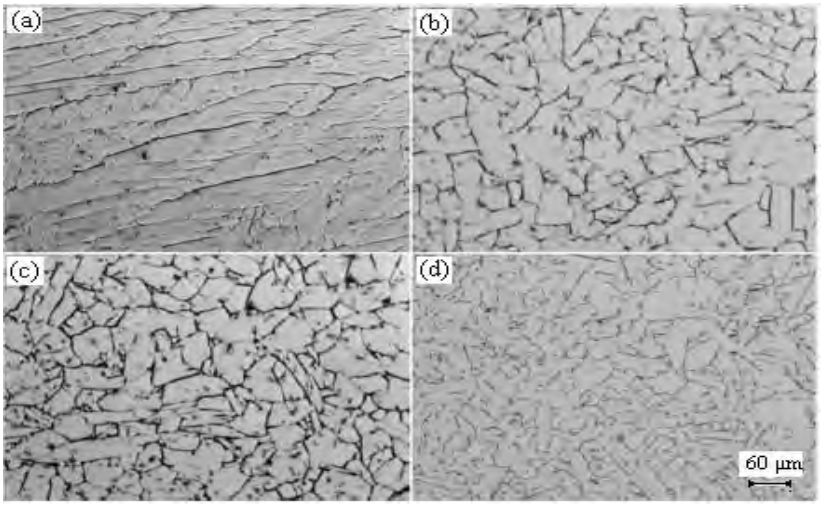

Figure 2-5. Optical Microscopy micrographs of Ti45Al8Nb(x)B (at.%) alloys after heat treatment, Boron additions (x) are (a) 0, (b) 0.3, (c) 0.5, (d) 0.8 at% respectively.

2.1.3 The manufacturing method of TiAl alloys

Over recent years, major efforts have been made to introduce titanium aluminides into the aerospace market with limited success [19]. The main factors which held back manufacture of ‗mass market' TiAl based components were the intrinsic properties of TiAl as determined by the microstructure and chemical heterogeneity, such as brittleness, low room temperature ductility and poor work ability [20]. Prilhar (2001) [21] managed to produce fabricated and forged gamma-TiAl compressor blades but suffered from poor ingot stock and the poor fluidity of the metal liquid. Due to these problems, the use of wrought processing methods such as forging and rolling, which were very prone to chemical and microstructure heterogeneity were limited, whilst powder metallurgy is considered very expensive and only suitable for the manufacture of large and complex TiAl components [1]. Therefore investment casting, which can directly give net-shape components, was one of the most promising ways to produce TiAl components [22]. Sung (2005) [23] demonstrated that investment casting can give a very precise net-shape with extremely smooth component surface thus keep waste material to a minimum.

Casting appears to be the favored route with regard to the manufacturing of near net-shape gama-TiAl turbine blades. The automotive parts made using counter gravity casting have already been successful for many years [24-26], see Figure 2-6 for the mould design for counter gravity casting. However, counter gravity casting method was limited for use in processing gamma TiAl blades because the shrinkage defects formed during cooling, and

oversized bubbles were detected at the cast component surface. Harding (2004) [27] reported large amount of misrun defects due to thin sections causing the metal to freeze before complete filling. While centrifugal casting can create large amounts of free surface turbulence, it offers the beneficial effects of the centrifugal force acting upon the metal, aiding both filling and feeding during solidification. It is apparent that investment centrifugal casting appears to be the most favoured method for casting of TiAl aerospace components.

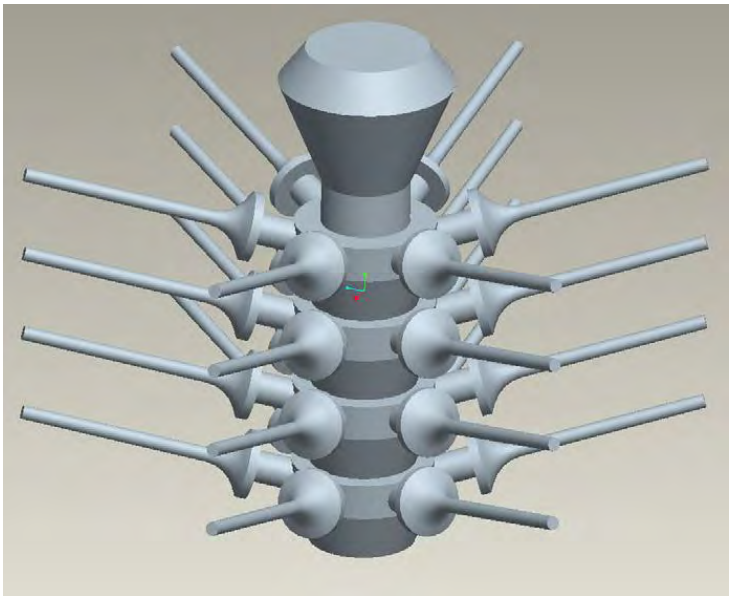

Figure 2-6. 3D model of cast valves in preliminary design [28]

2.1.4 Investment casting mould making process (lost-wax casting)

The basic investment casting production processes are summarized schematically in Figure 2-7 [29]. During the investment casting process, wax patterns which have same net-shape as the components to be cast (with contraction allowances) are assembled together with the runner and filling system, Figure 2-7 (a-c). Then these patterns are cleaned using a wax

cleaning liquid (Trisol-60) and then dried for a few hours. After that, wax patterns are dipped into a multi-component slurry system, which normally consists of a mixture of refractory fillers and a binder. A layer of ceramic stucco (coarse ceramic particles) is then applied and allowed to dry, see Figure 2-7 (d-e). These processes are repeated until the ceramic mould attains a certain thickness. The ‗green' mould is then de-waxed using a Boilerclave^{TM} and fired to attain full strength. The charge of molten alloy can then be poured into the ceramic mould. After cooling, metal components are mechanically broken out from the thin wall moulds, and the adhered mould oxide on the metal surface was removed by using shot blasting or chemical milling [30], see Figure 2-7 (h-j).

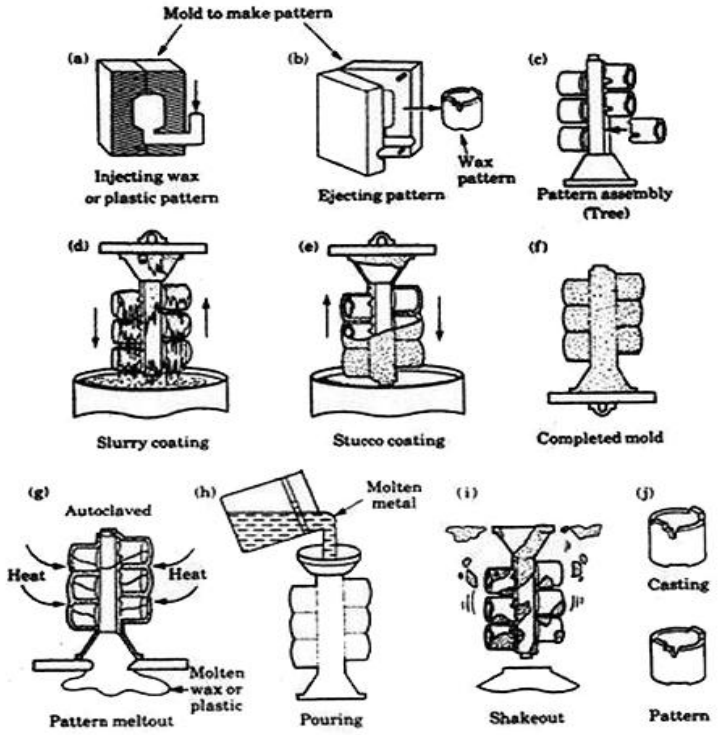

Figure 2-7. The investment mould making process [29]

The slurry used in Figure 2-7 (d) is a mixture of filler, binder, anti-foam, wetting agent etc. The main composition of the slurry is the filler [30]. Filler is a powder with particle size around -200 to -375 mesh (particle size around 30 to 75 μm). The binder in the solution can be organic or inorganic, and it is used to increase the bonding between the filler particles to improve the green strength of the shells. E.g. colloidal silica (particle size around 3 to 150 nm) is a very desirable and widely used binder for investment casting moulds. Anti-foam is a chemical solution which effectively reduces foam formation during the stirring and dipping process. The wetting agent is used to change the surface tension of the slurry for better coating. Sometimes, polymers are used as shell/coat strengtheners into the slurry to enhance the green strength of the mould [31].

The coat of investment casting mould can be generally separated into two parts, see Figure 2-8. First is the primary coat, and then there are the secondary coats (backup coats). The physical requirement of the primary coat is that it should be smooth, chemically stable and with sufficient strength to sustain the pressure of the chemically reactive molten metal. The secondary (backup) coat contains multi-layers (5-7 coats), while a large stucco with particle size around 300-500 μm is mainly used in this coat to provide sufficient strength for the mould before sintering [32].

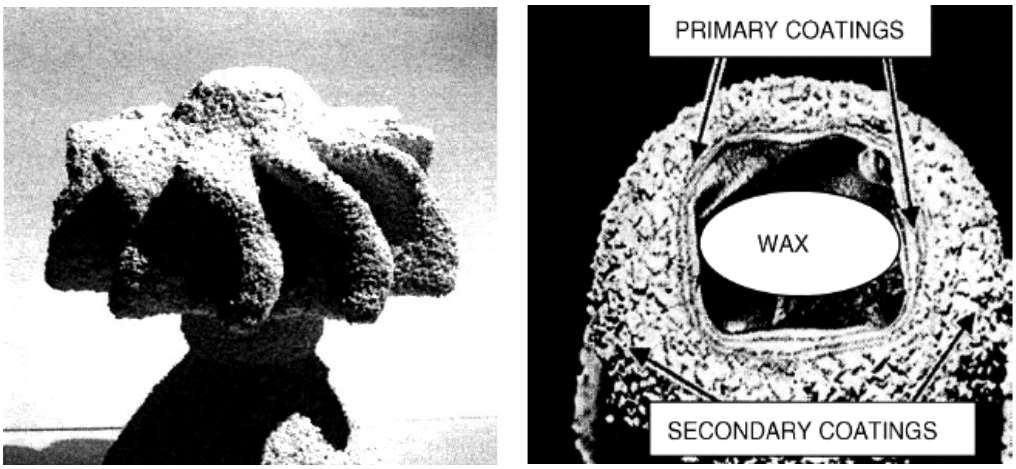

(a) (b)

Figure 2-8. (a) a finished turbo-charger wheel mould and (b) the cross section of the pattern before de-wax [32]

2.1.5 The problems of investment casting of TiAl alloys

There are three major problems associated with the investment casting of TiAl alloys. First is the large coarse grain size which has very poor mechanical properties [33-34]. Second is the poor fluidity of TiAl alloys around their melting temperatures, which causes poor filling of the cast moulds, leads to large defects formation during casting process [35-39]. The third problem is the interaction between the mould and molten metal due to the very reactive TiAl alloy during casting [40-65].

2.1.5.1 The coarse grain size

After casting, large and coarse grains are formed due to the slow cooling rate, and which will give rise to low ductility, a large scatter in properties and lead to an increased tendency to pre-yield cracking [33]. Figure 2-9 shows the coarse grains cause a decrease in the yield stress, the elongation, and material tensile strength, etc. The grain refining elements boron

and carbon as studied previously, can largely refine the as cast component, but the formation of large borides can become crack initiation sites. It also should be noted that in thermo-mechanical processes, borides are broken down during the process and are very effective at pining grain boundaries during the re-crystallization process.

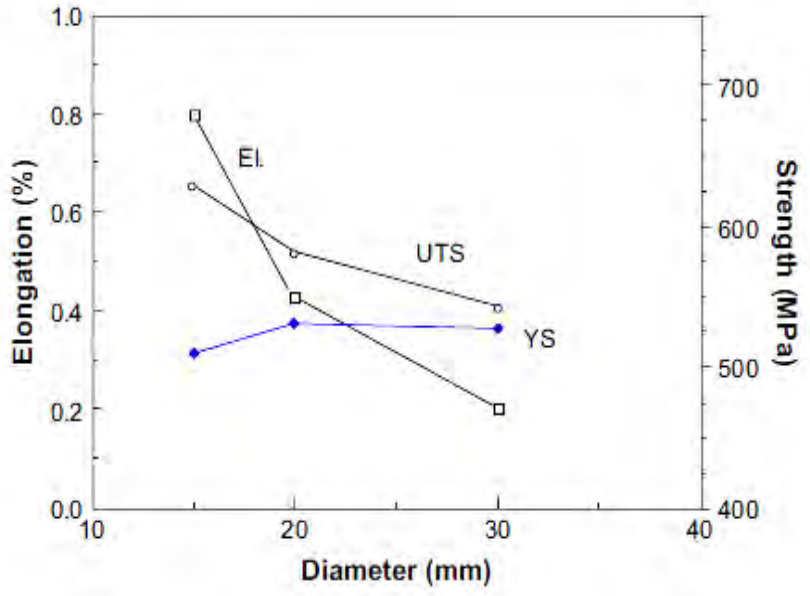

Figure 2-9. The effect of grain diameter of tensile test of a Ti-44Al-8Nb-1B alloy. [34]

2.1.5.2 Defect formation and improvement

Although TiAl has low fluidity at the melting temperature, Harding & Wikins (2001) [35], Harding (2007) [36], and Harding & Wickins (2011) [37] found that it is still possible to cast thin walled TiAl components by using a high powered Induction Skull Melting (ISM) furnace. However, rapid gravity filling creates a high level of turbulence in the metal liquids that caused large bubbles trapped and forming large porous defects when the metal cooled down [38], see Figure 2-10. By using a pre-heated mould with alloy superheating, the alloy

fluidity is largely improved thus allowing bubbles to escape or break down, reducing the number of bubbles in the cast component. The best methods to produce TiAl components suggested by Harding and Wang [37, 39] are tilt or centrifugal casting.

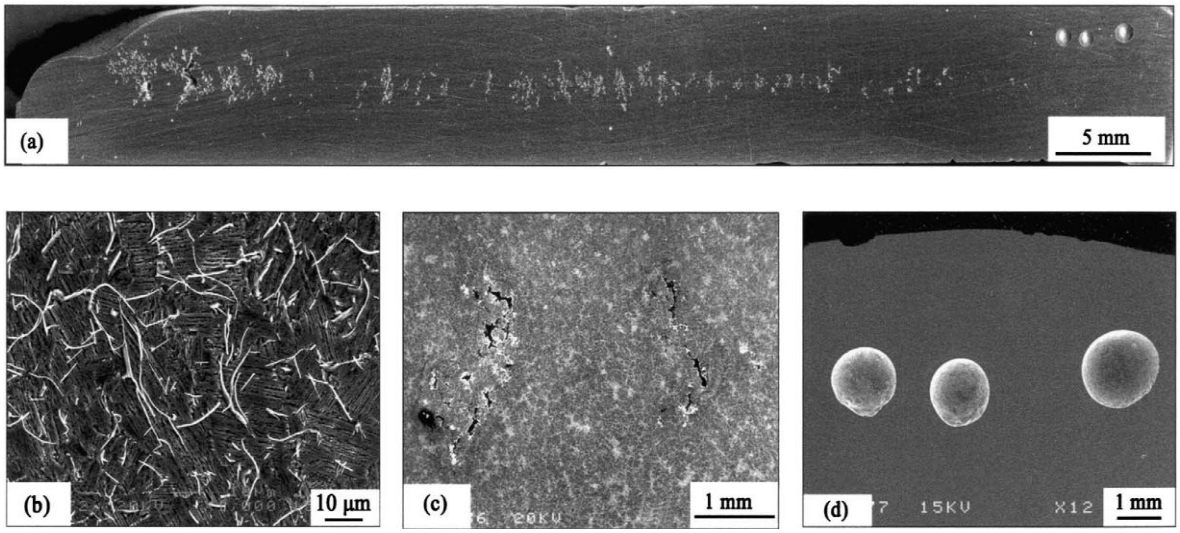

Figure 2-10. A polished surface of a sectioned cast TiAl bar and SEM micrographs, showing (a) macrostructure, (b) microstructure, (c) porosity and (d) entrained bubbles [38].

2.1.5.3 Interaction between metal and ceramic shell

M. Lamirand (2006) [9] pointed out that titanium and its alloys had a strong affinity to oxygen, and oxygen is presented in TiAl alloys in a significant concentration usually around 800 wt ppm or more. These oxygen atoms in TiAl occupy the octahedral interstitial sites in the closed-packed plane and result in poor mechanical properties such as yield stress, hardness and fracture stress.

Therefore, the problem encountered in TiAl casting was the oxidation due to the interaction

between the ceramic mould and molten metal during the casting process. Reaction was usually manifested as an increased near-surface oxygen concentration, decreasing with distance from the interface to the inner part of casting, Figure 2-11[40].

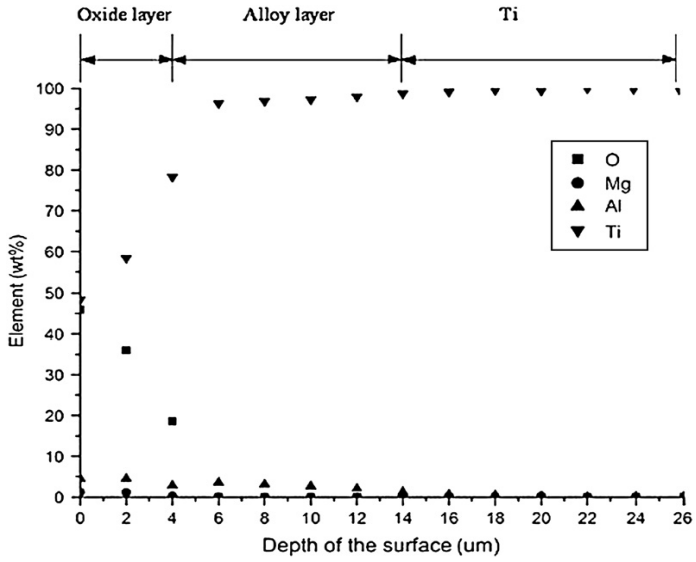

Figure.2-11. Element content as function of depth from the metal/shell interface using SEM [40].

Barbosa *et al*, (2003, 2006, 2007) [41-43] showed the oxygen penetration thickness is similar to the detected hardened layer thickness at the metal/shell interface, after comparing the matrix hardness of the $\alpha_{2+}\gamma$ and γ phase, see Figure 2-12.

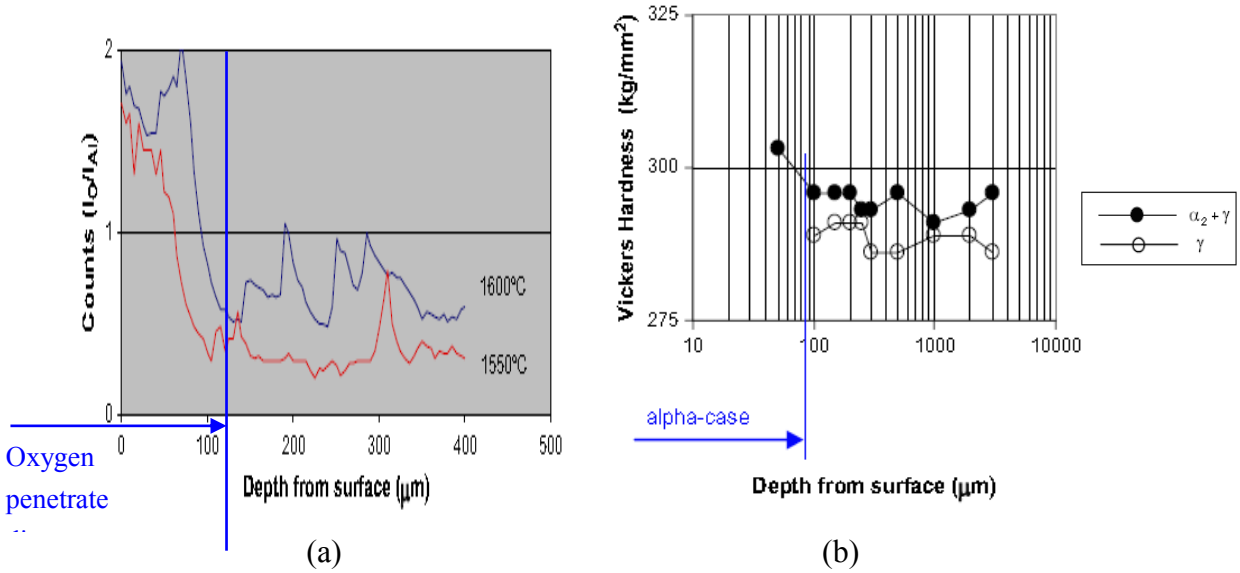

(a) (b)

Figure 2-12. (a) Oxygen concentration profile of a TiAl samples surface to the inside after 120s holding time at 1550 and 1600 °C in a yttria crucible. (b) Micro-hardness variation profile from the surface to the inside of sample in both micro-constituents, for a heating times at 1550°C, 60s.[42]

Yu Guilin (2007) [40] suggested that the interaction layer can be divided into two different layers, which are the oxide layer and the alloy layer, see Figure 2-13.

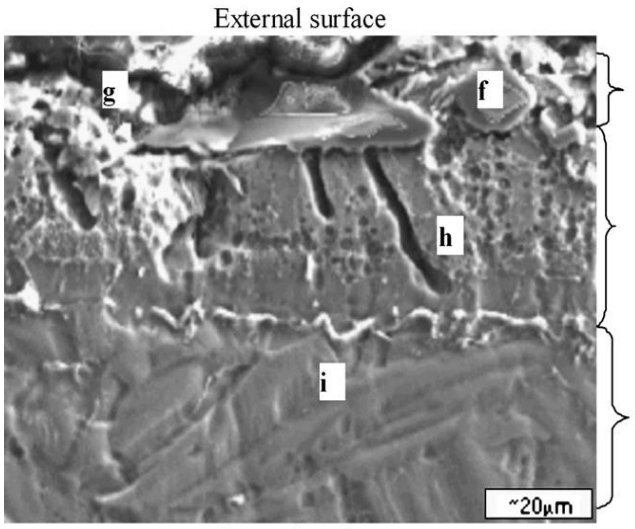

Spot	Element O	Al	Ti
f	67	33	0
g	64	18	18
h	0	17	83
i	0	0	100

Spot f is Al_2O_3; *spot g* is Al_2TiO_5 (Al_2O_3·TiO_2) and Ti_xO_y; *spot h* is Ti_3Al; *spot i* is Ti.

Figure 2-13. SEM micrograph of interaction layer of pure titanium castings made with Al_2O_3-based investment, indicating that surface reaction layer (approximately 50 μm) consisted of oxide layer (approximately 10 μm) and alloy layer(approximately 40 μm).

At the oxide layer, which directly contacts the shell, the alloy elements have already fully oxidized, and the oxide layer thickness depends on the amount of penetrated oxygen from the ceramic mould. By increasing the distances away from the interface, the oxygen concentration continues to decrease till it can not be detected. Compared to the oxide layer, the alloy layer has lower oxygen concentration but high concentration of elements from the mould materials (Si, Zr, Ca. etc) [44-46].

Jia. Q (2002) [44] found Zr contamination to a depth of 25 μm in a component cast in a ZrO_2 based mould. Kuang *et al* (2000) [45] found Ca ions in the surface region of the samples cast into CaO moulds. Li *et al* (2007) [46] found high Si content in the near surface region of samples cast into a SiO_2 mould. These elements in the TiAl interface will interact with TiAl alloy to form some high melting temperature phases, which possibly degraded the mechanical properties of the cast component. Figure 2-14 and 2-15 shows the very serious interaction between metal and ceramic shell during the casting process, and massive interaction products (light colour phase) which had been found along the grain boundary area from the interface down to around 200-300 μm away in the metal matrix. The very wide interaction layer thickness makes the mechanical removal of these layers, without influencing, the cast component‘s dimensional accuracy seems impossible.

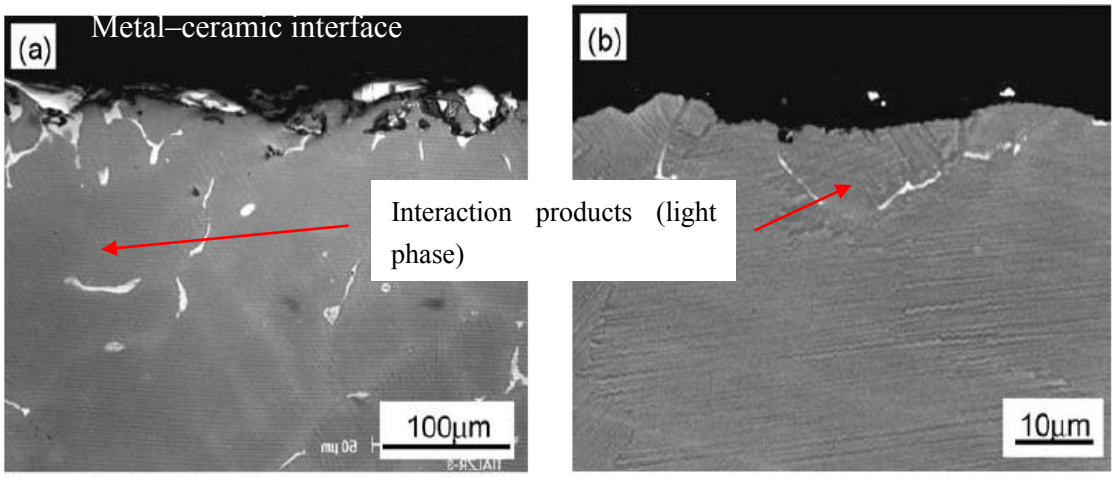

Figure 2-14. Backscatter electron images of longitudinal section as-cast Ti-46Al interface by using different mould materials. (a) ZrO_2 and (b) Al_2O_3 [46]

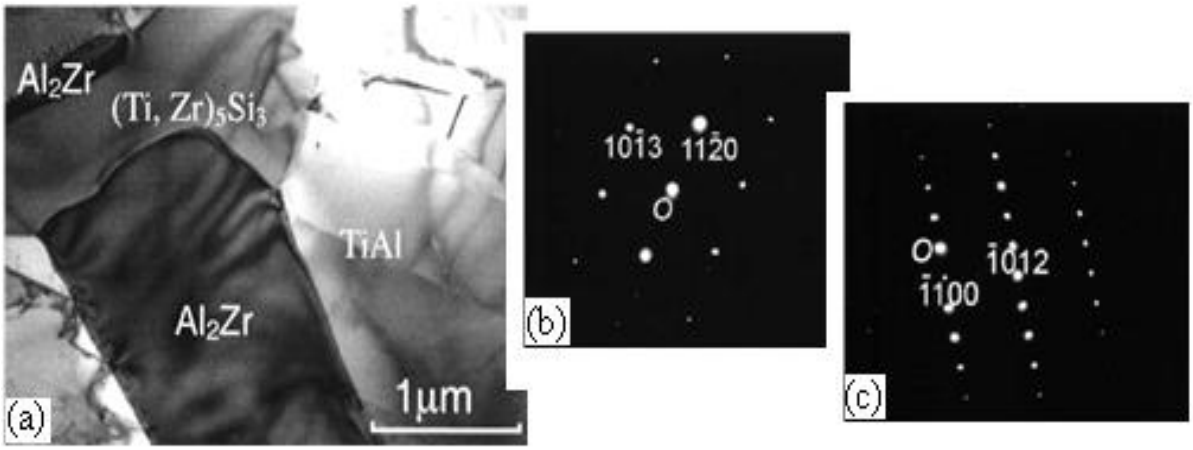

Figure 2-15. (a) Bright field transmission electron micrograph showing a Al_2Zr and $(Ti,Zr)_5Si_3$ particles at dendrite spacing, and the diffraction pattern of (b) Al_2Zr, and (c)Ti_5Si_3 phase.[47]

The interactions between the ceramic and liquid alloys will also change the surface tension of the molten TiAl on the ceramic shell [48]. In order to analyse the wetting behaviour of the metal on the ceramic shell, the sessile drop technique is used by a large number of researchers [49-52]. Zhou *et al* (1996) [53] and Landry *et al* (1996) [54] found that by increasing the contact time between the molten metal and ceramic mould, the contact angle

will reduce till a final angle was achieved, see Figure 2-16, where, θ_0 is the original contact angle value and θ_f is the final contact angle value.

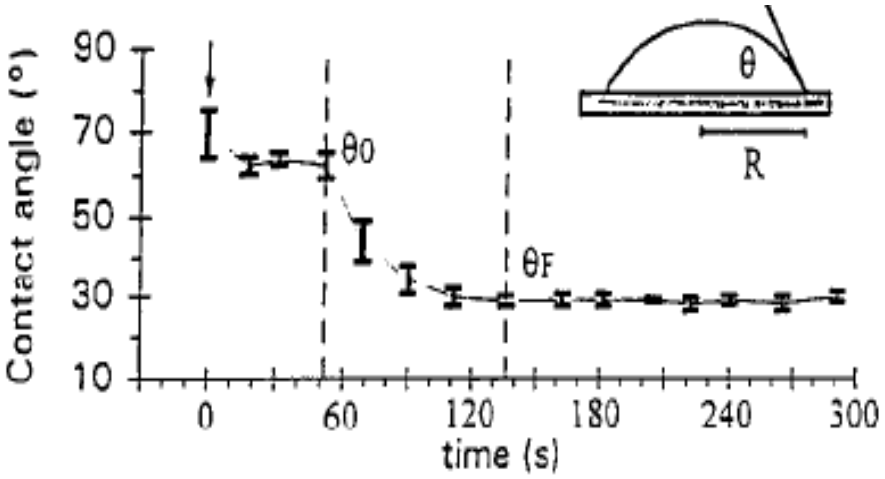

Figure 2-16. Variation of contact angle of Cu-11Ti alloy on an Al_2O_3 substrate. [51].

The contact angle on the substrate can also be influenced by substrate surface roughness, heterogeneity of the surface, flux, temperature, trace elements, atmosphere, and liquid properties [55, 56]. The wetting angle on the substrate for a reactive system can be express as equation 2-2 [57, 58].

$$\cos\theta_{\min} = \cos\theta_0 - \frac{\Delta\gamma_r}{\gamma_{LV}} - \frac{\Delta G_r}{\gamma_{LV}} \qquad 2\text{-}2$$

where γ_{LV} is the surface tension of the liquid, θ_0 is contact angle on the substrate in the absence of any reaction, $\Delta\gamma_r$ represents the change in interfacial energy due to interfacial reaction and ΔG_r is the change in free energy per unit area released by the reaction of the material contained in the immediate vicinity of the metal/substrate interface.

Li *et al* (2007) [46] studied the minimum contact angle between molten Ti-50Al and different ceramic substrates and found that, for different ceramic systems, the final contact angle is different. An yttria substrate has the largest contact angle followed by the ZrO_2 shell, the smallest wetting angle used a MgO substrate, see Figure 2-17.

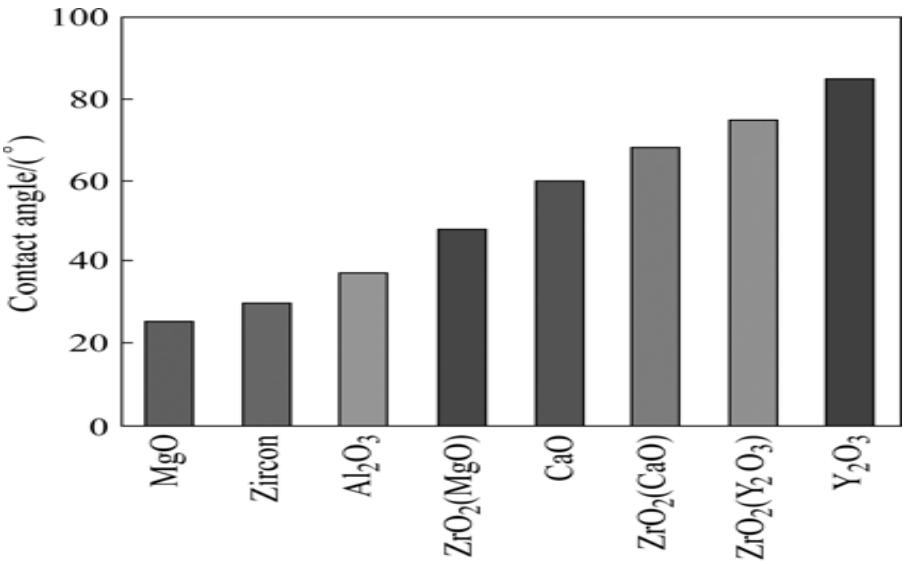

Figure 2-17. Contact angle between liquid Ti50Al and different mould materials [46].

The ability of a refractory material to resist wetting by a molten metal is a valuable property because interaction can only occur if both metal and mould contact. Thus, poor or non-wetting of a refractory by a liquid metal or alloys tends to indicate an increased resistance to attack by the molten metals [45].

Contreras, A (2007) [59] studied the wetting behavior of the contact angle change rate of an Al-Cu alloy on the TiC substrate, and found that the change of the metal drop contact/wetting angle on the ceramic substrate was a function of the interaction time. By

studying the wetting process of the molten metal drop, the contact angle change on the substrate can be separated into three parts, see Figure 2-18.

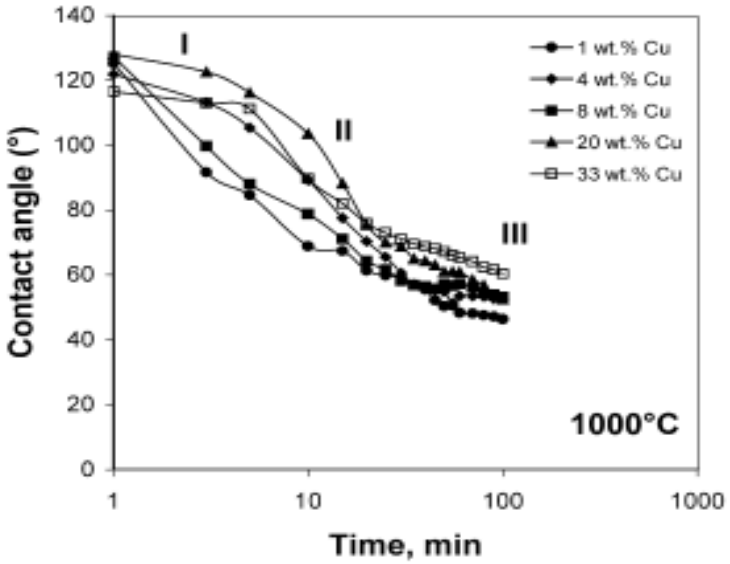

Figure 2-18. The contact angle change at different contact times. [56]

In the first part, I, the metal is de-oxidized, i.e. the oxide layer on Al alloy surface, and in this stage the interaction between metal and shell has not yet begun. In part II, the interaction between the mould starts and the wetting angle between metal and shell changed dramatically. In Part III, the interaction is finished and the new wetting angle was established between the metal and interaction products. Plotting the drop contact angle change rate against the interaction temperatures in part II, the metal spreading activation energy can be calculated from an Arrhenius relationship [59, 60]. A large activation energy value means the wetting/spreading of metal on ceramic shell is not only dominated by viscous flow, and the interaction between metal and shell is the reason for the metal spreading behaviour [61-64].

Table 2-4 shows the calculated wetting activation energy based on this method, and Figure 2-19 shows the experimentally observed interaction layer thickness.

Table 2-4. The wetting interaction energy of a Al-Cu alloys on TiC substrate.[55]

Alloy (wt%)	E_a (kJ/mol)
Al–1Cu/TiC	145.30
Al–4Cu/TiC	68.03
Al–8Cu/TiC	63.86
Al–20Cu/TiC	45.07
Al–33Cu/TiC	108.55

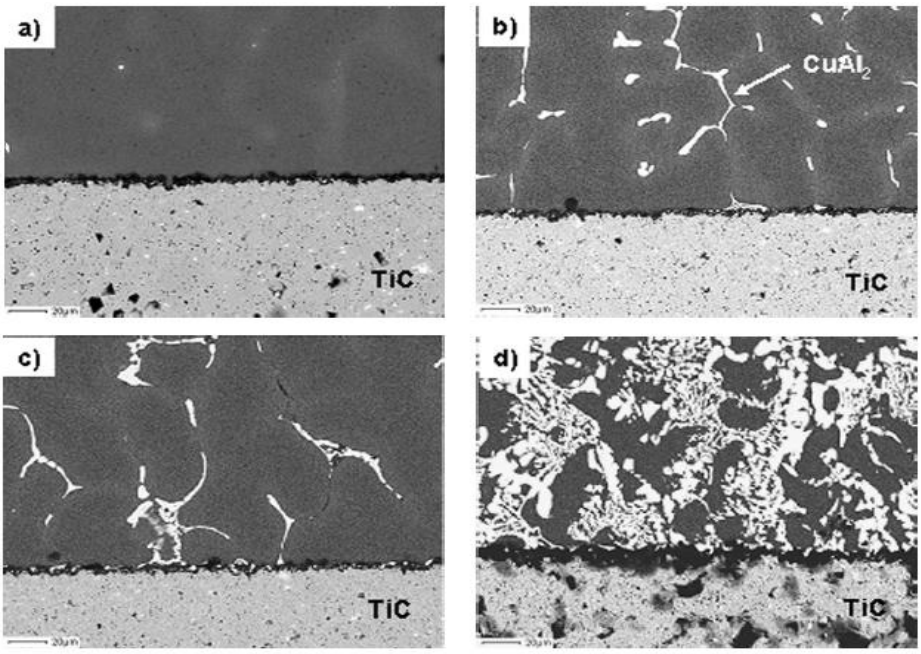

Figure 2-19. Cross-sections of the sessile drop–substrate interface obtained at 900 °C. (a) Al–1Cu/TiC, (b) Al–4Cu/TiC, (c) Al–8Cu/TiC, and (d) Al–20Cu/TiC.[55]

There are no refractory materials which have been found that are absolutely inert to the molten titanium or TiAl alloys during the casting process. Research into refractory materials for investment casting began last century. Barbosa *et al*, 2001 [65]; Saha et al, 1989, 1990 [66-67], used a SiO_2 based face coat mould and have an interaction layer larger than 500 μm,

later, oxides CaO, ZrO_2, Al_2O_3 were also developed for the face coat, but still, serious interaction between the mould and molten metal were seen. Therefore, for developing the aerospace market, the requirement to develop suitable materials for investment casting Ti alloy, especially TiAl alloys has been undertaken for the last 30 years.

2.2 Mould/shell materials selection

2.2.1 Chemical reactivity of Ti and Al in Ti-Al alloy

Kostov, A, 2006 [68] calculated the activity of titanium and titanium aluminide alloys at different temperatures using the Factstage thermo-chemical software and data base [69]. The activity of Ti and Al as a function of titanium concentration was calculated at the temperature arrange between 1273 and 2273 K and is shown in Figure 2-20.

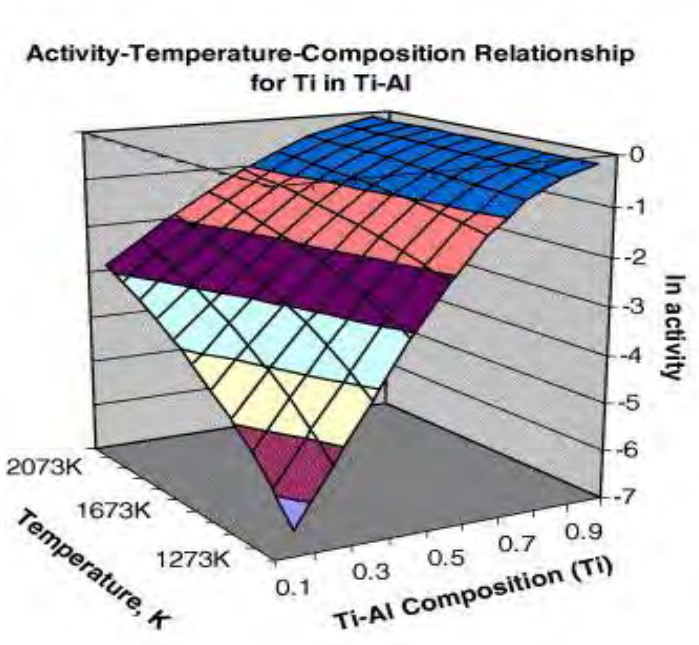

Figure 2-20. The activity-temperature-composition relationship for Ti in Ti-Al alloy [68].

Form the Kostov‘ [68] study, the activity-temperature relationship of TiAl alloys shows that Ti activity decreases with increasing Al mole fraction and with decreasing temperature. Therefore, compared with commercial pure titanium alloys, the reactivity for the gamma TiAl alloy is lower.

2.2.2 Thermodynamics of the dissolved solute in Ti alloy

The inertness of ceramics with Ti alloys depends on their thermodyanamic stability. Three titanium oxides have been selected that may occur in reactions with the molten Ti alloy. Those are TiO, TiO_2 and Ti_2O_3. The free energy of Ti-oxides as a function of temperature is shown in Table 2-5 [68].

Table 2-5. The Gibbs formation energy ($\triangle G_r$) as a function of temperature.

Oxides	ΔG_f^0	T, K
TiO	$-542.95+0.1005T-3\times10^{-6}T^2-6\times10^{-10}T^3$	273–1973
Ti_2O_3	$-1523.1+0.3099T-3\times10^{-5}T^2+7\times10^{-9}T^3$	273–2073
TiO_2	$-945.42+0.1908T-1\times10^{-5}T^2+3\times10^{-9}T^3$	273–2073

Because all the titanium oxides have large negative formation energy based on Table 2-5 at all investigated temperatures, the oxides TiO, Ti_2O_3 and TiO_2 are stable and not will interact with the Ti alloy. However, in real casting conditions, the interaction between the metal and mould is more complicated such that the chemical inertness of the ceramic shell can not be determined by only considering the thermodynamic data alone, other factors such as the mould pre-heating temperature, melt fluidity and the relative movement between the crucible

wall and the melt are also need to be considered [197].

2.2.3 Development of new refractory materials for TiAl casting

The research of refractory materials and the development of suitable slurry to make the investment cast mould for titanium and titanium aluminides started last century. Some basic requirements of the refractory mould are shown in below [28].

1) The face coat should have high chemical inertness against molten TiAl alloy.

2) Low water vapour and gas absorption, which reduce the amount of gas released during the casting process.

3) Low thermal conductivity, reducing the formation of defects caused by rapid solidification.

4) Easily to productionize.

2.2.4 First stage of materials selection (from 1960-1970s)

At this stage, the shell development for reactive alloys is based on the cheap but high melting temperature graphite mould.

Graphite moulds made from colloidal graphite with a particle size around 1-5 μm had been developed in 1966, US patent No. 3241200 [70]. Later, patents US 3296666 [71], US 3256574 [72], US 3266106 [73], and US 3321005 [74] are reported to use this material but

the serious interaction between molten metal and alloys had been found, therefore new mould development was urgently required.

Around the 1970s, a tungsten and molybdenum coated graphite mould was developed as an improvement for casting reactive alloys such as titanium, zirconium etc. and US patent No 3422880 [75], 3537949 [76] and 3994346 [77] has reported this new invention. Unlike pure graphite, the shell manufacturing methods were slightly more complicated than the original versions. Robert Brown *et al*, (1976) [77] reported that ‗the first dip coat includes a tungsten and/or molybdenum compound inhibitor-former which was reducible by hydrogen to metallic tungsten or molybdenum'. After removal of the pattern, the green mould was dried and then pyrolyzed in an atmosphere of hydrogen under conditions predetermined to convert the inhibitor-former to the metallic condition. This created, on the mould interface, a coating of metallic Mo and W which serve as a physical barrier, inhibiting the reaction of molten metal with the mould. Although this kind of material had less interaction between mould and metal compared with the graphite mould, the interaction was still very serious.

2.2.5 The secondary stage of mould development --metal oxide (from 1970s-2000s)

New developments of the ceramic shell based metal oxide were begun in the 1960s by selecting metal oxides from the Ellingham diagram, see Figure 2-21.

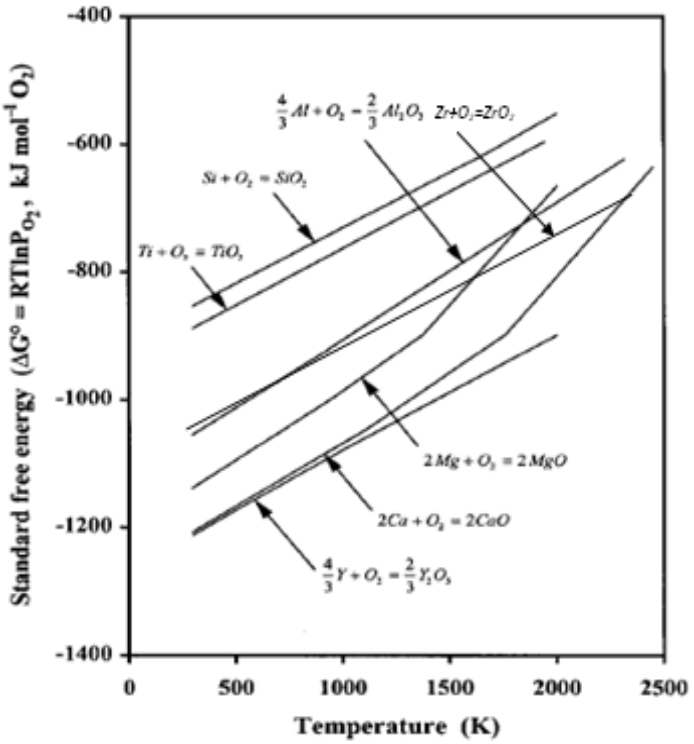

Figure 2-21. Standard free Gibbs energy of formation some relevant oxide. [45]

In order to better understand the reactivity of TiAl alloys, the decomposition Gibbs energy of different oxides should be considered together with the TiAl oxidation data. Kostov. A, *et al* (2006) [68] predicted the thermodynamic stability of crucible oxides in contact with molten titanium alloys by calculating the reaction Gibbs energy changes $\triangle G_r$, based on the reaction equation 2-3 below:

$$MxOz \rightarrow ZO(Ti\text{-}Al) + xM \qquad 2\text{-}3$$

where M illustrates any metallic/non-metallic element, x and z is the numerical constant.

The results, shown in Figure 2-22, suggested that yttria, calcia and zirconia have good oxidation stability compared to silica and magnesia at high temperatures.

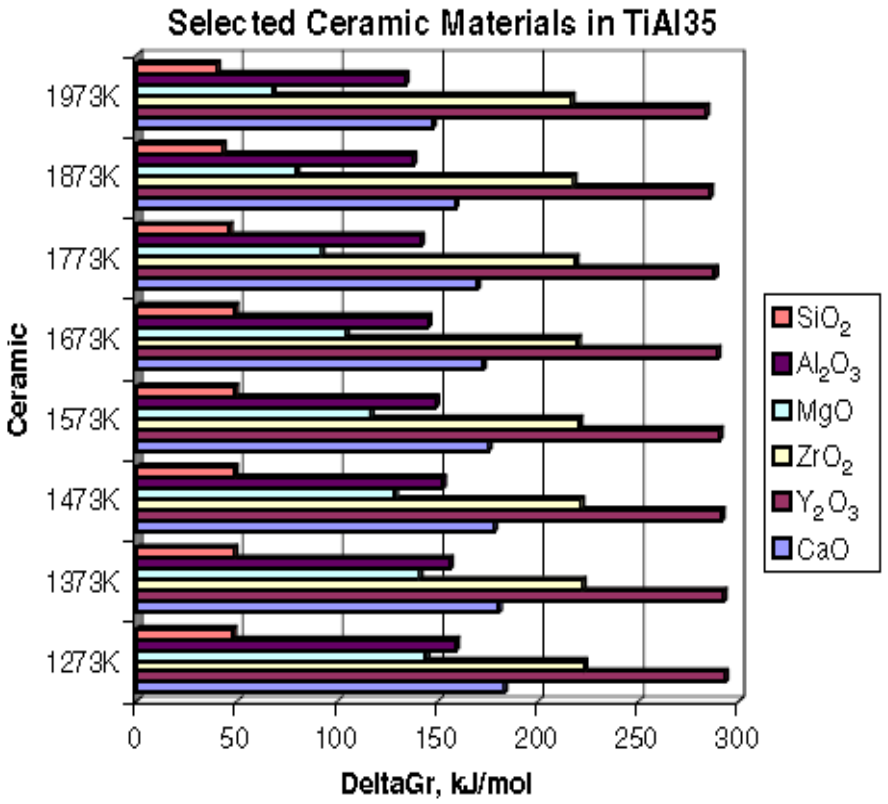

Figure 2-22. Estimated Gibbs formation energy of selected ceramic in Ti-35Al alloys [68].

By researching the thermodynamic inertness of variety oxides for many years, some mould materials such as ZrO_2, Y_2O_3, and ThO_2 have been chosen to make the shell mould for casting TiAl alloy at temperatures around 1650 °C.

Zirconia has a density of around 5.56×10^3 kg/m^3 [122] and very high melting temperature around 2677 °C, which allows it to be used to temperatures around 2500 °C. Due to the very large volume change associated with its phase transformation, ZrO_2 based moulds are usually used by adding small amount of compounds such as CaO, MgO or Y_2O_3 to stabilize the cubic structure during sintering process [78, 79]. It acts as a relatively inert interface

between the molten titanium alloy and the more reactive and less costly refractory materials in the backup coats.

Yttrium oxide has density around 4.84×10^3 kg/m^3 [122], and melting temperature around 2410 °C. Phase transformations will not cause a big volume change in the shell. Compared with ZrO_2, Y_2O_3 can provide an even more inert interface as the face coat material, but at higher cost. Renjie.C *et al*, (2010) [80], used a cold isostatic pressed yttria powder mould and found very little interaction between the mould and molten metal.

The rare earth material ThO_2 has a density around 9.63×10^3 kg/m^3 [122], and melting temperature around 3300 °C. The thermal expansion coefficient of this oxide is same as ZrO_2, and it is very inert at temperatures below 2700 °C. ThO_2 is the most stable oxide against molten TiAl alloys, but because of the radiation hazard, it was only used in making ceramic shells for casting TiAl for a short period of time [81].

Therefore, when comparing all the thermal properties and the hazard of different oxides, yttria, as a rare earth metal oxide, is frequently used to make refractory mould for TiAl investment casting.

2.2.6 Yttria based mould and its pre-gelation problems

Yttrium oxide is known to provide an even more inert interface than zirconium oxide, but the development of an yttria based slurry took a very long time. The main problem which limits

the use of yttria based slurries is pre-gelling which takes place during or after the slurry making process, and shortening the slurry life to minutes [82-83].

Yasrebi. M [84] suggested there are two main gelling mechanisms of the slurry. One is the different components in a slurry may interact with each other, and cause aging over time. For example, the dissolution of polyvalent cationic ions from oxide flours are preferential absorbed at the surface of the negatively charged colloidal silica particles [84-87]. The other reason may be due to the inorganic binder such as colloidal silica being chemically reactive, it permanently bonds the particles in the slurry as the result of siloxane formation between powder particles during face coat drying [88].

As was known, the dissolution of oxide flours can influence the slurry life [86]. Therefore, the modification of the yttria slurry was started by reducing the dissolution of yttria flour in the slurry, which can be achieved both by reducing the water content in the slurry [89-91] and replacing pure yttria powder to a fused yttria-(1-10 wt%) zirconia powder [85, 92]. Until 1998, two binders, ammonium zirconium carbonate (Ti-coat) and zirconium acetate, were developed [93-94] and successfully used in yttria face coat slurries to date. But the life of the new slurry is still very short (less than 3 hours).

2.2.7 The third stage of mould development – non-gelation slurry development (from 2000s-now)

At this stage, because a lot of methods were known previously to stabilize colloidal suspensions i.e. preventing the suspensions from agglomeration, while simultaneously reducing the dissolution rates [95], scientists tried to design slurries which can last for days rather than a few hours.

The improvements were made by adding fluoride containing compounds into yttria to make new slurry and thus increasing the slurry life. EP patent 1,992,430 (A) [96] published in November 2008 opened a new window for researchers. This patent illustrated that the slurry containing a fluoride such as YF_3, ZrF_4, AlF_3, TiF_4, TiF_3, LaF_3, and ZrF_3 were less sensitive to water. The Binder used in this research were Ti-coat, yttria sol, and zirconia sol. The slurry with the longest life used a YAZ (Y_2O_3-0.5wt%Al_2O_3-0.5wt%ZrO_2) powder blend with 0.8 wt% ZrF_4, together with Ti-coat sol as the binder. The slurry life was increased from a few hours to 150 hours, see Figure 2-23.

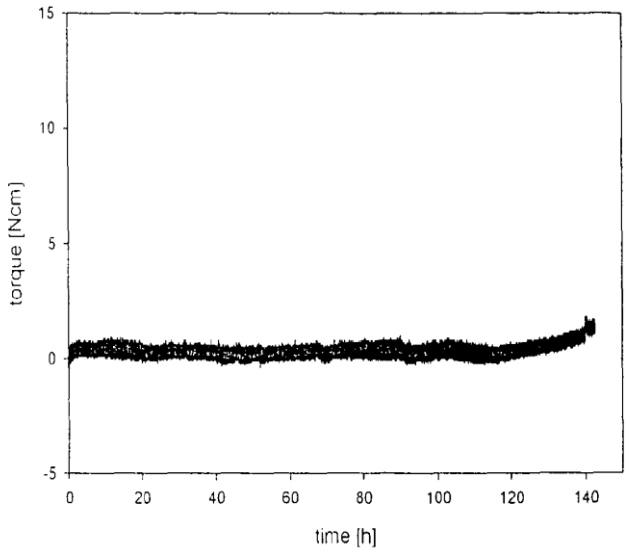

Figure 2-23. The life time of the new designed slurry.[96]

Then, Treibacher Industrie A.G. in 2010 [97] developed a fluorine-doped (F-doped) filler to replace pure yttria in the slurry. This new filler increases the life of the slurry to more than 150 days, see Table 2-6. The benefit of using fluorine is to reduce the dissolution of the yttria powder in the slurry, thereby making the slurry possible by reducing the aging [97-98]. Because fluorine has a low evaporation temperature at above 1000 °C [155], this type of face coat has good chemical inertness of the face coat after mould sintering (>1200 °C).

Table 2-6. The life time and the composition of the reported patent [97]

		Summary of the results						
Raw material flour	Dopant flour	Fluorine [wt %]	heat-ing rate [° C./ min]	cal-cination temper-ature [° C.]	dwell time [h]	binder system	Ratio binder:flour(:H_2O)	Slurry lifetime [h]
Y/Al/Zr-Oxide (95.88/0.12/4)	$Zr_7O_{8.79}F_{9.71}$	2.4	1.1	450	7	Ammonium Zirconium Carbonate	1:3.3	70.3
Y/Al/Zr-Oxide (95.88/0.12/4)	$Zr_7O_{8.79}F_{9.71}$	1.7	1.1	400	4	Ammonium Zirconium Carbonate	1:3.6	44.9
Y/Al/Zr-Oxide (95.88/0.12/4)	$Zr_7O_{8.79}F_{9.71}$	0.1	1.1	400	4	Ammonium Zirconium Carbonate	1:3.3	21.6
Y/Al/Zr-Oxide (95.88/0.12/4)	$Zr_7O_{8.79}F_{9.71}$	6.9	1.1	400	4	Ammonium Zirconium Carbonate	1:2.7	>110 days
Y_2O_3	$Zr_7O_{8.79}F_{9.71}$	1.9	1.1	400	4	Ammonium Zirconium Carbonate	1:3.3	74.1
Y_2O_3	$Zr_7O_{8.79}F_{9.71}$	1.9	1.1	1100	4	Ammonium Zirconium Carbonate	1:3.3	26.5
Y_2O_3	$Zr_7O_{8.79}F_{9.71}$	2.0	1.1	900	4	Ammonium Zirconium Carbonate	1:3.3	26.9
Y_2O_3	$Zr_7O_{8.79}F_{9.71}$	1.9	1.1	800	4	Ammonium Zirconium Carbonate	1:3.3	33.4
Y_2O_3	$Zr_7O_{8.79}F_{9.71}$	2.0	1.1	300	4	Ammonium Zirconium Carbonate	1:3.3	50.3
Y_2O_3	YF_3	2.0	1.1	400	4	Ammonium Zirconium Carbonate	1:3.3	35.7
Y_2O_3	YF_3	2.0	1.1	1100	2	Ammonium Zirconium Carbonate	1:3.3	17.1
Y_2O_3	YF_3	1.9	1.1	900	4	Ammonium Zirconium Carbonate	1:3.3	16.3
Y_2O_3	YF_3	1.9	1.1	800	4	Ammonium Zirconium Carbonate	1:3.3	26.1
Y_2O_3	YF_3	2.1	1.1	300	4	Ammonium Zirconium Carbonate	1:3.3	26.7
Y/Al/Zr-Oxide (95.88/0.12/4)	LaF_3	1.3	1.1	550	4	Ammonium Zirconium Carbonate	1:3.3	47.0
Y/Al/Zr-Oxide (95.88/0.12/4)	YbF_3	1.6	1.1	550	4	Ammonium Zirconium Carbonate	1:3.3	44.7
Y/Al/Zr-Oxide (50/25/25	$Zr_7O_{8.79}F_{9.71}$	1.7	1.1	400	4	Ammonium Zirconium Carbonate	1:3.2	>150 days

.

Although yttria has very inert thermochemical properties, the cost of this slurry is very high due to the increased price of the filler and binder. So, some high melting point metal compounds have been used to make the mould for TiAl investment casting. These metal compounds including carbides, nitrides, and borides [99-101].

In 2009, Kartavykh A.V.*et al* [99], first used AlN to make the mould for a TiAl-Nb alloy but found a very large interaction between the molten metal and shell, Figure 2-24.

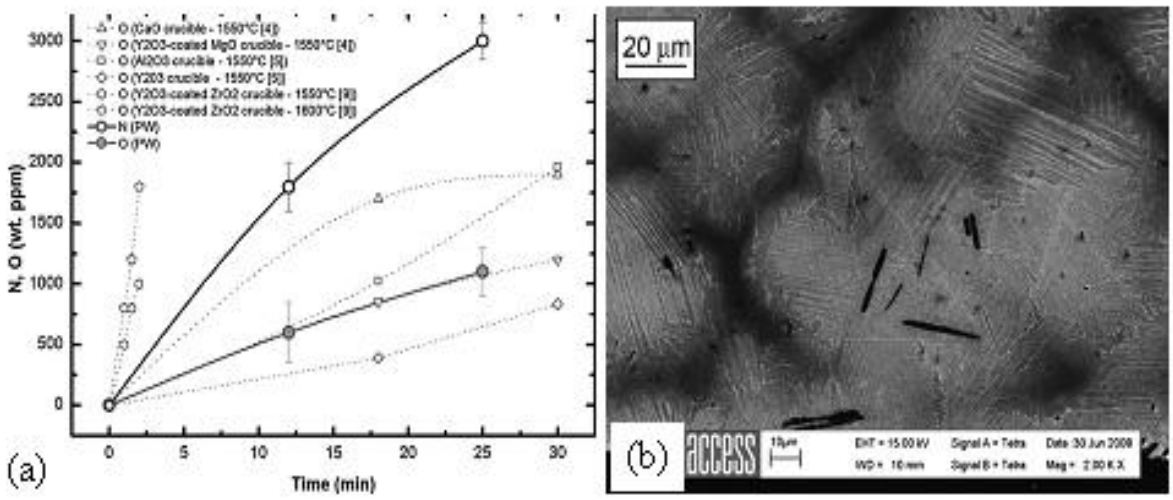

Figure 2-24. (a) The major interstitial pickup by alloy vs. the superheating time for an AlN crucible use in comparison with the literature data for oxide crucibles (PW: present work). (b) The bottom of the casting microstructure (SEM–BSE) image. [99]

A year later, Kartavykh A.V. *et al* [100] and Shen Bin [101] used boron nitride based materials to make the casting mould but also found a very thick interaction zone at the metal/ceramic interface, see Figure 2-25. Even now, the improvement and development of new slurries for casting titanium alloys and TiAl alloy is still ongoing.

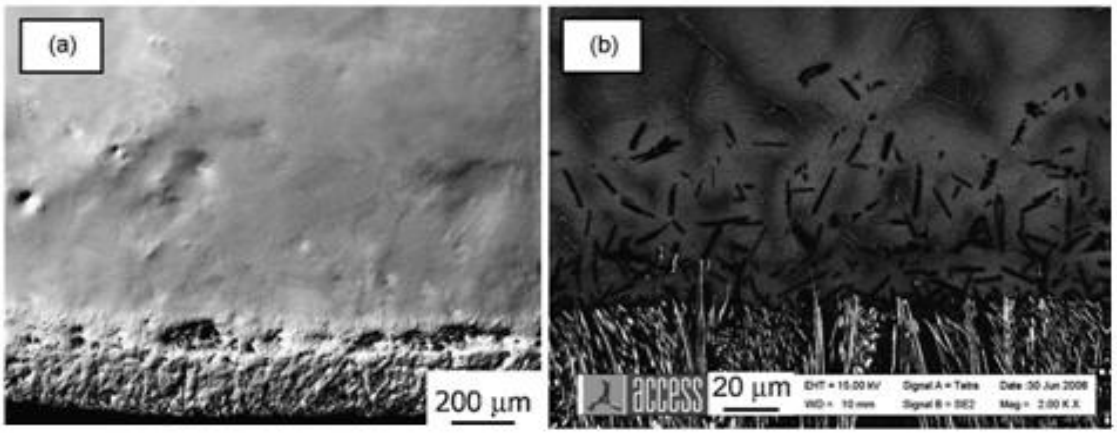

Figure 2-25. Optical micrographs (on the left) and SEM-BSE microstructure images (on the right) at the interface between the reaction layer and Ti–46Al–8Nb alloy in samples processed at 1670 °C in BN crucible for 5 min.

2.2.8 Summary of the TiAl alloy processing background and the objective of this project

Investment casting is one of the most promising ways to produce near net shape TiAl turbine blades for aerospace applications. However, interaction between metal and mould is undesirable, degrading blade quality by forming a hard, brittle layer at the interface.

Industrial production requires moulds, when used for TiAl casting, which have a high chemical inertness, good sintering properties and strength. Slurries for use in mould making should have a long life time and stable chemical properties. Yttria (Y_2O_3) as a mould face-coat filler material has an improved chemical inertness in contact with molten metal and is used in TiAl mould production. The major problem of using this kind of face-coat is the limited life of the yttria slurry due to pre-gelation of the slurry.

This research aims to design low cost water-based binder slurries to replace the sol in yttria slurry, increasing slurry life time, whilst achieving a reasonable sintering ability combined with thermal stability and chemical inertness.

2.3 The new design of water-based binder yttria slurry

2.3.1 The introduction of new designed slurry

Compared to the commercial slurry, the new slurry replaced the binder (sol) with water, and the sintering additives were added into the filler to enhance face coat sintering properties,

while polymer was also added to improve the shell green strength, see Table 2-7. By replacing colloidal sol with water, the cost of slurry will be reduced therefore making this slurry more economically attractive.

Table 2-7. The changed slurry composition of the new slurry system compared to the conventional used slurry system.

Composition	**Traditional yttria slurry**	**New designed slurry**
Filler	Yttria-based powder (could be F-doped, YAZ)	Yttria powder (with different sintering additives)
Binder	Colloidal particle Sol (yttria sol, silica sol, Ti-coat sol)	De-ionised Water
Polymer	Poly-vinyl Acetate (option)	High temperature polymer

2.3.2 Sintering mechanisms and filler powder design (promoted sintering by added sintering additives)

The sintering of particles can be divided into two categories [102]; first is solid state sintering which is mostly related to non-liquid phase sintering, and takes place at comparably low sintering temperatures. The second is liquid state sintering, which mostly happens at very high sintering temperatures. For powder sintering, they both will occur when increasing the sintering temperature.

2.3.2.1 Solid state sintering

For solid state sintering, the mechanisms of sintering polycrystalline materials are defined by the different paths used to transport materials. Material is transported from regions of higher

chemical potential to regions of low chemical potential (the neck between particles) [102]. There are at least six sintering mechanisms in sintering polycrystalline materials [103]. They are schematically shown in Figure 1-26.

The surface diffusion mechanism describes a process in which the material transport from the material surface to the neck, and lattice diffusion (bulk diffusion) mechanism is used to define a process in which the material in the grain boundary or surface transport to the neck through movement of atoms or vacancies. The grain boundary diffusion mechanism is described as a process in which the materials transport to neck through the grain boundary. The plastic flow mechanism illustrated is a process where materials move to the neck through the dislocations in the particles.

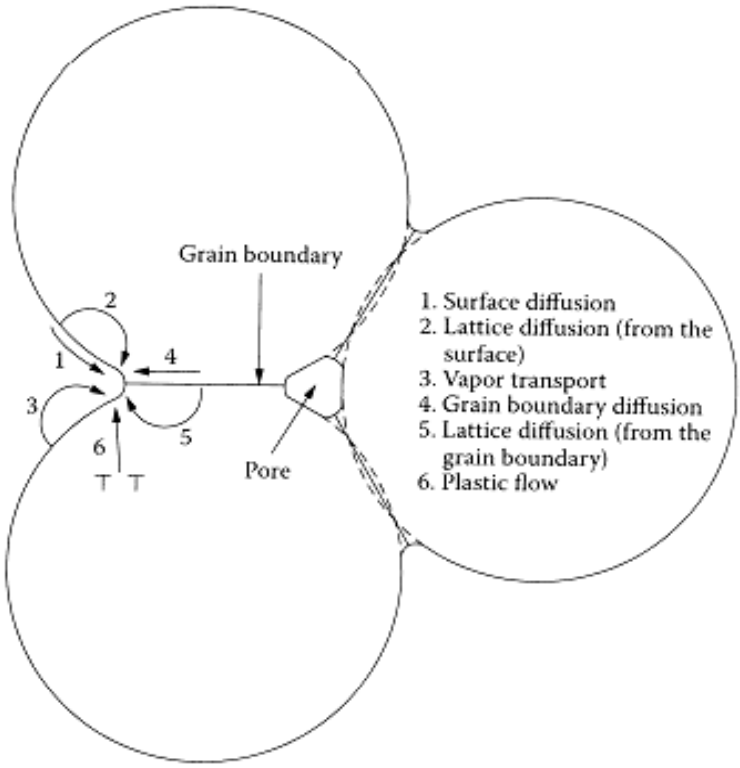

Figure 2-26. Six sintering mechanisms of a consolidate mass of crystalline particles. (1) surface diffusion, (2) lattice diffusion from the surface. (3) vapour transport, (4) grain boundary diffusion, (5) lattice diffusion from the grain boundary, (6) plastic flow. [103]

All six mechanisms shown above can promote bonding and growth of necks between ceramic particles, therefore increasing the strength of the sintered ceramic body. But only some of them can lead to powder compact densification. E.g. surface diffusion and lattice diffusion from the particle surfaces to the neck, and vapour transport (mechanism 1, 2, 3) lead to neck growth without densification and are referred to as non-densifying mechanisms. Grain boundary diffusion and lattice diffusion from the grain boundary to the pore (mechanism 4 and 5) are the most important densification mechanisms in sintering polycrystalline materials. Plastic flow by dislocation motion (mechanism 6) also leads to neck growth and densification but is more common in the sintering of metal powders. The

non-densification mechanisms will change the curvature of the neck surface and so reduce the rate of the densification. All the densification mechanisms and their effect are listed in below Table 2-8.

Table 2-8. Mechanisms of sintering in polycrystalline and amorphous materials.[103]

Type of solid	Mechanism	Source	position	densification	Non densification
polycrystalline	Surface diffusion	Surface	Neck		Yes
	Lattice diffusion	Surface	Neck		Yes
	Vapour diffusion	Surface	Neck		Yes
	Grain boundary diffusion	Grain boundary	Neck	Yes	
	Lattice diffusion	Grain boundary	Neck	Yes	
	Plastic Flow	Dislocation	Neck	Yes	
amorphous	Viscous flow	Unspecified	unspecified	yes	

The whole sintering process consists of three different stages; the initial stage, the intermediate stage and the finial stage. The initial sintering stage is always associated with powder particles‘ neck growth by various diffusion mechanisms such as vapour transport, plastic flow, etc. At this stage, the large surface curvature of powder is removed and there is around 3 to 5 % linear shrinkage taking place. The intermediate stage begins when the pores reach their equilibrium shapes. It covers the major part of the sintering up to around 90 % of final density. Final stage starts when pores pinch off and become isolated at the grain corners

and disappear to achieve final density. [104]

The simplest ‗two sphere neck growth model' describes the shrinkage in equation 2-4 & 2-5 [105] is shown in Figure 2-27 with the definitions of parameters.

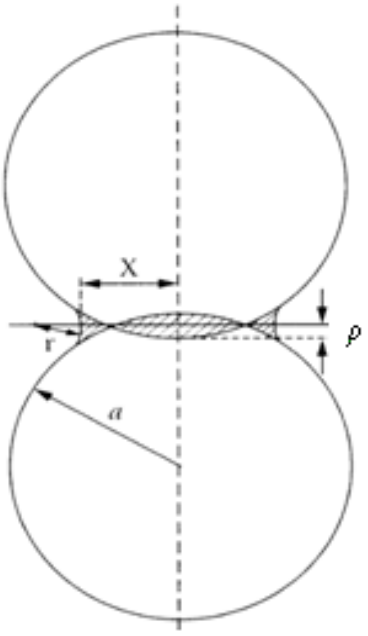

Figure 2-27. A schematic two sphere model of neck growth.

$$\left(\frac{\rho}{a}\right)=\frac{\Delta L}{L_0} \qquad 2\text{-}4$$

$$\left(\frac{X}{a}\right)^m=\frac{H}{a^n}t \qquad 2\text{-}5$$

where ρ is the necking distance (m), a is the particle diameter (m), X is the distance from the particles contacting centre to the lowest point of the neck (m), ΔL is the pellet diameter (m) after sintering, L_0 is the pellet original diameter. m, n are numerical components that depend on the mechanisms of sintering, and H is a function that contains the geometrical and

materials parameters of the powder system. The *m*, *n*, and *H* values depend on different mechanism and are shown in Table 2-9.

Table 2-9. The constant *n*, *m* value of different sintering mechanisms in initial sintering stage. [106, 107]

Mechanisms	***m***	***n***	***H***
Surface diffusion	7	4	$56D_s\delta_s\gamma_{sv}\Omega/kT$
Lattice diffusion from the surface	4	3	$20Dl\gamma_{sv}\Omega/kT$
Vapour transport	3	2	$3p_o\gamma_{sv}\Omega/(2\pi mkT)^{1/2}kT$
Grain boundary diffusion	6	4	$96D_g\delta_{gb}\gamma_{sv}\Omega/kT$
Lattice diffusion from grain boundary	5	3	$80\pi Dl\gamma_{sv}\Omega/kT$
Viscous flow	2	1	$3\gamma_{sv}/2\eta$

* D_s, D, D_{gb}, diffusion coefficients for surface, lattice, and grain boundary diffusion, δ_s, δ_{gb} thickness for surface and grain boundary diffusion; γ_{sv}, specific surface energy; P_o, vapour pressure over a flat surface; *m*, mass of atom; *k*, Bolzmann constant; *T*, absolute temperature; η visicosity.

2.3.2.2 Liquid phase sintering

Compared to solid state sintering, liquid state sintering has a transient liquid phase appearing during the sintering process, this transient liquid phase leads to an enhanced densification through rearrangement of the particulate solid and matter transport through the liquid, see Figure 2-28. The activated sintering is described a process, in which minor amounts of additives that segregate strongly to the grain boundaries to enhance mass transport along the

grain boundary, giving rise to accelerated densification [108]. If sufficient liquid is present (25-30 vol%), rearrangement of the solid phase coupled with liquid flow can lead to a fully dense material, without the need for contributions from other process. [108]

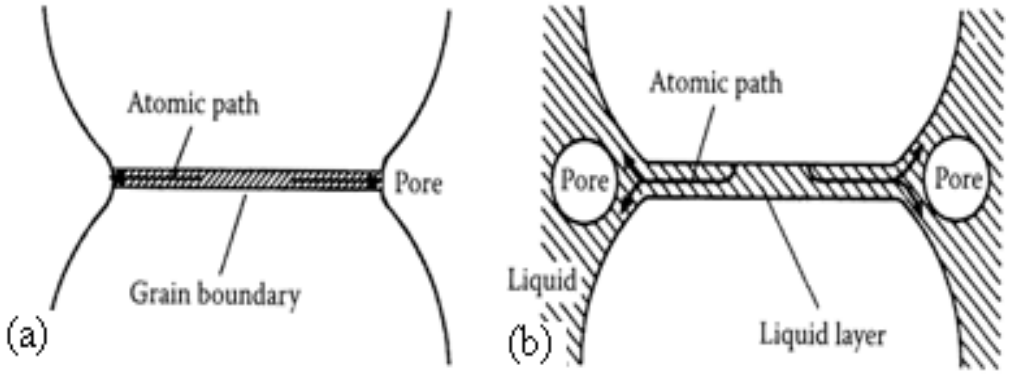

Figure 2-28. ‗Two sphere model' of the powder sintering (a) solid state sintering, and (b) liquid state sintering. [109]

The sintering mechanism of liquid phase sintering consists of three stages; stage 1 is the rearrangement and liquid redistribution; stage 2 is the solution-precipitation; stage 3 is the Oswald ripening. [110, 111]

In the stage 1, after forming the liquid, as the liquid wets and spreads over the solid surfaces, particles begin to rearrange very quickly. Rearrangement determines the initial microstructure of the sintering compact, which influences further densification and microstructure development. In stage 2, rearrangement decreases and the solution-precipitation mechanism become dominant [110, 111]. The major process during the solution-precipitation process is densification and coarsening of the microstructure. There

are two models of densification; first is the densification by flattening [112] and the densification accompanied by Ostwald ripening [113], see Figure 2-29. The third stage, densification speed slows down and the microstructures are coarsening.

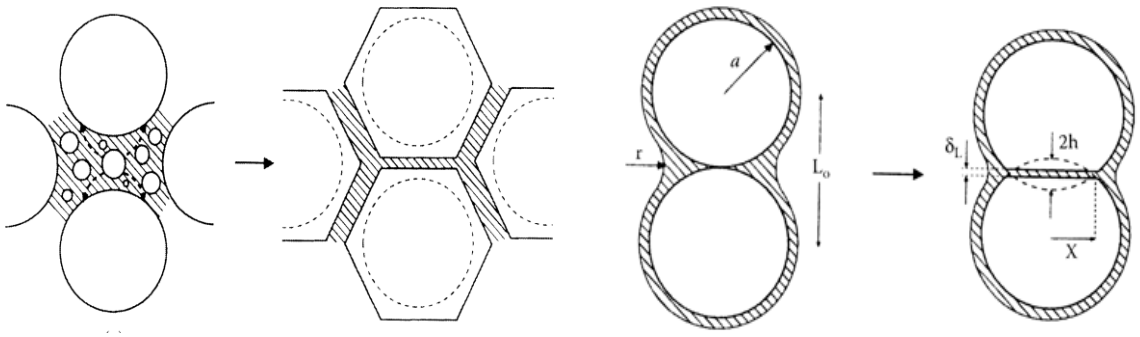

(a) (b) (c) (d)

Figure 2-29. Two densification mechanisms of liquid state sintering (a)&(b) is the Oswald ripening (dash area represents liquid phase), and (c)&(d) by contact flattening. [114]

Therefore, compared to the solid state sintering process, liquid state sintering has higher efficiency in promoting powder sintering at lower sintering temperatures. So, in order to promote yttria powder sintering, sintering aids were designed and added into yttria powder to form low temperature liquid transient phases to help enhance the yttria based face coat sintered at relatively low temperatures.

2.3.3 The other factors which can influence the sintering properties of the powder

There are many other factors that affect the sintering properties of face coat filler powders such as particle size and distribution, particles shapes and particle structures, particle green densities as well as the sintering temperatures [115-121].

2.3.3.1 The powder particles size and distribution

The sintering properties of a powder compact are strongly dependent on particle size. The reduction of particle size can accelerate sintering, and enhance sintering rates at lower sintering temperatures [115]. E.g. for sintering nano-sized yttria powder, the actual sintering temperature is 1000 °C, much lower than its theoretical sintering temperature around 1700 °C [116, 117]. But, the smaller the particles size, the increased chance for them to agglomerate and accelerate the hydration of the particles in the solutions due to the larger electrically charged surface.

2.3.3.2 Particle shape, structure and compact

Particle shape influences primarily the initial packing or green density. Mohamed N (2008) [118] illustrated that the deviation from the spherical or equiax shape leads to a reduction in the packing density and a reduction of densification. Compacts of acicular (elongated) particles can be sintered to high density only if the powder particles are aligned during packing. Normally, the wider the particle size range the denser the green compact, and the better the sintering. Most alloy powders tend to have more spherical shapes while oxide powders have angular or irregular shapes. Figure 2-30 and 2-31 shows the different morphology of oxide powders and alloy powders.

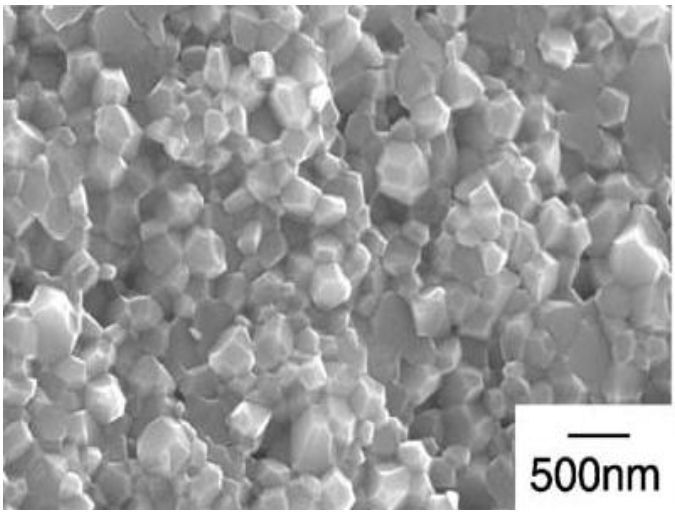

Figure 2-30. A SEM image of TiO_2 powders.[119]

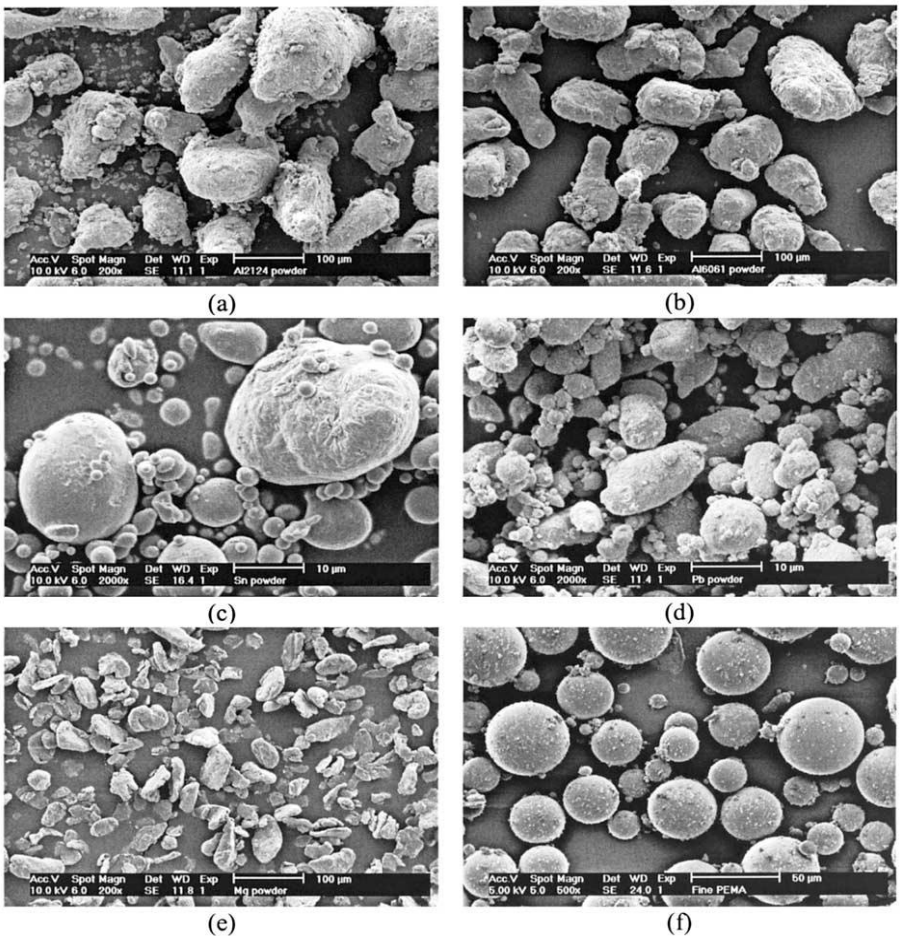

Figure 2-31. Scanning electron images of (a) pre-alloyed Al 2124, (b) Al 6061, (c) Sn, (d) Pb, (e) Mg and (f) PEMA powder [120].

2.3.3.3 Sintering temperature and speed

The heating schedule and isothermal sintering temperatures are very important for the powder compact to achieve final density. Rather than very simple heating and cooling cycles, industrially sintered power always has a more complicated heating profile, and each heating and holding stage has a different purpose. There are at least 5 basic stages for sintering powder. Stage 1 is the binder burn out; stage 2 is the low temperature soak to promote homogenization or the reaction of powder components, e. g. sintering precursor decomposition; stage 3 is the heating-up to the sintering temperature; stage 4 is the isothermal sintering; stage 5 is the cooling down stage. A example of real sintering profile by sintering Fe-1.25 Mo-1.4 Ni-0.42 Mn (wt%) powder is illustrated in Figure 2-32 [121].

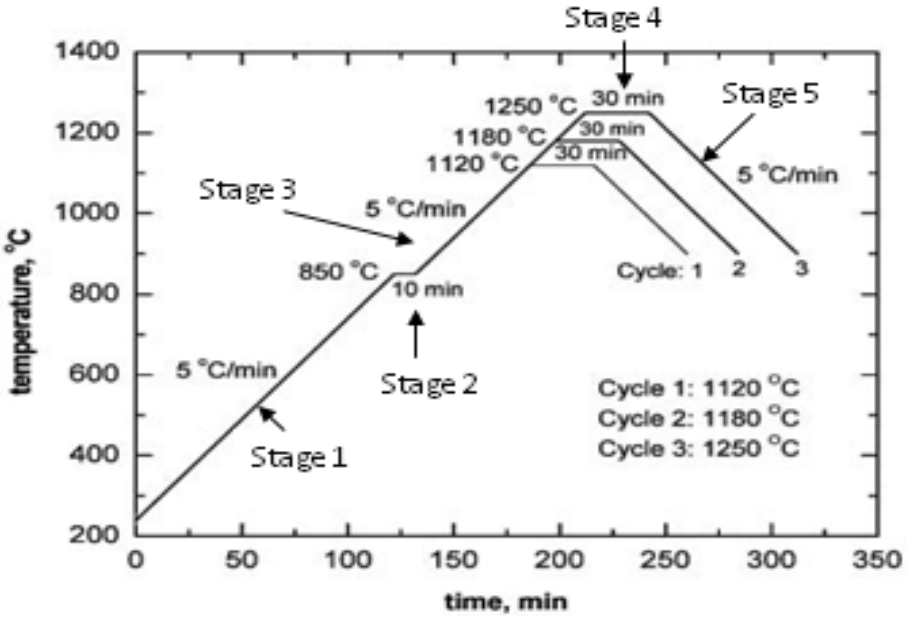

Figure 2-32. The heating cycle of Fe-1.25 Mo-1.4 Ni-0.42 Mn (wt%) powder.

A higher sintering temperature can enhance powder sintering by promoting mater diffusion and transport speed, but needs to avoid grain coarsening taking place rather than

densification. Sometimes, the industry will have some specific heating profiles that can give the highest economic benefits.

2.3.4 Sintering additives

In order to explore the needs sintering aids to help a yttria face coat sinter at a lower firing temperature, a lot of research has been done and the effective elements or compounds are listed below：

2.3.4.1 Titanium oxide (TiO_2)

Titanium dioxide exists in nature as the well-known minerals rutile, anatase and brookite. It has three different forms, a monoclinic baddeleyite-like form, an orthorhombic α-PbO_2-like form, and the equilibrium form rutile [122]. TiO_2 has the density of around 4×10^3 kg/m^3. Gasgnier, G and his co-workers in 1994 [123] found that a small amount of titanium oxide can effectively enhance the sintering properties of yttria at a lower sintering temperature compared to other metal oxides. Fully dense of yttria parts can be produced by sintering at 1400 to 1500 ℃. They also reported that the basic mechanism reducing the yttria sintering temperature by adding TiO_2 is that titanium oxide will form some low temperature eutectic/eutectoid phases with yttria, these transient liquid phases will promote grain growth therefore densification of the ceramics.

The effect of using different titanium doped yttria compounds are listed in Table 2-10 from

Gasgnier, G [123]. The most effective titanium containing species is Y_2TiO_5 and Ti $(OC_4H_9)_4$. Based on this research, the TiO_2 lower the yttria powder sintering temperature around 300 °C. Therefore, the sintering temperature reduces from 1700 °C for pure yttria to around 1400 °C by using less than 2 wt% of titanium oxide. The final dense body of the ceramic is shown in Figure 2-33.

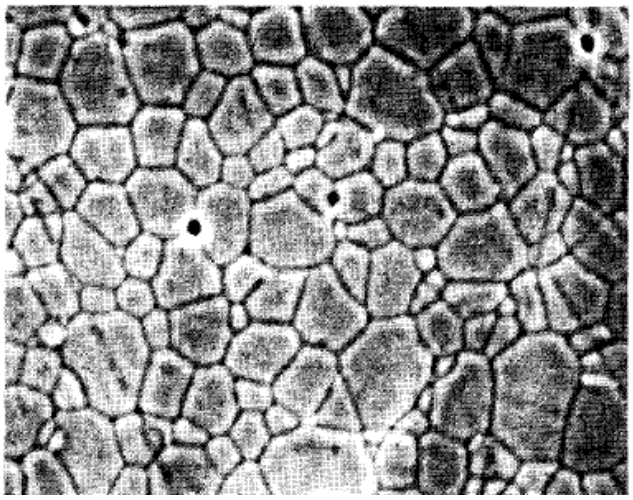

Figure 2-33. A typical microstructure of yttria samples containing 0.2 wt% titania and sintered at 1500 °C for 3 hrs. [123]

US patent 5,308,809 [124] and 5,508242 (A) [125] published in 1994, also added titanium oxides into the yttria powder, reducing this densification temperature from 1700 °C to 1300 °C. This brings a huge advantage to the manufacture of transparent yttria. The titanium and yttrium oxide will form Y_2TiO_5 and $Y_2Ti_2O_7$ liquid phases at temperatures around 1300 °C, which is the main method of promoting yttria particle sintering from solid state sintering to liquid state sintering.

Table 2-10. The relative densities of samples containing titanium oxide and fired at 1500 °C for 3 hrs.

Additive used	0.2 wt% additive	1 wt% additive
TiO_2 anatase	--	96.0
$Y_2Ti_2O_7$	84.5	99.0
Y_2TiO_5	90.5	99.6
$Ti(OC_4H_9)_4$	98.8	99.5

2.3.4.2 Boron oxide (B_2O_3)

Boron oxide is a semi-transparent or white crystal. It has a melting temperature of around 450 °C with density around 2.46×10^3 kg/m^3 [122]. It is moderately soluble in water to form boric acid, which is a weak acid. Boron oxide has generally low chemical reactivity, is used as an insecticide, as the starting materials for the synthesis of other boron compounds, a fluxing agent in glass and a bonding agent in the hot isostatic pressing of boron nitride ceramics [126].

US patent No 2,007,161,499 (A1) [127] used B_2O_3 powder to aid the sintering Y_2O_3. In this work, boron oxide powder was added to Y_2O_3 around 0.2 wt% to 23.6 wt%. The densification process of the powder compact begins from 1000 °C, and is explained by the formation of Y_3BO_6 phases. Y_3BO_6 phase forms at a temperature of around 1130 °C and the powder densification rate is enhanced by liquid phase sintering. The secondary densification take place at temperatures around 1600 °C, at this sintering temperature Y_3BO_6 will transform to YBO_3, and a new sintering mechanism is established which enhances the

powder densification further.

2.3.4.3 Zirconia (ZrO_2)

Zirconia has a density of 5.68×10^3 kg/m^3 and melting temperature of 2715 °C, and has three different crystal structures; monoclinic, tetragonal and cubic dependent on temperature. ZrO_2 is wildly used in dental applications as crown and tooth bridges. [122]

Japanese patent 2,005,075,726 [128] and WO 2,007,107,954 [129] used ZrO_2 powder blended with ThO_2 and HfO_2 to achieve very high density components. The benefits of these sintering additives are that they can oppress the grain growth of the yttria by a solute drag mechanism [130]. But the sintering atmosphere in those two patents was in a hydrogen atmosphere and with a very high sintering temperature around 2000 °C. By checking the Y_2O_3-ZrO_2 phase diagram [131], yttria interacts with ZrO_2 at very high temperatures, so the use of pure ZrO_2 as a single additive is not efficient in enhancing yttria sintering. In this work, ZrO_2 powder was added with other additives to help yttria sintering.

2.3.4.4 Alumina (Al_2O_3)

Aluminium oxide has the theoretical density $2.40\text{-}3.97\times10^3$ kg/m^3 [122]. It shows a pH value around 7-9 and has a melting temperature of 2072 °C. Because of the poor thermal and electrical conductivity and high melting temperature, it is normally used as a refractory material for many industrial applications.

Alumina was added to yttria powder to form new components long time ago, and these compounds are called YAG ($Y_3Al_5O_{12}$) [132], YAP ($YAlO_3$) [133, 134] and YAM ($Y_4Al_2O_9$) [135]. US patent 4,166,831 [136] added a small amount of Al_2O_3 with a range from 0.01 to 5 wt% into yttria (optimum range of 0.05 to 0.25 wt%) to enhance powder sintering. The patent also pointed out that the Al_2O_3 can also be added as a sintering precursor such as Al $(NO_3)_3$ and Al $(OH)_3$, etc. The method first sieved the powder to get a particle size of less than 100 μm, and first sintered at 1000 °C for one hour, then the powder was heated to a temperature around 1700-1850 °C in air for more than one hour for sintering.

2.3.4.5 Lanthanum oxide (La_2O_3)

Lanthanum oxide is a white solid that is insoluble in water, but soluble in dilute acid. It has a theoretical density of around 6.51×10^3 kg/m^3 with a high melting temperature about 2315 °C. It is widely used to make optical glass and as an ingredient in the manufacture of piezoelectric and thermoelectric materials [122].

Rhodes, W. H. (1981) [137] and Patent No Japan 5294722 [138] used lanthanum oxides to promote yttria powder sintering at temperatures around 1500-1700 °C, obtaining nearly fully dense yttria compacts. Huang, Y. H *et al*, (2006) [139] studied the sintering mechanism of lanthanum doped yttria and found that La ions can enhance the grain boundary mobility of yttria, which can promote the densification process during sintering. US patent 4,115,134 [140] also reported the effective use of lanthanum oxide to enhance yttria sintering. But the

problems of using lanthanum is that this sintering additive only works at a very high sintering temperature (>1500°C) to achieve full or near full density.

Other rare earth metal oxides like CeO_2 are also used to help yttria powder sintering (CN 10111333 3(A)) [141]. The high density of the yttria powder compact is only achieved through a high sintering temperature similar to La_2O_3.

2.3.4.6 Sintering precursor

In order to obtain better sintering of yttria with small size (nano-scale) powder, a sintering precursor is used in industry. These sintering precursors include yttrium acetate, yttrium hydroxide, and yttrium carbonate etc. Sintering precursors have low decomposition temperatures (<1000 °C), and pure yttria oxides can be obtained through the evaporation of water and carbon monoxide or dioxides. This method can produce very fine yttria particles around nanometres in size. These small particles have a large surface area and tend to be very active at low sintering temperatures to promote the powder sintering. Rasmussen, M. D [142] and Ikegami *et al* [143] prepared nano-sized yttria powder by using an yttrium hydroxide precursor and this powder can be used to get nearly fully dense compact at temperature around 1000 °C. Gong, H *et al* [144] and Venkatachalam. N [145], Yu. Kopylov [146] also used yttrium carbonate and acetate to make very fine yttria powder.

2.3.5 Binder design

The purposes of using a binder in the slurry are to assist filler particles bond to each other to have a reasonable green compact strength. The basic requirements of the binder are; [147]

1) Filler particles can be suspended into the binder solution uniformly.
2) The bonding provided by the binder between filler particles should be strong enough to withstand the forces generated by the molten wax during de-wax process.
3) The residual element of the binder after face coat sintering should be chemically inert and giving no more interaction between the face coat and the molten metal during casting process.
4) Binder should have a certain viscosity range to allow the slurry to be applied to the wax surface.
5) Not expensive and easy to store.
6) Should have a reasonable life.

The binders used in slurries can be generally divided into two categories: one is organic, the other is inorganic. Organic binders usually used are the low temperature binders such as Polyvinyl alcohol (PVA) [148, 149], PVB (Polyvinyl butyal) [150], cellulose [150, 151] which can decompose and soften at temperatures around 150 °C. But for inorganic binders such as ceramic sols [152], they can be used at high temperatures up to 300 °C with no degradation taking place.

2.3.6 Summary

The new type of water based binder face coat slurry development opens a new area of non-gelation slurry without using very costly colloidal sols as the binder. The long life of the slurry will be a large advantage for TiAl refractory shell applications. The conclusion Table 2-11 compares this new system with existing face coat system.

Table 2-11. The comparison of the new slurry and the commercial used slurry.

Composition	Traditional yttria slurry	New designed slurry
Filler	Yttria-based powder (could be F-doped, YAZ)	Sintering additives were added into yttria powder; 1. B_2O_3 2. TiO_2 3. Al_2O_3 4. ZrO_2 5. La_2O_3 6. CeO_2 7. YF_3 8. Yttrium acetate 9. Yttrium carbonate
Binder	Colloidal particle Sol (yttria sol [152])	De-ionised Water
Anti-foam	Burst RSD-10 [153]	Burst RSD-10
Wetting agent	Victawet 12 [154]	Victawet 12
Polymer	option	High temperature polymer; 1. Poly vinyl alcohol 2. cellulose acetate

*Red colour shows the changed information

Chapter 3. Filler powder development

The aims of this chapter were to make and select the best filler powder compositions to make slurry, which have superior sintering properties at low to medium sintering temperatures (1000-1200 °C). In this chapter, the new filler powder sintering properties were investigated through comparing their particle size and distribution, particle shape and linear thermal expansion rate at different sintering temperatures.

3.1 Sample preparation

3.1.1 Filler powder preparation.

Based on the published data (Chapter 2), some sintering aids (sintering precursors and sintering additives, see Table 3-1) were selected and blended into 100 g of yttria powder (-200 mesh, 99% purity, Treibacher Industrie AG) at 0.15 and 2.0 wt%. These new filler powders were made by first dissolving the additives into de-ionized water and blended over night on a rolling mill. Then they were dried in a furnace at 100 °C for at least 8 hours. The added elements proportion (*M %*) of different oxides are calculated using equation 3-1. Supposing the metal oxide used is M_xO_y., therefore, the added element in the metal oxide is:

$$M\% = \frac{x \times m_M}{x \times m_M + y \times m_O} \times 100\% \qquad 3\text{-}1$$

where x and y are numerical constants in oxides $M_xO_{y,,}$ m_M and m_O are the molecular weights of the metal elements and oxygen, e. g, for TiO_2, from equation 3-1, the Ti % in this oxide is 60 %. The added amount of metal oxide x_1 (g) (0.5 wt% of pure element) and x_2 (g)

(2.0 wt% of pure element) into 100g of yttria powder can be calculated using equation 3-2 and 3-3 with the calculated results shown in Table 3-1 below:

$$0.5\% = \frac{x_1 \times M\%}{x_1 + 100} \times 100\% \quad 3\text{-}2$$

$$2.0\% = \frac{x_2 \times M\%}{x_2 + 100} \times 100\% \quad 3\text{-}3$$

Table 3-1. Sintering additives and their adding amount in 100 g yttria powder.

Sintering additives	**wt% of pure element**	**mol% of additives**	**Added weight (g)**
yttria	--	--	--
Sol	0.15	--	--
(contain 14wt% Y_2O_3)	2.0	3.01	22.2
B_2O_3	0.15	1.53	0.48
	2.0	17.4	6.51
TiO_2	0.15	0.70	0.25
	2.0	8.56	3.31
CeO_2	0.15	0.25	0.19
	2.0	3.10	2.43
YF_3	0.15	0.60	0.39
	2.0	7.43	5.18
La_2O_3	0.15	0.13	0.18
	2.0	1.57	2.30
Yttrium acetate	0.15	0.58	0.69
($YC_6H_9O_6$)	2.0	7.70	9.84
Yttrium Carbonate	0.15	0.30	0.54
($Y_2C_3O_9 \cdot 3H_2O$)	2.0	3.94	7.46
Yttria-0.5wt%Al_2O_3-0.5wt%ZrO_2 (YAZ)	commercially available powder		

* Sol used in this experiment is yttria sol.(Nyacol Colloidal yttria sol)

3.1.2 Powder pellet preparation

Powder pellets were made by pressing the powder in a steel die (13 mm diameter) using a Instron^{TM} machine (series Number 4467H1959) with a constant pressure of around 22.6 MPa. Each powder pellet weighted 3.00 g, was 13 mm diameter. The binder used in this process is

a PGA water solution (15 wt%). The heights of the pellets depended on the powder particle size, agglomeration etc, but was around 7 to 10 mm, see Figure 3-1.

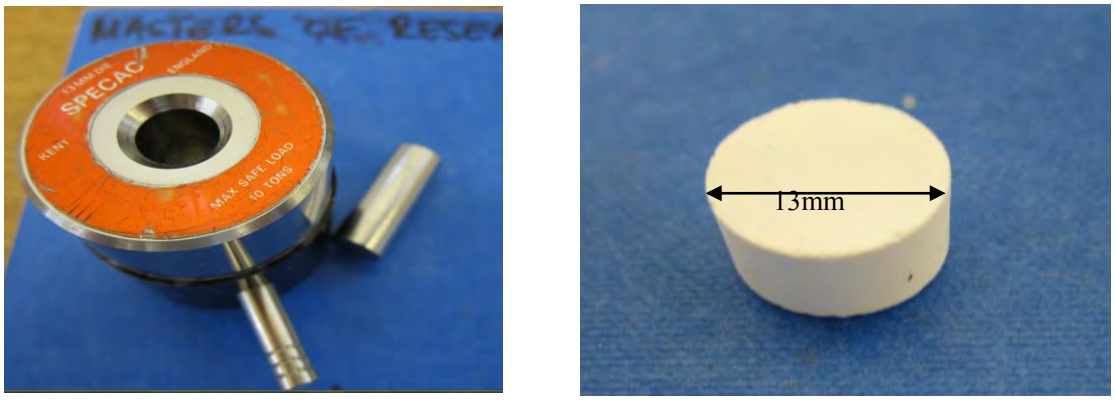

(a) (b)

Figure 3-1. (a) Cylindrical shaped die, (b) powder pellet.

3.2 Sample characterization

3.2.1 Powder particle size and distribution test

The particle size distributions of the various fillers were analyzed using laser powder particle size measuring equipment (Coulter LS230). Firstly, the powders were suspended into a glycerol solution, and then slowly poured into the test tube. As the particles passed through the orifice, they displaced an equivalent volume of the electrolyte and caused a change in the electrical resistance, the magnitude of which is proportional to the volume of the parties. The changes in resistance are converted to voltage pulses, which are amplified, sized and counted to produce data for the particle size distribution of the suspended particles.

3.2.2 Density test

When powders were sintered at temperatures around 1000-1300 °C, the density of the pellets

was very difficult to measure using the Archimedes method due to the very loose structures (yttria has a high sintering temperature around 1700 °C). After considering these problems, the density of every powder pellet was measured by calculating a pellet's dimensional change before and after sintering at 1000 °C, 1200 °C, 1400 °C and 1600 °C for one hour in air. The pellets' densities were calculated using equation 3-4. For the measurement, a caliper with an accuracy of 10^{-5} m was used to measure the pellets' dimensional change after firing at different temperatures. In order to reduce the error, the density ρ, tested in this experiment was the average value from 5 pellets sintered in a batch.

$$\rho = \frac{M}{V} = \frac{M}{\pi r^2 h} \qquad 3\text{-}4$$

where M is the mass of the pellets.

3.2.3 Dilatometer test

A dilatometer (DiL 402E, NETZSCH) was used to measure the powder compact linear dimension change during heating or isothermal processes up to a temperature of 1600 °C. The dilatometer technique provided accuracy of shrinkage measurement in a controlled environment. The shrinkage/expansion for a powder compact is defined as the change of dimension $\Delta L/L_0$, (where L_0 is the initial length and $\Delta L = L - L_0$, where L is the actual length at time t) for certain time t. The structure of the dilatometer is shown in Figure 3-2 (a) & (b). During testing, the dimensional changes of the samples were recorded using a pushrod which pressed against the sample with a constant force. The movement of the rod was recorded by a computer. To obtain the true sample behaviour,, it necessary to correct the raw dilatometer data. In this experiment a corrected curve from standard Al_2O_3 is used to correct

the raw data of the test samples at the given heating profile, see Figure 3-2 (c).

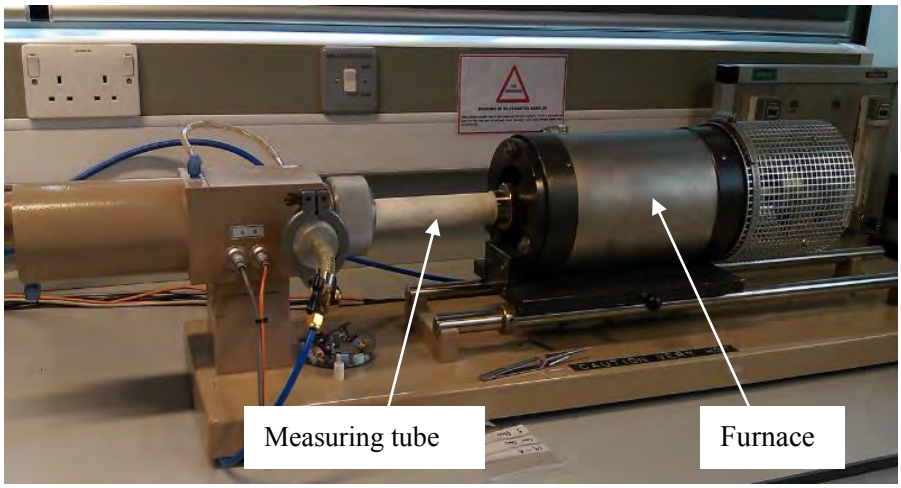

(a)

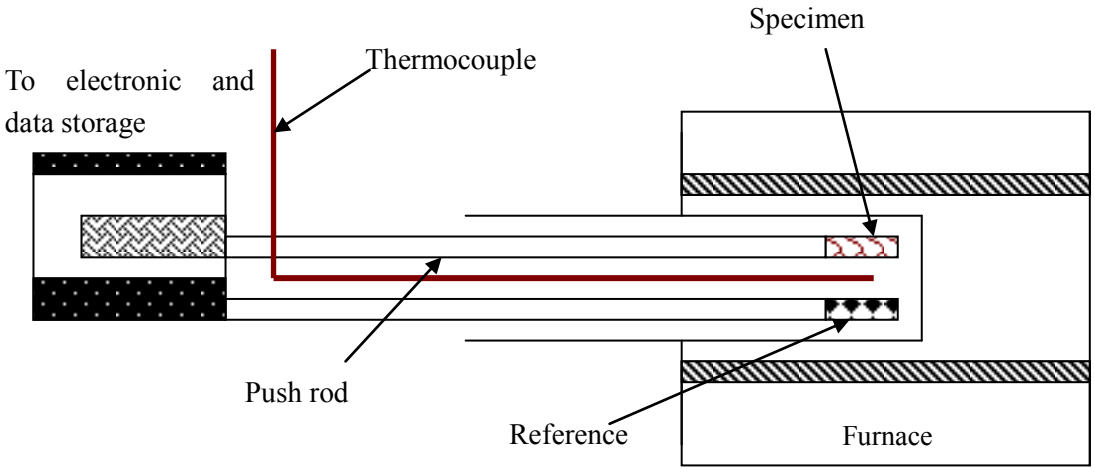

(b)

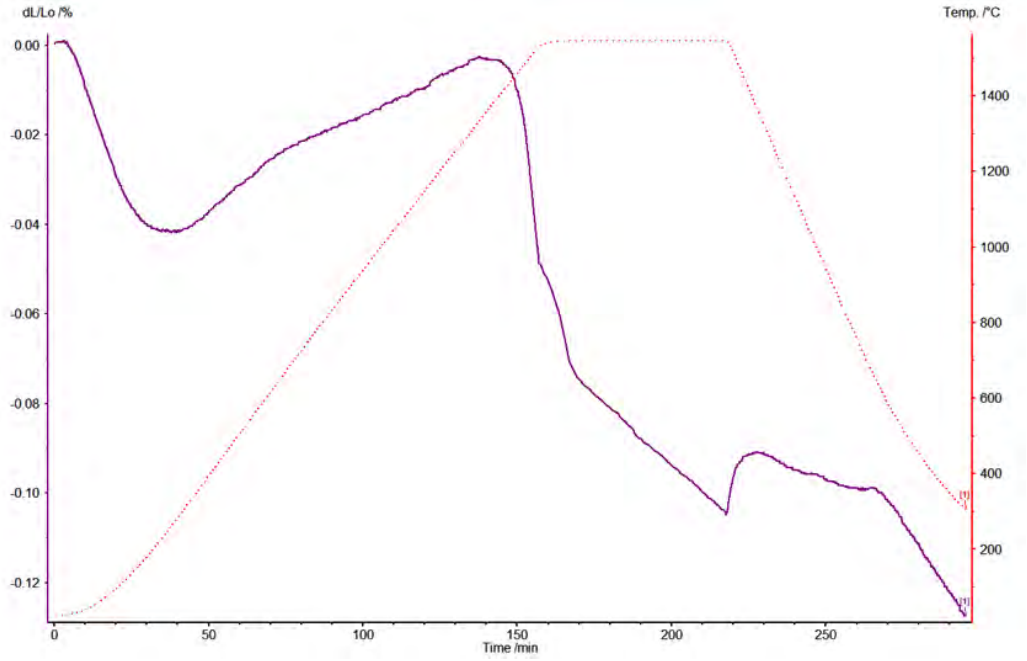

(c)

Figure 3-2. The dilatometer, (a) the equipment, and (b) the schematic diagram, (c) a example of the standard Al_2O_3 trace.

3.2.4 Isothermal shrinkage Measurement

Isothermal sintering is described as a process where the compact is sintered at a fixed temperature, and it is widely used to predict the sintering mechanism of the powder at different temperatures [156]. Because of the limitation of the heating rate, the powder compact will start to densify and the microstructure will change during the heating-up process, so some of the corrections should be made to this method before being used to predict the powder sintering behaviour. During testing, samples were heated at a rate of 20 °C per minute to isothermal temperatures of 1000 °C, 1200 °C, 1300 °C and 1550 °C, and then cooled down at a rate of 20 °C per minute to room temperature. The shrinkage of the compact was measured as a function of time at each isothermal temperature.

3.2.5 Constant Rate heating shrinkage measurement (CRH)

Constant rate heating sintering is described as a process in which a sample is heated at a constant rate to a specified temperature and immediately cooled. Constant heating rate experiments are usually used to analyze the powder sintering activation energy [157-159]. There were two heating profiles used in the isothermal temperature sintering test, 5 °C and 10 °C per minute from room temperature to 1500 °C and then cooled down at the same rate.

3.2.6 Scanning electron microscope

A scanning electron microscope (SEM) was used to observe the sample surface characteristics to identify powder particle shapes and networks. Backscattered images and EDX analysis were also used to observe the powder compact microstructure and composition changes at different sintering temperatures.

SEM samples were made by mounting these powder compacts (after sintering at different temperatures) into a transparent epoxy resin (epoxy resin was made by blending 25:3 by weight of EpoFix resin with a hardener, Struers), and allowing them to dry for around 8 hours. The surface was then carefully ground and polished. Finally, the sample surfaces were carbon coated for the test.

3.2.7 X-ray diffraction (XRD)

The compounds formed after each isothermal sintering were identified using a Philips X‘pert

X-Ray Diffractometer with a Cu-K_α radiation (λ=1.540598Å).

During the test, a monochromatic X-ray beam was projected on to the surface of the sample at incident angles with a range of 10 ° to 100 °. Diffracted rays were generated by the lattice spacing d of each element or compound, satisfying the Bragg equation: nλ=2dSinθ. The diffraction patterns were analyzed and indexed using the X'pert High Score analytical software.

3.3 Equations Derivation

3.3.1 Constant Rate Heating (CRH) shrinkage

Assuming an isotropic shrinkage of the green compact, the density $\rho(T)$ at a temperature T is given in following equation 3-5 [157]:

$$\rho(T) = (\frac{L_f}{L_T})^3 \rho_f \qquad 3\text{-}5$$

Where, L_f and L_T are the final length and the length at a temperature T of the specimen, respectively. ρ_f is the final compact density measured by the Archimedes method.

The material transport path and activation energy of diffusion at the initial sintering stage were studied by Koji, Matsui [156, 159], and sintering rate equation of the CRH method is defined as:

$$\ln\left[T\left(\frac{dT}{dt}\right)\left(\frac{d\rho}{dT}\right)\right] = -\frac{Q}{RT} + \alpha(n,p) \qquad 3\text{-}6$$

$$\alpha(n,p) = \ln[f(\rho,n)] + \ln\left(\frac{K\gamma_s \Omega D_0}{k}\right) - p\ln a \qquad 3\text{-}7$$

where, K is a numerical (rate) constant, γ is the surface energy, Ω is the atomic volume. D is the diffusion coefficient, t is the time (s), ρ is the density of the compact, T is the absolute temperature (K), k is Boltzmann's constant, a is the spherical particle radius and n and p are the sintering indices, which are dependent on the diffusion mechanisms. Q is the activation energy (kJ/mol), R is the gas constant, $f(\rho,n)$ is the density function which depends on n, and D_0 is the pre-exponential term defined as:

$$D=D_o \exp(-Q/RT). \qquad 3\text{-}8$$

3.3.2 Isothermal shrinkage

The sintering-rate equation for isothermal shrinkage during the initial sintering stage in equation 3-9 is given in below [163]:

$$\left(\frac{\Delta L}{L_0}\right) = \left(\frac{K\gamma\Omega D}{kTa^p}\right)^n t^n \qquad 3\text{-}9$$

On taking logarithms, equation 3-10 is obtained:

$$\log\left(\frac{\Delta L}{L_0}\right) = n\log\left(\frac{K\gamma\Omega D}{kTa^p}\right) + n\log t \qquad 3\text{-}10$$

Where the numerical constant n in the equation 3-9 and 3-10 depends on different sintering mechanisms, see Table 3-2.

Table 3-2.The *n* values for each sintering mechanisms

Mechanisms	***n***
Dissolution-precipitation process controlled by diffusion [160]	~0.10
Grain boundary diffusion [161]	0.25-0.31
Bulk diffusion [161]	0.33-0.5
Vapor diffusion [162]	~0.66

Johnson and Cutler (1963 & 1969) [161, 164] reported that equation 3-10 was not entirely satisfactory for the kinetic analysis of isothermal sintering due to the errors in sintering data and times. These errors were introduced through pre-sintering taking place before the sample temperature reached the isothermal holding temperature. The correction to equation 3-10 can be made through applying a correction factor δL, so that, ΔL became $\Delta L+\delta L$, L_0 became $L_0+\delta L_0$, and t became $(t-t_0)$ [156]. Equation 3-10 was then changed to:

$$\log\left(\frac{\Delta L+\delta L}{L_0+\delta L}\right)=n\log\left(\frac{K\gamma\Omega D}{kTa^p}\right)+n\log(t-t_0) \qquad 3\text{-}11$$

The variable δL and t_0 in equation 3-11 were defined in Figure 3-3 from Koji's methods [156]

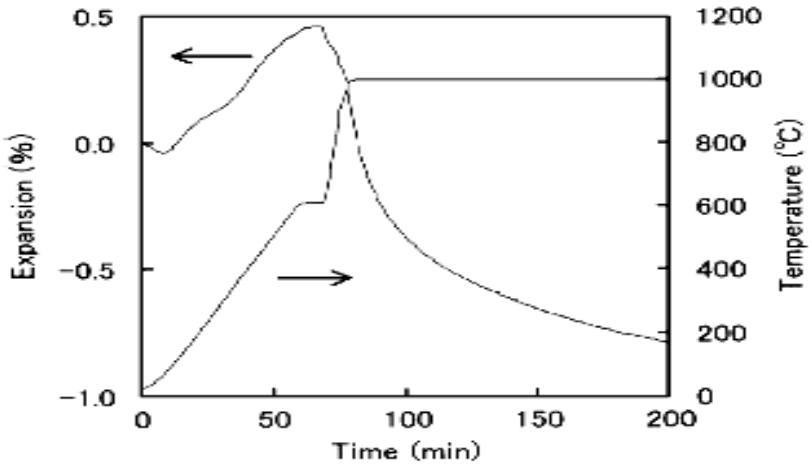

(a)

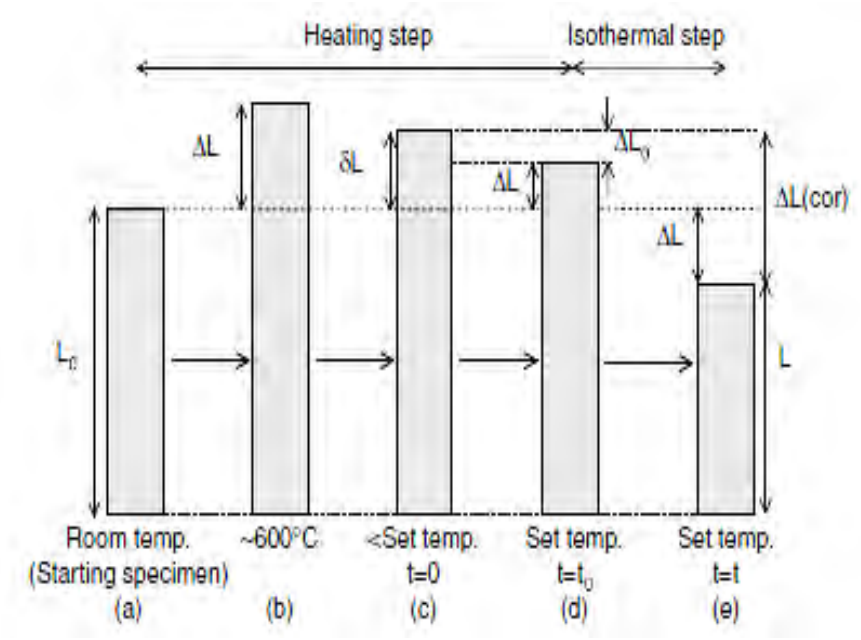

(b)

Figure 3-3. The shrinkage and expansion trace for the powders. (a) The real temperature profile and (b) the change of the powder compact length from heating to isothermal step [156].

From Figure 3-3, it can be seen that, instead of using the real sample dimension, Koji's new method uses the sample dimension when the isothermal heating starts as the new L_o (supposing that sintering starts at this temperature). But, as can be seen from the picture, the powder compacts have already sintered with the reduced thermal expansion rate before its isothermal temperature (the sintering onset temperature should be the temperature where the compact's linear expansion finishes). If no sintering takes place, powder compacts should keep on linearly expanding until the holding temperature. Therefore in this thesis, a new correction method was developed and used, supposing to describe the powder sintering behavior more accurately. This new method used a corrective length $\Delta L_{(cor)}$ to replace ΔL, a corrected isothermal sintering time (t-t_o) to replace t in equation 3-10. This new method will

be introduced in the discussion part later in this chapter.

3.4 Results and Discussion

3.4.1 Powder particles size distribution

Some of the samples' particle size and distribution are shown in Figure 3-4, and powders d_{10}, d_{50}, d_{90} and mean radius values of each sintering additive are reported in Table 3-3:

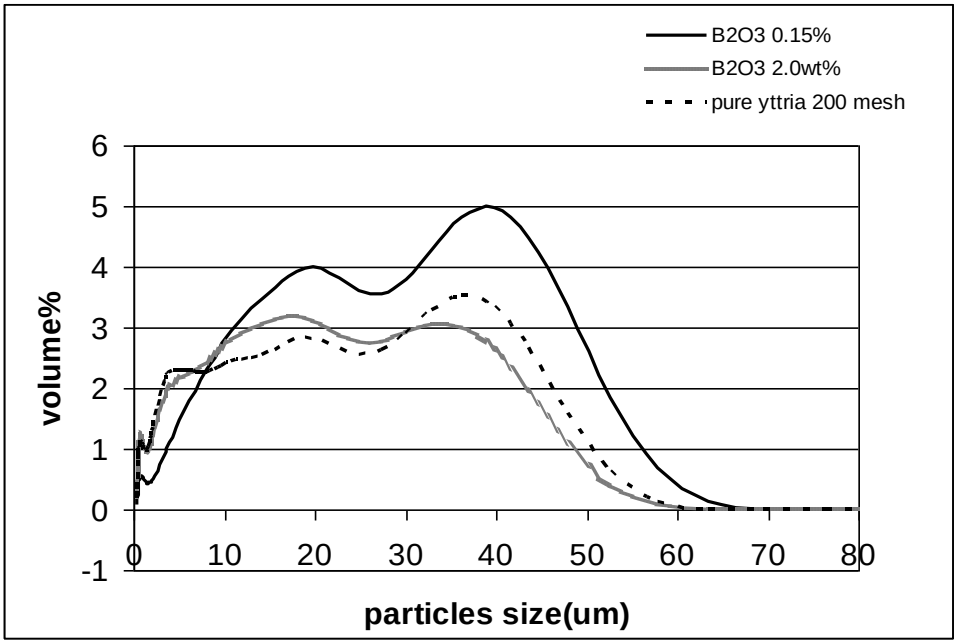

(a)

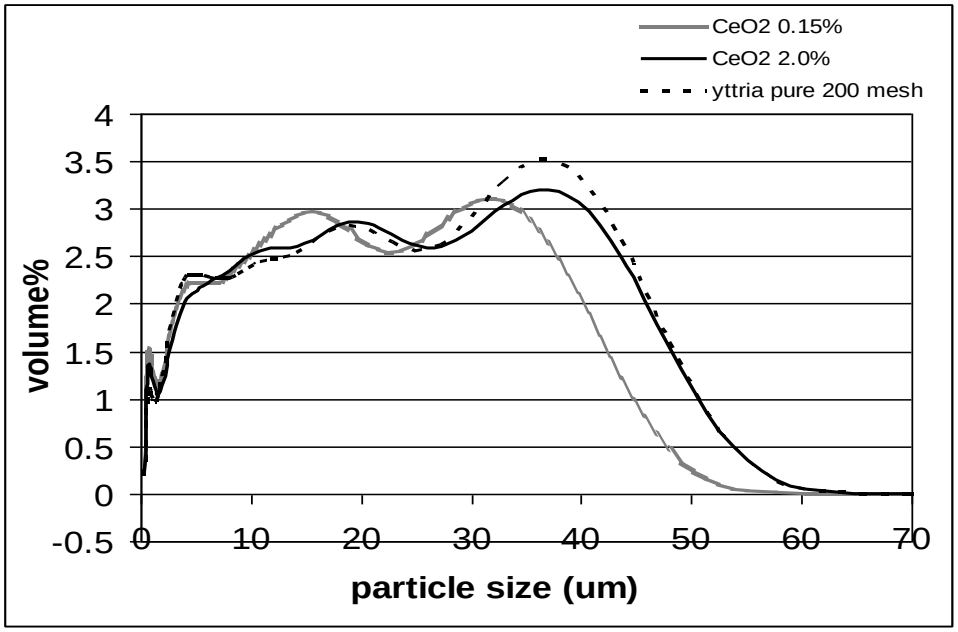

(b)

Figure 3-4.Particles distribution of (a) B_2O_3, and (b) CeO_2 addition.

Table 3-3. $d_{10,}$ d_{50}, d_{90} and mean radius values obtained for each powder formulation (μm).

Samples ID		d_{10}	d_{50}	d_{90}	d_{mean}
Yttria		**1.15**	**9.534**	**38.15**	**14.88**
Yttria + Sol	2.0 wt%	1.23	9.54	37.23	12.06
YF_3	2.0 wt%	1.278	11.45	39.02	12.95
La_2O_3	0.15wt%	0.863	7.317	31.77	13.22
YAZ		0.978	9.206	37.81	13.78
Yttrium Acetate	2.0wt%	0.746	9.911	39.9	14
Yttrium Carbonate	2.0wt%	1.613	8.911	31.14	14.27
TiO_2	0.15wt%	0.994	10.73	36.50	14.64
TiO_2	2.0wt%	0.933	9.010	28.06	14.8
B_2O_3	2.0wt%	1.122	10.47	40.68	15.025
La_2O_3	2.0wt%	1.742	14.12	38.97	17.44
CeO_2	2.0wt%	0.984	9.404	37.48	17.48
Yttrium Carbonate	0.15wt%	1.019	7.754	52.58	19.325
CeO_2	0.15wt%	0.985	10.11	37.4	19.5
B_2O_3	0.15wt%	1.728	16.27	44.39	20.53
YF_3	0.15wt%	2.66	18.16	46.45	21.49
Yttrium Acetate	0.15wt%	3.149	13.96	46.24	21.66

Table 3-3 shows that, all the filler powder has similar mean particle size of around 12-20 μm and distribution. The average d_{10} is around 1 μm, d_{50} around 9 μm and d_{90} around 40 μm. Compared to pure yttria filler powder, the addition of some of the sintering additives will influence mean filler particle size due to powder particle agglomeration. The smallest mean particle size is 12.06 μm by adding 2.0 wt% sol to yttria, followed by filler powder with 2.0 % YF_3 and 0.15 % La_2O_3. Otherwise, the sintering precursor with 0.15 % Yttrium acetate added has the largest mean particle diameter. The different filler particles and distributions may influence the future powder sintering properties.

3.4.2 Sintered pellets density

Powder pellet densities at different sintering temperatures are reported in Table 3-4. As can be seen, powder green compact density is different for different filler powders, which was influenced by powder particle size, distribution, shape, etc. Pure yttria powders, YAZ, yttria with TiO_2 and CeO_2 groups have very high green compact density before sintering. After isothermal sintering in air for one hour, the powder compacts with high green compact density seem to have a larger density increase than the compacts with low green density, e.g. YAZ, and TiO_2 added powder.

Table 3-4. The density of the powder pellets at different isothermal sintering temperatures in air for one hour.

Sample ID		Room T (kg/m^3)	1000.°C (kg/m^3)	1200.°C (kg/m^3)	1400.°C (kg/m^3)	1600.°C (kg/m^3)
Yttria		**2.9**	**2.89**	**2.9**	**2.95**	**3.05**
Yttria + Sol	2.0 %	2.51	2.01	2.51	2.53	2.56
TiO_2	0.15%	2.88	2.87	2.85	2.86	3.05
TiO_2	2.0%	2.89	2.85	2.86	2.90	3.01
YAZ		3.01	3.00	2.98	3.04	3.18
La_2O_3	2.0%	2.82	2.72	2.74	2.78	2.83
La_2O_3	0.15%	3.00	2.98	3.02	3.00	3.08
CeO_2	2.0%	3.035	3.03	3.02	3.06	3.08
CeO_2	0.15%	3.04	3.02	3.02	3.03	3.04
Yttrium carbonate	0.15%	2.75	2.59	2.74	2.67	2.79
Yttrium carbonate	2.0%	2.79	2.72	2.75	2.74	2.84
Yttrium acetate	0.15%	2.84	2.79	2.81	2.78	2.80
Yttrium acetate	2.0%	2.57	2.38	2.37	2.42	2.51
YF_3	2.0%	2.78	2.71	2.66	2.67	2.75
YF_3	0.15%	2.86	2.82	2.82	2.8	2.92
B_2O_3	0.15%	2.92	2.92	2.88	3.01	----
B_2O_3	2.0%	2.67	2.45	2.5	2.55	----

* B_2O_3 group has large pellet volume expansion due to new phases forming when sintered at 1600 °C, and the volume of the compact anisotropic expanded making it difficult to calculate their density.

After sintering at a temperature of around 1000 and 1200 °C, nearly all the powder compacts showed a decreased density change compared to their green density, and these powder compact samples were very loose and easily be broken during measurement. These decreases in powder compact density at temperatures from 1000-1200 °C may be explained by evaporation of the water and burning out of polymer binder in the compacts which released the force in the compact and caused a slight volume expansion (poor bonding).

Because of the loose structure of these powder compacts, some experimental errors may have taken place during the measurement for accurately calculating the densities.

Total density change (*Δρ%)* of the pellets after being sintered at different isothermal temperatures were calculated using equation 3-12 and the density increase (%) was reported in Table 3-5.

$$\Delta\rho\% = \frac{\rho_T - \rho_0}{\rho_0} \times 100\% \qquad 3\text{-}12$$

where, ρ_o is pellet green density, and ρ_T is the pellet density after sintering at temperature (T) for one hour.

As can be seen from Table 3-5, the powder compact with sintering precursors added (e.g yttrium carbonate, yttrium acetate, and sol) have the largest volume expansion at the sintering temperature of around 1000 °C. These very large volume expansions of the compacts may due to evaporation of the sintering precursors, and the larger the amount of precursor the larger of the powder compacts volume expanded. Meanwhile, powder compacts with more sintering additives seemed to have higher volume expansion at temperatures around 1000 to 1200 °C.

Table 3-5. % Density increase of the powder pellets at different temperatures.

Sample ID		1000.°C (%)	1200.°C (%)	1400.°C (%)	1600.°C (%)
Yttria		**-0.34**	**0.00**	**1.72**	**5.17**
Sol	2.0%	-19.92	0.00	0.80	1.99
TiO_2	0.15%	-0.35	-1.04	-0.69	5.90
TiO_2	2.0%	-1.38	-1.04	-0.35	4.15
YAZ		-0.33	-1.00	1.00	5.65
La_2O_3	2.0%	-3.55	-2.84	-1.42	0.35
La_2O_3	0.15%	-0.67	0.67	0.00	2.67
CeO_2	2.0%	-0.16	-0.49	0.82	1.48
CeO_2	0.15%	-0.66	-0.66	-0.33	0.00
Yttrium carbonate	0.15%	-5.82	-0.36	-2.91	1.45
Yttrium carbonate	2.0%	-2.51	-1.43	-1.79	1.79
Yttrium acetate	0.15%	-1.76	-1.06	-2.11	-1.41
Yttrium acetate	2.0%	-7.39	-7.78	-5.84	-2.33
YF_3	2.0%	-2.52	-4.32	-3.96	-1.08
YF_3	0.15%	-1.40	-1.40	-2.10	2.10
B_2O_3	0.15%	0.00	-1.37	3.08	---
B_2O_3	2.0%	-8.24	-6.37	-4.49	---

Some samples such as 2.0 wt% B_2O_3, 2.0 wt% yttrium acetate and YF_3 2.0 wt% show a decreased density (compact expansion) even when sintered at very high temperatures such as 1600 °C, but with a very quick densification rate. The high temperature compact volume expansion can be explained by the interaction between yttria powders and sintering additives (shown in later XRD results), the release of heat during these processes caused the compact volume to expand. Normally, this internal reaction process is accompanied by new phase formation or a chemical interaction process.

3.4.3 Dilatometer test results

An example of a dilatometer test trace of the pure yttria filler is shown in Figure 3-5 together with annotations.

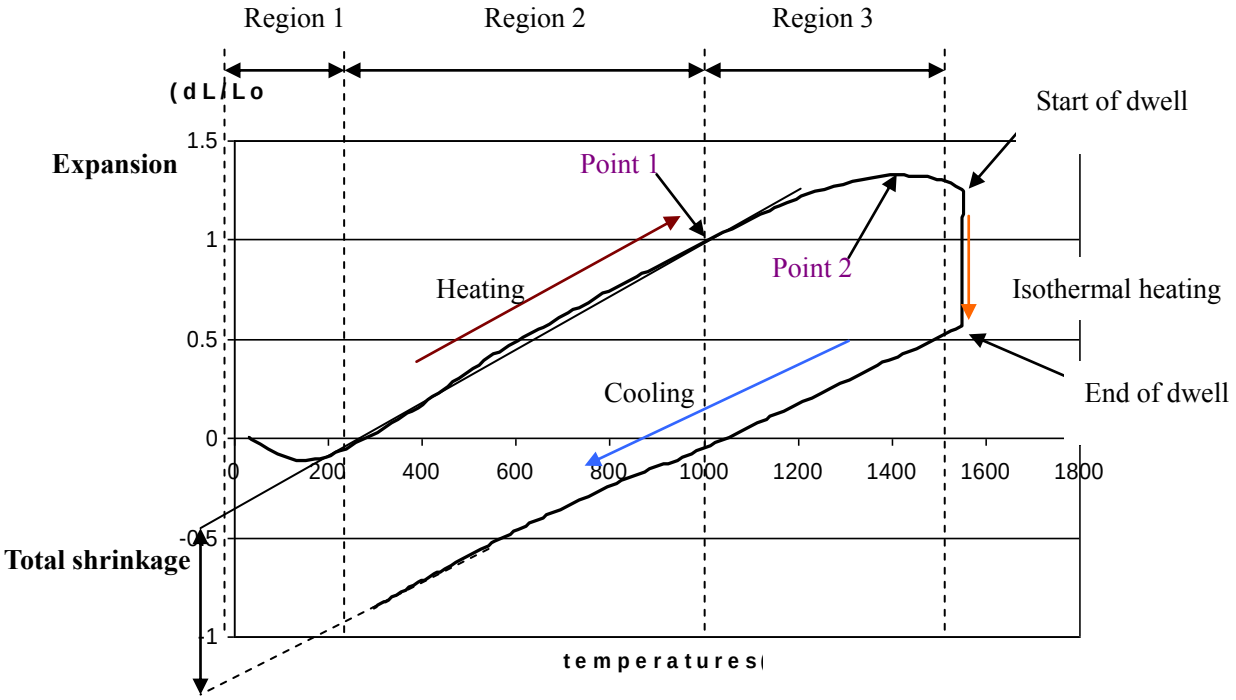

(a)

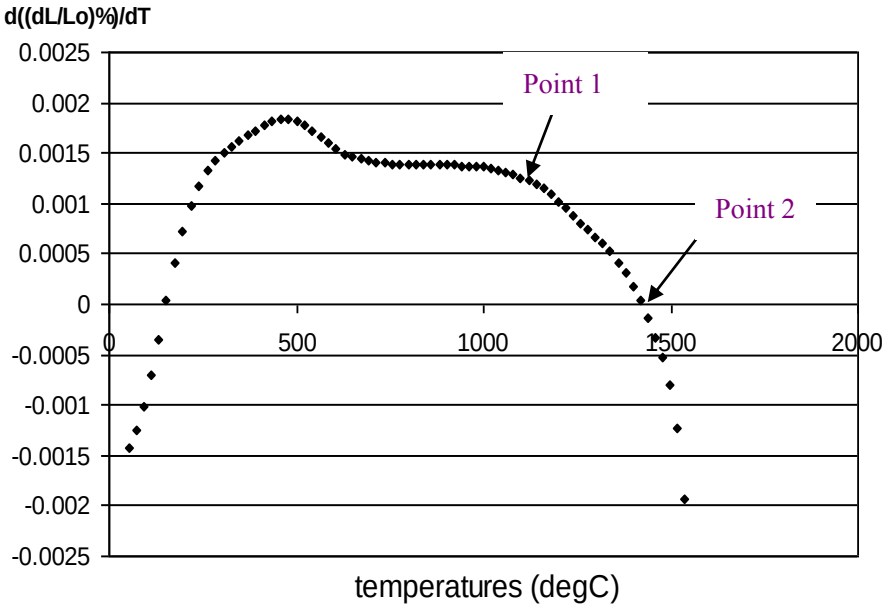

(b)

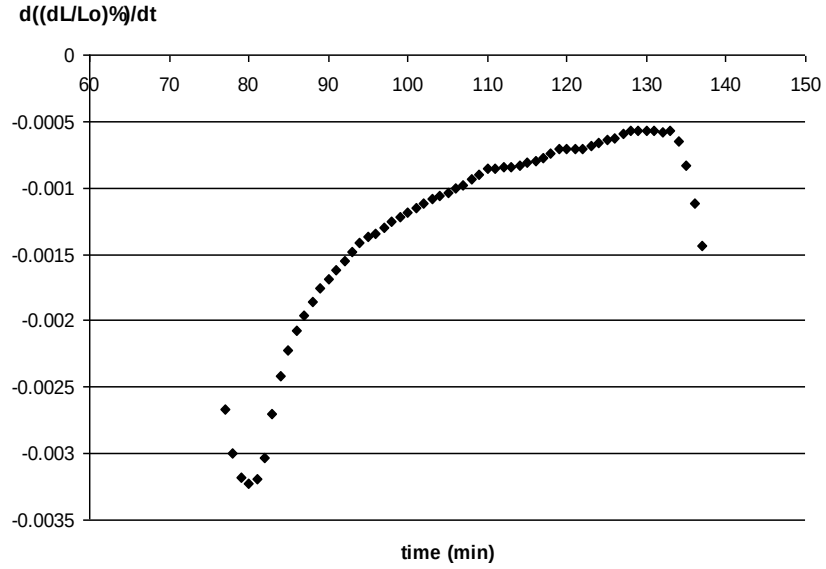

(c)

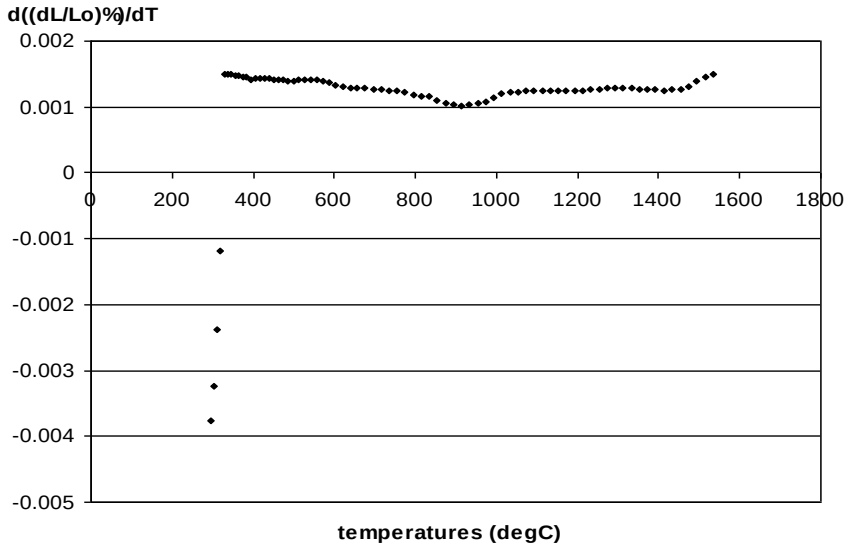

(d)

Figure 3-5. (a) The thermal expansion trace for the isothermal shrinkage test (20 °C/min heating to 1550 and 20 °C/min cooling down) of yttria -200 mesh powders, (b) the expansion rate of heating, (c) isothermal shrinkage rate and (d) expansion rate on cooling

During heating, the trace can be divided into three regions as shown in Figure 3-5. A slight dimensional shrinkage of each sample taking place in region 1 corresponds to machine offsetting problems. Region 2 is the expansion stage. In this stage, as the temperature

increased, samples firstly exhibit a linear increase in their dimensions until point 1 is reached (see Figure 3-5 (a)). Point 1 is the linear expansion end point, after that, the powder will begin to shrink but the overall length is still increasing. Region 3 is the sintering stage. In this stage, the rate of sample expansion reduces after point 1. After point 2, the rate of shrinkage exceeds the rate of expansion, and the powder pellets show a net shrinkage. During the isothermal heating process, the powder will firstly suffer a rapid volume reduction, and then the densification rate will slow down after a few minutes to a constant value (Figure 3-5 (c)). When powder pellets cooled down, they underwent a linear shrinkage, which was of similar magnitude to that seen during heating but in the opposite direction.

Some powder pellet dilatometer traces for isothermal sintering at 1550 °C for one hour are shown in Figure 3.

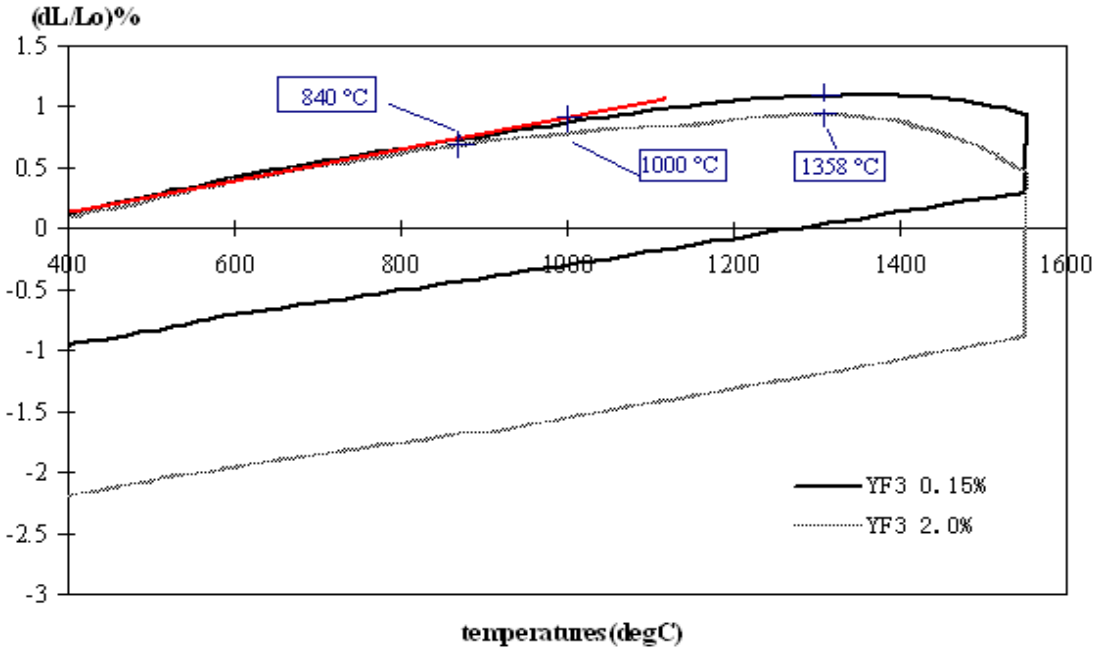

(a)

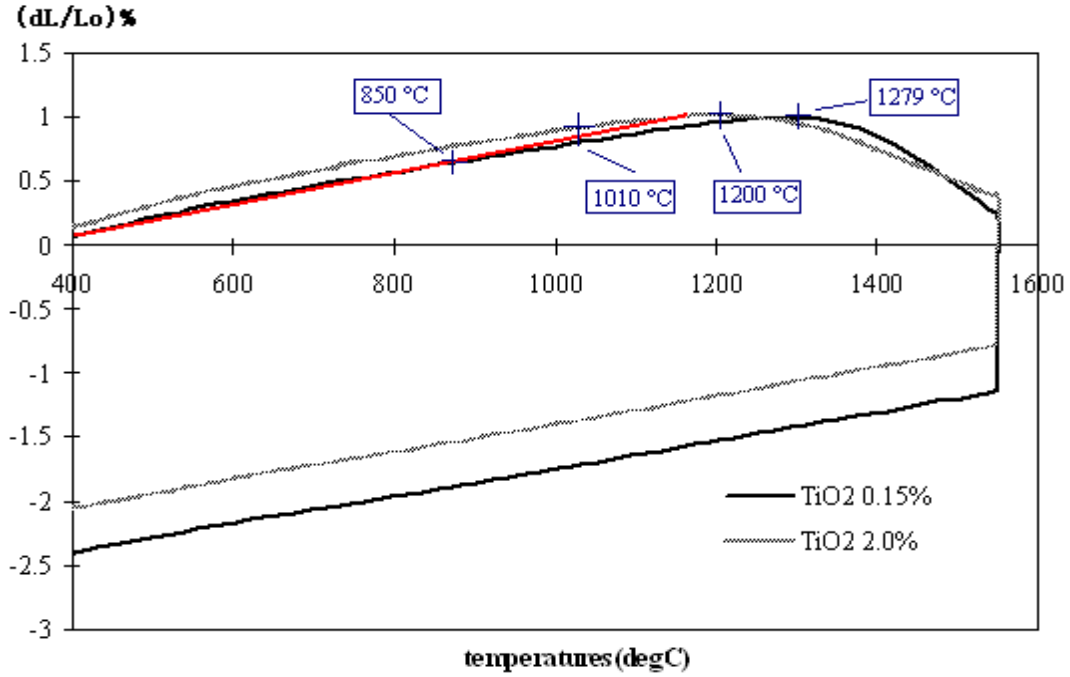
(dL/Lo)%
1.5
1
0.5
0
-0.5
-1
-1.5
-2
-2.5
-3
400
600
800
1000
1200
1400
1600
850 °C
1010 °C
1200 °C
1279 °C
TiO2 0.15%
TiO2 2.0%
temperatures(degC)

(b)

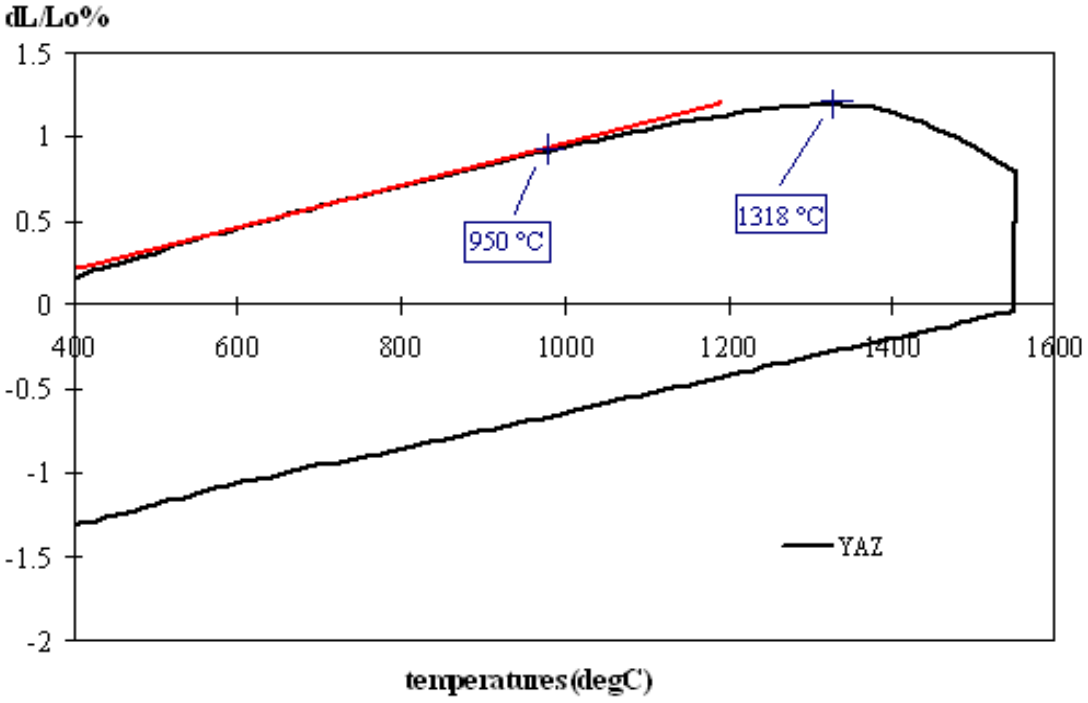
dL/Lo%
1.5
1
0.5
0
-0.5
-1
-1.5
-2
400
600
800
1000
1200
1400
1600
950 °C
1318 °C
YAZ
temperatures(degC)

(c)

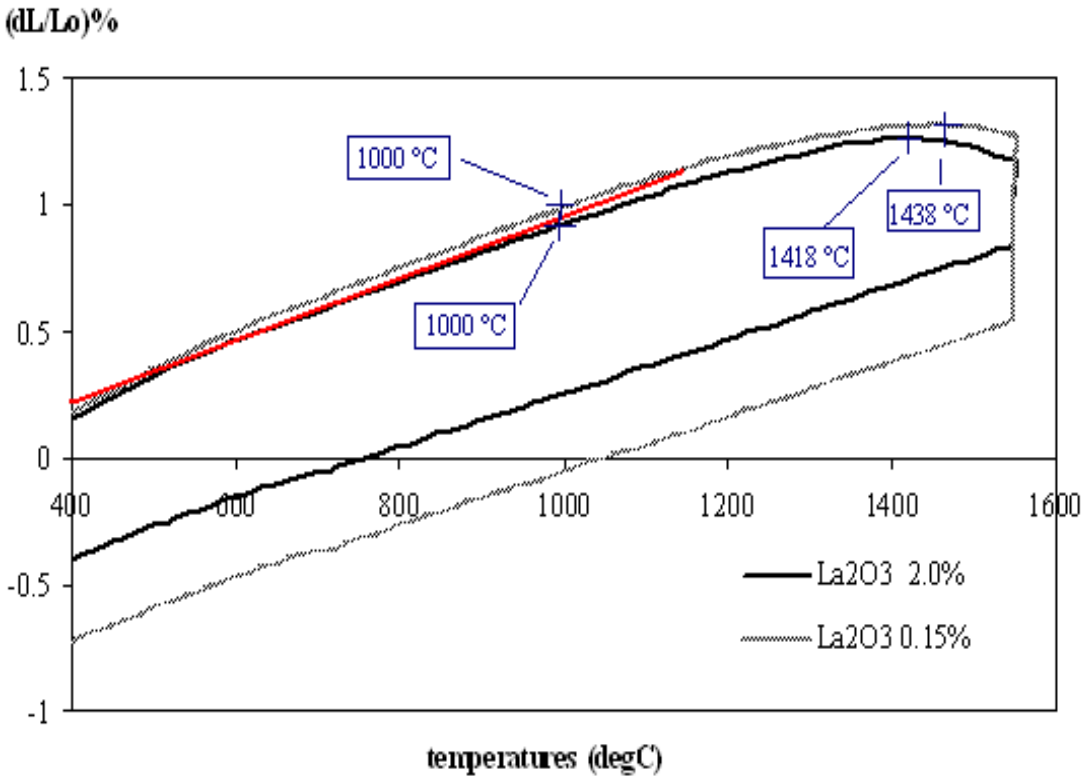
(dL/Lo)%
1.5
1
0.5
0
-0.5
-1
400
600
800
1000
1200
1400
1600
1000 °C
1000 °C
1418 °C
1438 °C
La2O3 2.0%
La2O3 0.15%
temperatures (degC)

(d)

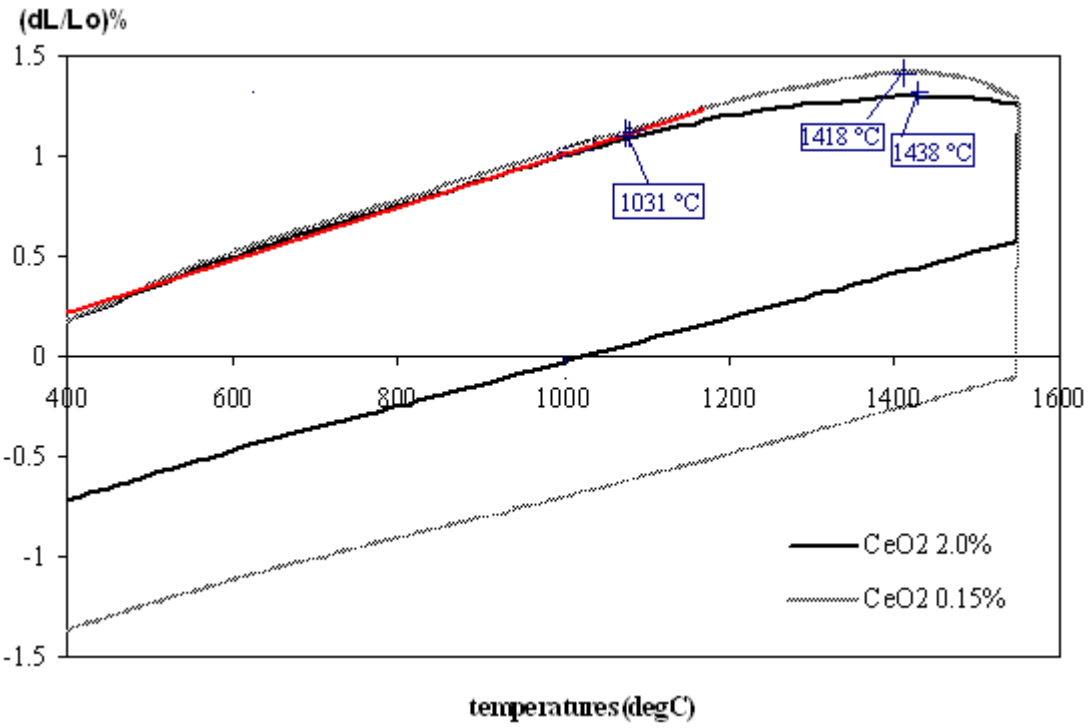
(dL/Lo)%
1.5
1
0.5
0
-0.5
-1
-1.5
400
600
800
1000
1200
1400
1600
1031 °C
1418 °C
1438 °C
CeO2 2.0%
CeO2 0.15%
temperatures (degC)

(e)

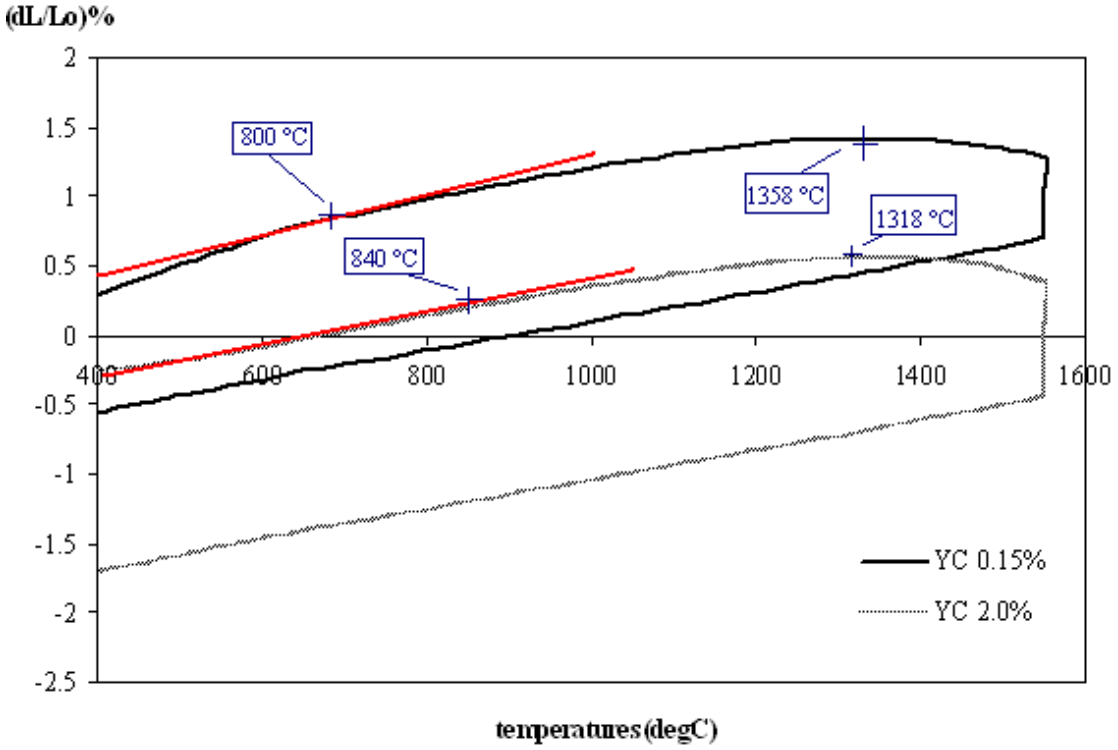
(dL/Lo)%
2
1.5
1
0.5
0
-0.5
-1
-1.5
-2
-2.5
400
600
800
1000
1200
1400
1600
800 °C
840 °C
1358 °C
1318 °C
YC 0.15%
YC 2.0%
temperatures (degC)

(f)

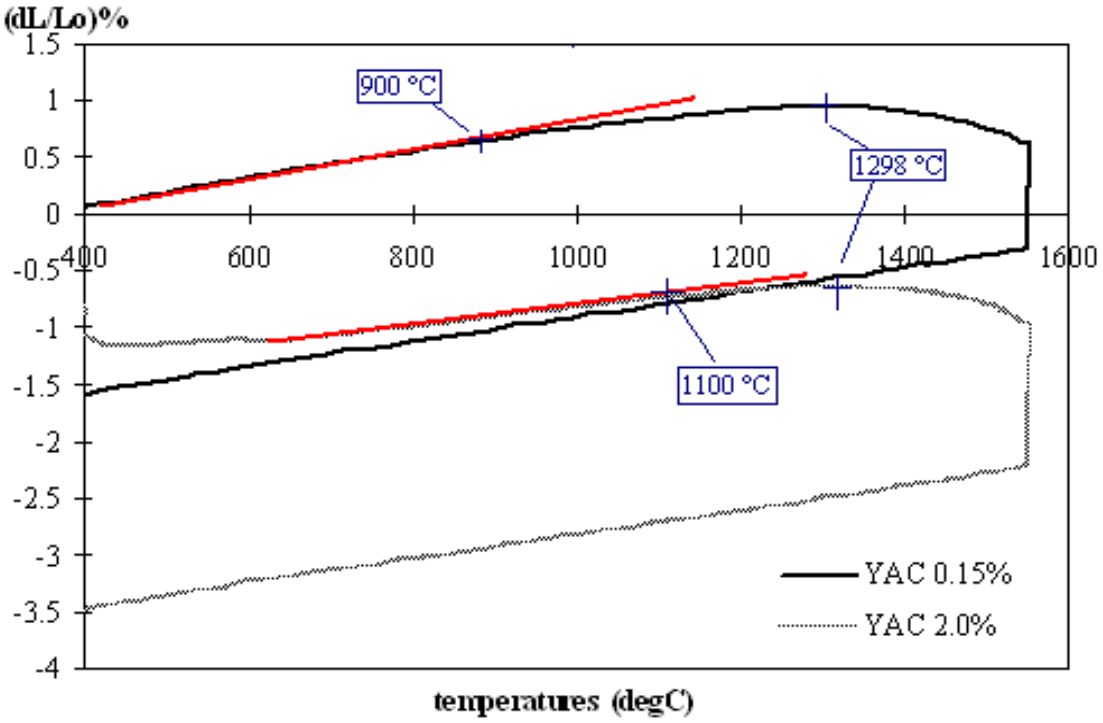
(dL/Lo)%
1.5
1
0.5
0
-0.5
-1
-1.5
-2
-2.5
-3
-3.5
-4
400
600
800
1000
1200
1400
1600
900 °C
1298 °C
1100 °C
YAC 0.15%
YAC 2.0%
temperatures (degC)

(g)

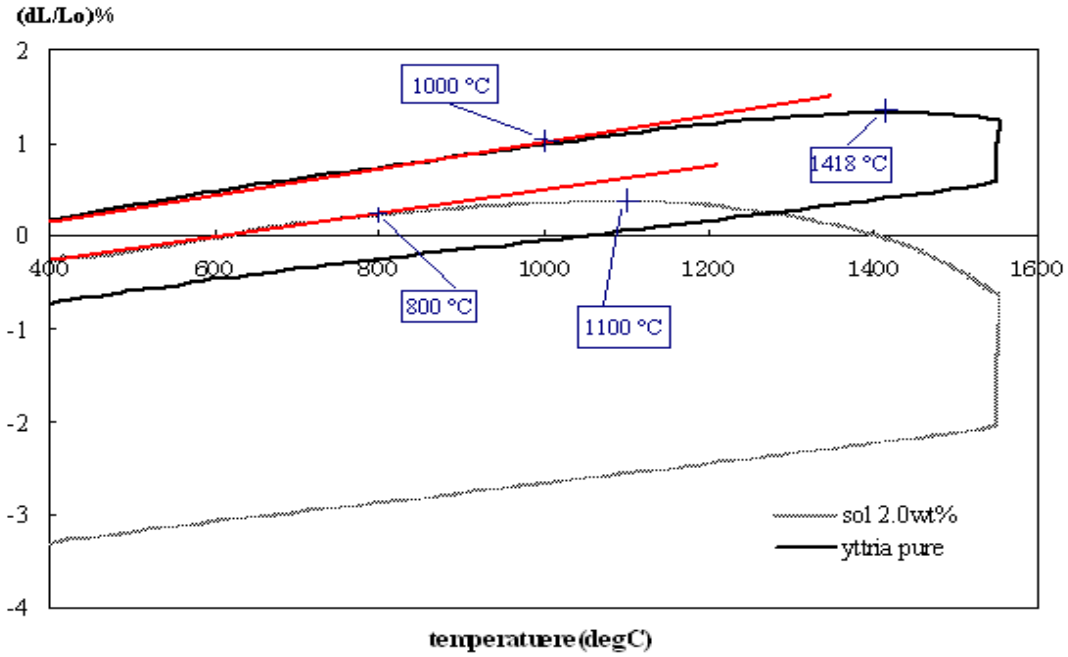

(h)

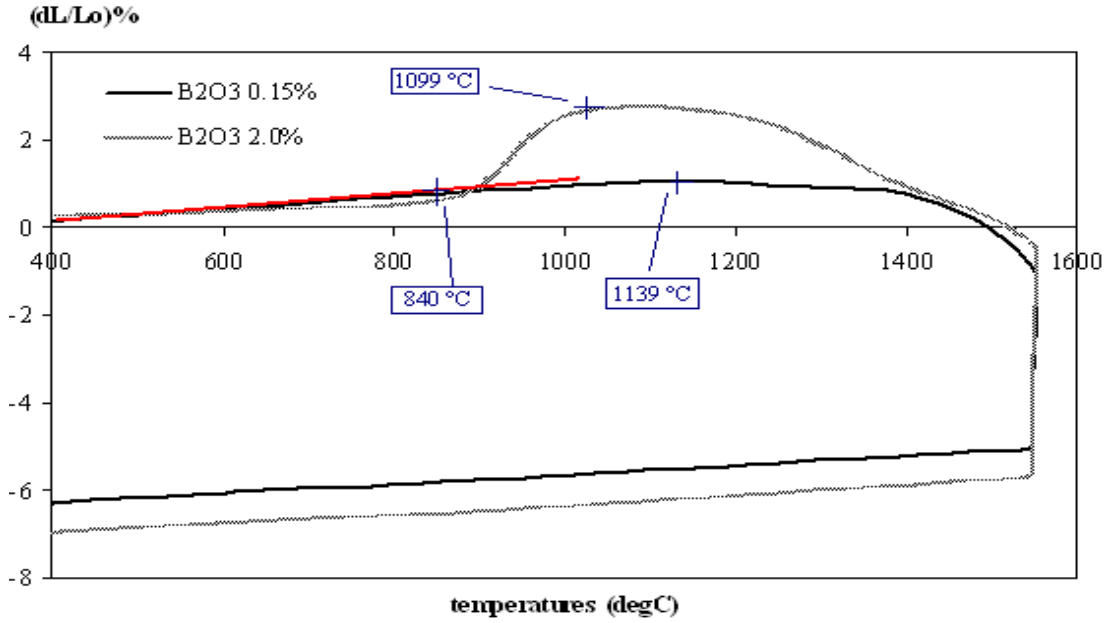

(i)

Figure 3-6. Powder pellet dilatometer traces for the isothermal sintering at 1550 °C: (a) YF_3 addition, (b) TiO_2 addition, (c) YAZ powder (99 wt% yttria, 0.5 wt% alumina, 0.5 wt% zirconia), (d) La_2O_3 addition (e) CeO_2 addition, (f) yttrium carbonate addition, (g)Yttrium acetate addition, and (h) yttria sol addition, (i) B_2O_3 addition.

Powder sintering onset temperatures, total shrinkage after sintering, and temperature where

sintering rate was equal to the expansion rate in Figure 3-6 are summarized in Table 3-6, 3-7 and 3-8 below.

Table 3-6. Powder sintering start temperature (point 1 in Figure 3-5):

Samples		**Sintering start temperature (°C)**
Yttria		**1000**
Sol	2.0wt%	800
YC	0.15wt%	800
YC	2.0wt%	840
B_2O_3	0.15wt%	840
YF_3	0.15wt%	840
TiO_2	2.0wt%	850
YAC	0.15wt%	900
YAZ		950
La_2O_3	2.0wt%	1000
La_2O_3	0.15wt%	1000
YF_3	2.0wt%	1000
TiO_2	0.15wt%	1010
CeO_2	2.0wt%	1031
CeO_2	0.15wt%	1031
YAC	2.0wt%	1100
B_2O_3	2.0wt%	------

*Key: B_2O_3 2.0wt% forms a high temperature phase formation around 800 °C.

As can be seen from Table 3-6, rather than sintering at the isothermal temperature at 1550 °C, all powder compacts have already begun to sinter/densify during the heating cycle as shown by the decrease in linear thermal expansion rate. Compared to pure yttria powder, a small amount of sol added into the powder reduced the sintering starting temperature by around 200 °C from its original 1000 °C. Compared to the sol, sintering additives can enhance yttria powder sintering rate at temperatures below 1400 °C. The sintering aids like yttrium carbonate, boron oxide, and titanium oxide reduced the onset of sintering by about

150-200 °C. For example, commercially blended YAZ powder started to sinter at 950 °C, 100 °C lower than pure yttria powder.

Also, the magnitude of reduction of sintering start temperatures is also highly dependent on the amount of additives. For compounds with TiO_2, CeO_2 and La_2O_3, by increasing the amount of sintering aids, the powder densification rate was largely moved to a lower sintering temperature. However, for some of the additives, such as B_2O_3, yttrium carbonates (YC), yttrium acetate (YAC), the high added amount will lead to a retarded densification rate. These candidates seem to be more effective in small amounts.

The powder dilatometer trace for 2.0 wt% B_2O_3 shows an abnormal volume expansion during the heating cycle around 850 °C. This dramatic volume change was closely related to a large exothermic effect, which may be due to the formation of a new phase. J. Madarasz *et al* [165] reported that a broad exothermic effect occurred by sintering 1:1 Y_2O_3 and B_2O_3 powder from temperatures of 720-980 °C using DTA. This effect is due to the interaction of B_2O_3 and yttria to form YBO_3. The formation of these transient liquid phases may enhance the material diffusion and therefore enhance powder sintering without volume densification.

Table 3-7. The Total Shrinkage of the Samples after Sintering at 1550 °C for one hour.

Samples	**Shrinkage (dL/Lo)%**
Yttria	**1.2**
B_2O_3 2.0wt%	7.3
B_2O_3 0.15wt%	6.8
YAC 2.0wt%	4.0
Sol 2.0wt%	**3.75**
TiO_2 0.15wt%	2.8
YF_3 0.15wt%	2.7
TiO_2 2.0wt%	2.55
YC 2.0wt%	2.2
YAZ	2.1
YAC 0.15wt%	2.1
CeO_2 0.15wt%	1.75
YF_3 2.0wt%	1.5
La_2O_3 0.15wt%	1.2
CeO_2 2.0wt%	1.2
YC 0.15wt%	1
La_2O_3 2.0wt%	0.8

Table 3-8. Powder compact densification starting temperatures (point 2 in Figure 3-5).

Samples	**Temperatures** (°C)
Yttria	**1418**
B_2O_3 2.0wt%	1099
Sol 2.0wt%	**1100**
B_2O_3 0.15wt%	1139
TiO_2 2.0wt%	1200
TiO_2 0.15wt%	1279
YAC 2.0wt%	1298
YF_3 0.15wt%	1298
YAC 0.15wt%	1298
YC 0.15wt%	1318
YAZ	1318
YF_3 2.0wt%	1358
YC 2.0wt%	1358
CeO_2 0.15wt%	1418
La_2O_3 2.0wt%	1418
La_2O_3 0.15wt%	1438
CeO_2 2.0wt%	1438

After isothermal heating at 1550 °C, the total shrinkage of the pellets is different for different sintering additive systems. Pure yttria powder has total linear shrinkage of only around 1.2 % compared with its original dimensions, see Table 3-7. Yttria with 2.0 wt% sol added has a total linear shrinkage of around 3.75 %, which is equal to around 10.8 % in volumetric shrinkage. Powders with 2.0 wt% boron oxide have the largest volume shrinkage of around 20.3 % followed by 0.5 wt% boron oxide at around 19.04 %. Powders using 2.0 wt% yttrium acetate also has very large volume shrinkage of around 11.5 %. The dramatic dimensional shrinkage causes very high density changes after the heating cycle. For other powder additives such as TiO_2 and YAZ, the linear shrinkages are all larger than 2 %. However, large shrinkages or contractions of the powder may be harmful for face coat quality. These may cause de-lamination of the face coat from the backup coat. Therefore, the filler powder should be carefully designed.

Table 3-8 illustrates the actual temperature for the onset of shrinkage for different sintering additive systems. From this table, it can be seen that the actual shrinkage of the powder compacts takes place at temperatures higher than the sintering start temperature. Therefore, powder sintering will not lead to densification taking place. For pure yttria powder, sintering starts at a temperature of around 1400 °C, similar to the published data [123]. By using sol as the binder, the filler powder begins to shrink at temperatures around 1100 °C, around 300 °C lower than pure yttria powder. Therefore, the benefits of using yttria sol as the binder in a face coat is not only to increase the green strength of the face coat, but also to enhance

powder sintering at temperatures around 1200 °C. Sintering additives can also decrease the powder sintering temperature as the sol does, such as B_2O_3 and TiO_2, but some of the sintering additives seem to retard powder sintering, e.g. CeO_2 and La_2O_3 at temperatures below 1600 °C.

An example of the shrinkage trace of a YAZ sample sintered at different isothermal heating cycles is shown in Figure 3-7 (a) with the measured total shrinkage of the powder at each heating cycle. Figure 3-7 (b) & (c) illustrate that the expansion rates of the powder compacts during heating were nearly the same, but the shrinkage rates were different dependent on the isothermal temperatures. Higher isothermal temperature caused a higher shrinkage rate. The total shrinkage of YAZ powder compacts after different heating cycles are summarized in Table 3-9.

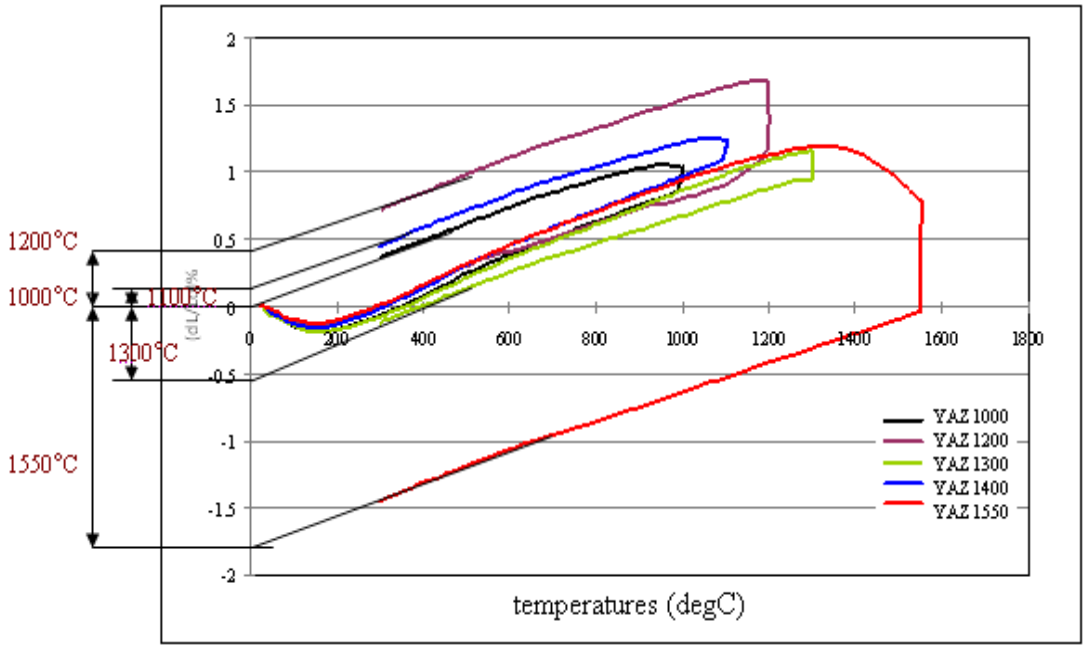

(a)

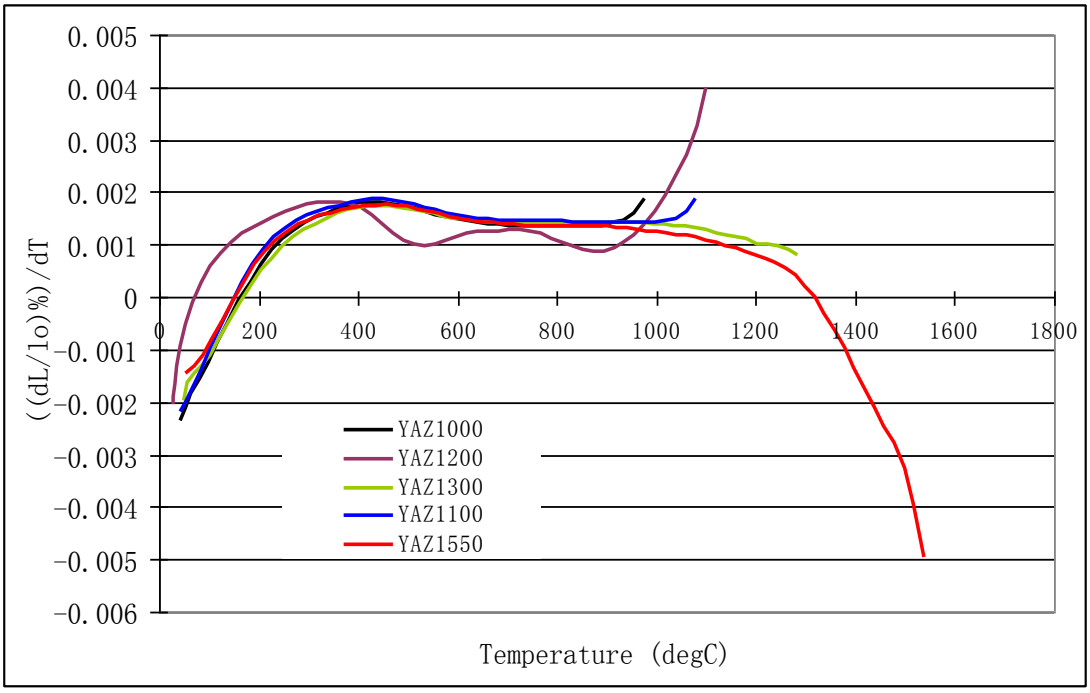

(b)

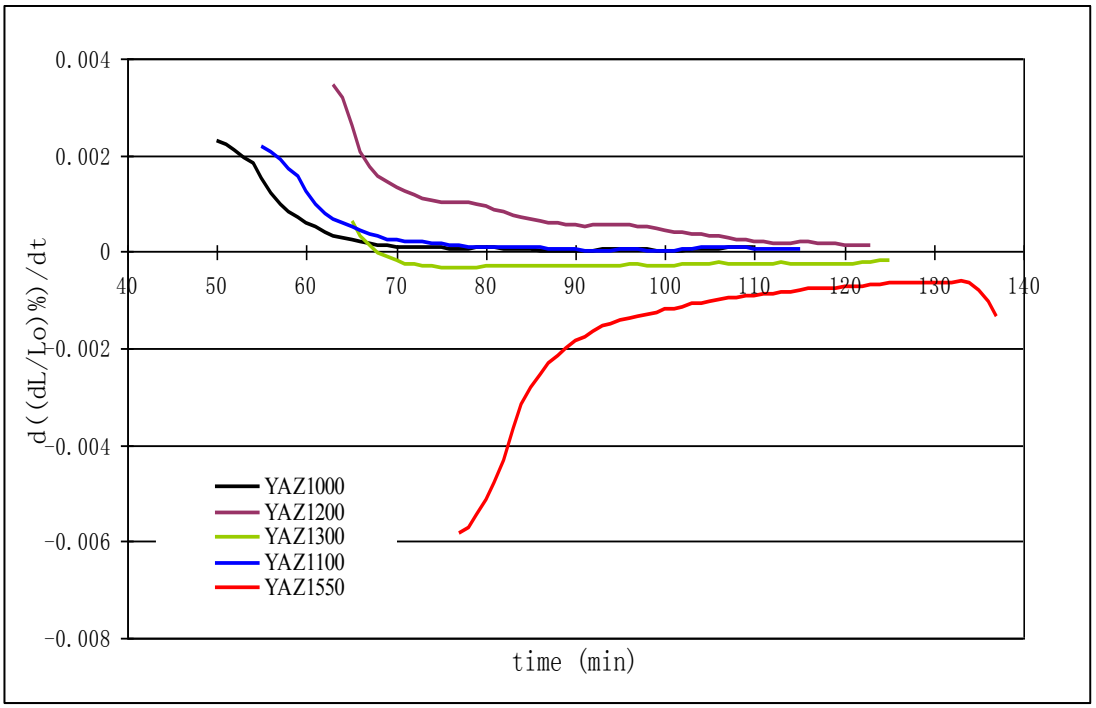

(c)

Figure 3-7. (a) The isothermal shrinkage trace of YAZ powder at different isothermal temperatures: 1000, 1100, 1200, 1300, and 1550 °C, (b) the expansion rate during the heating cycle, and (c) the shrinkage rate at different isothermal temperatures.

Table 3-9. The total linear shrinkage after sintered at different isothermal heating.

Isothermal temperatures	1000 °C	1100 °C	1200 °C	1300 °C	1550 °C
YAZ	0%	-0.22%	-0.43%	0.55%	1.75%

*Negative symbol represents expansion

From Figure 3-7, it seems that for different isothermal sintering temperatures, the sintering behaviour of the YAZ sample is different. Higher isothermal temperatures cause a faster densification rate with a higher sintering density. But it should be noted that, if powders are sintered below the temperature at which expansion is equal to shrinkage, point 2 temperature (defined in Figure 3-5), increasing sintering temperatures may cause the powder sintering but without densification.

Although the isothermal sintering starts from a different shrinkage rate (see Figure 3-7 (c)), the powder densification rate is then gradually slowed down and stabilized at a constant rate at that temperature. Therefore, the densification of the powder pellets is a temperature dependent process rather than time. So that, long sintering times of the powder at temperatures below the shrinkage temperature (e.g. lower than 1300 °C) will not lead to a high density. Some powders‘ isothermal heating traces with 2.0 wt% additives are shown in Figure 3-8.

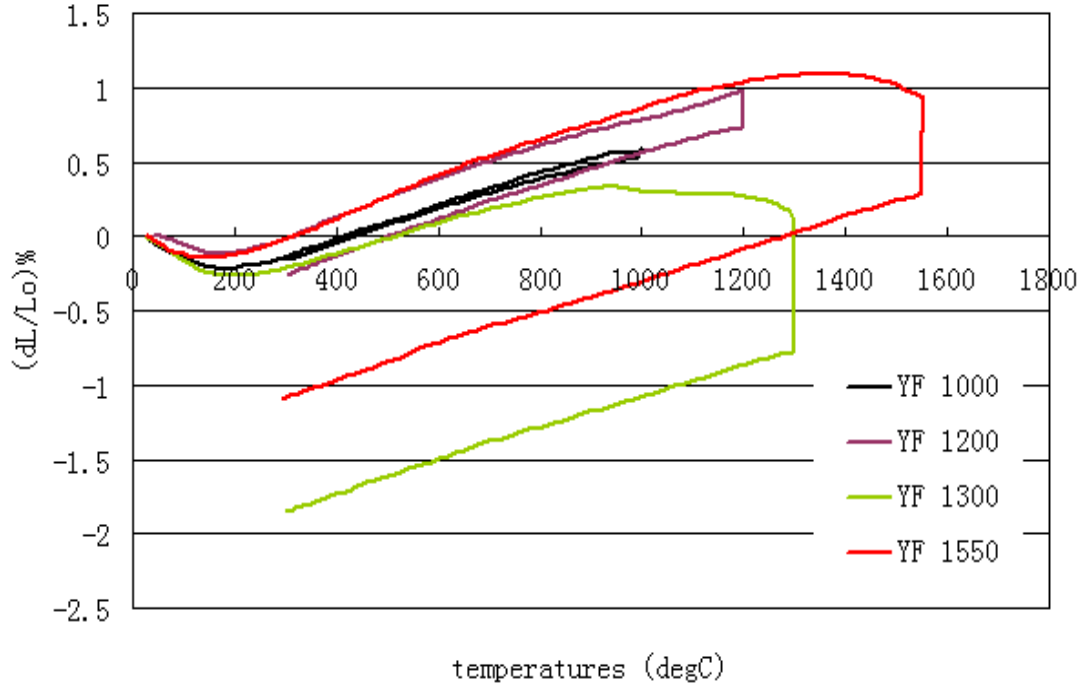
1.5
1
0.5
0
-0.5
-1
-1.5
-2
-2.5
0
200
400
600
800
1000
1200
1400
1600
1800
(dL/Lo)%
temperatures (degC)
YF 1000
YF 1200
YF 1300
YF 1550

(a)

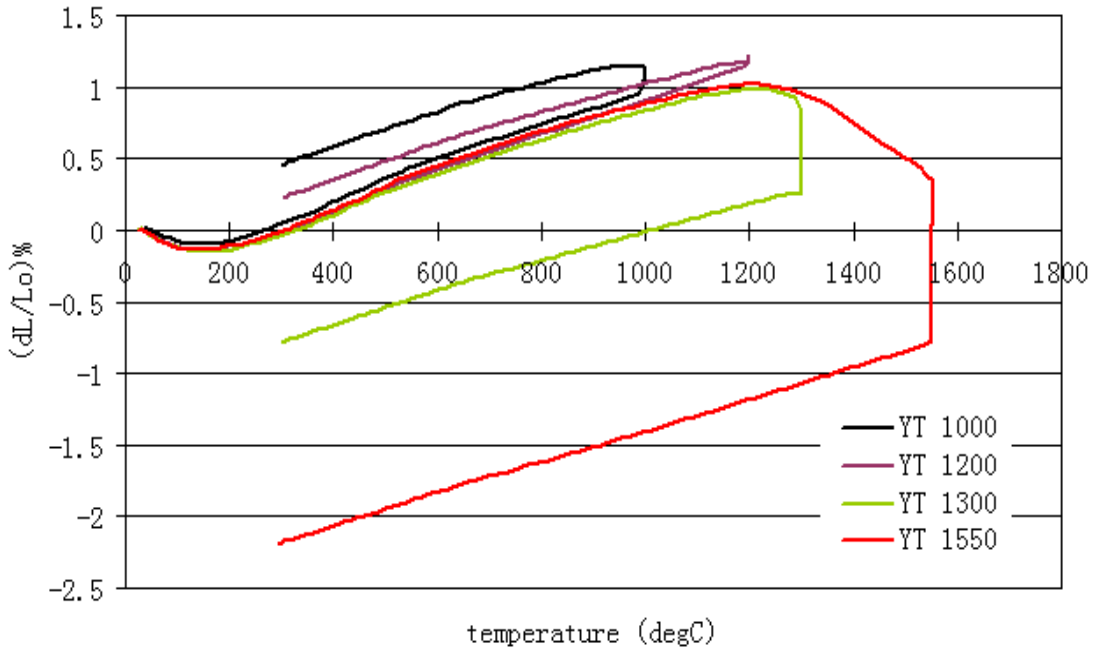
1.5
1
0.5
0
-0.5
-1
-1.5
-2
-2.5
0
200
400
600
800
1000
1200
1400
1600
1800
(dL/Lo)%
temperature (degC)
YT 1000
YT 1200
YT 1300
YT 1550

(b)

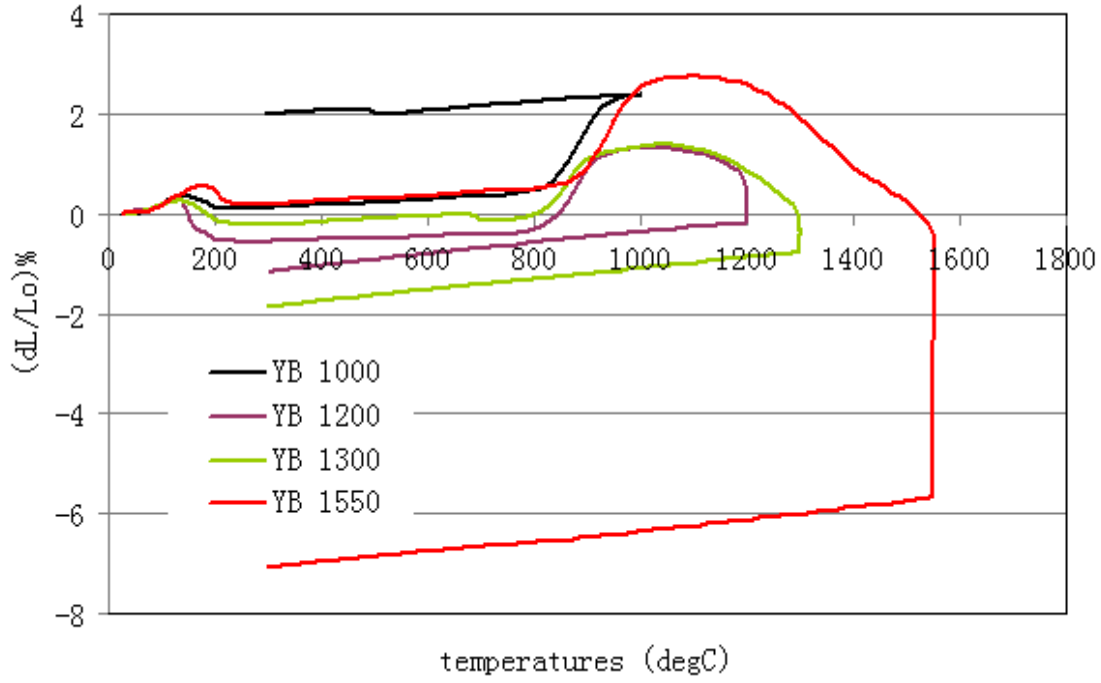
4
2
0
-2
-4
-6
-8
0
200
400
600
800
1000
1200
1400
1600
1800
(dL/Lo)%
YB 1000
YB 1200
YB 1300
YB 1550
temperatures (degC)

(c)

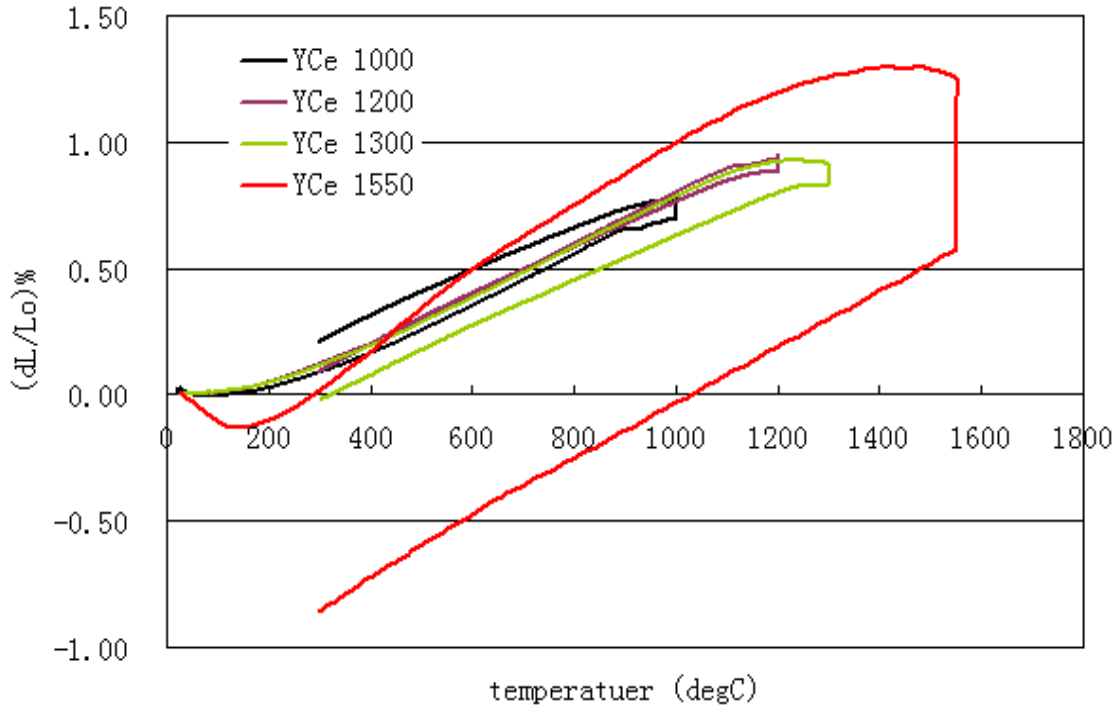
1.50
1.00
0.50
0.00
-0.50
-1.00
0
200
400
600
800
1000
1200
1400
1600
1800
(dL/Lo)%
YCe 1000
YCe 1200
YCe 1300
YCe 1550
temperatuer (degC)

(d)

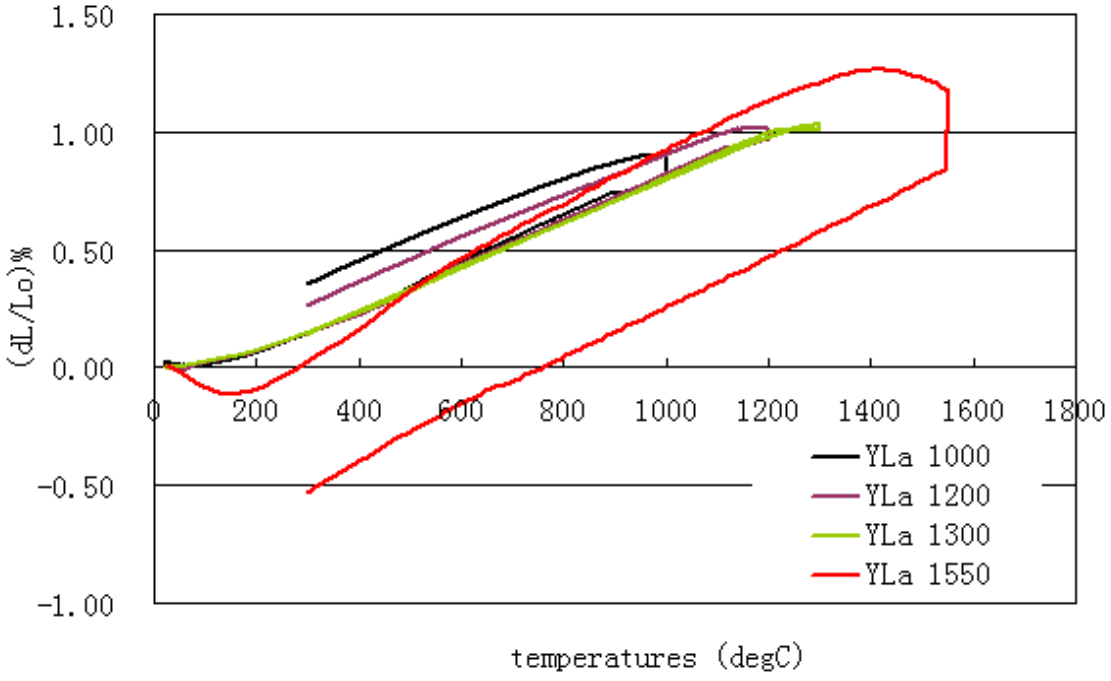

(e)

Figure 3-8. The isothermal shrinkage curves for different sintering additives at different sintering temperatures. (a) YF_3 2.0 wt%, (b) TiO_2 2.0 wt%, and (c) B_2O_3 2.0wt% (d) CeO_2 2.0 wt%, and (e) La_2O_3 2.0 wt%.

As can be seen from Figure 3-8, similar to YAZ powder described previously, all the powder compacts showed a volume expansion when sintered at temperatures below 1200 °C. Higher temperatures caused more shrinkage to take place at the same isothermal sintering time. It seems that powders with B_2O_3, TiO_2 and YF_3 additives have larger shrinkage taking place than the powders containing La_2O_3 and CeO_2 at the same sintering temperatures.

Powder sintering behaviour is not only influenced by the sintering temperatures, but also affected by the heating rate during heating cycles. Figure 3-9 shows the sintering behaviour of YAZ powder using different heating rates.

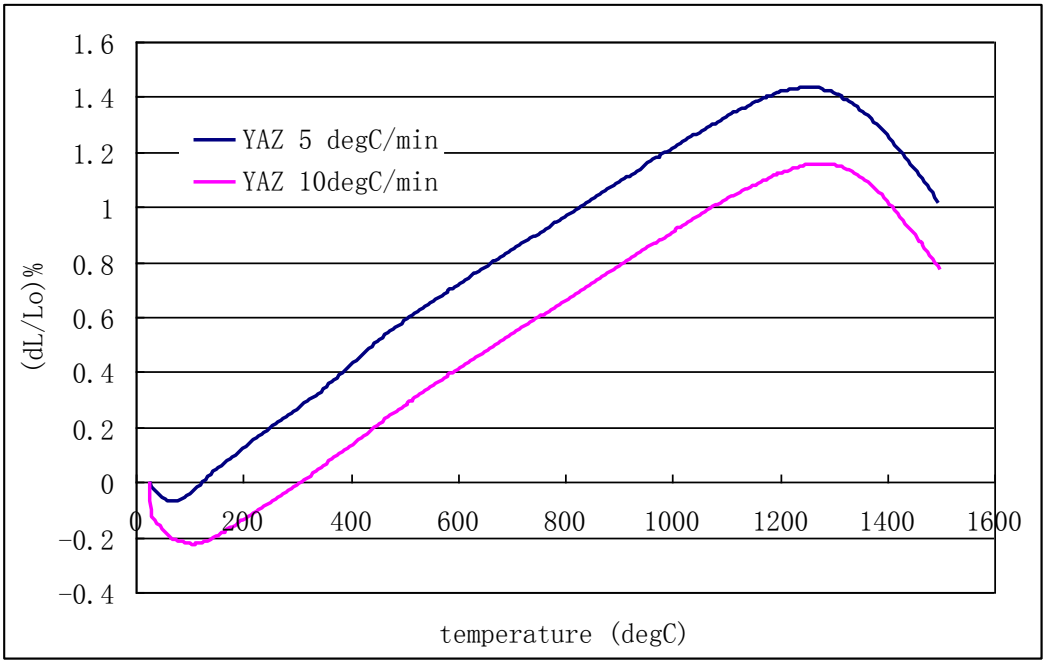

(a)

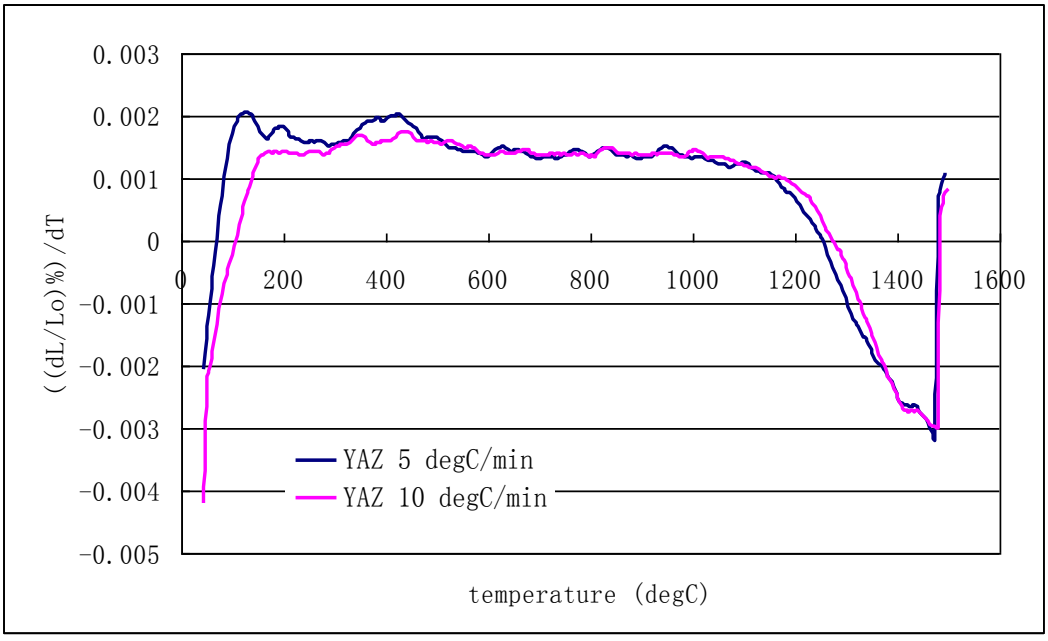

(b)

Figure 3-9. Constant rate heating (CRH) of YAZ powder (a) dL/Lo% linear shrinkage curve at different temperatures, (b) the shrinkage rate ((dL/Lo)%)/dT curve.

From the above curves, it can be seen that, by changing the heating rate of the pellets from 5 to 10 °C /min, the sintering curve is changed with around a 25 °C shift taking place at the

different heating temperatures. Some of the powder shrinkage rate curves are shown in Figure 3-10.

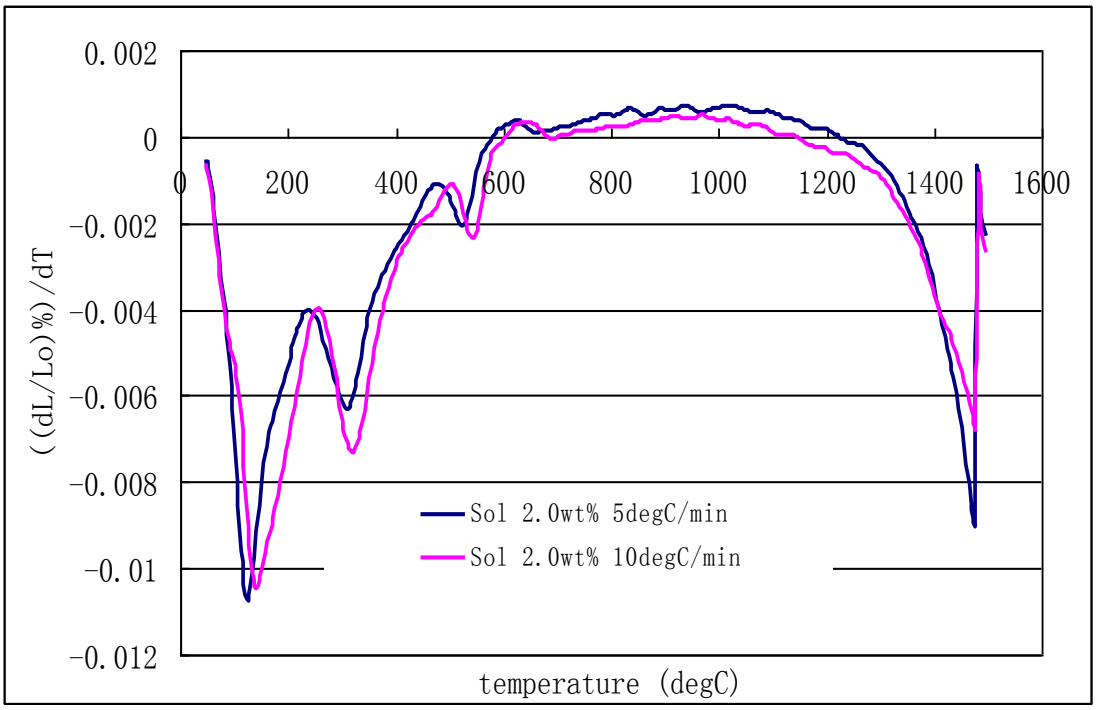

(a)

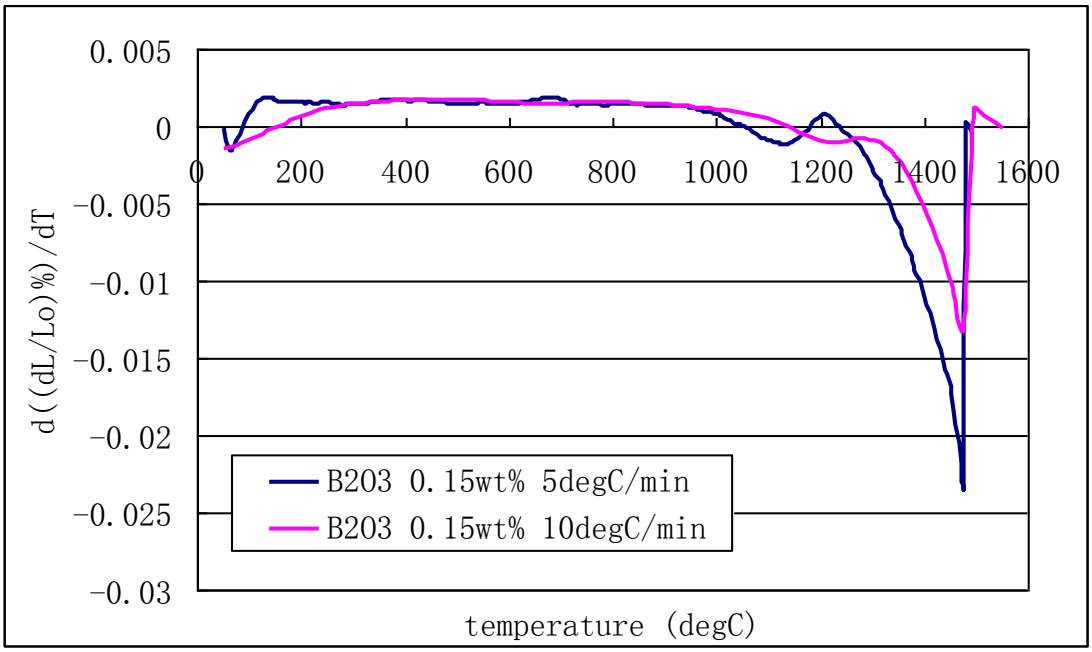

(b)

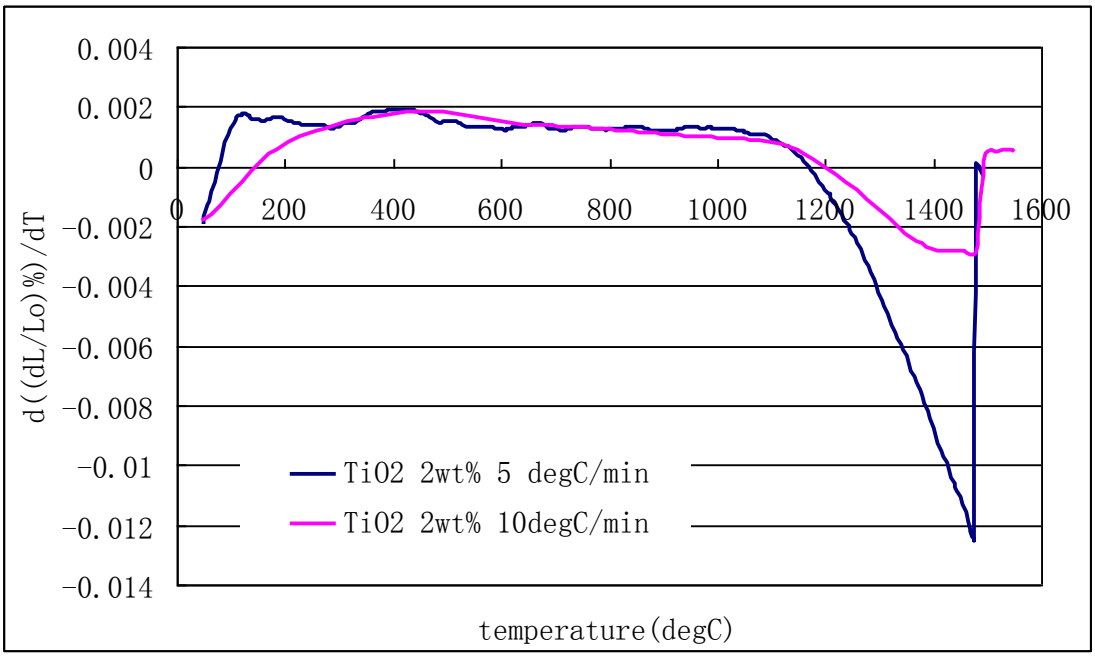

(c)

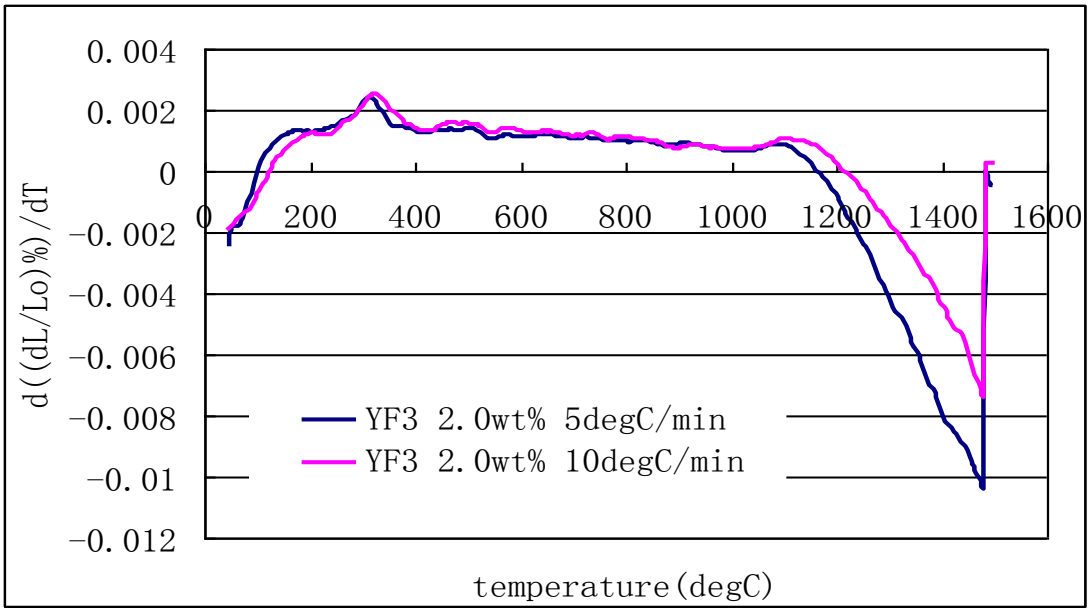

(d)

Figure 3-10. The constant heating shrinkage rate of different powder pellets. (a) sol, (b) 0.15 wt% B_2O_3, (c) 2.0 wt% TiO_2 and (d) 2.0 wt% YF_3.

From Figure 3-10 it can be seen that, except for the sol added yttria powder, by decreasing the heating rate, the same shrinkage of the powder compacts can be achieved at lower temperatures (around 20 to 40 °C below its original value). Therefore, a slower heating rate

seems to be more beneficial in promoting powder sintering during the heating process.

3.4.4 Powder sintering microstructure

Yttria -200 mesh powder particles shape and arrangement in the pellets is shown in Figure 3-11.

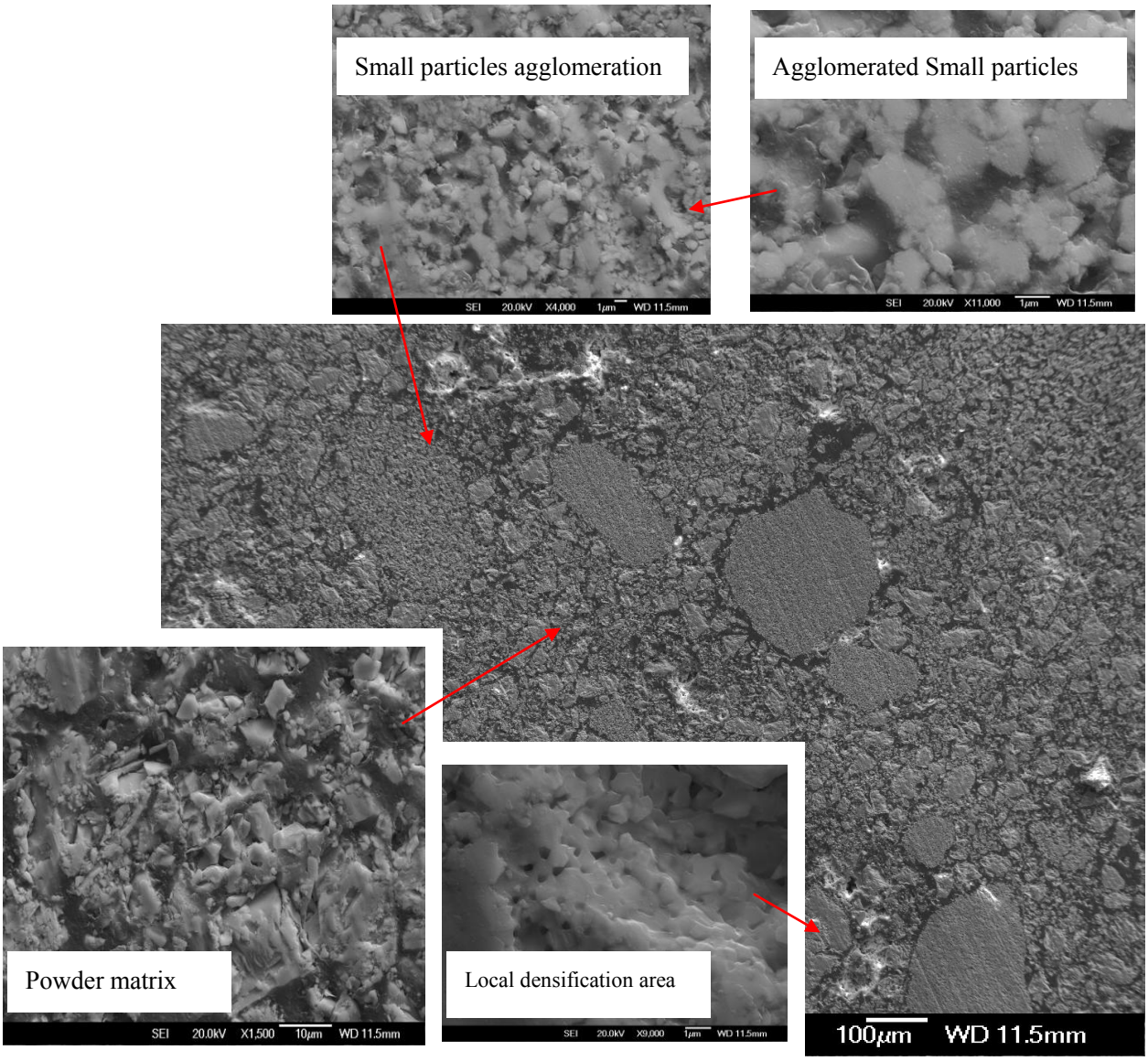

Figure 3-11. Yttria -200 mesh powder pellet surface after sintering at 1600 °C for 1 hour.

As seen from Figure 3-11, yttria -200 powder particles have a wide range of particle size

distributions from 0.1 μm to hundreds of micrometers. The particle shape of these powders is irregular and angular. Small particles tend to fill the gaps between large particles in the matrix or are forming agglomerated grains with high packing density observed.

3.4.4.1 Powder particle size effect

After sintering at different temperatures, due to the different surface area between the small and large particles, the sintering microstructure is different, see Figure 3-12 and Figure 3-13.

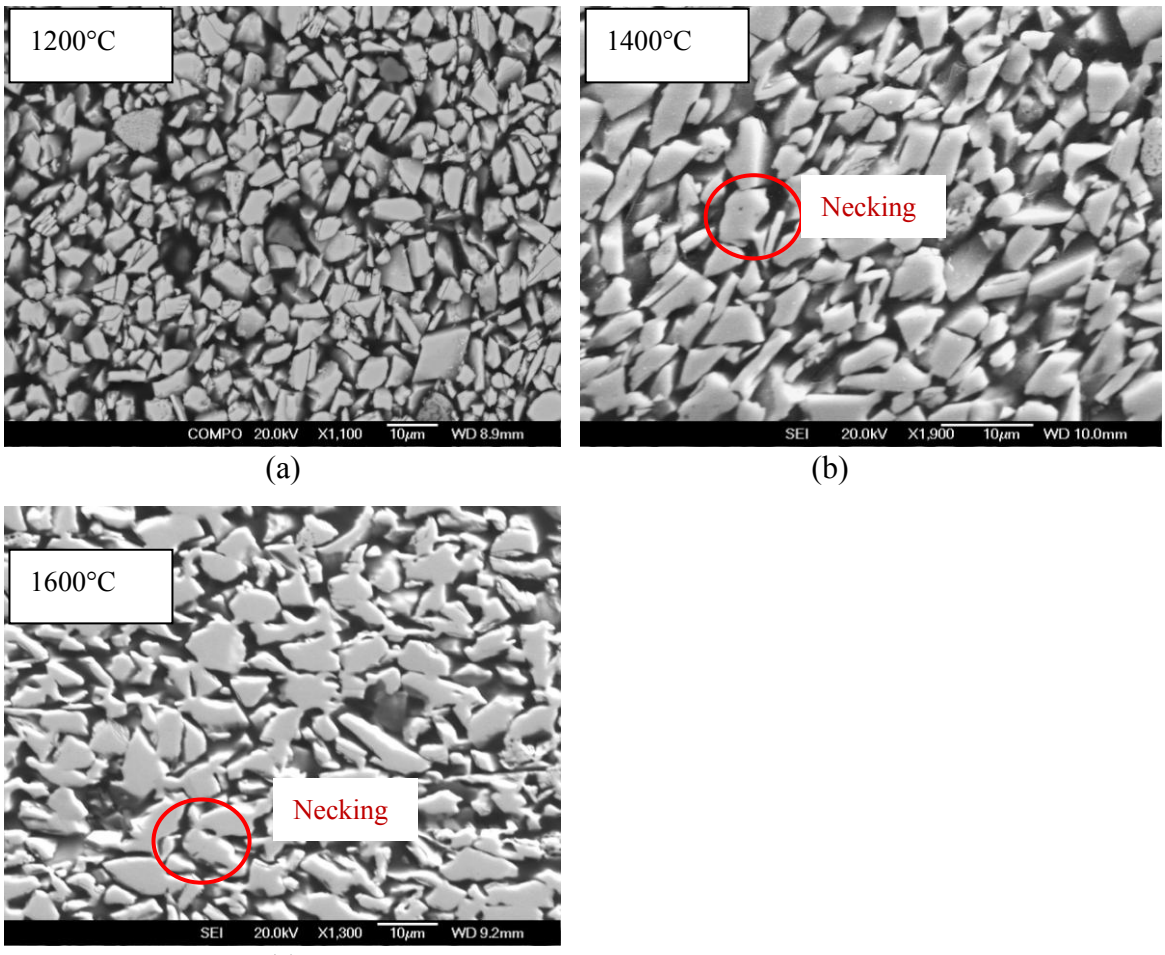

Figure 3-12. SEM images for small particles (~10 μm) of sample 2 wt% TiO_2 addition powder pellet surfaces after sintering at (a) 1200 °C, 1400 °C (b) and 1600°C (c) for 1 hour.

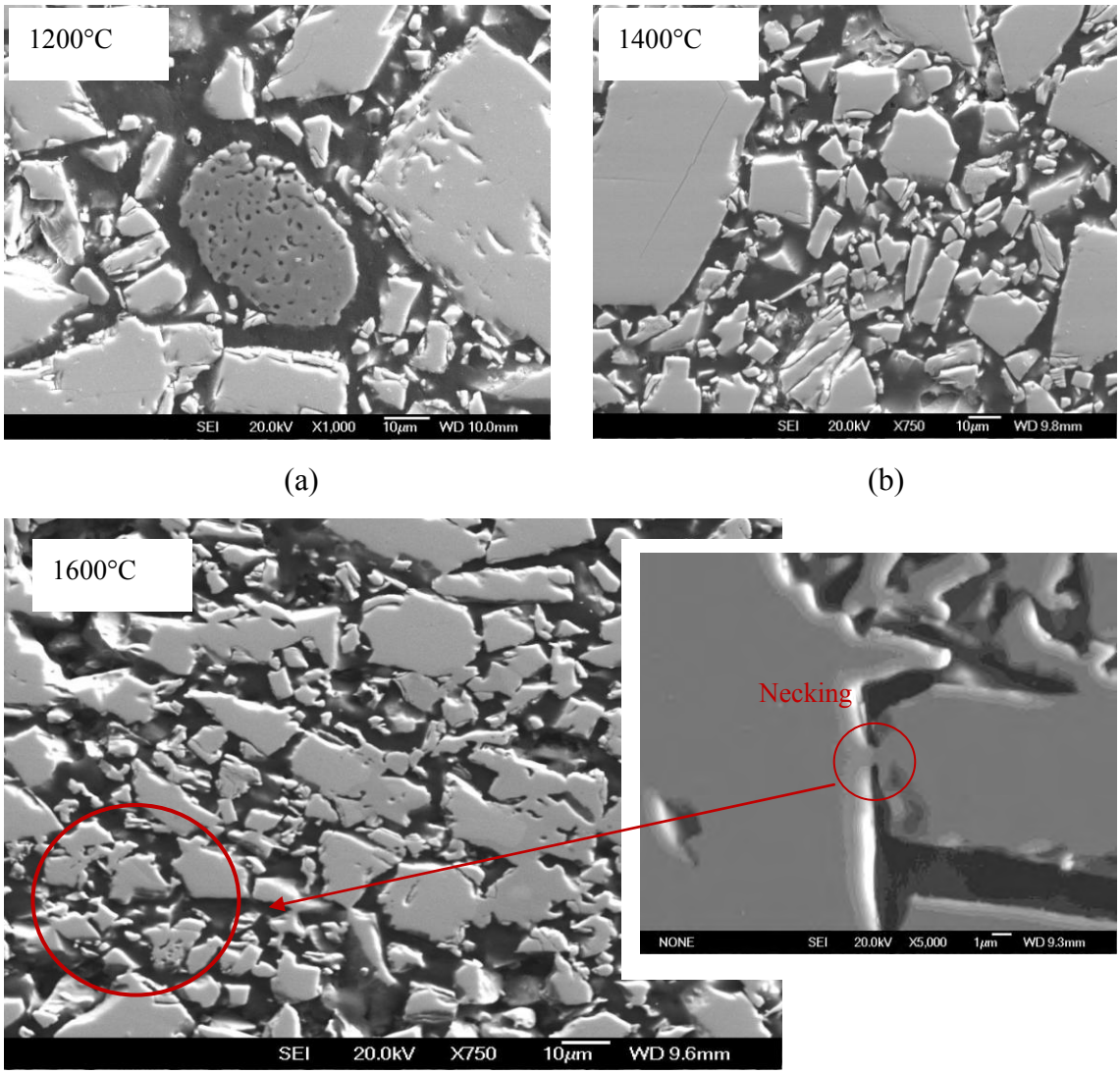

Figure 3-13. SEM images of large particles (~30 μm) of sample 2 wt% TiO_2 addition powder pellet surfaces after sintering at (a) 1200 °C, 1400 °C (b) and 1600 °C (c) for 1 hour.

Comparing the powder microstructures in Figures 3-12 and 3-13, the obvious neck growth between small particles seems to start at a lower sintering temperature (around 1400 °C) when compared to larger particles, which take place at around 1600 °C.

3.4.4.2 The effect of additive elements

The additive elemental distribution mapping (EDX), of the 2.0 wt% TiO_2 sample surface is

shown in Figure 3-14.

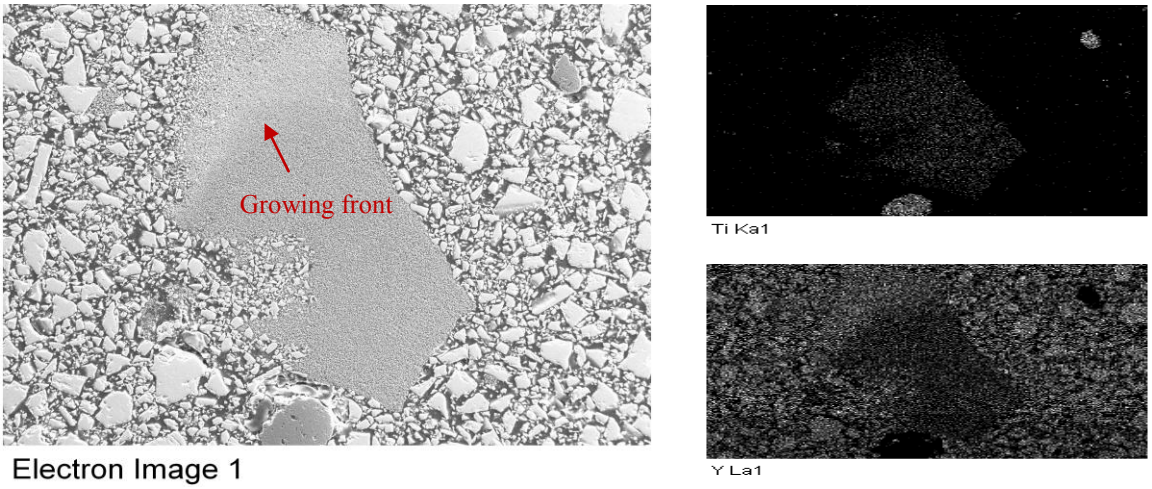

Figure 3-14. EDX mapping of a sample of 2 wt% TiO_2 surface after sintering at 1200 °C for 1 hour.

Figure 3-14 shows that the sintering additives in the powder are non-uniformly distributed with higher concentrations in some areas. During sintering, these additive elements diffuse out into the yttria matrix and form liquid phases, see Figure 3-15.

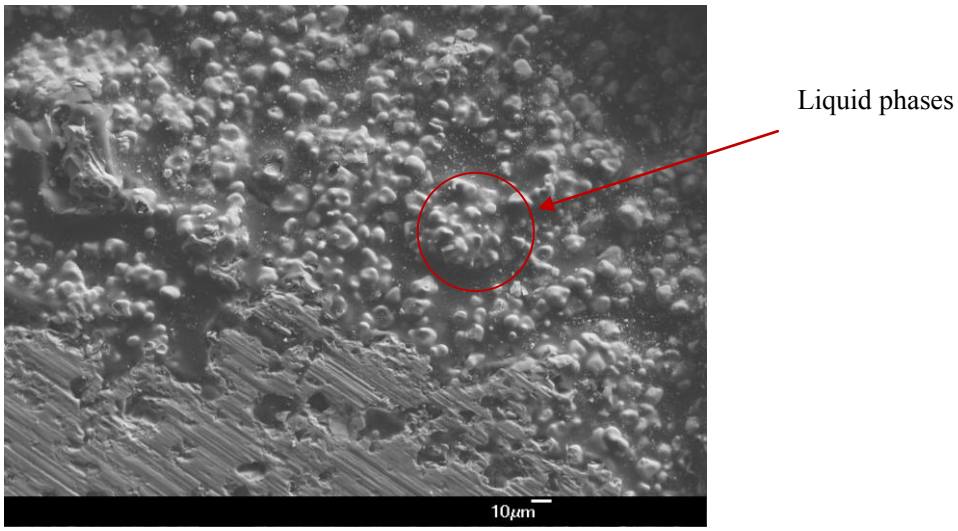

Figure 3-15. „Mushroom‘ shaped liquid phase formation of 2.0 wt% TiO_2 pellet surface after sintering at 1600 °C for one hour.

The enhanced diffusivity of the material between powder particles by adding sintering additives was first observed as the change of particle shapes (the edges of the powder particles changed from sharp to smooth) (Figure 3-16 (a)). When increasing the sintering temperature, the amount of material diffusing between particles was increased and bonded particles together (Figure 3-16 (b)). Then, the powder compact will quickly densify within a short period of time.

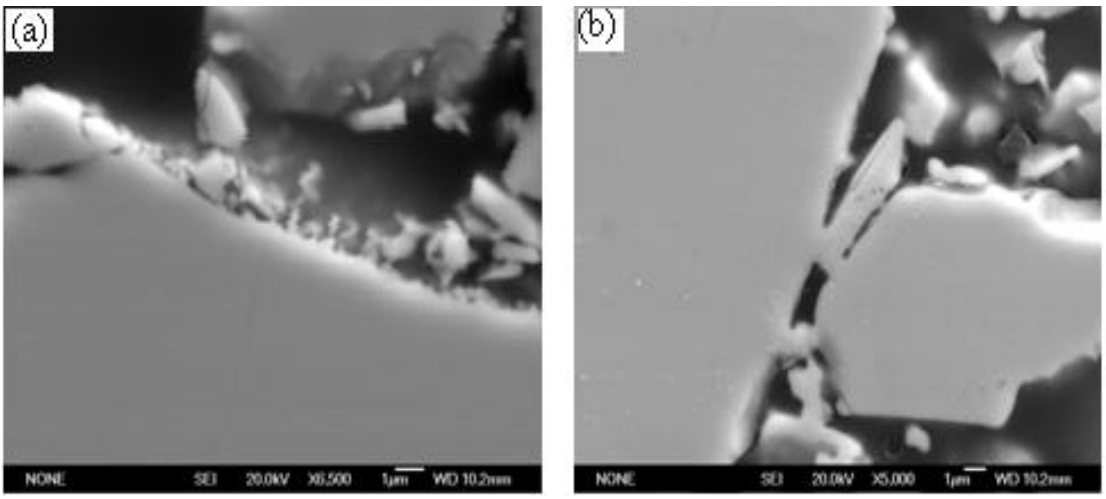

Figure 3-16. 0.15wt% YB Powder Microstructure at, (a) 1200 °C, and (b) 1400 °C.

The powder densification process can be observed at temperatures of 1000, 1200, 1400 and 1600 °C and are shown in Figure 3-17.

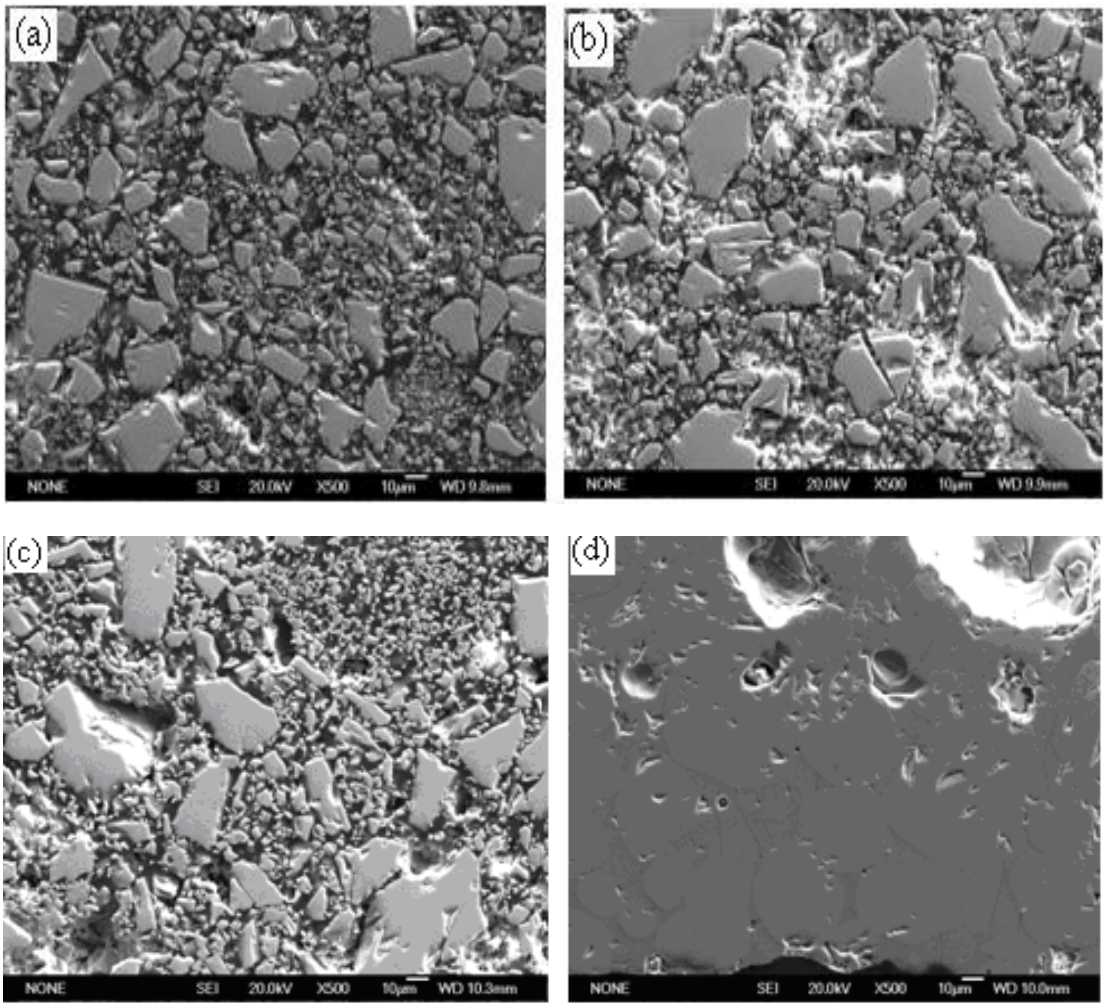

Figure 3-17. 2 wt% B_2O_3 addition powder sintered at (a) 1000 °C, (b) 1200 °C, (c) 1400 °C, and (d) 1600 °C.

A higher isothermal sintering temperature (Figure 3-17 (d)), powder with 2.0 wt% B_2O_3 undergoes a quick densification taking place with pore elimination. The powder particle morphology changes to a circular shape with enclosing pores at the grain junctions. At the end of sintering, these pores will remain between grain boundaries, trapped between grains.

3.4.4.3 The effect of sintering precursors (yttrium carbonate, yttrium acetate)

With the use of sintering precursors, the microstructures of the powder compacts are totally

different from the powder using sintering aids (e.g. B_2O_3, YF_3, CeO_2. etc). This is because of the different density between the transformed oxides and the original organic compounds. When the precursor particles decompose, there are some holes generated in the powder matrix, see Figure 3-18. Because there are no additive elements that can assist in material diffusion during the sintering process, the densification rate for the precursor added powder systems will much slower than for the powder with added sintering aids. Sintering precursors used in this experiment have decomposition temperatures lower than 1000 °C.

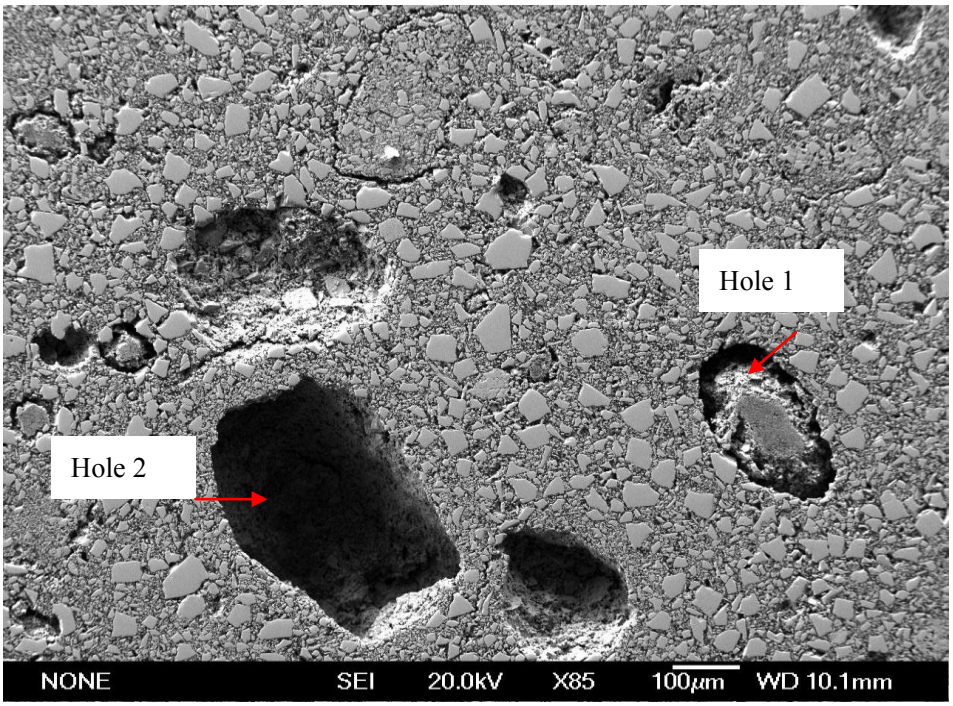

(a)

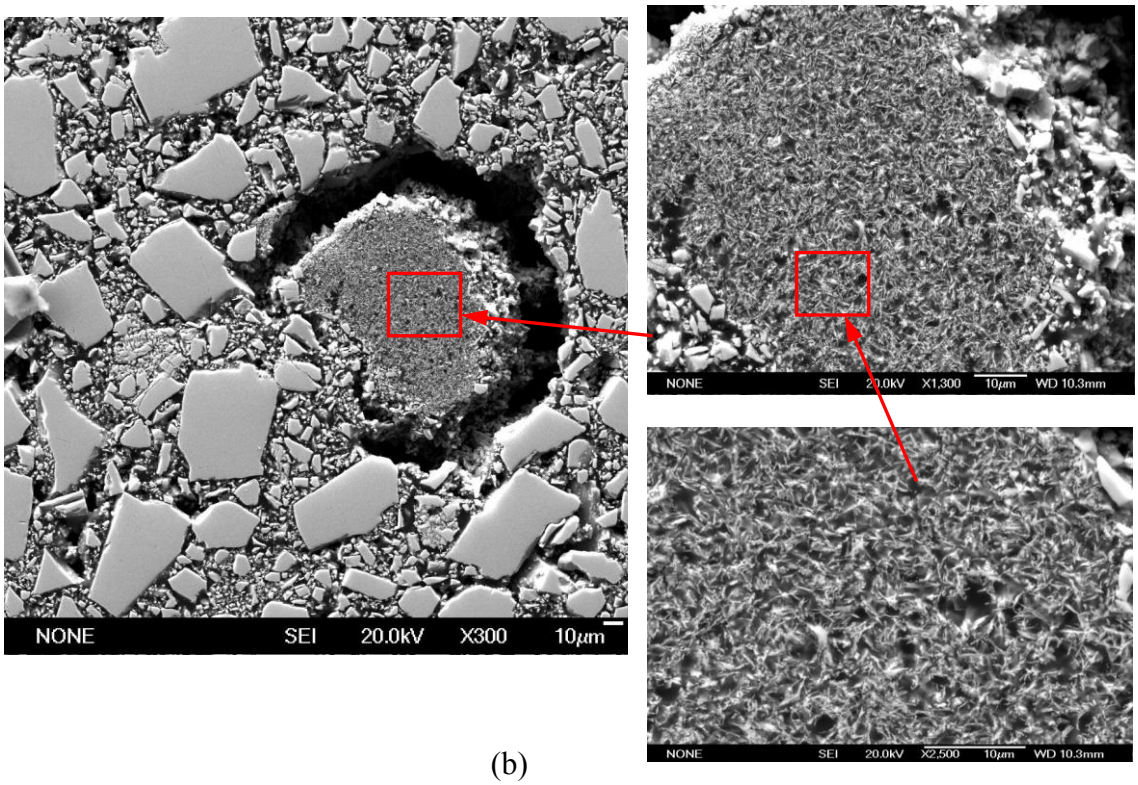

(b)

Figure 3-18. Sintering precursor 2.0 wt% yttrium acetate powder pellets sintered at 1400 °C for one hour surface microstructures. (a) powder pellets matrix structures, and (b) the local decomposition area.

As can be seen from Figure 3-18, there are two types of holes observed in the 2.0 wt% yttrium acetate samples‘ ground surface. One type of hole has morphology like an island with a narrow channel surrounding a locally dense area (see Figure 3-18 hole 1). A look at the central dense part illustrates that it consists of nano-size particles and EDX shows the composition of these small needle like particles is pure Y_2O_3. These holes may form due to the volume change of the organic compounds to oxides after the decomposition reaction. The other type of hole (hole 2) has a large size (more than 100 μm) with a shape similar to the original yttria particles. It is thought that the formation of these large holes may be due to the poor bonding between large particles which easily fall out during the sample preparation

process, e.g. grinding and polishing.

Therefore, compared to all the sintering aids, metal oxide sintering additives can give a more uniform microstructure than sintering precursors. Sintering precursors added into pure yttria have some benefits in promoting powder sintering but seem unsuitable for using in face coat slurry. The large holes formed after the decomposition of precursor particles may influence the cast component surface quality and hence increasing the chance for the molten metal to penetrate into the face coat. It also seems to have very limited benefits to enhance the bulk powder sintering rather than small local areas.

3.4.5 XRD test results

The samples with 2.0 wt% sintering additives were sintered at different temperatures from 1000 to 1600 °C, and the powder composition were detected and analyzed using their X-Ray diffraction patterns, see Figure 3-19.

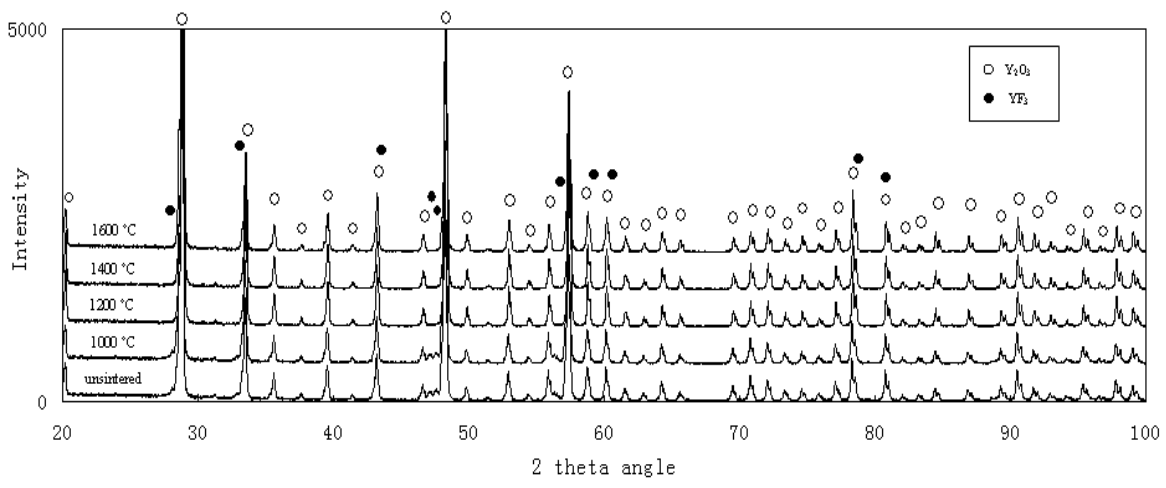

(a)

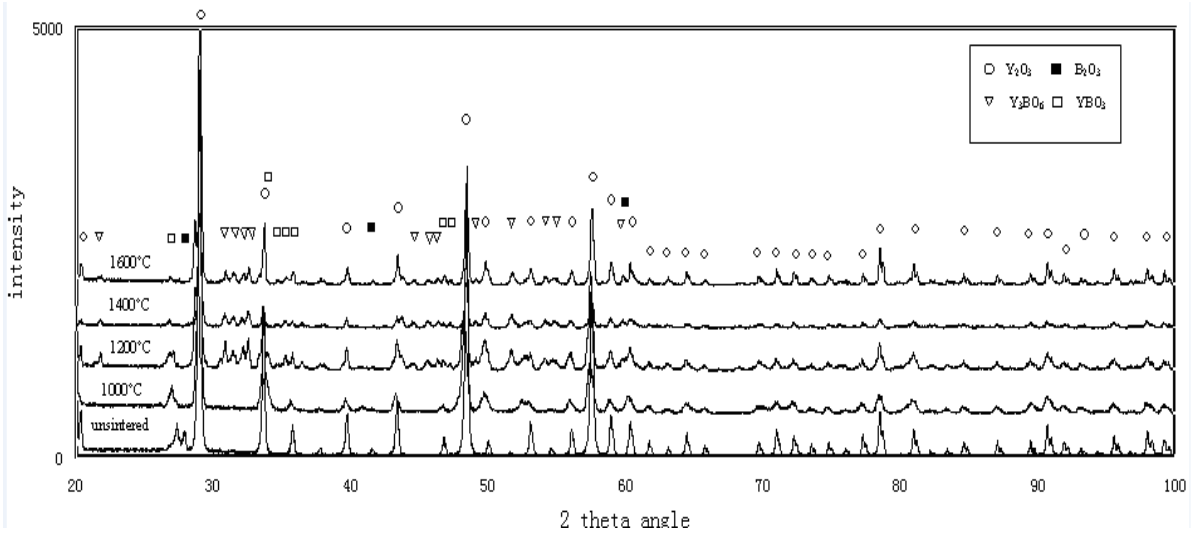
5000
0
intensity
20
30
40
50
60
70
80
90
100
2 theta angle
Y_2O_3 B_2O_3
Y_3BO_6 YBO_3
1600°C
1400°C
1200°C
1000°C
unsintered

(b)

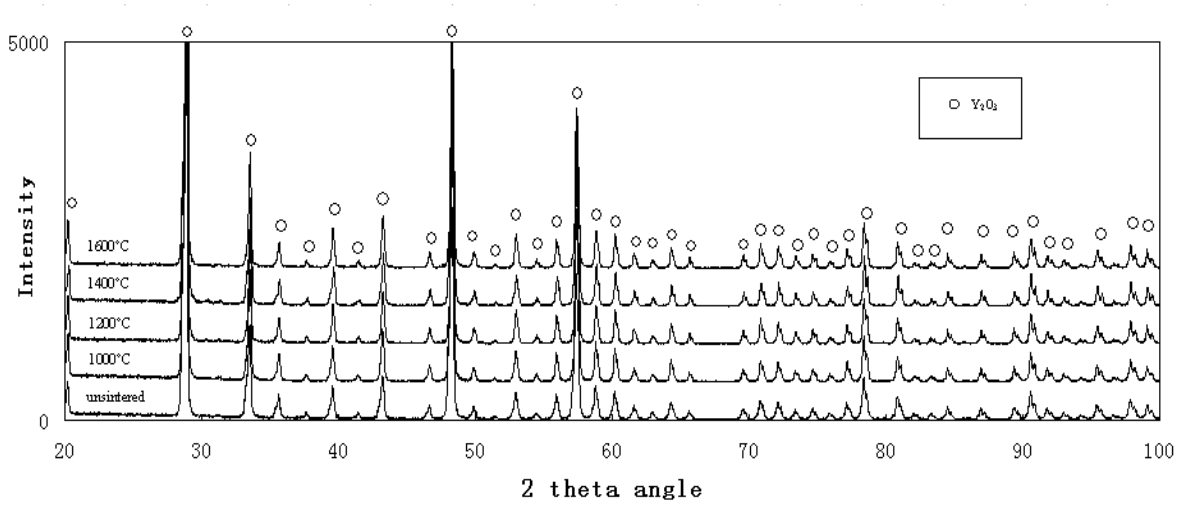
5000
0
Intensity
20
30
40
50
60
70
80
90
100
2 theta angle
Y_2O_3
1600°C
1400°C
1200°C
1000°C
unsintered

(c)

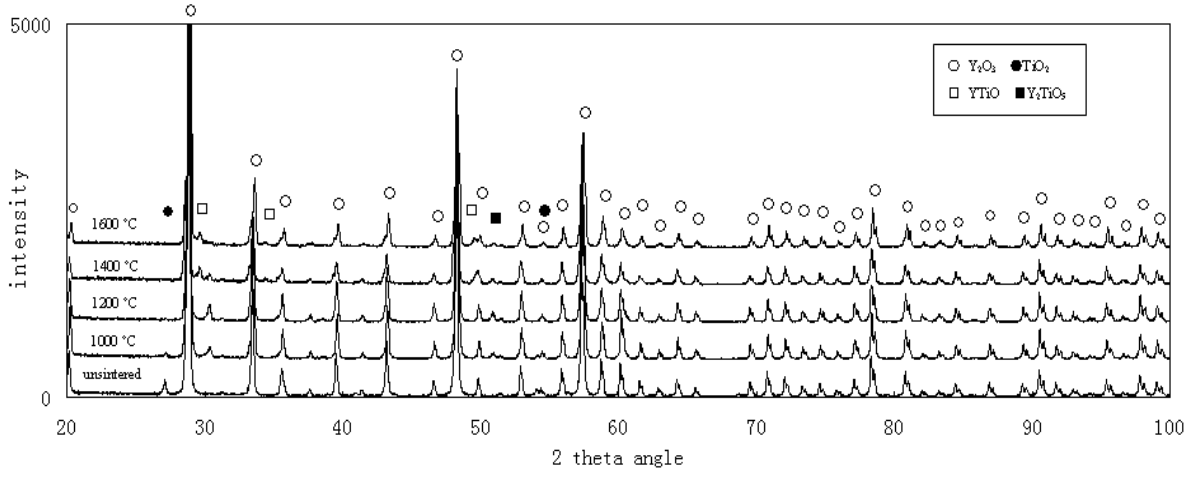
5000
0
intensity
20
30
40
50
60
70
80
90
100
2 theta angle
Y_2O_3 TiO_2
YTiO $Y_2Ti_2O_5$
1600 °C
1400 °C
1200 °C
1000 °C
unsintered

(d)

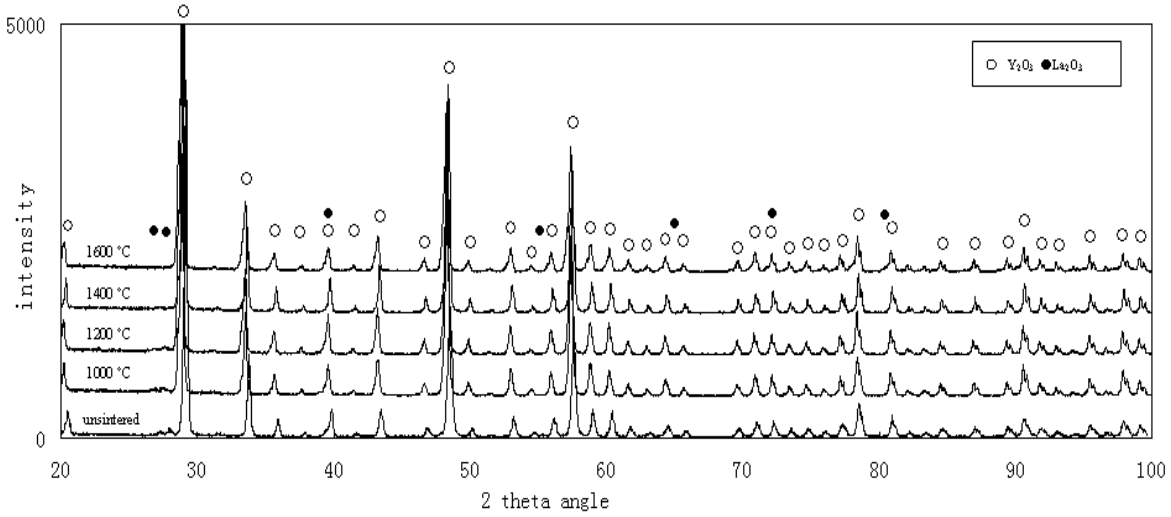

(e)

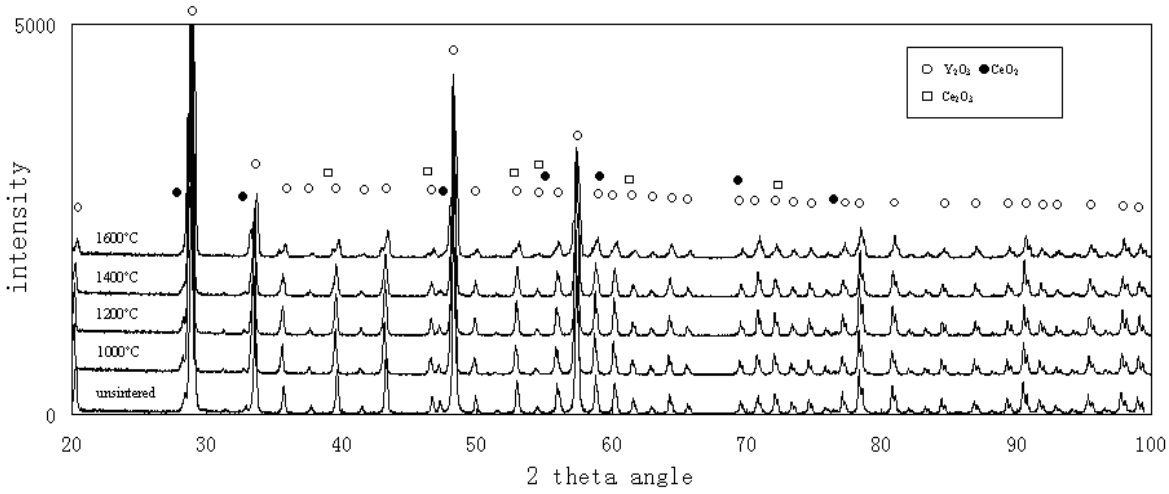

(f)

Figure 3-19. X-ray diffraction pattern of (a) 2.0 wt% YF_3, (b) 2.0 wt% B_2O_3, (c) YAZ, (d) 2.0 wt% TiO_2, (e) 2.0 wt% La_2O_3, (f) 2.0 wt% CeO_2.

As can be seen from Figure 3-19 (a), by adding 2.0 wt% YF_3 into pure yttria powder at different temperatures, the YF_3 phase is only detected at a temperature of 1000 °C with unchanged yttria peaks appearing at high sintering temperatures. Because YF_3 has an evaporation temperature of around 1000 °C [155, 166], high temperature sintering may cause the small residual YF_3 phase to evaporate and thus is hardly detected.

Boron oxide in powder 2.0 wt% B_2O_3 will interact with yttria to form YBO_3 at a temperature of around 1000 °C, and this new phase will transform to another yttrium borate Y_3BO_6 at higher sintering temperatures (1200°C), see Figure 3-19 (b). The formation temperature of YBO_3 was detected by J. Madarász [165] at around 720-980 °C. The high temperature phase Y_3BO_6 reported by Boyer. D and Lin. JH [167, 168] has a formation temperature around 1100 °C [169], and which was confirmed with this experiment observation of around 1200 °C.

By increasing the sintering temperature, TiO_2 will interact with yttria to form Y_2TiO_5 at a around 1200 °C, then continuously increasing the sintering temperature Y_2TiO_5 will transform into a YTiO (fluorite) type at temperatures around 1400 °C. This test result was confirmed with the available binary phase diagram of Y_2O_3-TiO_2 [170-172], and the Y_2TiO_5 eutectic phase will only exist at temperatures below 1400 °C. At high temperature, fluorite type is the dominant structure.

No element peak changes have been observed in the YAZ sample through all test temperatures. These unchanged peaks in Figure 3-19 (c) illustrate that there is no phase transformation taking place in the sample of YAZ (Y_2O_3-0.5wt% Al_2O_3-0.5wt% ZrO_2) at these temperature ranges. Compared to the peak positions of pure yttria, the peaks of the YAZ sample had the same positions. By checking the binary phase diagram of Y_2O_3-ZrO_2 [131, 173-174] and ternary diagram of Y_2O_3-ZrO_2-Al_2O_3 [175], small amounts of ZrO_2 and

Al_2O_3 can dissolve into the yttria with increased crystal lattice parameter with no peak position change. Another explanation maybe that the amount of additives of ZrO_2 and Al_2O_3 were too low in this commercially available powder to be detected using this XRD tester.

La_2O_3 peaks can be detected in samples by adding 2.0 wt% La_2O_3 into yttria at low temperature. By increasing the temperature, the peak intensity of La_2O_3 phase decreased and disappeared at a temperature of around 1600 °C. Rhodes [137] studied the effect of La_2O_3 in sintering a transparent yttria compact for laser device applications. His experimental results showed that after firing, there is no peak change by introducing around 2 wt% La_2O_3 into pure yttria, but the peak positions only slightly shifted to the low 2theta angle when sintered at high temperatures, which is similar to Yihua Huang [139]‘s finding by adding 9 wt% La_2O_3 into pure yttria. In their experiments, by adding around 9 wt% La_2O_3, Huang found the detected powder peaks 2theta angle position shifted to a lower angle by about 0.3 degrees. These detected peaks shifts can be explained by the lattice expansion due to the solid-solution of lanthanum ions into the yttria crystal lattice [139, 176].

CeO_2 peaks in Figure 3-19 (f) can be detected through test temperatures from 1000-1600 °C but with decreasing peak intensity. At high sintering temperatures (1600 °C), the CeO_2 phase changed to a Ce_2O_3 phase and there is no evidence found to confirm that there is interaction between CeO_2 and Yttria.

Therefore, comparing the test results so far, sintering additive systems with B_2O_3, YF_3, TiO_2,

and YAZ were selected as the new filler powder to make the water based binder face coat slurry.

3.5 Conclusions

Based on this research, sintering additives added into pure yttria -200 mesh powders can promote powder sintering at comparably low sintering temperatures, and they possibly could be used in slurries to enhance the sintering properties of the face coats.

1. Sol used as a binder in the face coat can not only help filler powder particles uniformly suspend and increase the face coat green strength, but also can act as a sintering aid to reduce the powder sintering onset temperature by around 200 °C. The densification temperature reduces from 1400 °C for pure yttria powder to around 1100 °C with 2.0 wt% sol added in.

2. Sintering precursors like yttrium acetate and yttrium carbonate can effectively promote yttria powder sintering due to the very reactive nano-sized particles formed on the decomposition of the precursors. However, because of the volume and density difference after the decomposition process, large holes will be generated and influence the powder compact quality.

3. Sintering additives B_2O_3, YF_3 and YAZ added into the yttria can effectively enhance material diffusion between particles at certain temperatures in the range between

1000-1200 °C.

4. Sintering additive TiO_2 retards the powder sintering at temperatures between 1000-1200 °C, but it shows a very good performance after sintering at temperatures higher than 1300 °C.

5. Sintering additives CeO_2 and La_2O_3 will retard the powder sintering start temperature, and no obvious densification of the powder pellet was observed by using those sintering additives at temperatures between 1000-1500 °C from the isothermal shrinkage results.

Therefore, comparing the test results so far, sintering additive systems with B_2O_3, YF_3, TiO_2, and YAZ were selected as the new filler powder to make the water based binder face coat slurry in Chapter 4.

Chapter 4. Face coat slurry development

In this chapter, new face coat slurries were made using the filler powders developed in Chapter 3. Then the new slurry and the face coat properties were characterized by measuring slurry life, microstructure, surface roughness, and sintering properties to compare to a standard sol based slurry. After these experiments, the best face coat slurries were selected and their chemical inertness was then examined in next Chapter 5.

4.1 Experimental procedure

4.1.1 Slurry preparation

Slurries were prepared by mixing yttria powder (-200 mesh, 99% purity, Treibacher industrie AG)) with different additives into a polymer water solution (30 wt% polymer). Slurries were then rolled on a rolling mill at 25 °C for at least 2 days before use. The sol containing yttria face coats and the pure yttria water based binder face coat slurries (without sintering aids) were used as two baselines face coats to compare with the new slurry. The slurry formulation of both baseline and the newly developed slurry are shown in Table 4-1 and Table 4-2 separately with filler loading 4.0 kg/litre. The backup coat used in this experiment was an industry standard backup up coat containing alumina and silica.

Table 4-1. The baseline yttria face coat slurry composition.

Sample ID	Filler	Binder	Wetting agent	Anti-foam
Wt % in slurry	80 wt%	19.8 wt%	0.15 wt%	0.05 wt%
Yttria+ sol (Baseline)	yttria	Yttria colloidal sol	Victawet 12	Burst RSD-10
Yttria+ water	yttria	PV alcohol water solution	Victawet 12	Burst RSD-10

Table 4-2. The new designed face coat slurry formulations.

Sample ID	Filler	Binder	Wetting agent	Anti-foam
Wt % in slurry	80 wt%	19.8 wt%	0.15 wt%	0.05 wt%
YB	Yttria+ 0.15wt%B_2O_3	Cellulose water solution	Victawet 12	Burst RSD-10
YF 2.0	Yttria + 2.0wt% YF_3	PV alcohol water solution	Victawet 12	Burst RSD-10
YF 0.15	Yttria + 0.15wt% YF_3	PV alcohol water solution	Victawet 12	Burst RSD-10
YAZ	Commercial YAZ	PV alcohol water solution	Victawet 12	Burst RSD-10
YT 2.0	Yttria + 2.0wt% TiO_2	PV alcohol water solution	Victawet 12	Burst RSD-10
YT 0.15	Yttria +0.15wt% TiO_2	PV alcohol water solution	Victawet 12	Burst RSD-10

*There is no B_2O_3 2.0 wt% slurry due to the heavy interaction with polymer (mismatch of the pH value of B_2O_3 water solution and polymer).

4.1.2 Shell preparation

Test shell face coats were made by applying the face coat slurry to a wax cylinder of 15 mm diameter and, after draining off the excess, the pattern was stuccoed with pure yttria stucco (125-250 μm, Treibacher Industry AG) and dried over night. Then several backup coats were applied using the same method (around 7 layers). Each backup coat was dried at a

temperature of 21 °C, 50 % relative humidity, and an air speed of 0.2 m/s for 1.5 hours. Details of shells making processes are shown in Table 4-3. Upon completion, the moulds were de-waxed in a Quicklock Boilerclave™ (Leeds and Bradford Boiler Company Ltd, UK in Figure 4-1), and then fired at different temperatures from 1000 to 1400 °C to produce a range of densities. The wax tube and green ceramic shell are shown in Figure 4-2.

Table 4-3. Detail of shell making process.

Layer	Coating	Stucco	Dip time (secs)	Air Speed	Dry Time
1	Face coat	Mol 50/80	30	10% (0.1ms^{-1})	24.0
2	Backup coat 1	Mol 30/80	30	50% (3ms^{-1})	1.5
3	Backup coat 2	Mol 30/80	30	50% (3ms^{-1})	1.5
4	Backup coat 3	Mol 16/30	30	50% (3ms^{-1})	1.5
5	Backup coat 4	Mol 16/30	30	50% (3ms^{-1})	1.5
6	Backup coat 5	Mol 16/30	30	50% (3ms^{-1})	1.5
7	Backup coat 6	Mol 16/30	30	50% (3ms^{-1})	1.5
8	Backup coat 7	Mol 16/30	30	50% (3ms^{-1})	1.5
9	Seal		30	50% (3ms^{-1})	1.5

Figure 4-1. Quicklock Boilerclave ™ de-wax machine

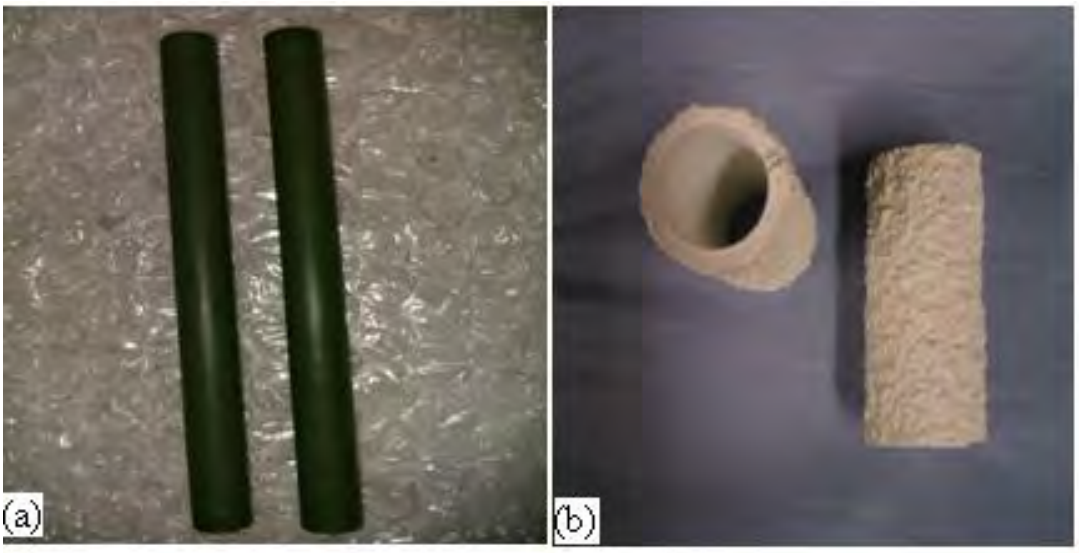

Figure 4-2. (a) The cylindrical wax pattern, and (b) the final tube shell.

4.1.3 Slip cast test piece preparations

The slip cast face coat shells were prepared by pouring the slurries into a rubber mould, see Figure 4-3. The slurries were then dried at room temperature for two days. After the slurry had dried, the bulk pieces were removed from the rubber mould and ground down to a cubic shape.

Figure 4-3. Rubber mould for preparation slip cast samples.

4.2 Sample characterization

4.2.1 Slurry flow time

Slurry flow time was determined by allowing a definite volume of slurry to flow through the orifice in the bottom of a metal flow cup (Series number of 405/4, orifice diameter 4.39 mm, viscosity range 200-1200 cSt, Flow time 20-80 s) shown in Figure 4-4. The flow time of the slurry was tested through the following steps: Firstly, seal the orifice (usually with a finger) and fill with test liquid until the cup is full. During the filling, make sure no bubbles and debris were in the test fluid. Secondly, removing the finger from the orifice and simultaneously start to time. At the first break in flow under the cup, stop the timer. This elapsed time represents the 'flow-time' of the slurry. This procedure was repeated at least three times to get an average flowing time for the slurry.

Figure 4-4. The schematic diagram of flow cup

4.2.2 Face coat slurry dilatometer test

The dilatometer test is same as the method described in Chapter 3, which was used to test the

linear thermal expansion or shrinkage rate of the filler powder. For this test, samples were prepared by grinding down the slip cast face coat samples to a cubic shape to measure their sintering behavior.

4.2.3 Friability

A Friability test was developed by S. Jones *et al* (2008) [177] to evaluate the ability of the face coat shell to withstand brush abrasion. Friability was quantified as weight loss per unit area due to mechanically brushing the sample surface. A higher friability value represents poor sintering and particle bonding, while the lower the value, the stronger the bonding between filler particles. The test sample tube and the brush used in this experiment are shown in Figure 4-5. Before the test, the shell tubes with different face coats were sintered at three different temperatures (1000 °C, 1200 °C, and 1400 °C) for one hour in air. The shell friability in this research is the average friability value from 5 shells.

Figure 4-5. Test ceramic tube and the brush

4.2.4 Face coat surface roughness

Shell surface roughness was measured using a roughness tester (Mitutoyo basic model, see Figure 4-6). The roughness of the sample was tested by using a probe lightly pressed on the sample surface. The movement of the probe was recorded when scratching the sample surface as the surface roughness profile. In this experiment, The arithmetical mean roughness (R_a), which describes the average value of the departures from its centerline through a prescribed sampling length in Figure 4-6 (b), was used to analyze the face coat surface roughness.

(a)

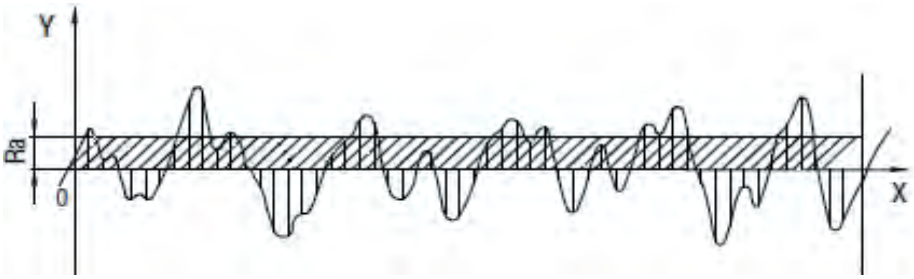

(b)

Figure 4-6. (a) The Mitutoyo roughness tester, (b) the definition of R_a value.

4.2.5 Face coat surface microstructure

Sample surface morphologies were studied using a scanning electron microscope (Joel 7000, Philips XL-30 series). Then the test face coat slurry surface characterizations were compared to the filler powder compact in Chapter 3, which can be used to explain the different sintering behaviors of the filler powder compact and the slip cast face coat sample.

4.3 Results and discussion

4.3.1 Slurry flow time

The flow time of the yttria sol based slurry (4.0 kg/litre, no polymer added) was tested and shown in Figure 4-7. As can be seen, the useable life of this slurry is less than two hours from preparation, and after 2 hours blending, the flow time of this slurry increased dramatically and finally gelled.

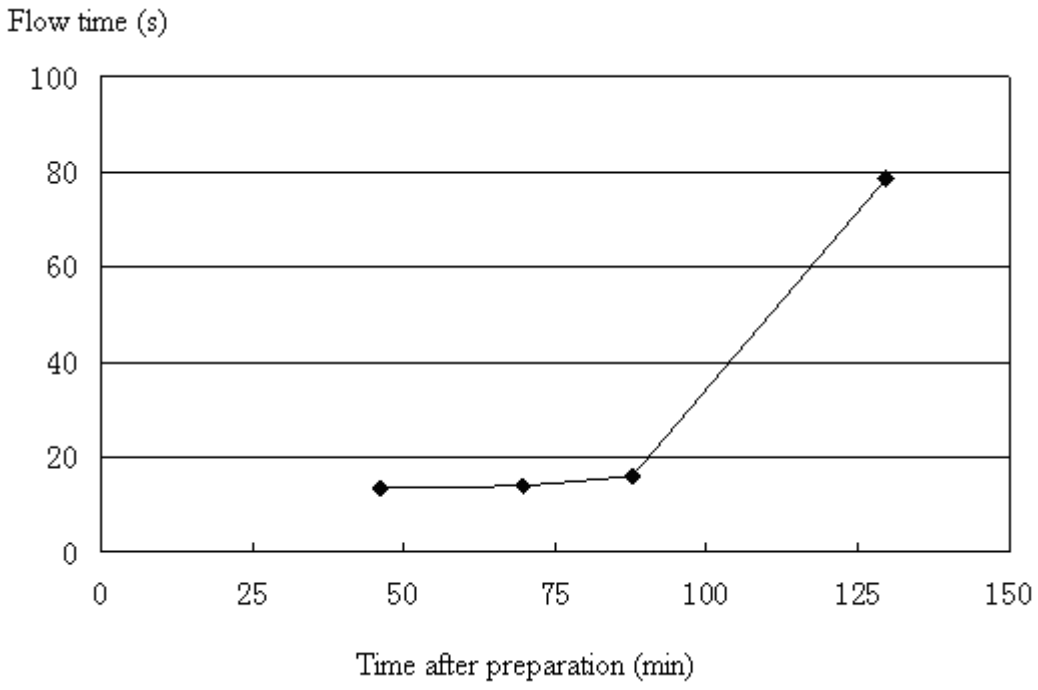

Figure 4-7. The flow time change of yttria sol based slurry at room temperature.

Meanwhile, the slurry life of the new face coat systems is depicted in Figure 4-8. As can be seen, the pure yttria water based binder slurry has a life of around 2 weeks, and the flow time increased quickly after around 18 days mixing. The slurries with fluoride doped (YF_3) have the shortest life of around 11 days even with only 0.15 wt% added in, and the sintering additive TiO_2 also shortened the life of the yttria slurry to around 10 days. Compared to YF_3 and TiO_2, YAZ filler powder based slurries can be stabilized for around 41 days. The B_2O_3 0.15 wt% added slurry has superior anti-gelation properties with the longest life of more than 100 days.

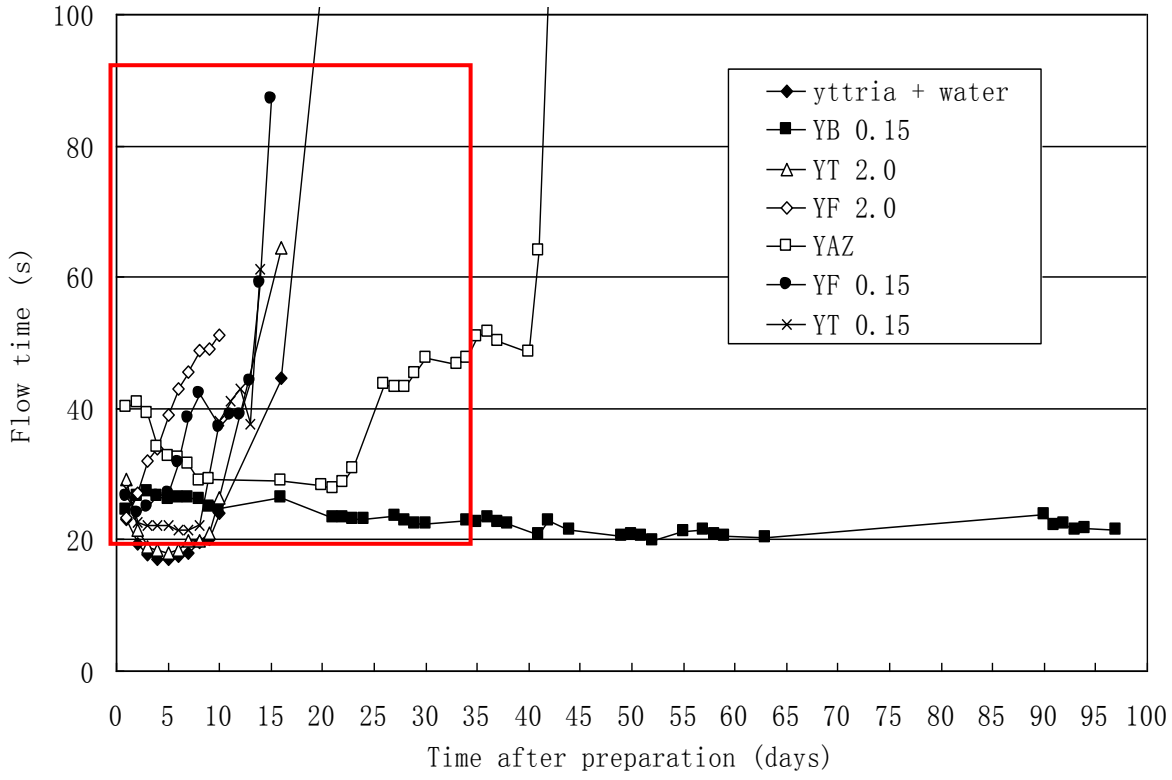

(a)

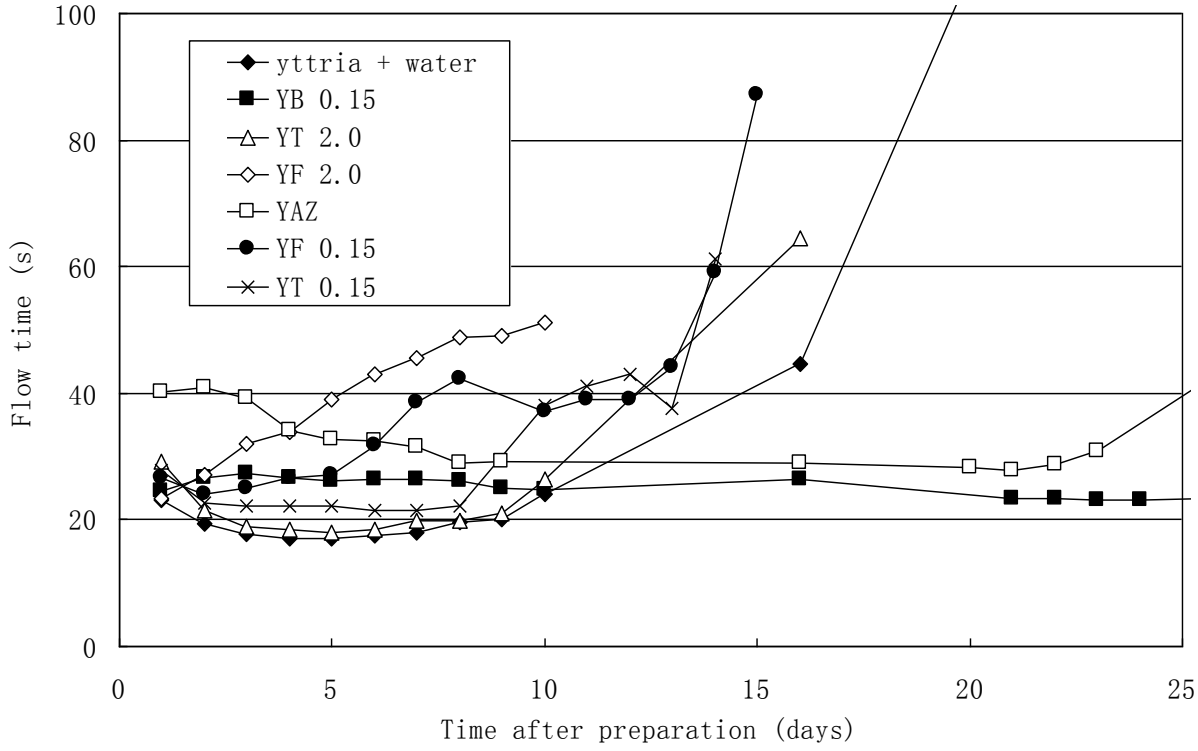

(b)

Figure 4-8. (a) The flow time of the slurry, (b) the enlarged image of the selected region

4.3.2 Face coat Friability

Table 4-4 reports three baseline yttria face coat friability test results, two of them belong to the sol based pure yttria slurry. The sol in the slurry acts as the binder to strengthen the face coat. In the water based yttria slurry, the slurry viscosity and face coat strength is modified by adding high melting temperature polymer. The strengthening effect of the sol is mostly from the gelation of the face coat due to the chemical interaction of colloidal yttria and filler particles [84-88]. But for the polymer, the strengthening effect is mostly due to the physical interaction through the cross linking of the polymer in the face coats, thereby making the face coat more dense giving enhanced sintering [198].

Table 4-4. Baseline yttria face coat friability test results at different sintering temperatures.

Sample ID	filler	binder	polymer	Friability (g/m^2) at different temperatures		
				1000 °C	1200 °C	1400 °C
Yttria+ S	Yttria	Yttria sol	-----	**48.2** ± 5.7	**12.91** ± 2.6	**3.12** ±0.7
Yttria+ S+ P	Yttria	Yttria sol	PV acetate	**25.81** ±5.5	**11.29** ±2.1	**3.06** ±1.7
Yttria+W+P	yttria	water	PV alcohol	**54.42** ±32.3	**19.58** ±19.6	**3.16** ±2.11

In this experiment, the increasing sintering temperature will cause a decrease in friability values. Polymers as the strengthener were added into slurries (Yttria + S+ P) and (Yttria+ W+ P), whilst in the slurry (Yttria+ S) and (Yttria+ S+ P), sol was added as the binder. As can be seen from Table 4-4, sol and polymer both seem to have some benefits in enhancing the yttria face coat strength. Slurry (Yttria + S + P), with both polymer and sol added has the best performance with lowest friability at all temperatures and half of the friability value of the other group at the sintering temperature of 1000 °C. The strength of the face coat can be largely enhanced when both polymer and sol used together. The friability of the new designed face coats are shown in Table 4-5.

Table 4-5. New designed face coat friability test results at different sintering temperatures.

Sample ID	Friability (g/m^2) at different temperatures		
	1000°C	1200°C	1400°C
YB 0.15	**34.31** ± 14.97	**8.47** ± 3.32	**3.21** ± 1.48
YF 0.15	**30.42** ± 6.63	**9.86** ± 5.08	**1.15** ± 0.41
YF 2.0	**25.31** ± 3.85	**8.74** ± 1.09	**3.83** ± 1.48
YAZ	**33.6** ± 20.07	**13.06**± 2.68	**3.2** ± 1.12
YT 0.15	**64.04** ± 25.93	**25.87**± 17.62	**1.92** ± 0.51
YT 2.0	**86.72** ± 53.15	**34.35** ± 16.19	**6.28** ± 0.19

As can be seen from Table 4-5, the increased sintering temperature caused a decreased average friability test value and standard deviation between different test moulds. Except for the face coat with added TiO_2 sintering additive, the friability value of new face coat samples shows higher strength than Yttria + Sol (industry based) face coat at the sintering temperature of around 1200 °C.

The face coat with 2.0 wt% YF_3 added has very good strengthening properties when sintered at 1000 °C for one hour, with the lowest friability of around 25.31 g/m^2. By sintering the YB 0.15 face coat, it showed the smallest friability of only 8.47 g/m^2 at the sintering temperature of 1200 °C among the group. Nearly all the friability values of the face coat dropped down to around 3 g/m^2 when sintered at 1400 °C for one hour with the smallest test standard deviation around 1 g/m^2. The superior strengthening properties of the new water based slurries at low sintering temperatures make these slurries possible candidates to replace the industry standard yttria sol based slurry giving longer life.

4.3.3 Face coat surface roughness

The surface roughness of different face coat systems is shown in Figure 4-9 when sintered at 1200 °C for one hour.

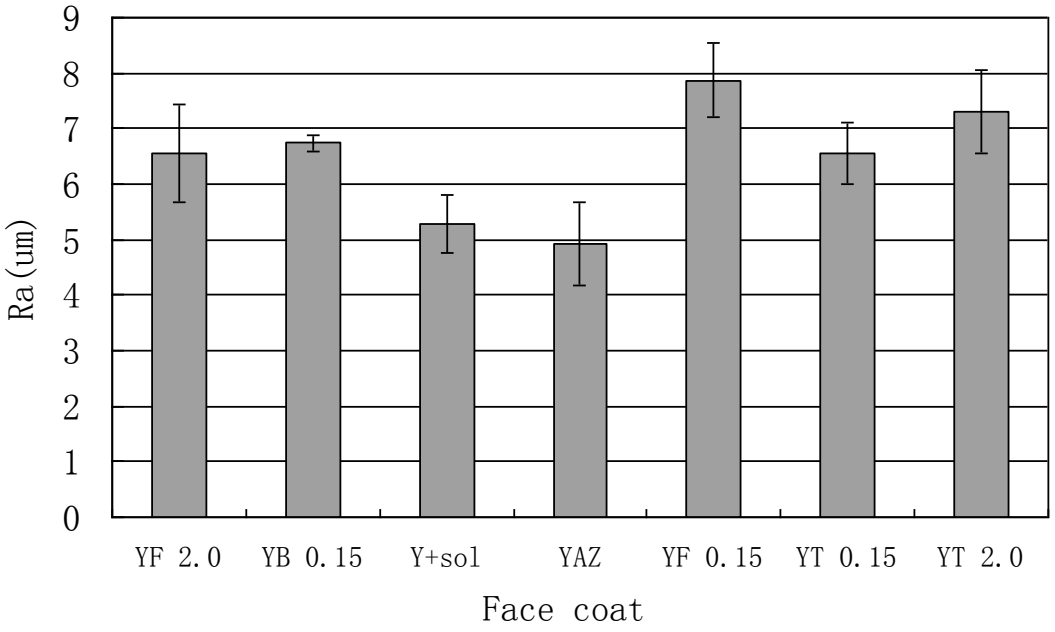

Figure 4-9. The shell face coat surface roughness after sintering at 1200 °C for one hour.

Compared to the standard yttria +sol slurry face coat in Figure 4-9, by adding the sintering additives into the slurry, the mould surface roughness (Ra) was increased. The increasing roughness of the shell face coat may due to the formation of the new phases at the shell and degradation of the shell surface quality (Figure 3-19, Chapter 3). The sample using YF 0.15 face coat slurry system has the highest roughness among all the test shells after sintering at 1200 °C for one hour, while the YAZ slurry face coat has the smoothest surface finish. Although the new slurry face coat systems seem likely to have higher surface roughness compared to the standard face coat, the maximum roughness difference between the best and the worst face coat is less than 3 μm. Therefore all the shell roughnesses are acceptable.

4.3.4 Surface microstructure

The microstructures of the face coat surface were different from the filler powder compact shown in Chapter 3. Compared to the powder compact introduced in Chapter 2, the filler powders in the face coat samples were distributed uniformly with a reduced number of agglomerated grains observed, see Figure 4-10.

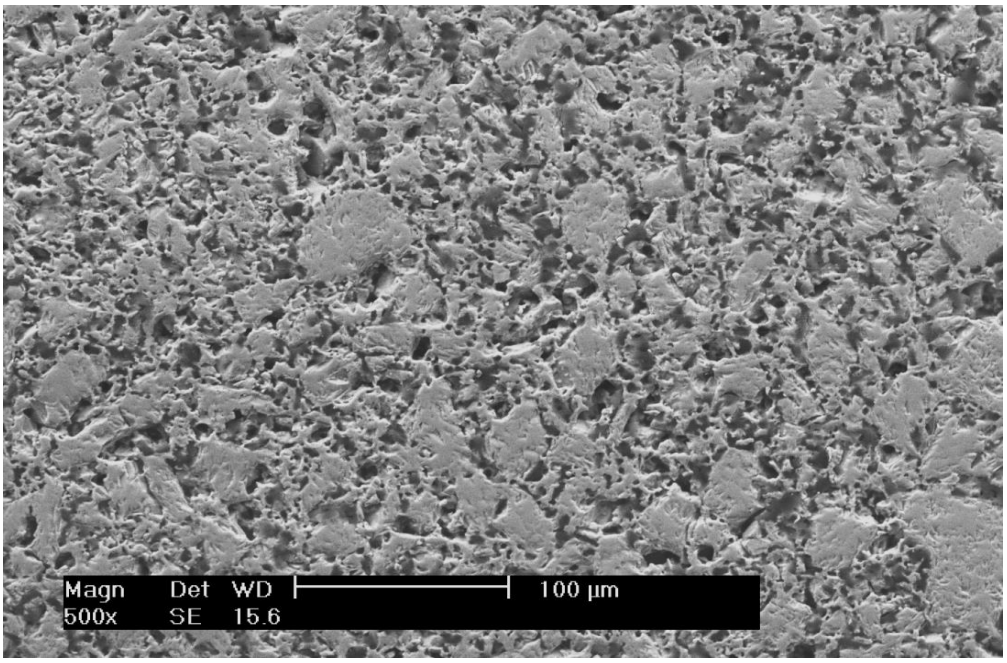

(a)

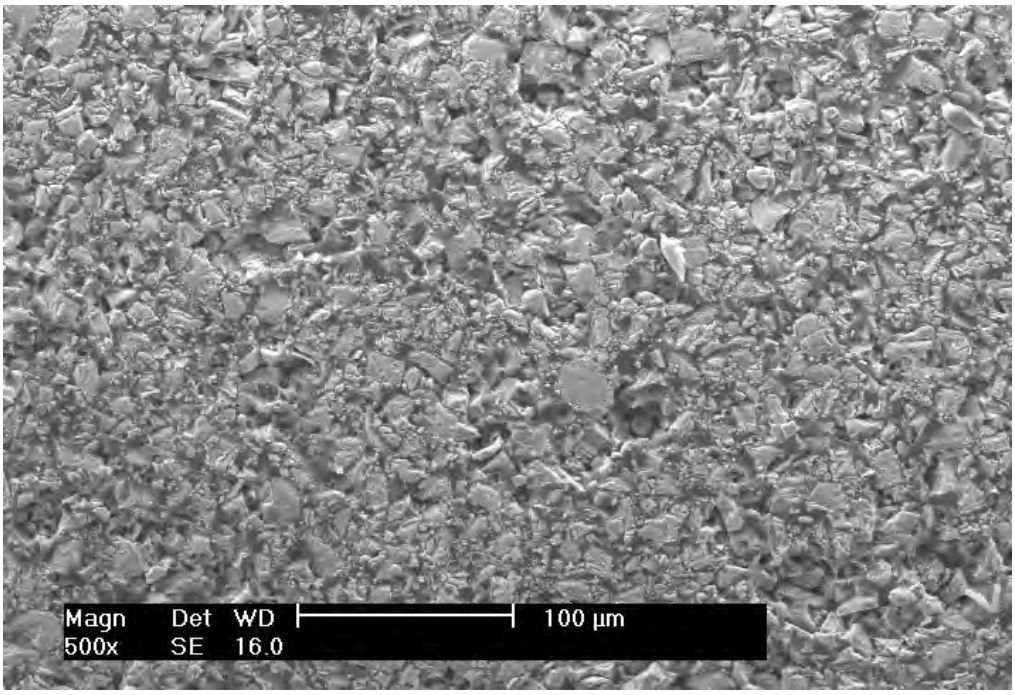

(b)

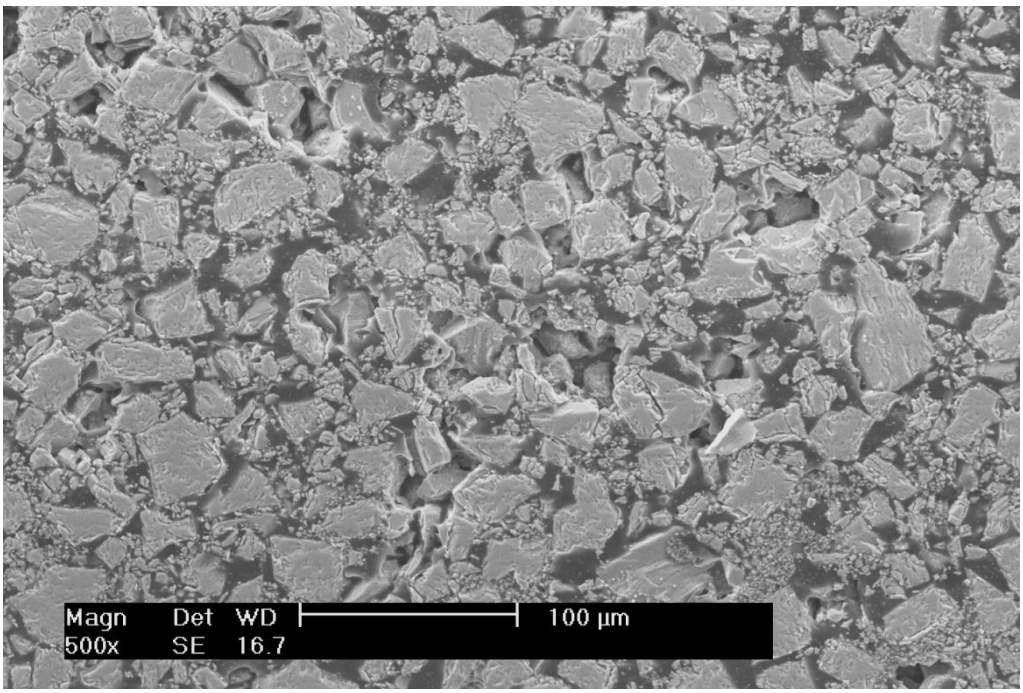

(c)

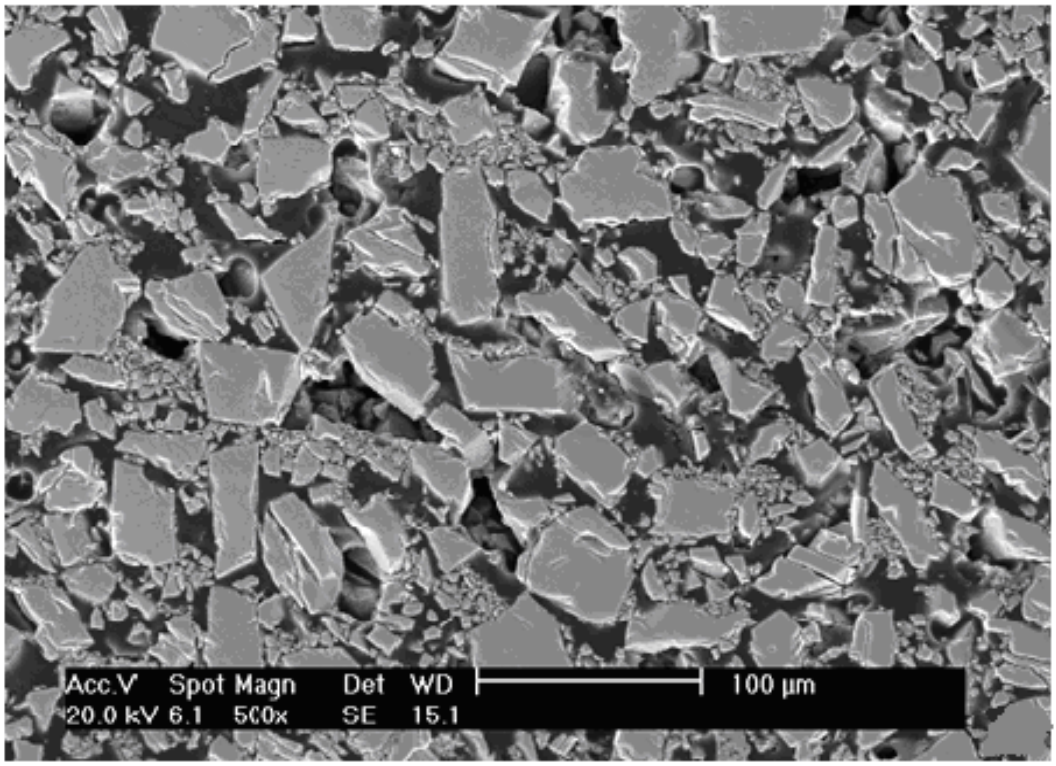

(d)

Figure 4-10. Surface microstructure of the face coat slurry sintered at 1550 °C. (a) B_2O_3 0.15 wt%, (b) YF_3 2.0 wt%, (c) YAZ and (d) Y.

4.3.5 Face coat dilatometer test

The face coat sintering properties were studied using a dilatometer test similar to that in Chapter 3, and the anisotropic dimension changes of the face coat slip cast samples were tested during the heating and cooling cycles and compared to the filler powder compact.

It can be seen from Figure 4-11 that all the samples have a similar thermal expansion rate at the early stage of the heating cycle. Compared to the pure yttria filler powder, the slip cast of Yttria + sol and new water based slurry face coat samples have a higher sintering rate after heating to temperatures above 1300 °C. The sintering temperature started for the Yttria + Sol

sample at around 1150 °C, and for yttria + W at around 1170 °C, they are 150 °C and 170 °C delayed compared to pure yttria powder pellets which started around 1000 °C.

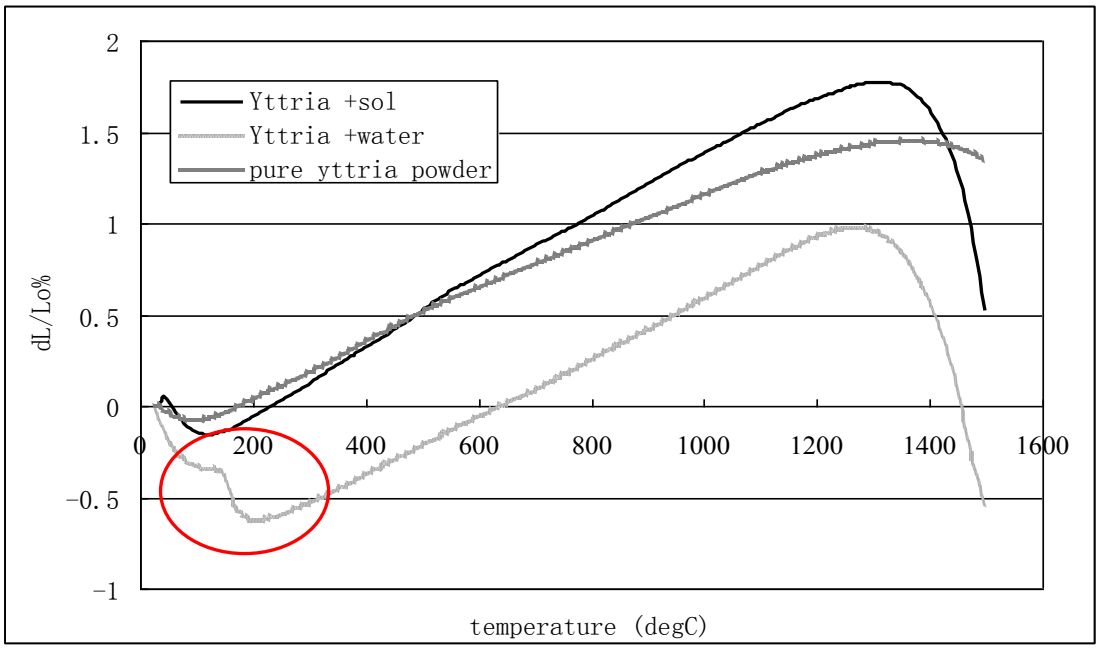

(a)

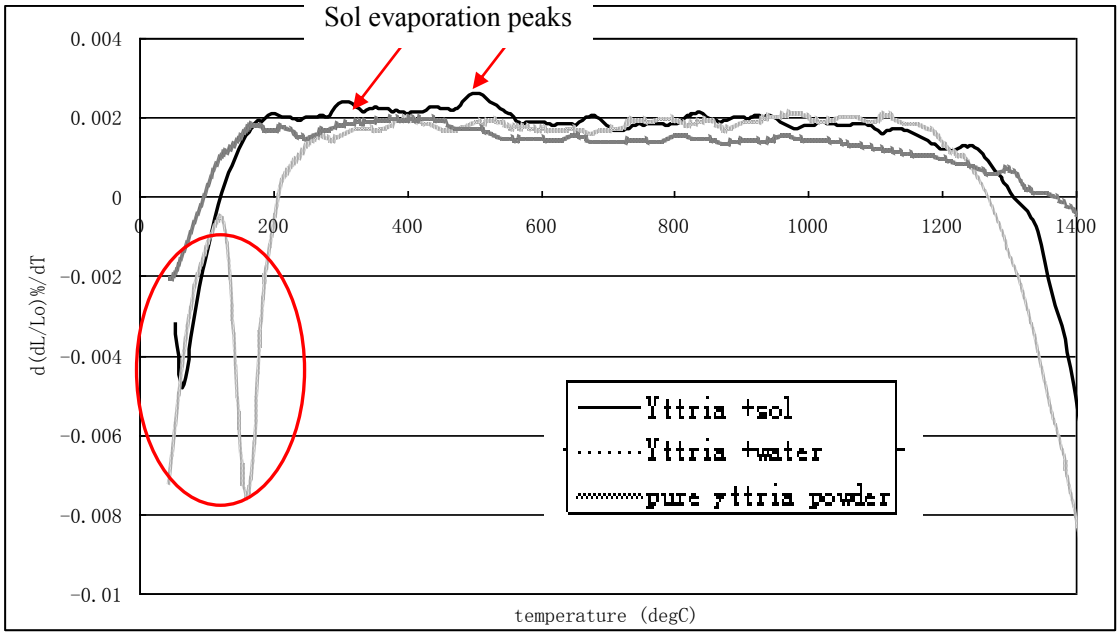

(b)

Figure 4-11. The dilatometer test trace for constant heating profile, (a) the overall trace, and (b) the dimension change rate trace during heating cycle.

During the heating stage, for the water based binder yttria slurry face coat sample, there is an obvious dimensional shrinkage peak found at a temperatures range between 100 to 200 °C. Considering the composition of the slurry, this peak may be due to the burn out of the binder (polymer). By checking the published data for Poly vinyl alcohol [148], the Tg and T_m are around 99 °C and 248 °C, which is similar to the temperature range of these detected peaks in the experiment. The thermal expansion rate of sol containing face coats at the temperature range between 300 and 500 °C are higher than the other samples with two obvious small peaks found at temperatures around 300 and 500 °C, see Figure 4-11 (b). As it is known, the yttria sol contains around 21 wt% yttrium acetate solution, and C.Y. Chen (2008) [178] studied the weight loss of the precursor and found that yttrium acetate will first convert to its oxide at temperatures between 300-500 °C, and the subsequent reaction will take place at temperatures around 500-750 °C. The published data confirms that those expansion peaks of the sample yttria + sol are the phase transformation of yttrium acetate.

After sintering at a temperature of 1200 °C, the shrinkage rate of all the slip cast samples increased dramatically. The water based binder slurry starts to densify at temperatures around 1250 °C with the sol binder slurry starting at temperatures around 1300 °C. The test slurry slip casting samples‘ sintering properties, compared to the filler powders are shown in Figure 4-12 at different heating temperatures.

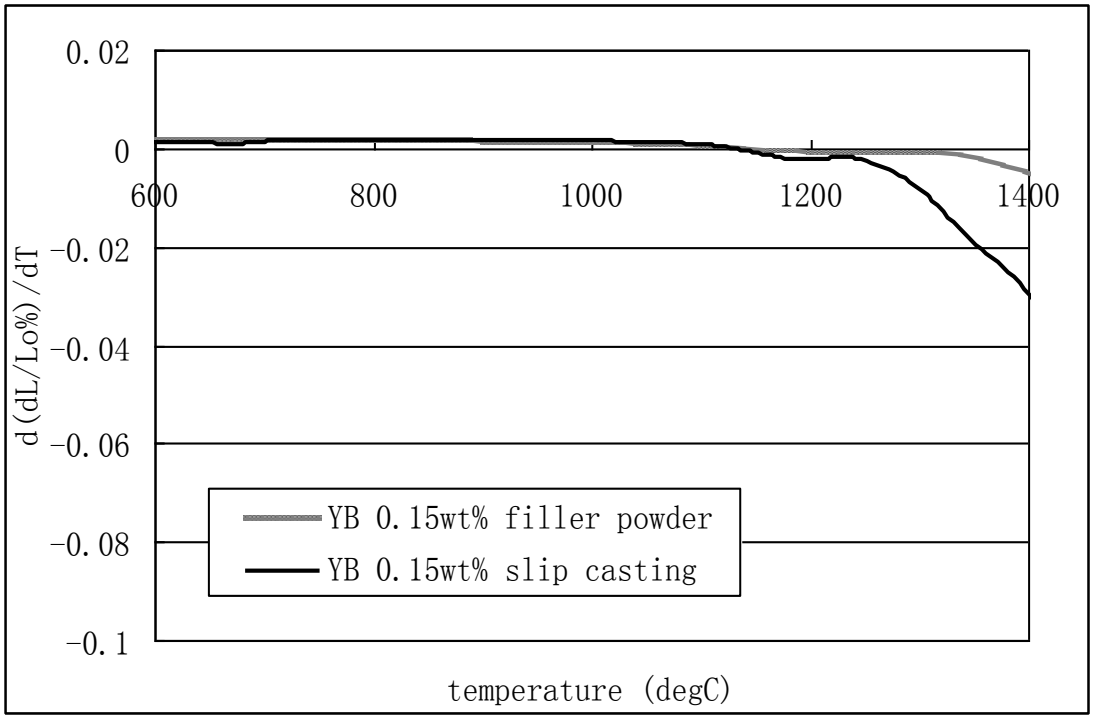
0.02
0
-0.02
-0.04
-0.06
-0.08
-0.1
600
800
1000
1200
1400
d(dL/Lo%)/dT
temperature (degC)
YB 0.15wt% filler powder
YB 0.15wt% slip casting

(a)

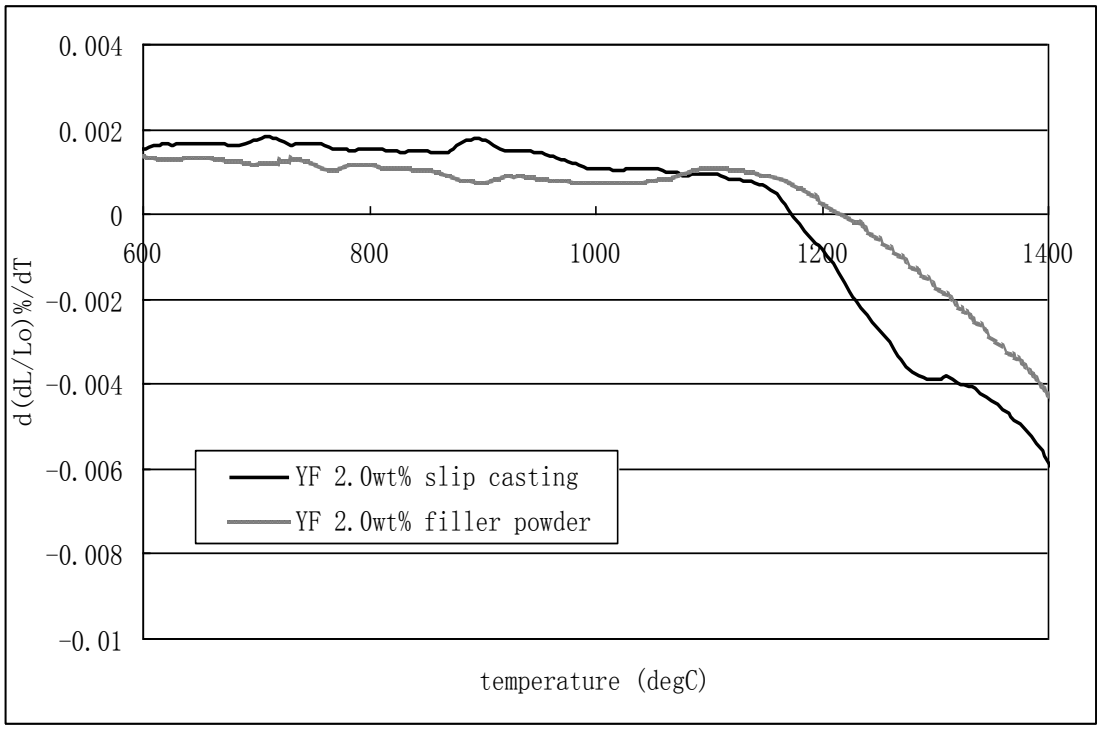
0.004
0.002
0
-0.002
-0.004
-0.006
-0.008
-0.01
600
800
1000
1200
1400
d(dL/Lo)%/dT
temperature (degC)
YF 2.0wt% slip casting
YF 2.0wt% filler powder

(b)

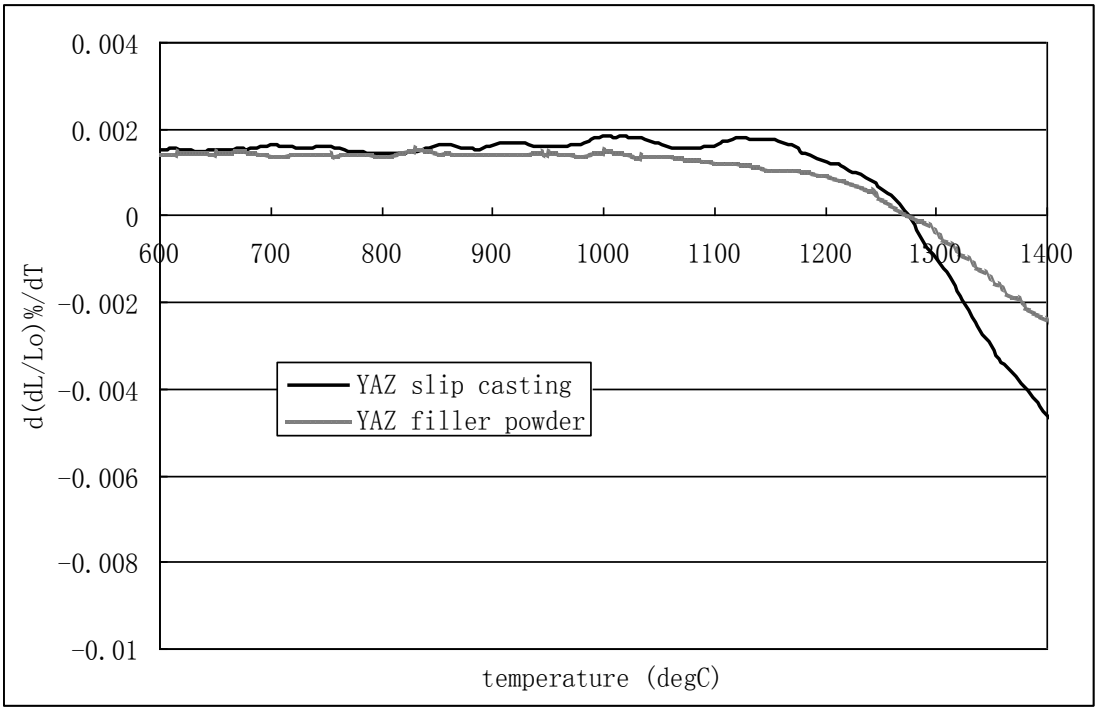
0.004
0.002
0
-0.002
-0.004
-0.006
-0.008
-0.01
600
700
800
900
1000
1100
1200
1300
1400
d(dL/Lo)%/dT
temperature (degC)
YAZ slip casting
YAZ filler powder

(c)

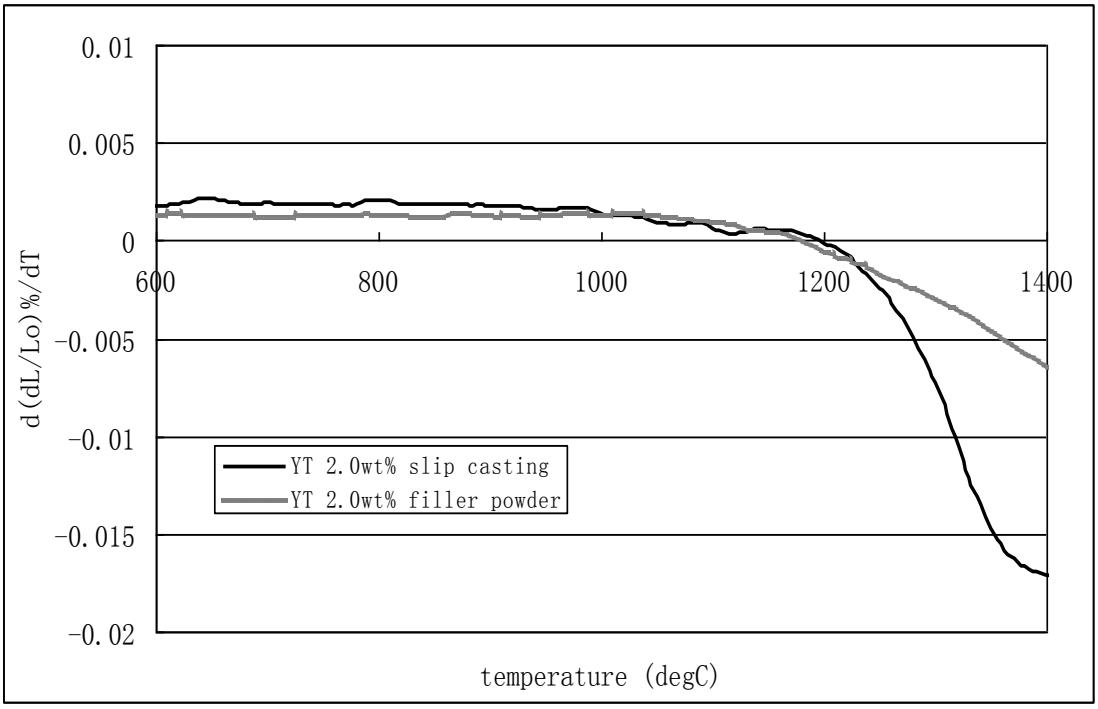
0.01
0.005
0
-0.005
-0.01
-0.015
-0.02
600
800
1000
1200
1400
d(dL/Lo)%/dT
temperature (degC)
YT 2.0wt% slip casting
YT 2.0wt% filler powder

(d)

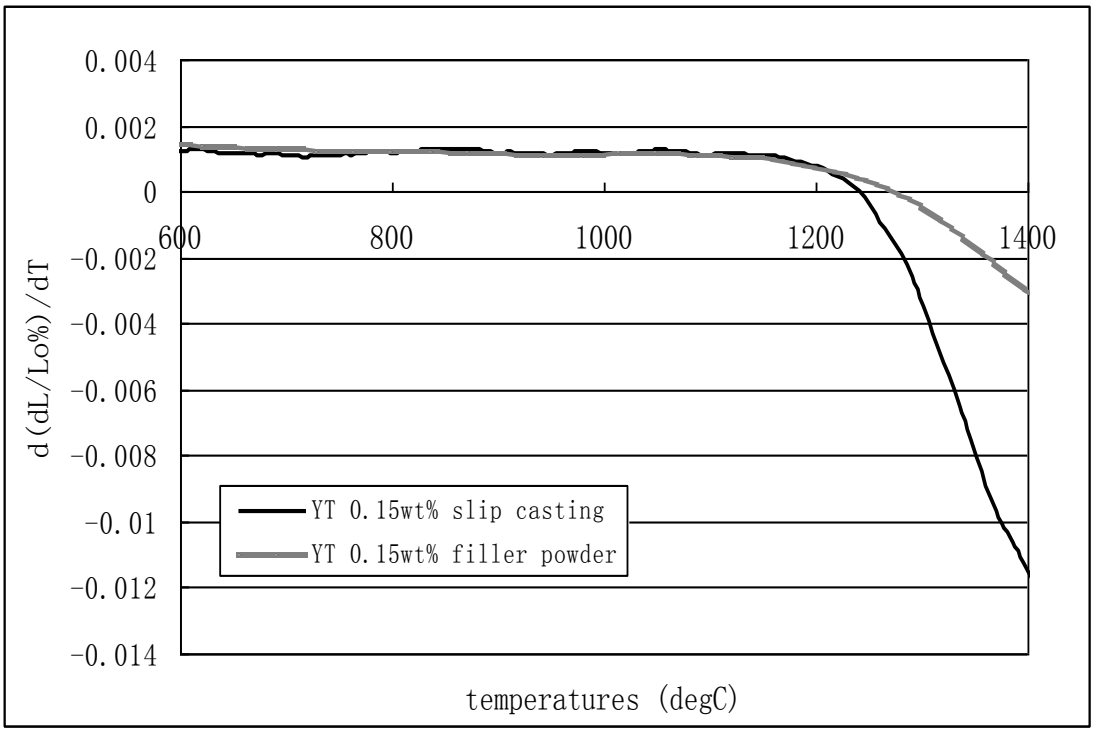

(e)

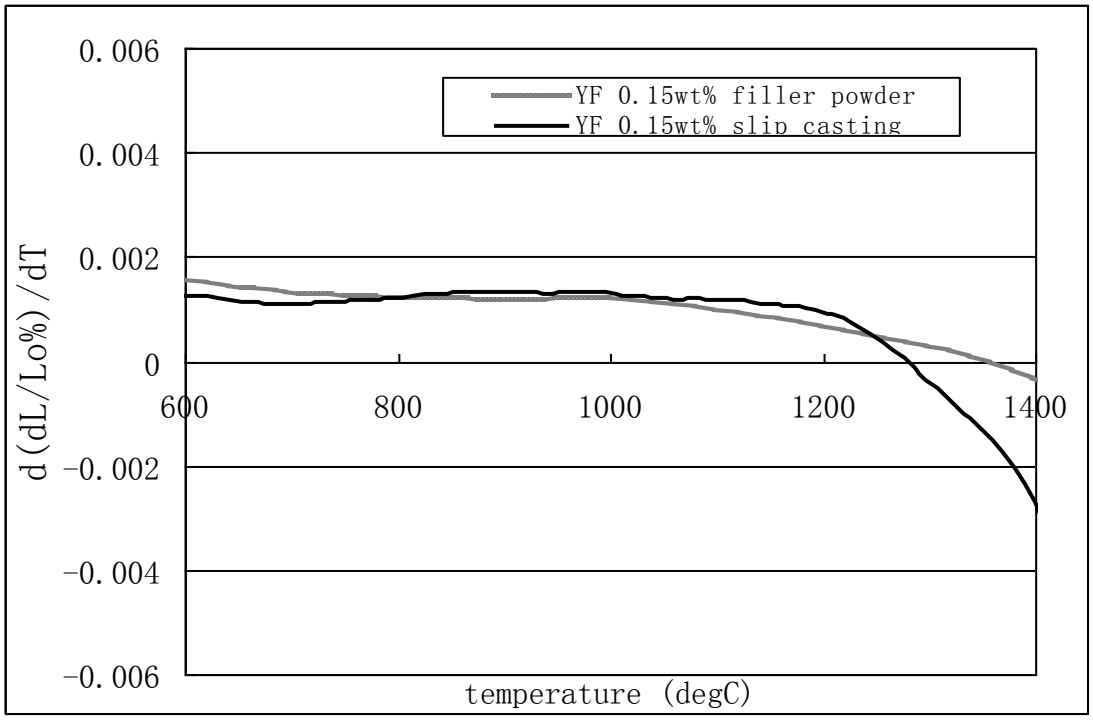

(f)

Figure 4-12. Powder expansion/shrinkage rates at different temperatures. (a) YB 0.15 wt%, (b) YF 2.0 wt%, (c) YAZ, YT 2.0 wt%, YT 0.15 wt%, and (f)YF 0.15 wt%.

From Figure 4-12, it can be seen that the slip casting face coat samples sintering behaviours are quite similar to their base filler powders at sintering temperatures lower than 1000 °C. At higher firing temperatures, the slip cast samples showed a much quicker densification speed than the filler powder compacts but with retarded sintering start temperatures. When heating to temperatures around 1200 °C, both slip casting and filler powder samples of YB 0.15 wt%, YF 2.0 wt% and YT 2.0 wt% have already started to shrink. The sintering behavior of the powder is also closely related to the amount of sintering aids, high concentrations had large effects.

The different sintering behaviour of the filler powder compact and slip casting face coat sample maybe due to their different composition and green density. As it is known, higher green density implies that less shrinkage is required to reach a given sintered density, therefore the sintered density is observed to decrease with decreasing green density for green density values [179, 180]. The increasing density is also found to delay the onset of grain growth at the later stage of sintering due to the reduced high energy solid-air areas (reduce the sintering driving force) [180]. In this experiment, because the filler compacts had higher green density compared to the slip casting samples, so the sintering start temperatures were earlier than slip casting samples, but due to the reduced high energy solid-air areas, the densification speed of the filler powders was slower than the slip cast face coats.

Figure 4-13 shows below is the slip cast sample dilatometer traces at a temperature range from 1000 to 1450 °C. Compared to the yttria sol face coat slurry and the water based binder

slurry systems, the new slurries have lower sintering start temperatures. When heating to temperatures around 1200 °C (typical industry shell firing temperatures), the densification rates of the powder were shown as: YB 0.15 wt% > YF 2.0 wt% > YT 2.0 wt% > YF 0.15 wt% = YAZ = YT 0.15 wt% = Yttria +sol = Yttria + polymer.

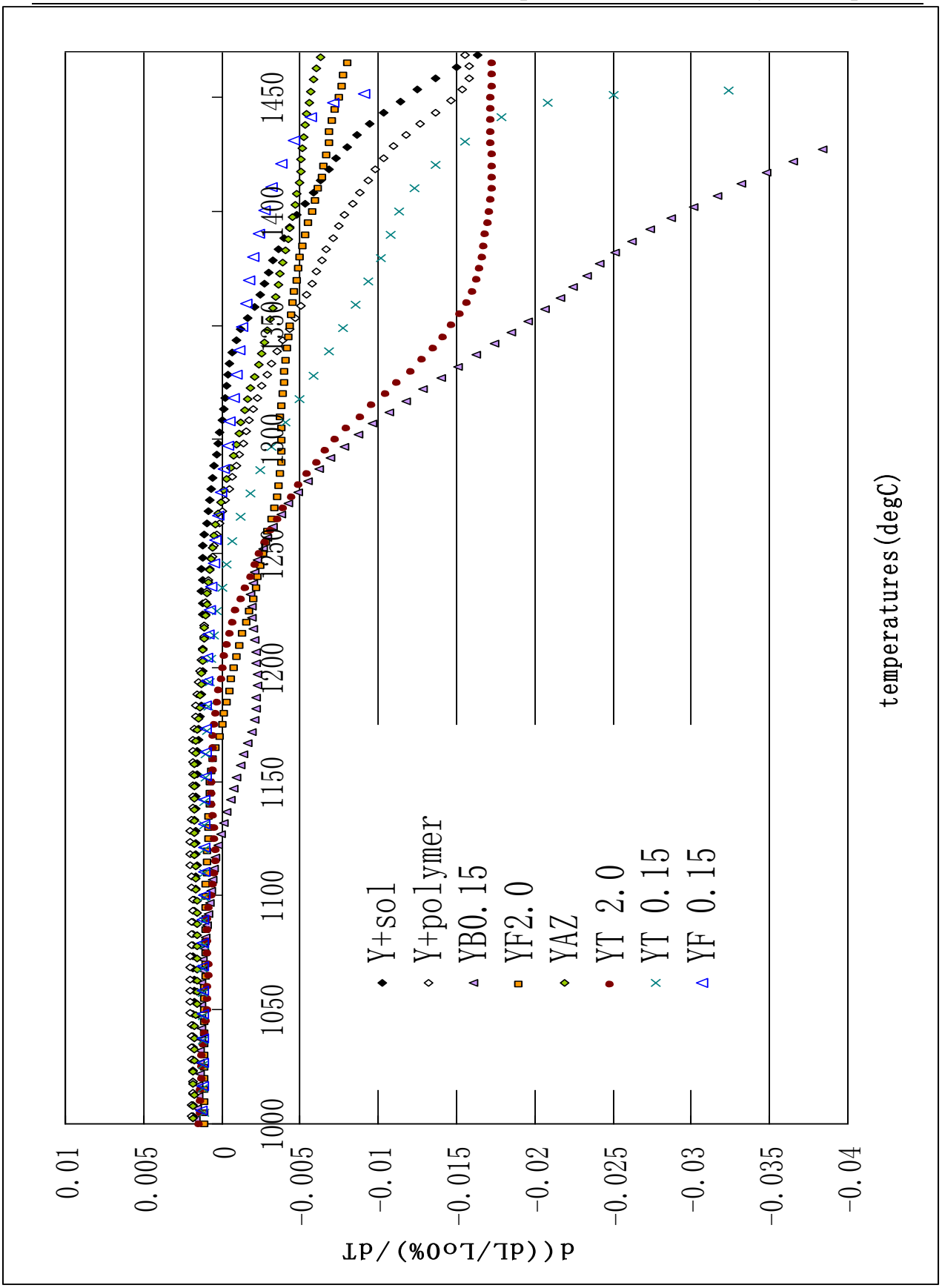

Figure 4-13. The slip casting dilatometer traces at different heating temperatures.

4.4 Conclusions

In this chapter, the new slurry properties were tested (life, face coat surface roughness, dilatometer and friability). So far, some conclusions could be made:

1. The yttria filler powder will suffer a very slow hydration reaction even without the sol added, and the life of the water based binder yttria slurry is around two weeks. The type of sintering aids and their added amount can influence the life of the slurry. The more additives are added the shorter the slurry life time, e.g YF_3, TiO_2. However, for the addition of B_2O_3 and YAZ to the slurry, the life times are increased to more than one month.

2. The shell surface roughnesses of the new slurries are quite similar, with the maximum roughness difference between the best and worst face coat is less than 3 μm after sintering at 1200 °C for one hour. Considering the later processing after casting, these roughness values of the face coat are all acceptable.

3. The sintering properties of the face coat are similar to the filler powder especially at higher sintering temperatures. Due to the different compact green density, the filler powder has a much quicker sintering speed at temperatures around 1000 °C but with a delayed densification rate at higher temperatures. TiO_2 added to the slurry has good sintering properties but due to the large dense Ti-containing grain formed with poor bonding to the matrix powder, the friability of these samples were poor.

Considering the slurry life and face coat sintering properties, the slurry system of YB 0.15, YF 0.15 and YAZ were selected to undergo the thermal-chemical sessile drop test for interaction with molten TiAl in Chapter 5.

Chapter 5 Chemical inertness of the face coat

In Chapter 4, three face coat slurry systems YAZ, 0.15 wt% B_2O_3 (YB 0.15) and 0.15 wt% YF_3 (YF 0.15) were selected for their good sintering properties and long slurry life. In this chapter, the chemical inertness of these face coat against molten titanium aluminide will be characterized using a flash re-melt (sessile drop) test method. During these experiments, metal pieces were located on the ceramic shell surface, and then re-melted in a vacuum furnace at different temperatures. The sessile drop contact angle and radius were analyzed using a 3D laser scanner and the interaction between the metal and ceramic were evaluated by hardness and secondary electron microscope.

5.1 Sample preparation

5.1.1 Mould production and characterisation

Test pieces were produced by coating wax plates of dimension 10×10×5 cm with slurry and stucco as shown in previous Chapter 4, Table 4-1 and 4-2. All test pieces were made using a standard shell build method [30], and then sintered at 1200 °C for one hour (the details of shell making process are described in Chapter 4). In these experiments, shells with the face coat composition of YF_3 0.15 wt%, YAZ, B_2O_3 0.15 wt% were prepared for inertness test.

5.1.2 Metal samples preparation

The TiAl alloy used in this experiment was a Ti-45Al-2Mn-2Nb-0.2B (at%) alloy with melting temperature around 1600 °C. TiAl alloy pieces were cut into cylindrical pieces 6 mm height and 10 mm diameter and placed on the face coat of the ceramic plates of dimension

around 2×4×0.5 cm.

5.1.3 Sessile drop flash re-melt test

A schematic of the furnace used for sessile drop flash re-melt is shown in Figure 5-1. Initially, each metal and ceramic disc sample pair was located in the cold chamber 1 under a vacuum of ~0.005 mbar, while chamber 2 was heated to 1600, 1625, and 1650 °C. A hydraulic ram then quickly raised the sample into chamber 2. The ‗contact time' (*t*) was measured as the elapsed time between the ram starting to move into chamber 2 and its return. After a designated time, the ram was retracted to chamber 1 after designed reaction time, allowing the specimen to cool rapidly. The designated time for holding in chamber 2 was different for different reaction temperatures. At 1600 °C, the contact time was 60 s, 70 s and 80 s. Contact times of 40 s, 50 s, 60 s, 70 s, and 30 s, 40 s, 50 s, and 60 s. were used at temperatues1625°C and 1650°C respectively.

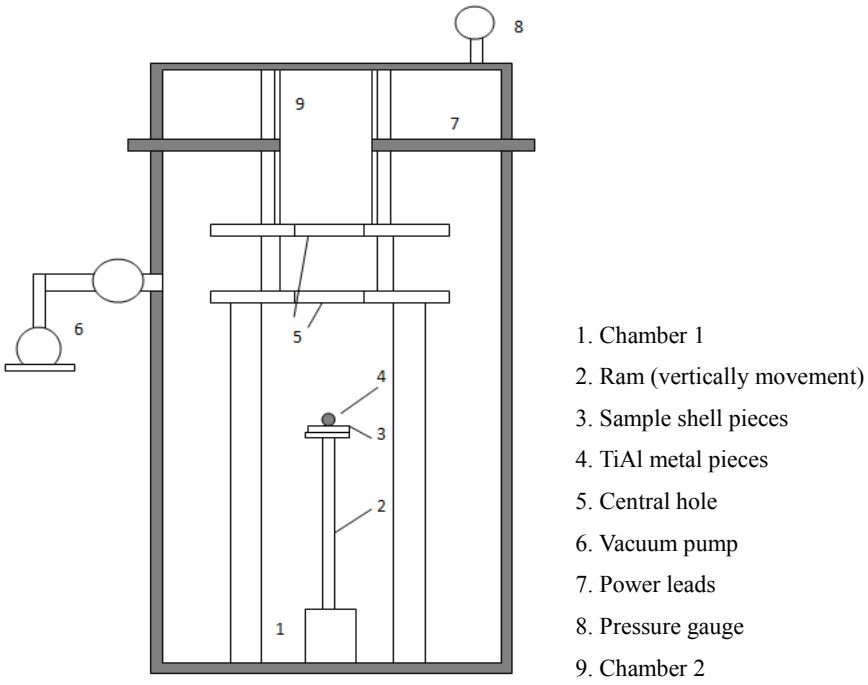

Figure 5-1. The flash re-melt furnace structure with annotations

5.2 Sample characterization

5.2.1 3D later scanner

In this experiment, the shapes of the sessile drop were reconstructed by a 3D laser scanner for more accurate measurement of their contact angles and diameter. The laser 3D scanner used in this experiment was from Keron Technique^{TM} (model: KZ-25-05, S/N: KZ-25-315 type), shown in Figure 5-2.

Figure 5-2. 3D laser scanner and working platform

After scanning, the metal drop surface information was analyzed using Polygonia software, and the shape of the sessile drops were reconstructed using software called Qualifiy 8. Subsequently, each drop contact angle, contact diameter and height was measured using a system defined plane to cut through the drop in four different directions. The cutting process and different cross sections are shown in Figure 5-3.

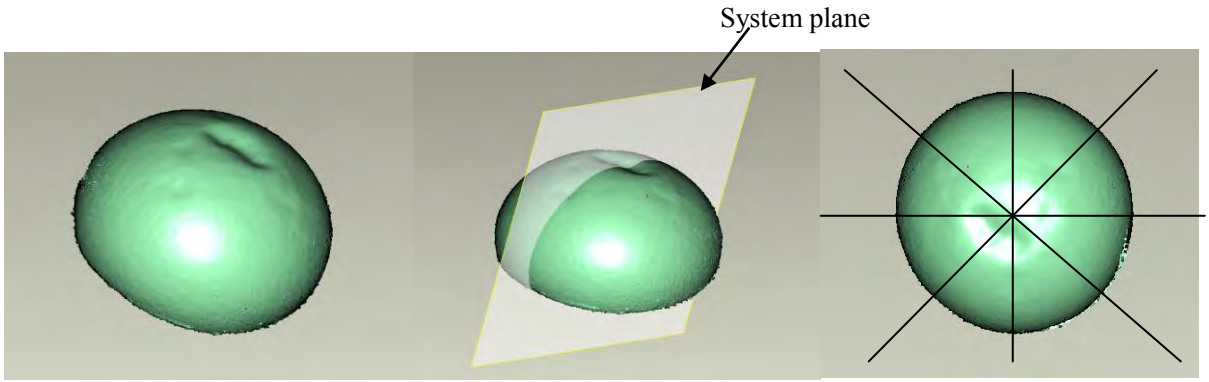

(a)

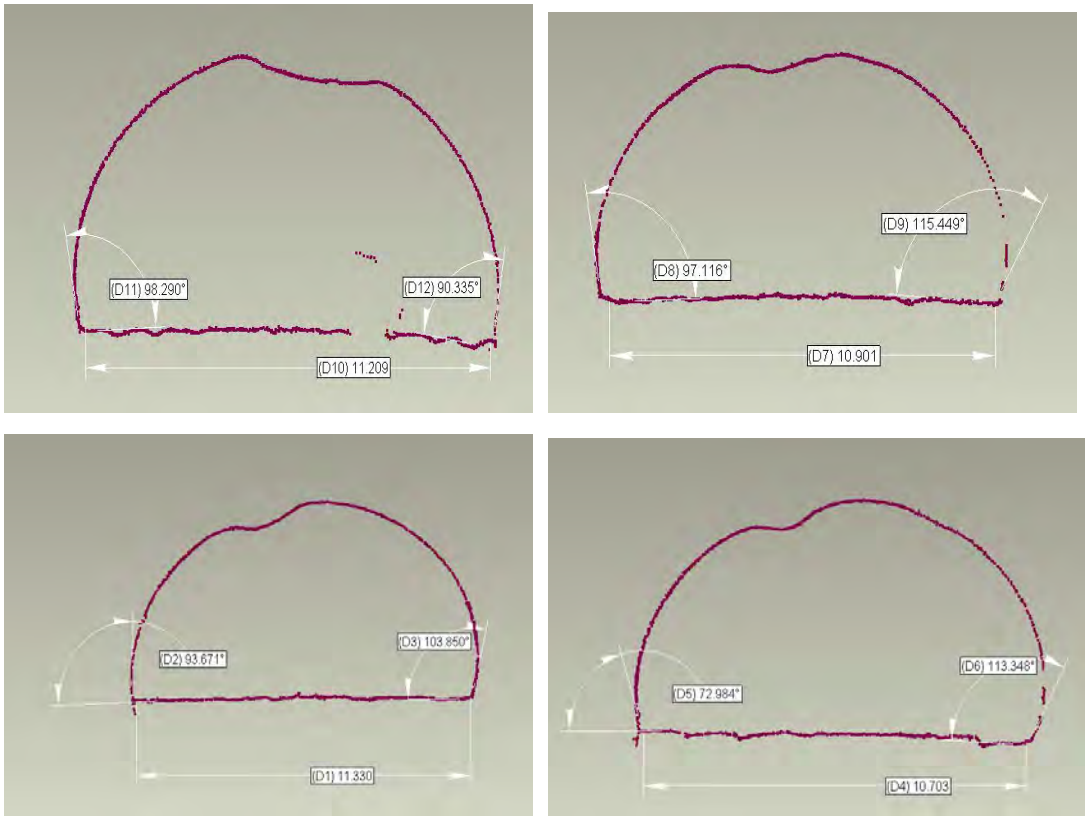

(b)

Figure 5-3.The measuring methods of sessile drop contact and contact diameters. (a) the cutting methods and (b) the drop cross section image and the measuring of contact angle and diameters.

5.2.2 Hardness test

An indenter was used in this experiment to press the sample with a known load, and sample hardness being calculated by measuring the dimension of the indentation. The hardness

tester used in this experiment is a Struers Durascan hardness tester, see Figure 5-4.

Figure 5-4. Hardness tester

Before the test, a software called ‗ecos workflow' was used to pre-set a hardness indentation position at the metal interface (Figure 5-5), which allowed the machine automatically put every indentation in the setting place and measured the sample hardness. Vickers hardness based on a mass of 0.025 kg (Hv 0.025) was measured, and five hardness points were tested at same distance away from the metal/shell interface up to a depth of around 500 μm into the metal matrix.

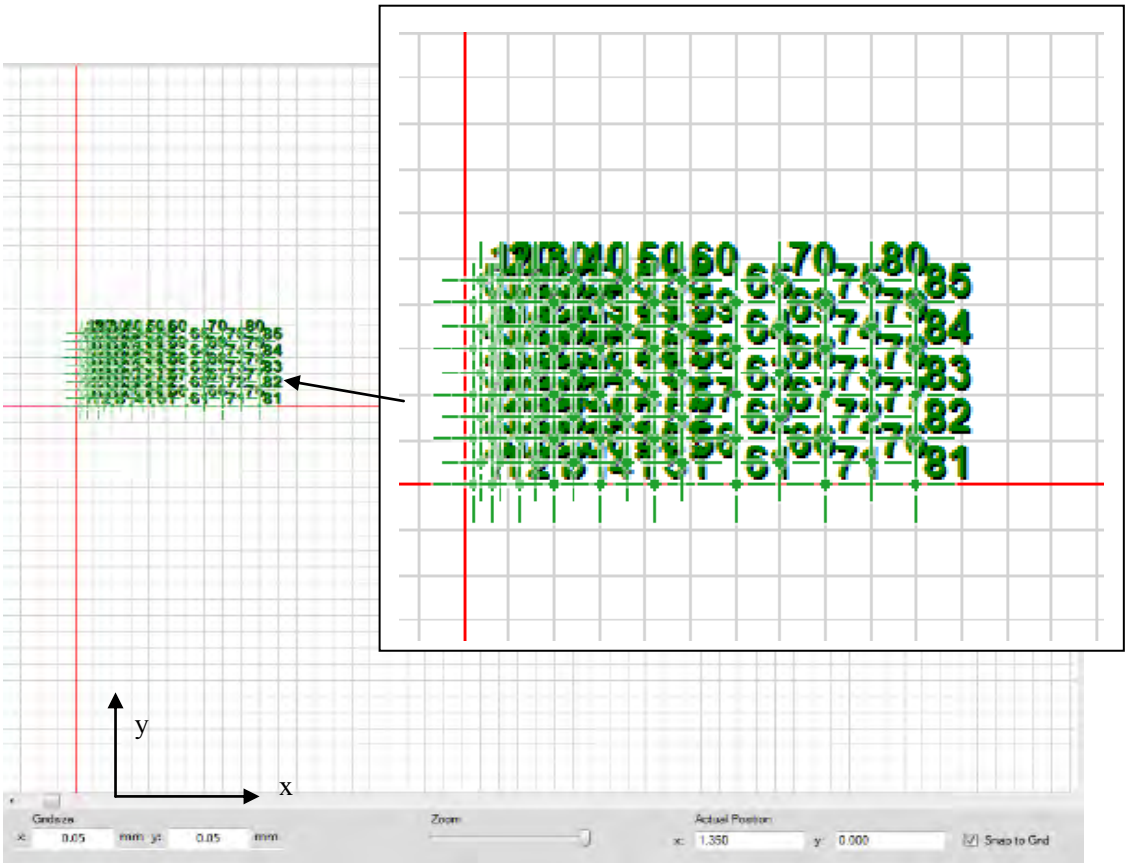

Figure 5-5.Computer setting program for the hardness indenter positions (for every lattice, x=0.05mm, y=0.05mm).

5.2.3 Scanning electron microscopy (SEM)

The metal and ceramic mould interface microstructure was observed using a Philips XL-30 series and a Joel 7000 SEM. Near-interface compositional variations and the interaction products were analyzed using an energy dispersive X-ray analysis device (EDX).

5.3 Results and discussion

5.3.1 Sessile drop contact angle and drop diameter test

In order to better analysis the chemical inertness of the sintering additive face coat systems,

the yttria with sol binder shell system was used as the baseline in these experiments. Some of the reconstructed sessile drop images are shown in Figure 5-6.

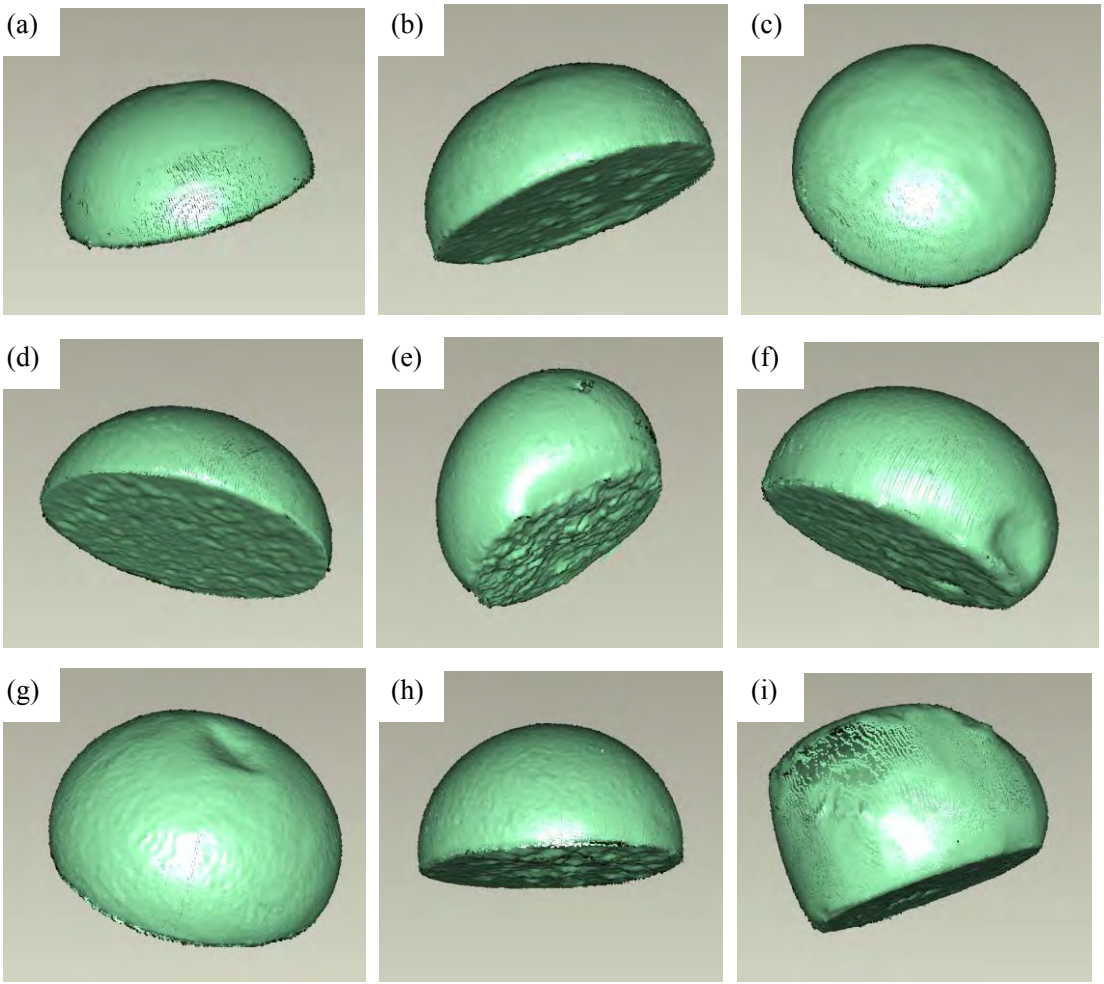

Figure 5-6.The 3D reconstructed sessile drop images. (a) 1650°C-YF 0.15-50s, (b) 1650°C-YF 0.15-60s, (c) 1650°C-YB 0.15-70s, (d)1650°C-YAZ-70s, (e) 1650°C-YAZ-40s, (f) 1650°C-Y+Sol-40s, (g) 1600°C-Y+sol-80s, (h) 1650°C-Y+sol-60s, and (i) 1625°C-YF_3 0.15-40s.

From Figure 5-6 it can be seen that, after the flash re-melt tests, the shape of all the test metal pieces changed from cylindrical to hemi-spherical in order to reduce the surface energy. Tables 5-1 to 5-6 show the measured contact angle and diameter change for each face coat

slurry systems from 4 system planes i.e. (8 angles and 4 diameter), and this data is presented graphically in Figures 5-7 to 5-12.

Table 5-1. Sample contact angle (°) with different times at an interaction temperature of 1600 °C.

Sample ID	60 s		70 s		80 s	
	average	Std dev	average	Std dev	average	Std dev
Y+sol	**121.96**	**9.26**	**117.49**	**7.79**	**102.04**	**15.40**
YAZ	141.19	8.90	113.68	4.78	111.11	11.83
YB 0.15	106.87	6.05	100.12	6.20	96.02	6.02
YF 0.15	121.75	19.17	104.00	7.34	115.97	15.47

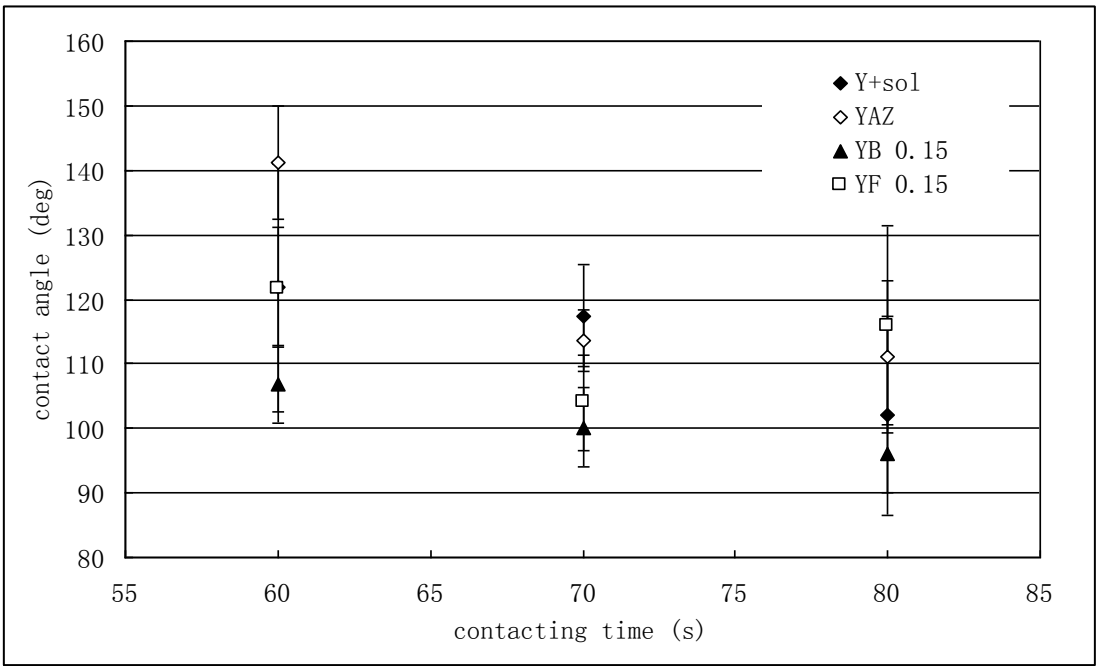

Figure 5-7.Sessile drop contact angles for different times at 1600 °C.

As can be seen from Table 5-1 and Figure 5-7, by increasing the contacting time of the metal drop and ceramic shell, the contact angle decreased from 120 ° to around 105 °. The rates of changing the contact angles were different for different ceramic systems. At the contact time

of 60 s, YB and YAZ systems had the smallest contact angle. By increasing the contact time, the contact angle of YAZ systems dropped down very quickly to 113.68 °, around 28 ° less than its original value. The contact angle of YF 0.15 face coat first decreased and then increased again at 80 s reaction time. The increase of contact angle may be due to the metal/shell interaction at longer contact times.

Table 5-2. Sample contact angle (°) with different times at an interaction temperature of 1625 °C

Sample ID	40 s		50 s		60 s		70 s	
	average	std	average	std	average	std	average	std
Y+sol	**130.66**	**5.88**	**105.55**	**14.82**	**99.46**	**2.74**	**90.06**	**9.94**
YAZ	122.41	8.12	114.33	11.07	109.80	5.06	104.73	7.97
YB 0.15	119.68	17.73	116.15	20.45	100.80	11.27	98.65	4.69
YF 0.15	130.51	8.90	107.10	8.16	102.05	7.58	93.41	5.09

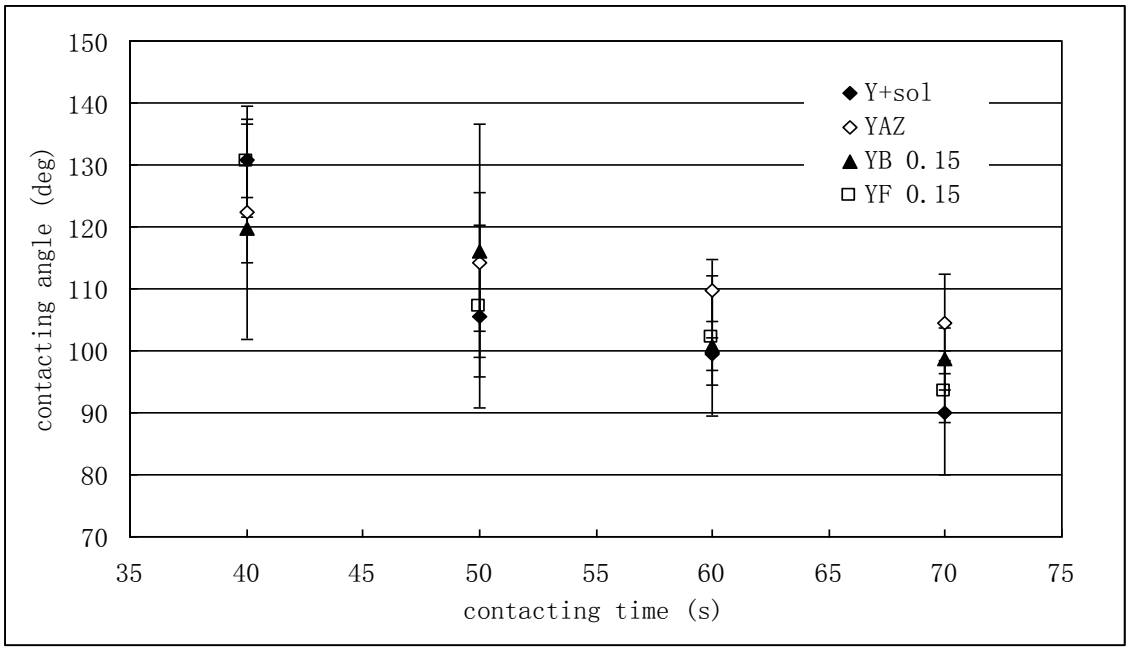

Figure 5-8. Sessile drop contact angles for different times at 1625 °C.

Table 5-2 and Figure 5-8 illustrate that increasing the interaction temperature by 25 °C, dramatically changed the contact angle of the yttria + sol sample from 130.66 ° at 40 s contact time to around 90 ° within 30 s, much quicker than other groups such as YAZ, YB 0.15 and YF 0.15. When increasing the interaction temperature to 1650 °C, the contact angle change rate for different face coat systems were similar, and reduced from around 135 ° to around 100 ° within 30 s, see Table 5-3. The metal contact angle reduction on the Yttria +sol face coat surface was the greatest of all the shells tested, decreasing from 138.57 ° to 119.56 ° in the first 10 s.

Table 5-3. Sample contact angle (°) with different times at an interaction temperature of 1650 °C.

Sample ID	30 s		40 s		50 s		60 s	
	average	std	average	std	average	std	average	std
Y+sol	**138.57**	**10.68**	**119.56**	**8.54**	**106.28**	**6.66**	**100.32**	**6.01**
YAZ	137.66	11.67	131.41	13.90	121.79	10.28	101.93	6.86
YB 0.15	133.77	12.58	134.60	13.79	122.93	9.3	98.62	11.56
YF 0.15	134.37	17.34	114.54	6.00	101.22	5.13	101.61	8.80

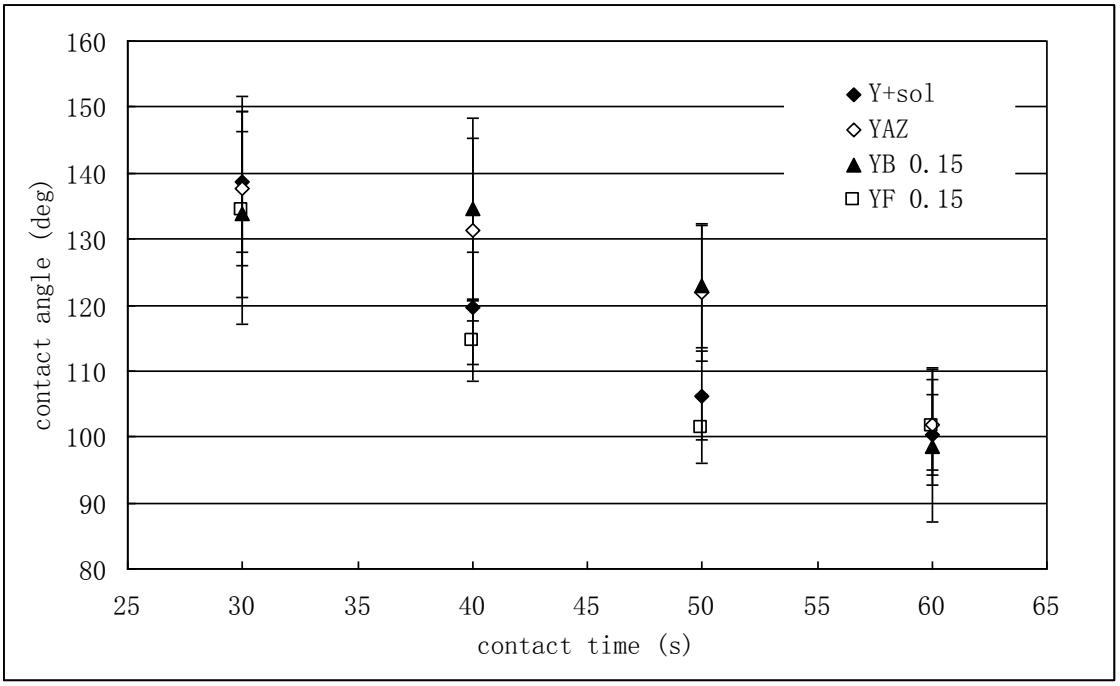

Figure 5-9. Sessile drop contact angles for different times at 1650 °C.

Table 5-4. Sample contact diameter (mm) for different times at an interaction temperature of 1600 °C.

Sample ID	60 s		70 s		80 s	
	average	std	average	std	average	std
Y+sol	**10.27**	**0.16**	**11.63**	**0.08**	**11.56**	**0.07**
YAZ	8.44	0.56	10.55	0.21	11.59	0.47
YB 0.15	11.78	0.06	11.27	0.04	11.59	0.16
YF 0.15	9.78	1.09	11.03	0.29	10.67	0.46

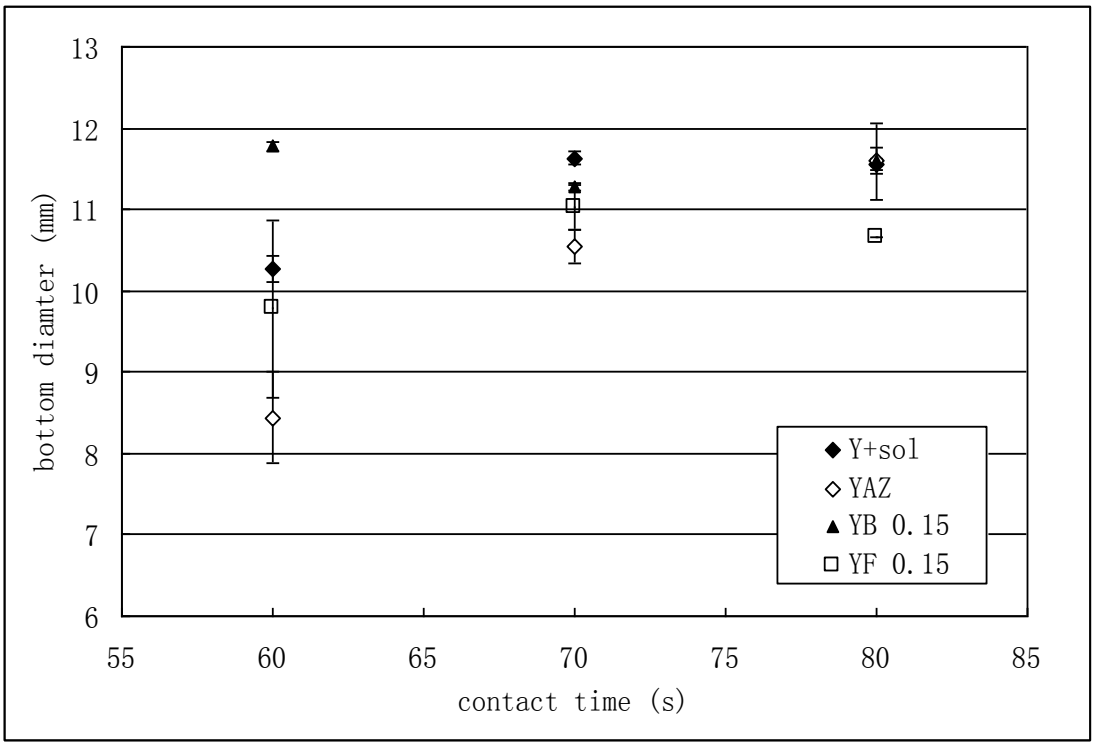

Figure 5-10. Sessile drop contact diameter for different times at 1600 °C.

Table 5-4 and Figure 5-10 show that, by increasing the contact time of the molten metal on the ceramic shell, the sessile drop contact diameters increase from their original 10 mm to around 12 mm. After melting, the molten TiAl alloys on the YAZ and YF 0.15 systems first shrink then increase again after a long time at each isothermal interaction temperature. The YB 0.15 face coat system has the largest contact diameter at the contact time of 60 s but smallest rate of increase among all the test face coat systems are noted.

Table 5-5. Sample contact diameter (mm) for different times at a temperature of 1625 °C.

Sample ID	40 s		50 s		60 s		70 s	
	average	std	average	std	average	std	average	std
Y+sol	**9.17**	**0.23**	**10.76**	**0.5**	**11.67**	**0.19**	**11.83**	**0.26**
YAZ	9.51	0.26	10.21	0.38	10.73	0.35	10.64	0.21
YB 0.15	10.12	0.27	10.71	0.38	11.37	0.05	11.87	0.17
YF 0.15	9.00	0.25	11.09	0.12	11.44	0.21	11.85	0.08

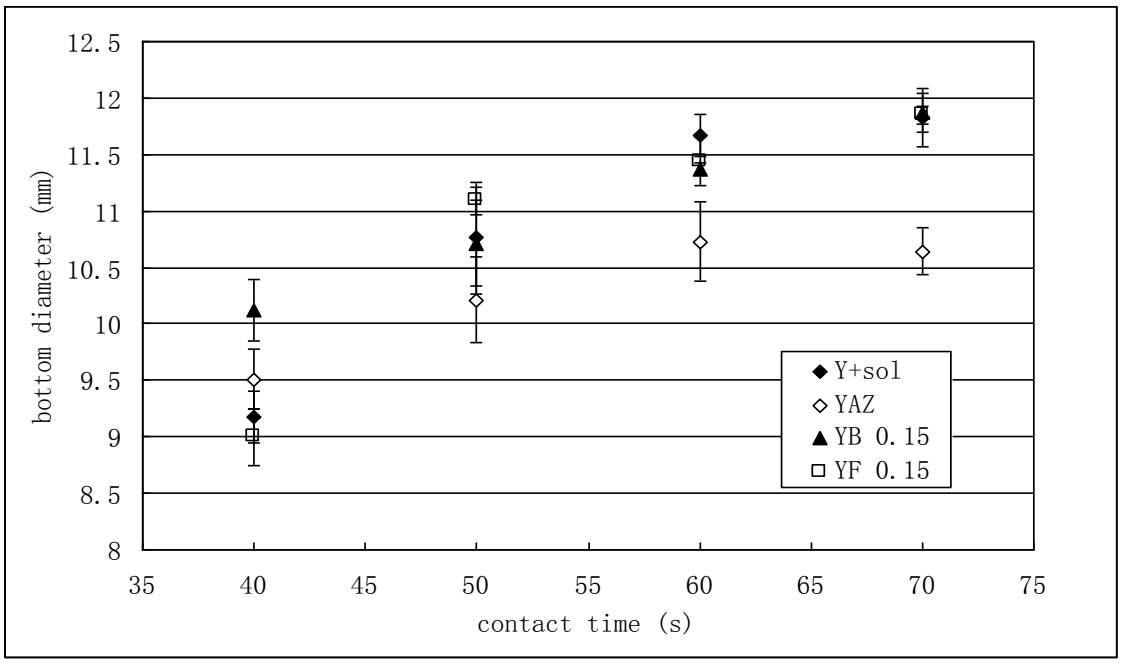

Figure 5-11. Sessile drop contact diameters for different times at 1625 °C

At the higher interaction temperature (1625 °C), nearly all the metal drop contact diameters firstly reduced a little then increased again. Except for the YAZ system, diameters of all the test drops after 70 s contact time increase to around 11.8 mm.

Table 5-6. Sample contact diameter (mm) for different times at an temperature of 1650 °C.

Sample ID	30 s		40 s		50 s		60 s	
	average	std	average	std	average	std	average	std
Y+sol	**8.57**	**0.27**	**10.02**	**0.25**	**10.84**	**0.16**	**11.86**	**0.21**
YAZ	8.37	0.38	9.24	0.53	9.38	0.27	12.33	0.19
YB 0.15	9.18	0.46	10.41	0.24	12.87	0.12	12.14	0.11
YF 0.15	9.83	0.12	9.68	0.17	12.80	0.10	12.76	0.12

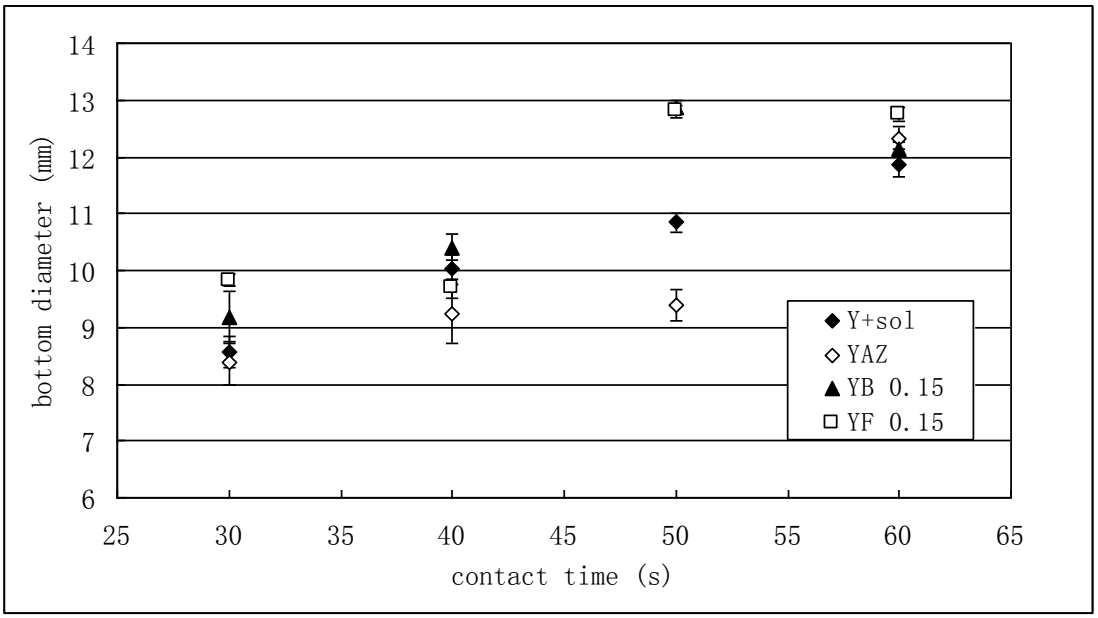

Figure 5-12. Sessile drop contact diameter for different contact times at 1650 °C

The most noticeable sessile drop contact diameter shrinkages were observed by increasing the interaction temperatures from 1625 to 1650 °C within the first contact 20 s. Except for the yttria+sol system, the entire sample bottom diameter increased to 12 mm after 60 s. The YF 0.15 wt% face coat system had a fastest diameter change between 40 and 50 s.

5.3.2 Hardness at the interface

Due to metal/mould interaction, some of the ceramic elements (O, Si, Zr) diffused into the metal causing solid solution hardening of the base alloy. This is illustrated in Figure 5-13 (a) where the metal/shell interface showed a high hardness which gradually decreases away from the interface. The hardened layer thickness was measured from the interface to the point where the average hardness was the same as of the metal matrix. By considering the interfacial damaging after metal removed from the shell, the first line of the indents was located around 10 μm away from the observed interface and continued to around 500 μm into the metal matrix (Figure 5-13 (b)).

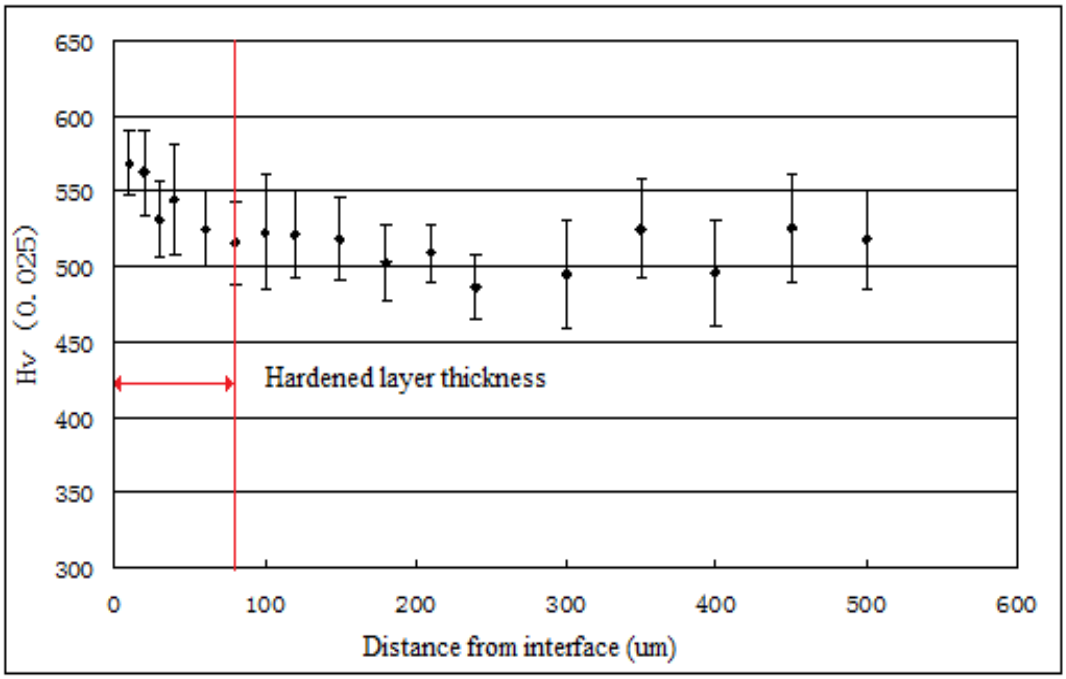

(a)

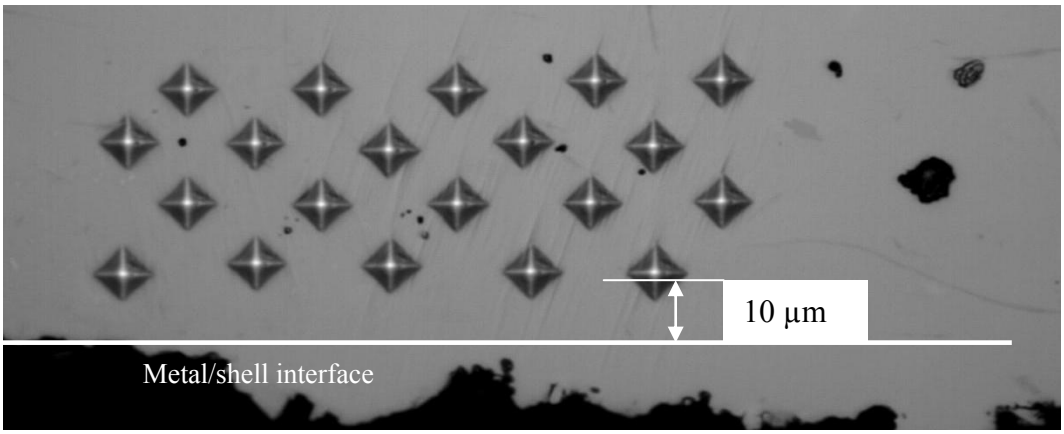

(b)

Figure 5-13. Hardness traces at the metal/shell interface region of sample Yttria+sol 1650°C 50s. (a) Hardness values from interface, and (b) the image of 4 rows of indents from metal/shell interface.

Some of the hardness profiles for varies ceramic systems sintered at different temperatures are illustrated in Figure 5-14. As can be seen, samples showed high hardness at the surface around 550, and then the hardness decreased gradually to around 500 to the metal matrix. For using different face coat, the hardened layer thicknesses at the sample surface were different. The hardened layer thickness measured from each sample hardness trace in Figure 5-14 are summarized and shown in Figure 5-15 with comparison of different face coat systems.

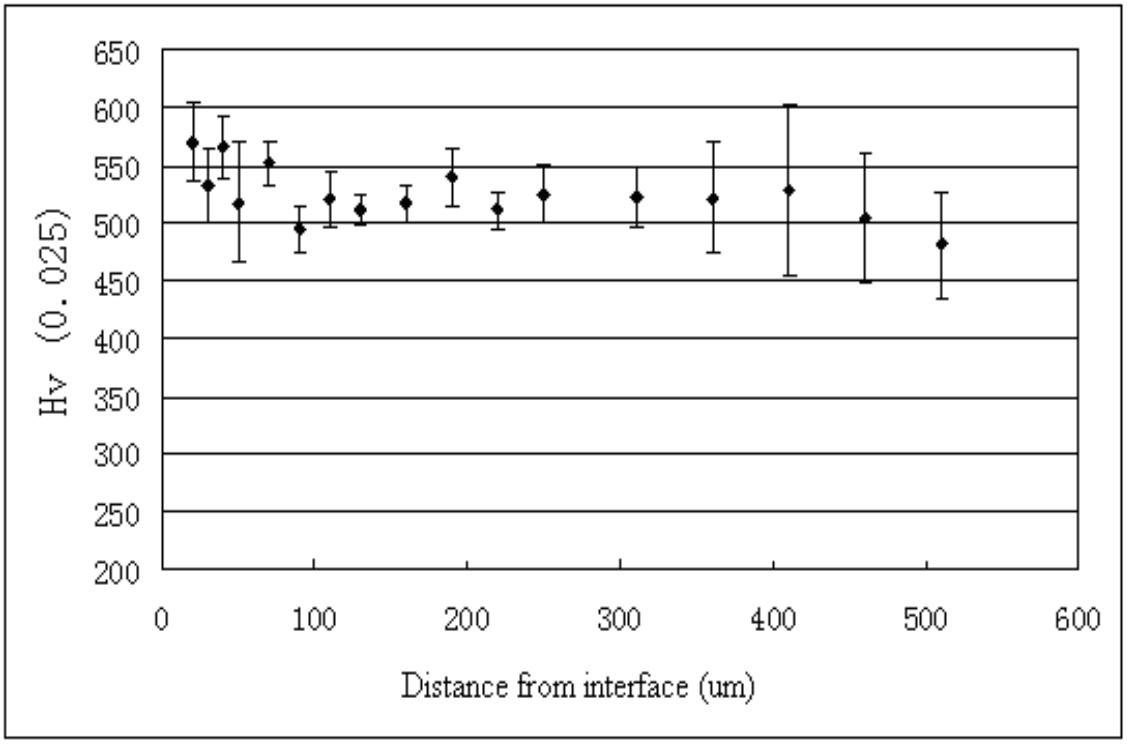
650
600
550
500
450
400
350
300
250
200
Hv (0.025)
0
100
200
300
400
500
600
Distance from interface (um)

(a)

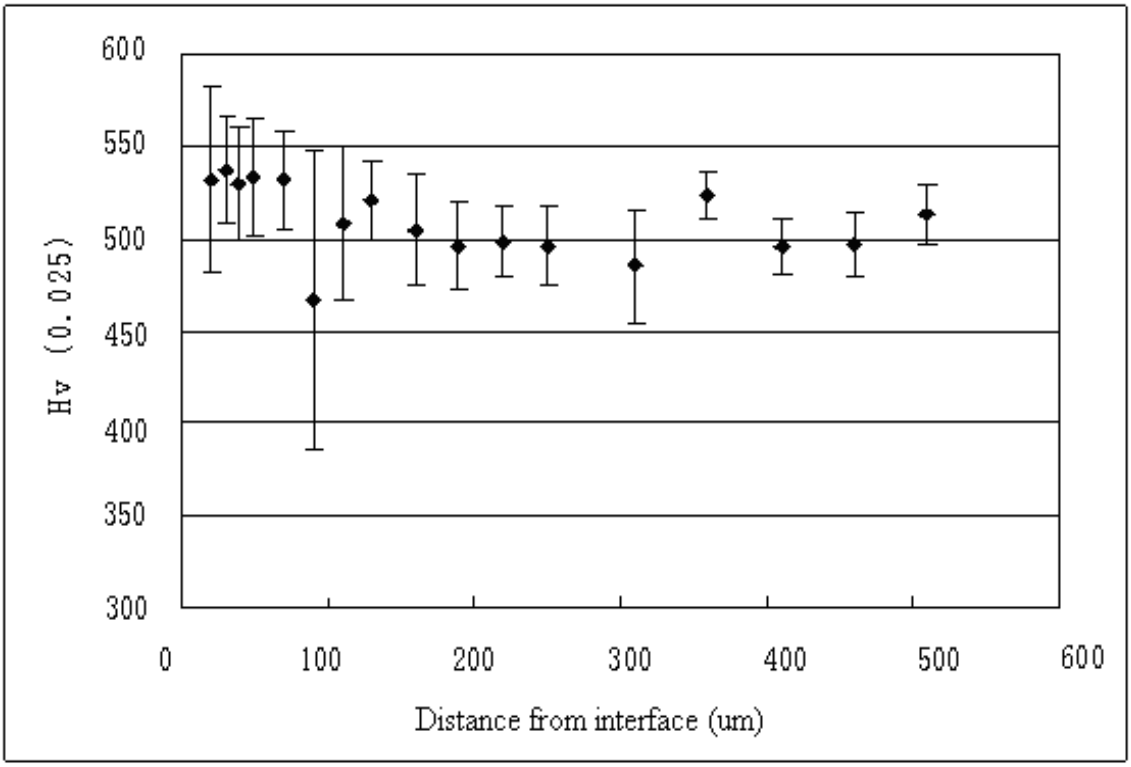
600
550
500
450
400
350
300
Hv (0.025)
0
100
200
300
400
500
600
Distance from interface (um)

(b)

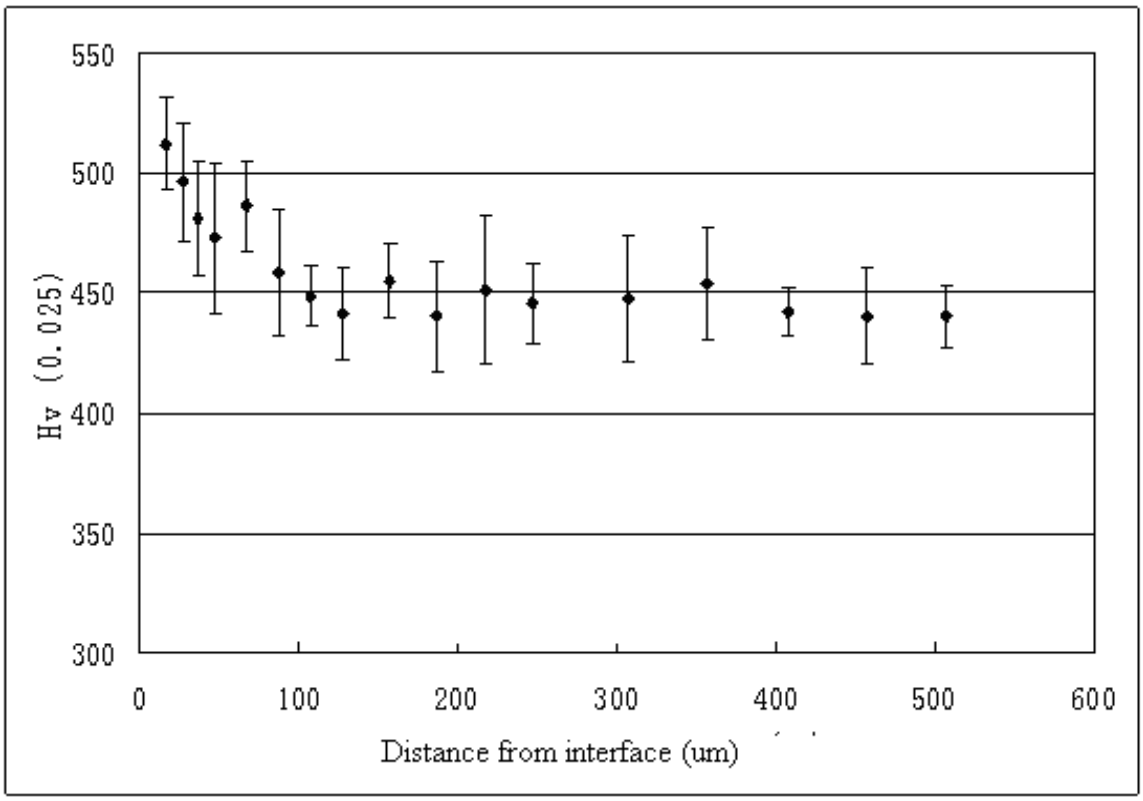
550
500
450
400
350
300
Hv (0.025)
0
100
200
300
400
500
600
Distance from interface (um)

(c)

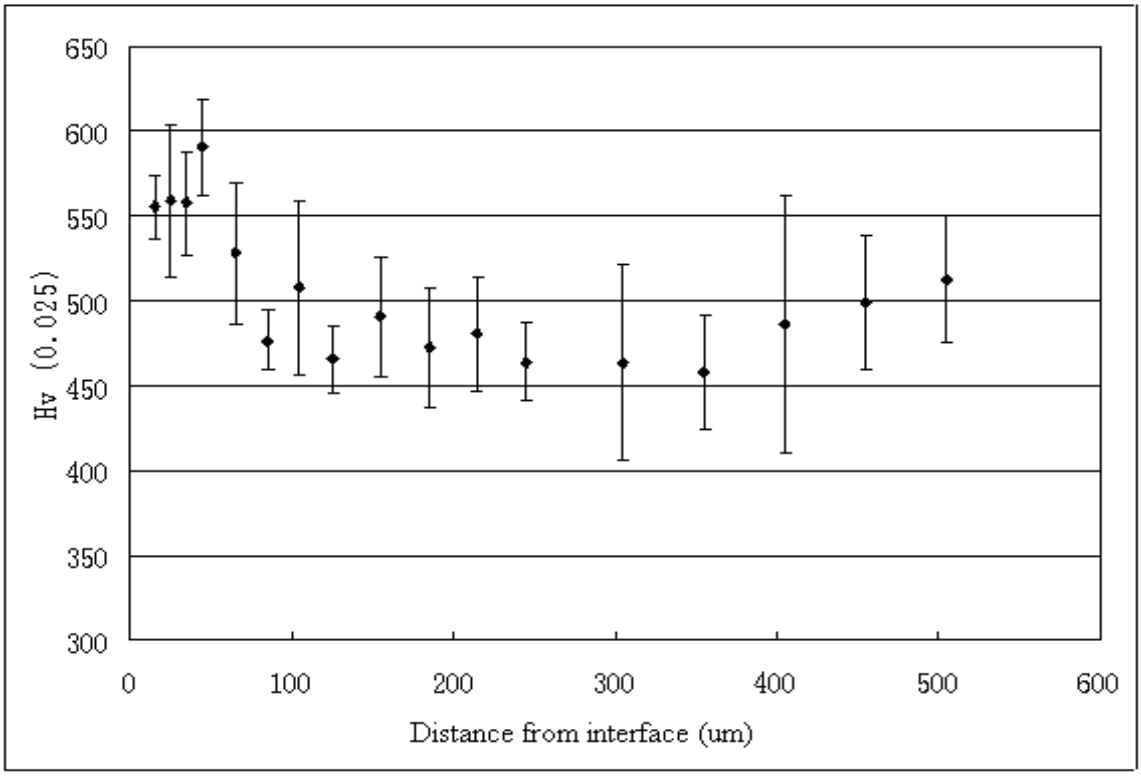
650
600
550
500
450
400
350
300
Hv (0.025)
0
100
200
300
400
500
600
Distance from interface (um)

(d)

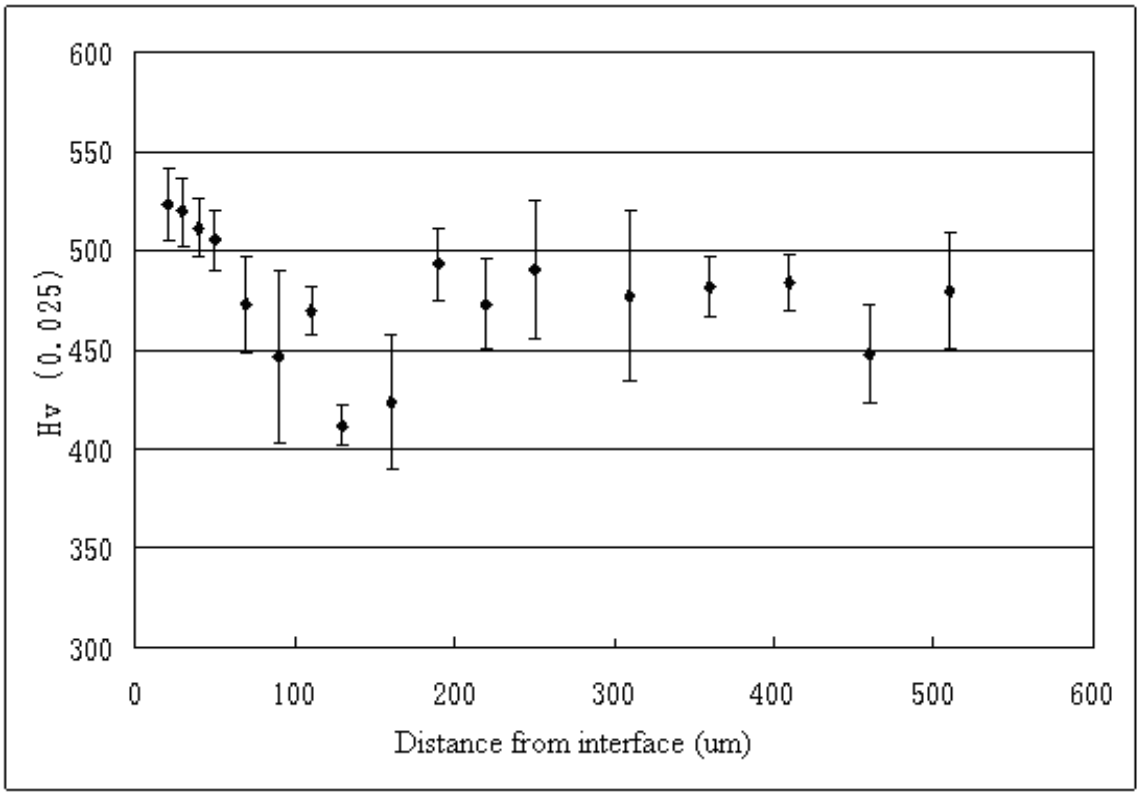

(e)

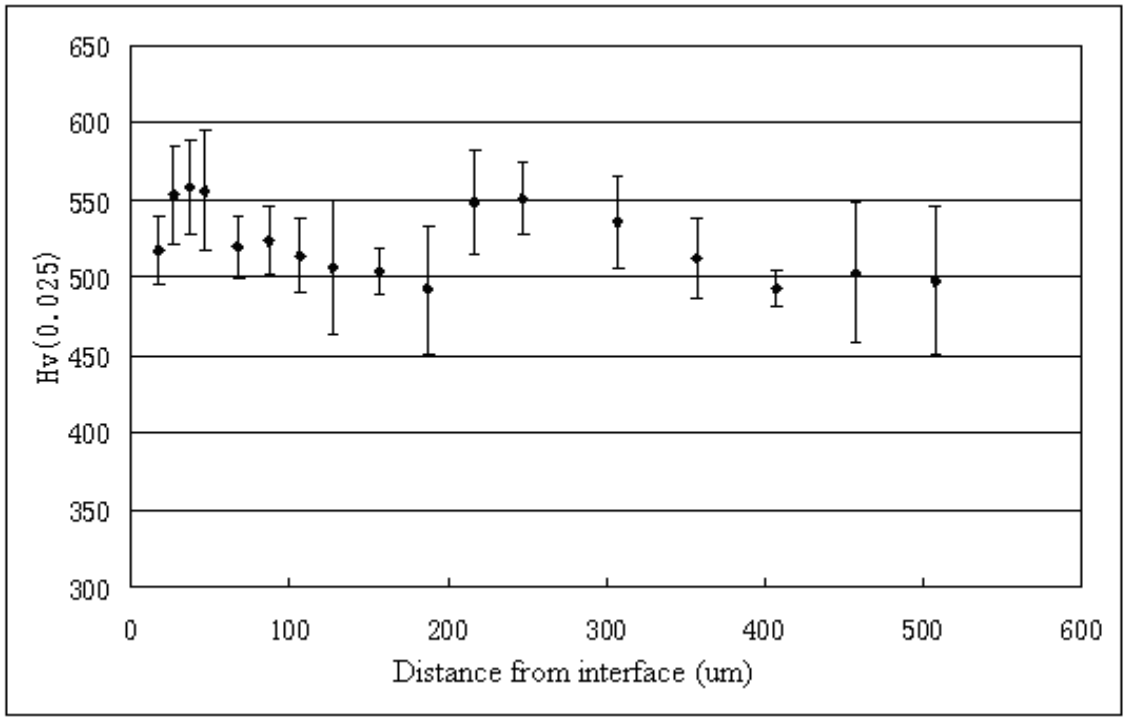

(f)

Figure 5-14. Hardness traces of different samples (a) 1650 °C-YB0.15-30 s, (b) 1650 °C-Y+sol-60 s, (c) 1600 °C-YAZ-80 s, (d) 1600 °C-YF0.15-60s, (e) 1625 °C-YF 0.15-50s, and (f) 1650 °C-YB 0.15-50s.

From Fick's law of diffusion, by increasing the interaction temperature, less time is needed for the elements to diffuse from ceramic shell into the interfacial area. The growth rates of the hardened layer dependent on the type of face coat systems and temperature. Within the first interaction time 10 s, the hardened layer thickness rose very slowly, but for the same holding time, increased significantly at higher interaction temperatures, see Figure 5-15 (b) & (c). For the Y+sol face coat system, the thickness of the hardened layer grew very slowly when compared to the other groups with the hardened layer thickness stabilized at of around 40 μm at 1600 °C and 70 μm at 1625 °C at different contact times. The hardened layer thickness of the YAZ system was around 170 μm at 1625 and 1650 °C with a contact time around 40 s, much thicker than any other systems. Therefore, the thermal inertness of the YAZ mould was greatly decreased by increasing the interaction temperature and contact time.

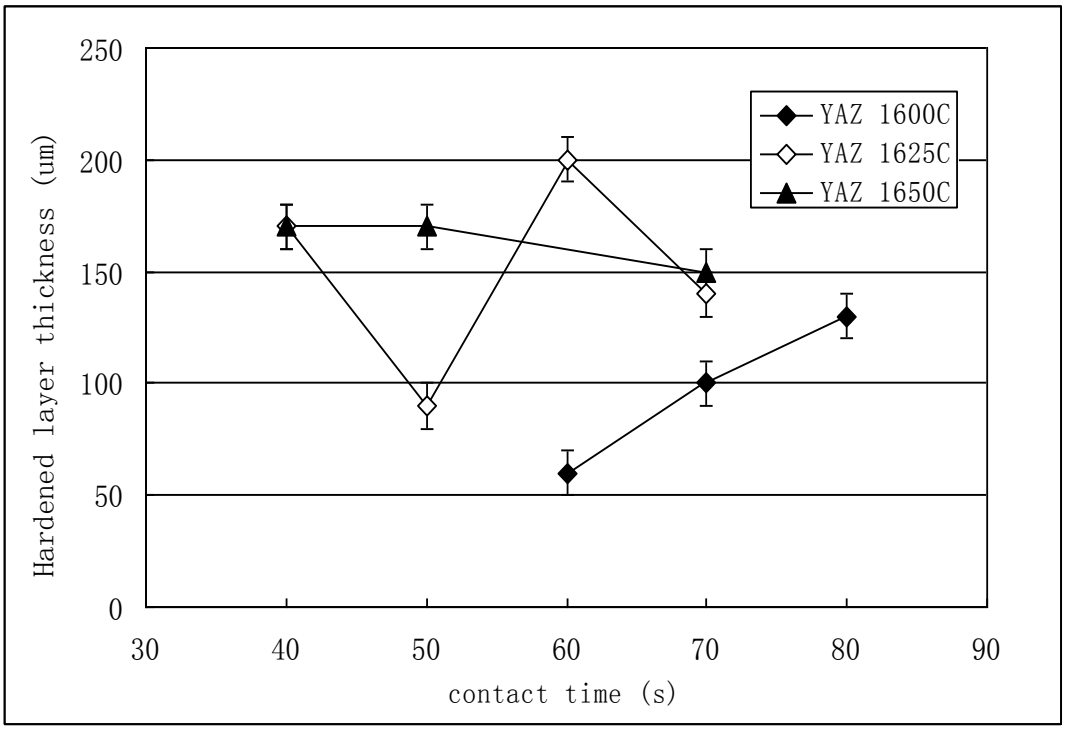

(a)

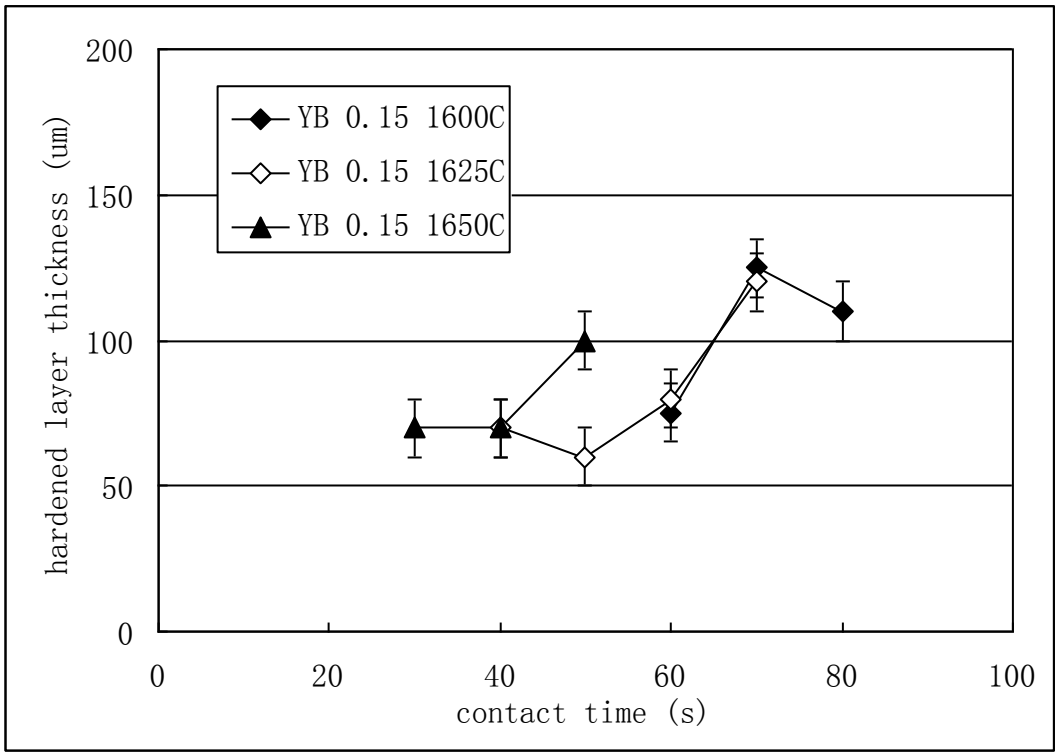
YB 0.15 1600C
YB 0.15 1625C
YB 0.15 1650C
hardened layer thickness (um)
200
150
100
50
0
0
20
40
60
80
100
contact time (s)

(b)

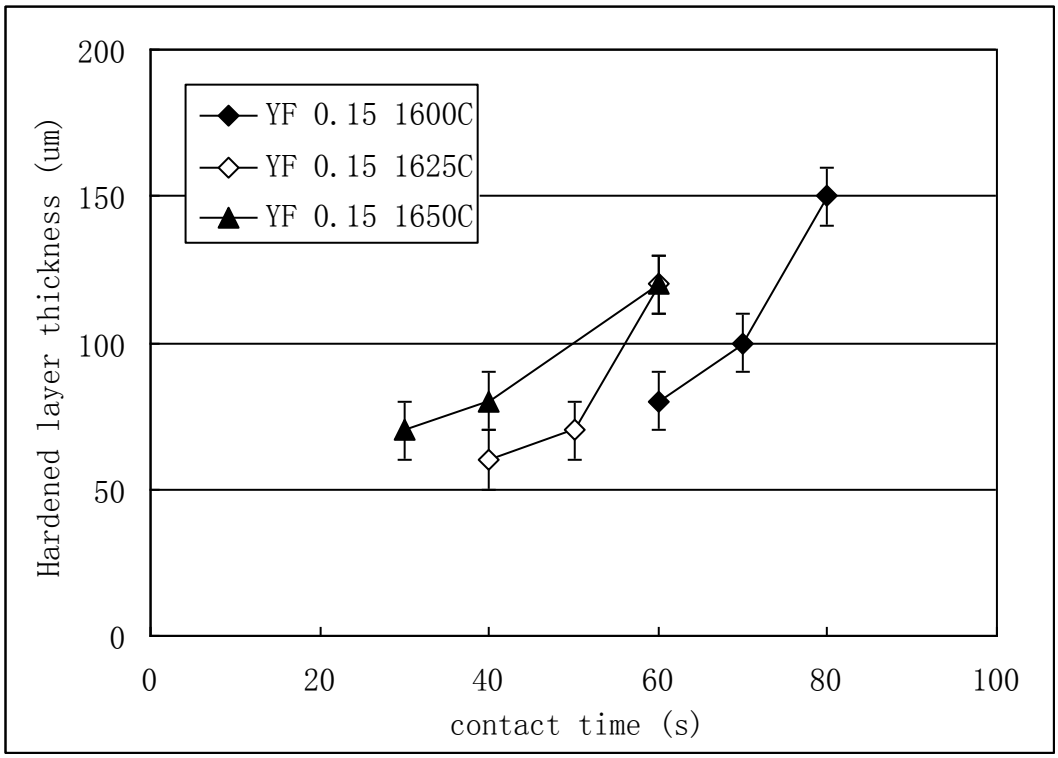
YF 0.15 1600C
YF 0.15 1625C
YF 0.15 1650C
Hardened layer thickness (um)
200
150
100
50
0
0
20
40
60
80
100
contact time (s)

(c)

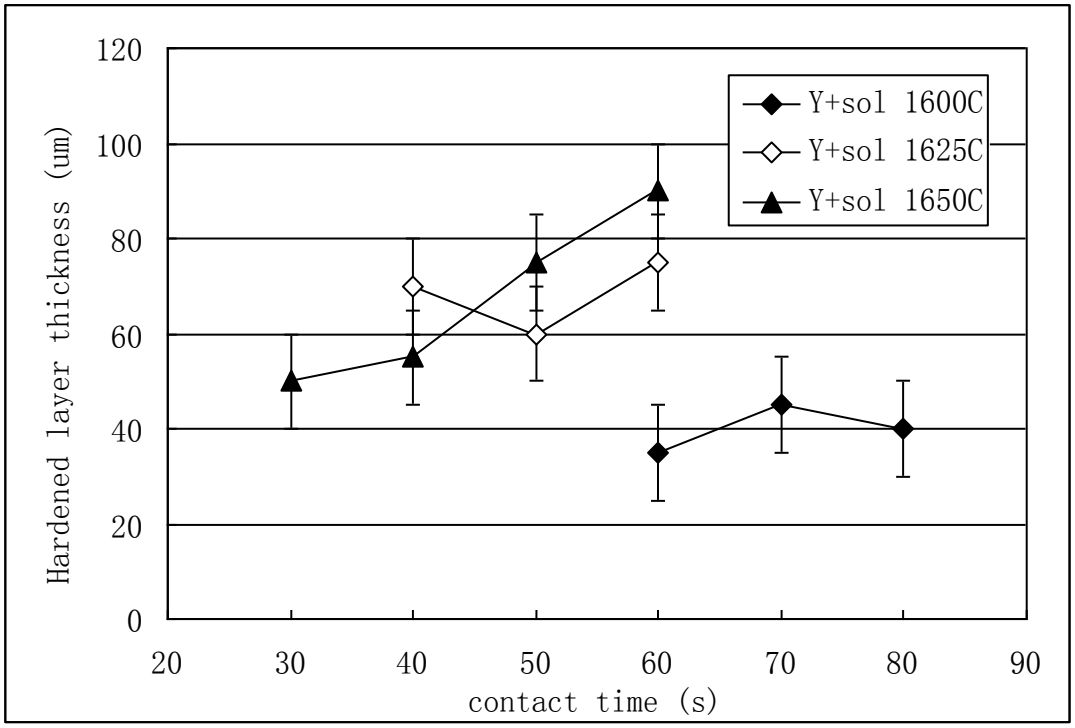

(d)

Figure 5-15 Hardened layer thickness of sample at different interaction temperature and time. (a) YAZ, (b) YB 0.15, (c) YF 0.15, and (d) Y+sol.

The hardened layer profile for different face coat systems at the same interaction temperature are shown in Figure 5-16. As can be seen, the increased contact times and temperature cause an overall increase of hardened layer thickness of each shell system. The hardened layer thickness is increased slowly of using yttria + sol face coat system, and at high temperatures around 1625 and 1650 °C, the sample using YAZ as the face coat has the thickest hardened layer thickness. The hardened layer thickness of metal using YB 0.15 and YF 0.15 face coat systems have the similar behaviour, especially at 1600 and 1650 °C.

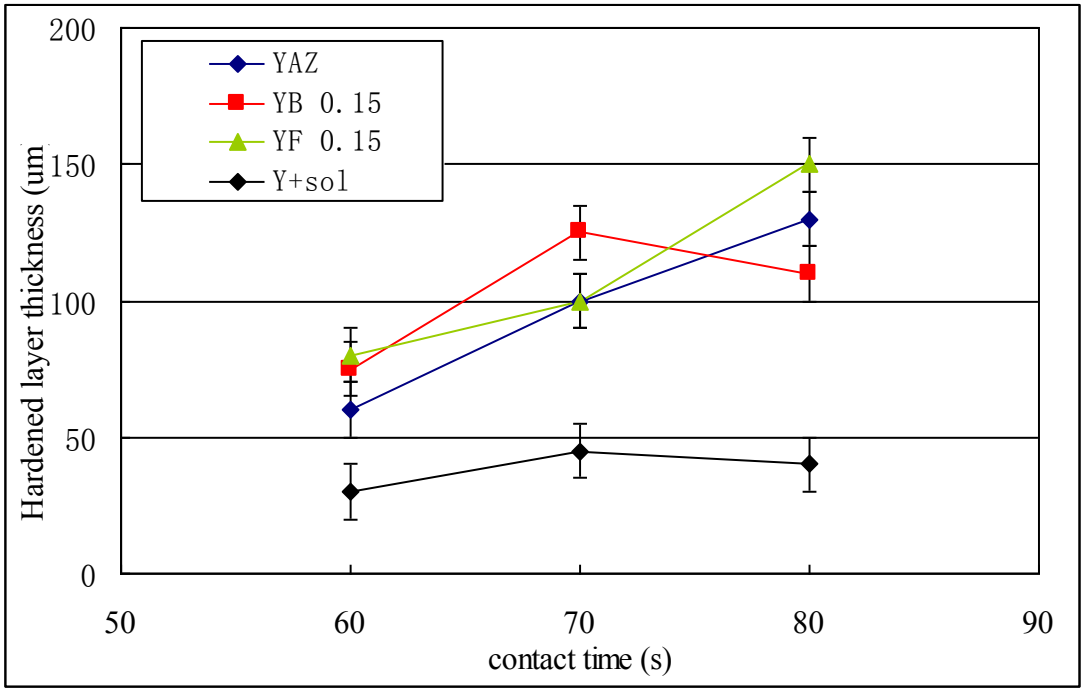
200
150
100
50
0
Hardened layer thickness (um
YAZ
YB 0.15
YF 0.15
Y+sol
50
60
70
80
90
contact time (s)

(a)

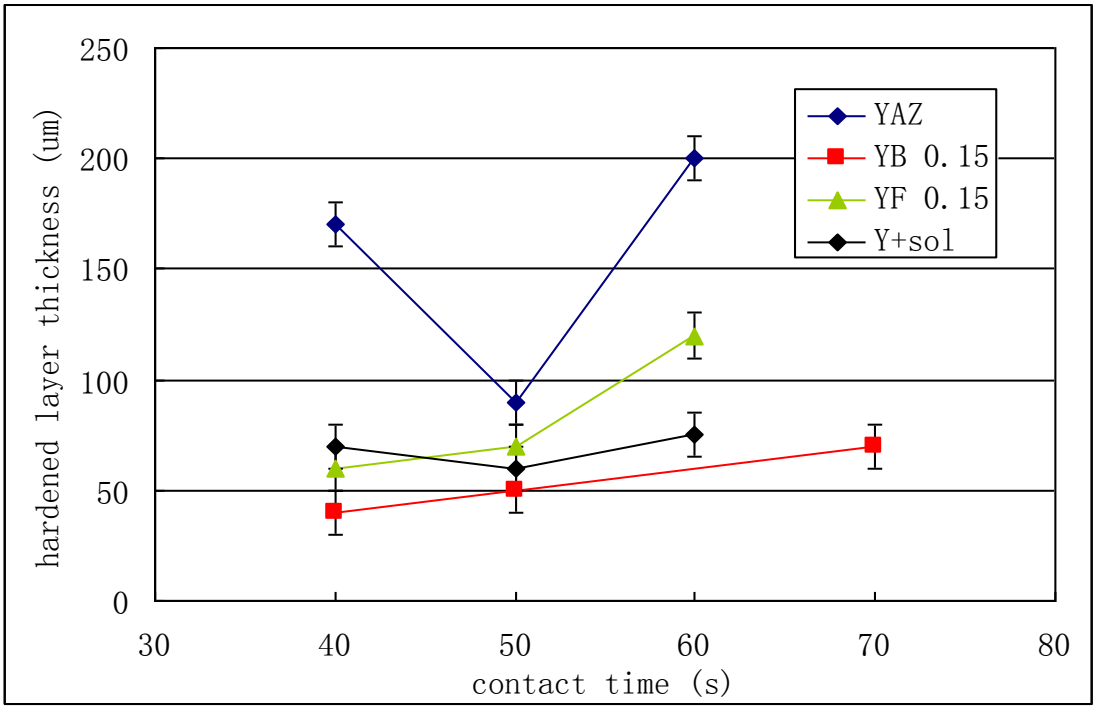
250
200
150
100
50
0
hardened layer thickness (um)
YAZ
YB 0.15
YF 0.15
Y+sol
30
40
50
60
70
80
contact time (s)

(b)

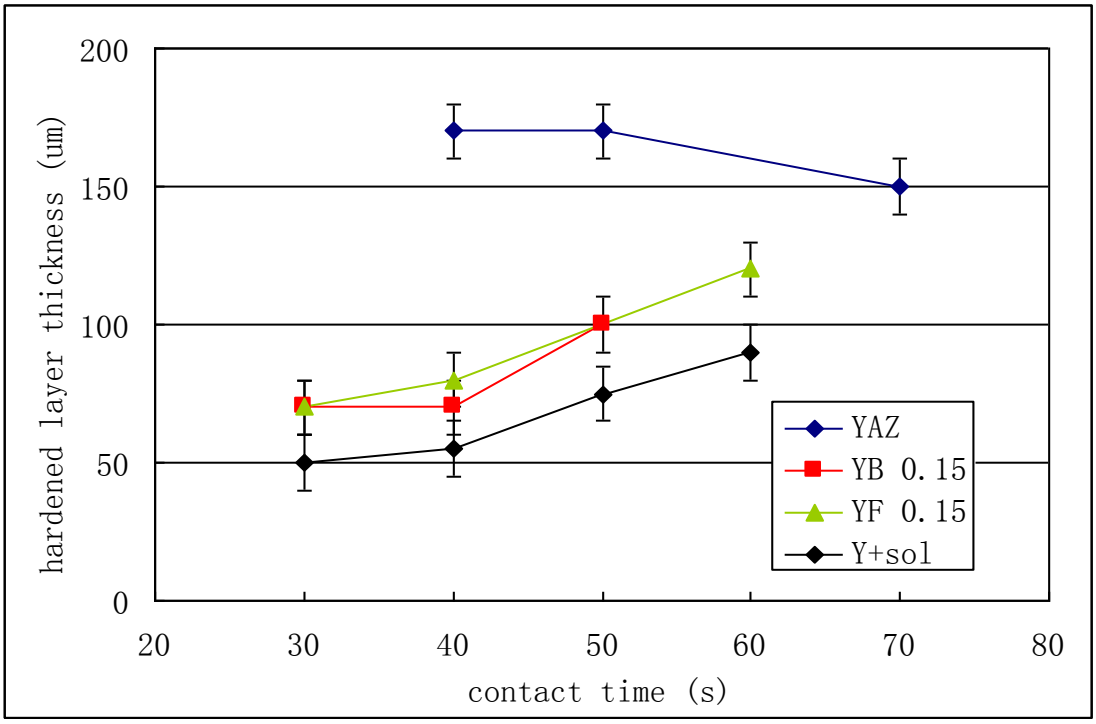

(c)

Figure 5-16. The hardened layer thickness of different face coat systems at same interaction temperature and time (a) 1600 °C, (b) 1625 °C, and (c) 1650 °C.

It was known, the hardened layer thickness of each sample is dependent to the chemical inertness of the face coat [41, 42]. Among all the test face coat systems, Yttria +sol face coat showed the smallest hardened layer thickness thus has the highest thermodynamic inertness. Samples of YB 0.15, YF 0.15 and YAZ systems showed similar behaviour when interacting with TiAl alloys at 1600 °C. Higher temperatures cause a much more severe interfacial interaction. The chemical inertness of the YAZ shell was most affected by temperature giving the thickest hardened layer of all the test systems. This face coat chemical inertness degradation of the YAZ shell may be due to the sintering additive Al_2O_3 and ZrO_2 at high temperatures. However for the YB 0.15 and YF 0.15 face coat groups, due to the very small amount of sintered additives added, the chemical inertness of these face coats were better

than the YAZ face coat at higher interaction temperatures.

5.3.3 The microstructure at the metal/shell interface

After the flash re-melting tests, the microstructures of the metal drops at the metal/shell interface using yttria face coat were a fully lamellar ($\alpha_2+\gamma$) morphology, see Figure 5-17. Compounds TiB with needle-like morphology (light phases) were found between the lamellar dendrite arms. Some filler particles were found at the metal-mould interface wetted by the alloy. No evidence was found of the interaction between the face coat and the alloy except that some Y_2O_3 inclusions were observed in the near-surface region around 30 μm into the metal.

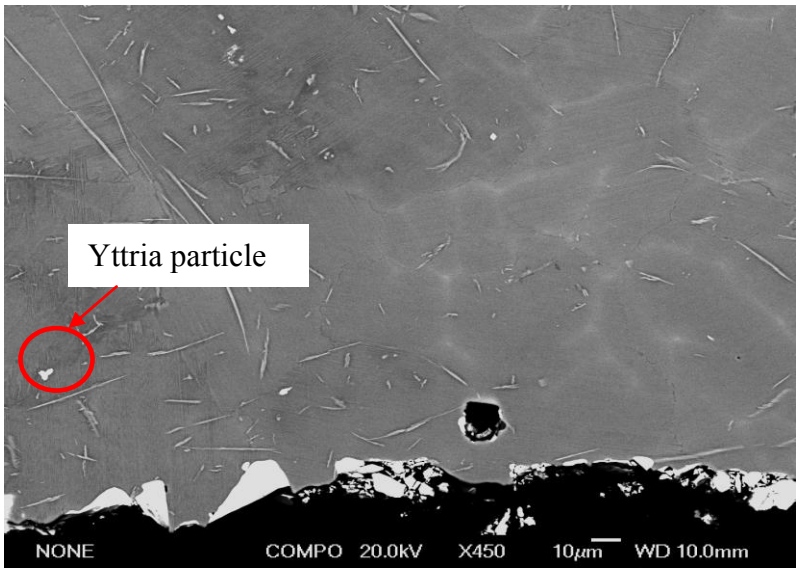

Figure 5-17. Sessile drop interface microstructures of sample Y+sol interact with TiAl at 1600 °C with 70 s contacting time.

Representative SEM images of the mould and metal interface areas for some of the ceramic mould systems are shown in Figure 5-18.

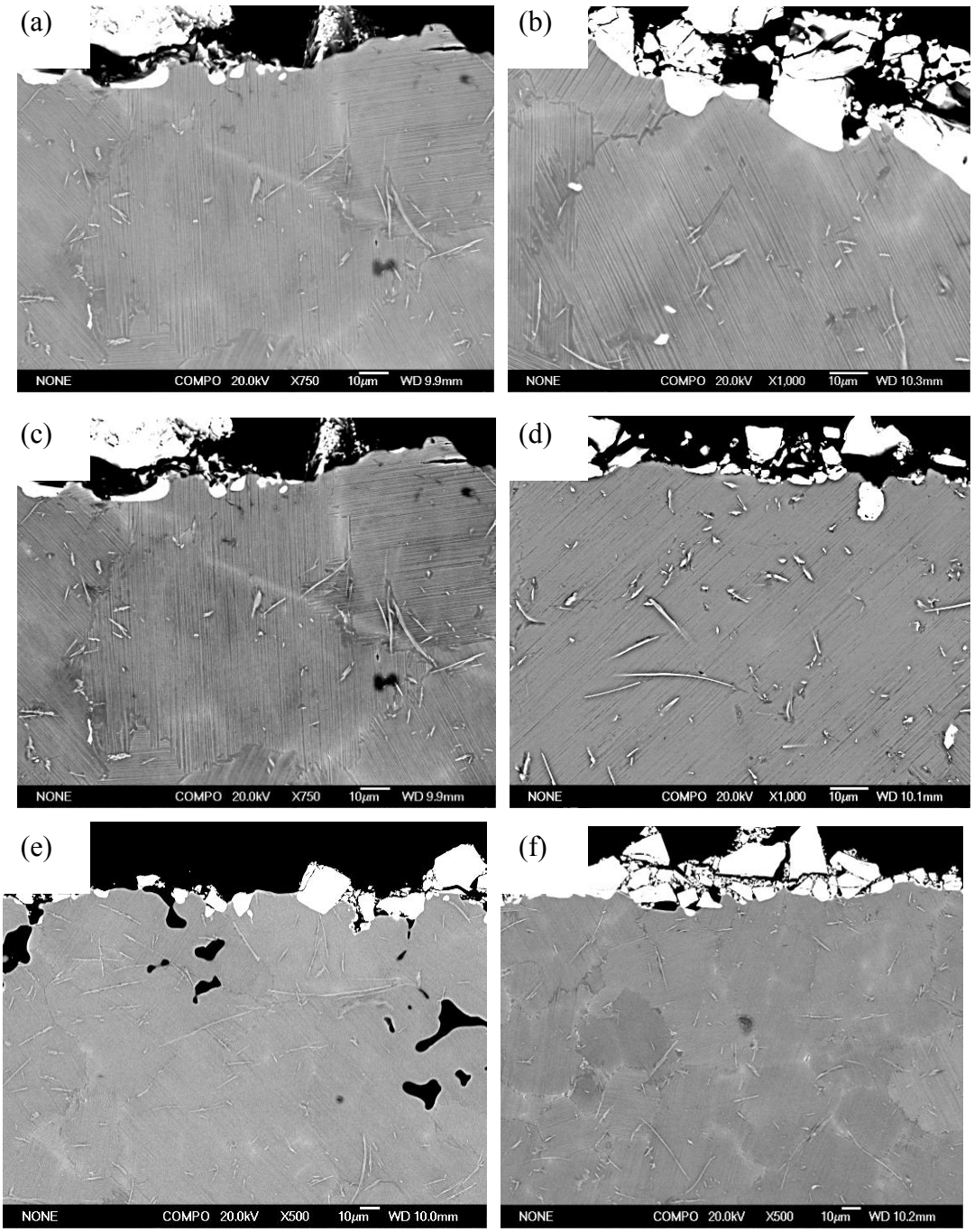

Figure 5-18. The metal/shell interface microstructure. (a)&(b) YF 0.15 1650 °C-50s, (c)&(d) YB 0.15-1600 °C -80s, and (e)&(f) YAZ-1625 °C -70s.

After flash re-melting, there was no interaction products observed at the metal interface for all the test face coat systems (yttria +sol, YAZ, YB 0.15 and YF 0.15), and the microstructure is nearly the same of using yttria +sol as the face coat.

5.4 Conclusions

In this chapter, the thermo-chemical inertness of the selected face coat slurry is evaluated using a sessile drop flash re-melt test. The conclusions so far for this experiment were:

1. The interaction between the metal and different ceramic substrates will cause a change of the spreading behaviour i.e. different contact angle and drop diameter. The metals on the yttria +sol face coat surface have the slowest spreading rate among the test group. By increasing the interaction temperature from 1600-1650 °C, the metal spreading speed on the YF and YB face coat were increased.

2. After interaction, the depth of the hardened layer thickness varies with different ceramic systems. High interaction temperatures and long contact times can cause an increased hardened layer thickness except with the yttria+sol system. At 1625 and 1650°C the greatest depth of hardening was recorded with the YAZ face coat system. The results of using face coat system YF and YB also showed an increased hardened layer thickness by increasing the contact time but with larger layer thickness than pure yttria and YAZ coat.

3. The microstructure at the metal surface was quite similar with all the ceramic systems, and no interaction products were found at the interface.

Chapter 6 The reliability of face coat slurry

This chapter consists of two parts. The first part will introduce casting mould manufacture process from the small scale plate crucible to the large ‗T' shape with the investigated mould surface finish. Some improvement in mould production methods will later be introduced to enhance the face coat strength using the newly developed slurry. During mould firing, Silicon in the backup coat layer penetrated into the face coat surface. Silicon penetration amount was dependent both on sintering temperature and the type of the face coat, which will introduce in the second part of this chapter.

6.1 Sample preparation

6.1.1 The mould shape design and preparation

Because the strength of the new face coat mostly comes from the polymers, so compared to the strength of sol used face coat, these new water based binder face coat is relatively poor. In order to verify the possibility using these new face coat in industry, small crucibles were first made to investigate the strength of the face coat, which is required have a smooth, uniform, and non de-laminated surface finish. Then, large crucibles with a ‗T' shape were designed and made, using the same procedures to investigate the surface finish before casting, see Figure 6-1.

The face coat slurry described in Chapter 4 (Table 4-1, yttria+water) were used to make the testing mould, and after finish all the mould were were fired at 1000 °C for 3 hours before the shell face coat surface finish was determined.

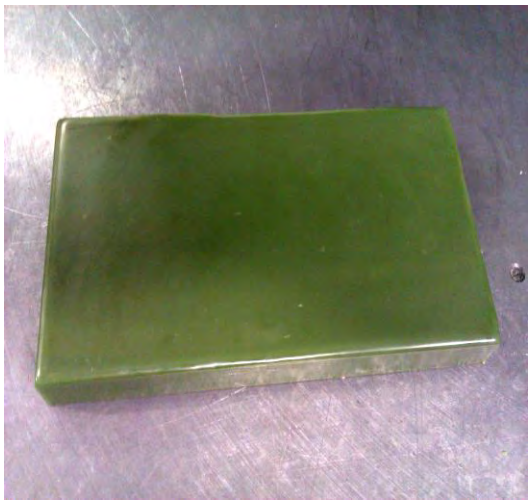

(a)

(b)

(c)

(d)

Figure 6-1.The wax pattern shape, (a) the crucible plate, and (b) the _T‘ shape, the ceramic shell of, (c) the plate, and (d) the _T‘ shape.

6.2 Results and discussion

6.2.1 Small crucibles

For the small crucible plate, the time needed for the molten wax to flow out the crucible is shorter than for the large components, therefore less chance for the molten wax to damage the face coat surface. From Figure 6-2 it can be seen that, after de-wax, the face coat surface in the shells was very smooth, and no face coat peels off and de-lamination are observed. So,

the newly designed slurry can be seen to be successful when used in small scale crucible production.

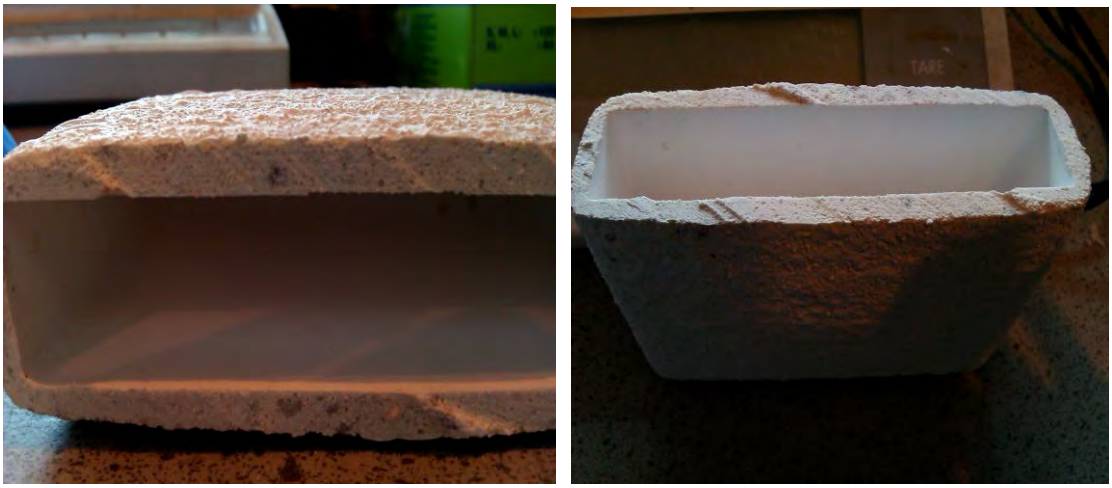

(a) (b)

Figure 6-2.The small plate crucible internal surfaces after firing at 1000°C for one hour, (a) side one, and (b) side two.

6.2.2 Large' T' shape investment mould

‗T' shape moulds were designed to test the green strength of the face coat on a large scale mould. After firing at 1000 °C for 3 hours, shells were broken up to check the surface finish and are shown in Figure 6-3.

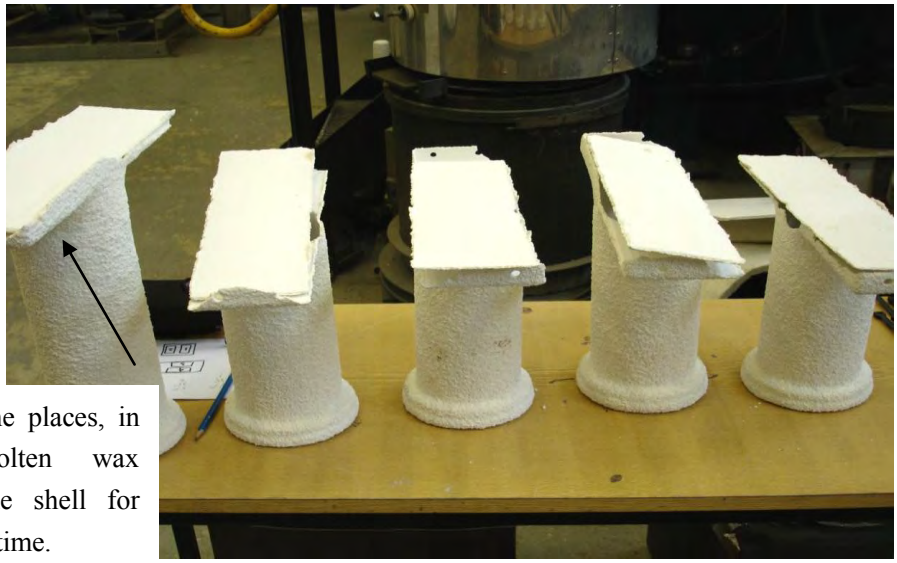

Here are the places, in which molten wax contacts the shell for the longest time.

(a)

(b)

(c)

(d)

Figure 6-3.The investment moulds. (a) all the tested ‗T' shape, and (b)&(c)&(d) test sample crucible inside surface.

From Figure 6-3, two types of failed face coat surface were observed. First type was the face coat peeling off and de-laminating (Figure 6-3 (b)). Second type was a very rough surface with some bumps (Figure 6-3 (c&d)). The predictions of these face coat surface degradations may take place during the de-wax process.

As it is known, most polymers have a glass transition temperature (Tg) around 100 °C with a melting temperature around 200 °C. e.g Poly methyl methacrylate (PMMA) has a Tg around 105 °C, and T_m around 160-200 °C [148]. For the Poly vinyl alcohol used in this experiment as the face coat strengthener, the Tg is 70-99 °C and the T_m is around 248 °C in the reference depending on the precise molecular weight [148]. So at a de-wax temperature of 180 °C, the PV alcohol in the face coat has already began to soften and lose its strengthening effect. Therefore, the failure of the face coat of the ‗T' shape mould is due to the polymer degradation (softening) during de-waxing and the face coat surface was quickly damaged

when the molten wax flowed out of the crucibles.

In order reduce the contact time of the molten wax on the mould surface, a new ‗T' shape (Figure 6-4) with two extra channels connected to the back surface was designed to help wax flow out during de-wax process.

(a)

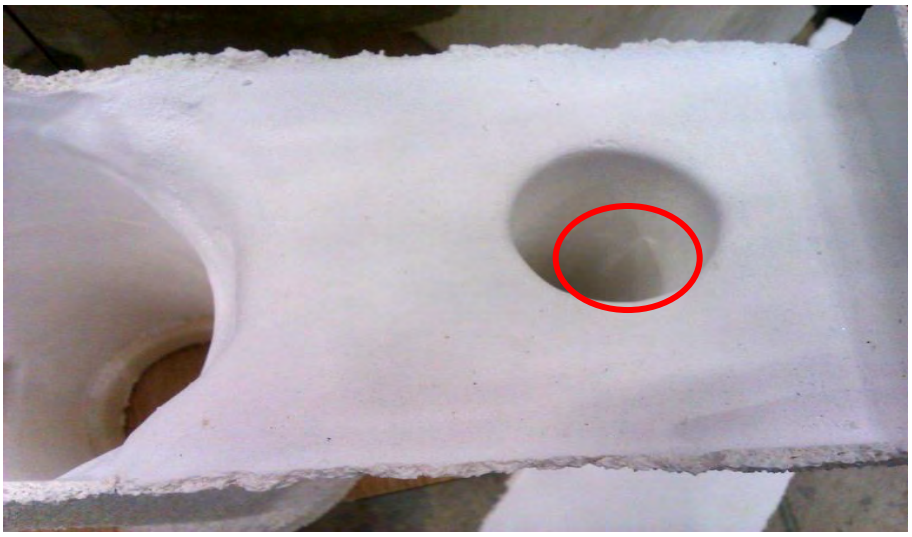

(b)

Figure 6-4.The surface finish of the new mould. (a) The left hand side of the mould, and (b) the right hand side of the mould.

As can be seen from Figure 6-4, by adding two extra channels in the plate to help liquid wax flow out during de-wax, the plate surface of the face coat has became smooth after sintering, but some yttria powder clusters were observed at the bottom of the channels. The face coat strength was still too low to be used for the large component shell applications in industry.

6.2.3 Shell making process improvement

It is known that the gelation interaction between sol and yttria powder can strengthen the face coat during drying, and this effect can be maintained up to the temperatures around 300 °C. But at the same time this gelation effect also limits the life of the face coat slurry to hours in some cases. In order to use this gelling effect whist not reducing the life of the slurry, new mould production methods were developed. In these new methods, rather than adding the sol into the slurry, sol was applied to the dried wax surface or the face coat surface before making the backup coat, enhancing the strength of the face coat. Figure 6-5 illustrates below shows the cross structures of the mould using these new improvements methods.

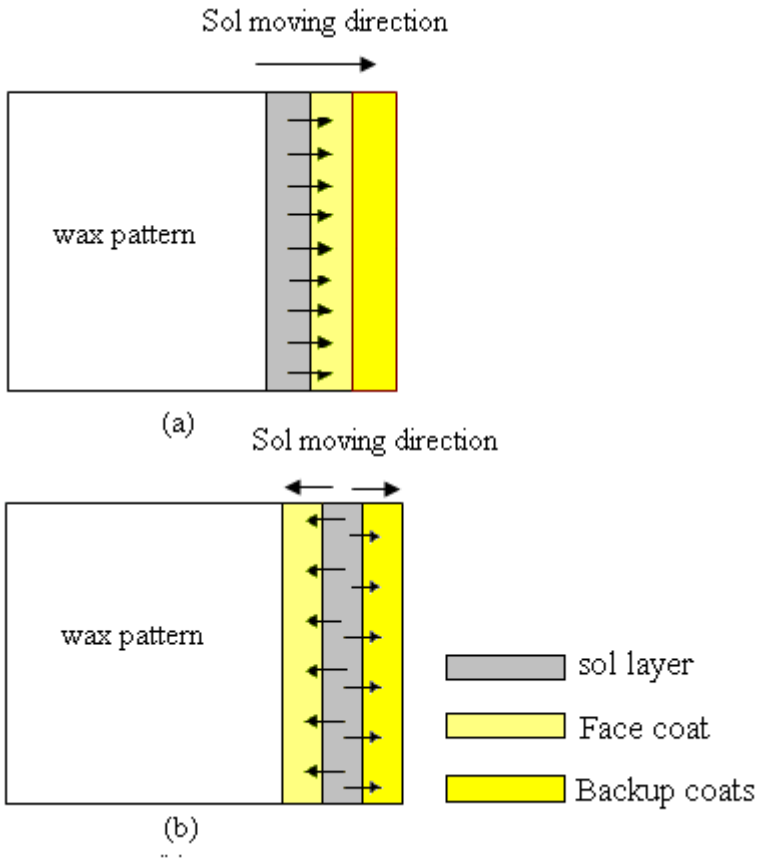

Figure 6-5.The new designed shell making process, (a) primary ‗sol' model, and (b) the ‗sol' backup penetrate model.

In the first method shown in Figure 6-5 (a), sol is first painted on the cleaned wax pattern, and then dried over night. Face coat slurry was then painted on the top of the sol pre-painted wax patterns, and allowed them to react and gel the face coat slurry. However, this method is very difficult to be used in manufacture due to the damage of the sol layer when applying the face coat slurry. Therefore, spraying slurry on the mould surface is the only valid method to be used in this method without damaging the sol layer. Another problem with this method is that pre-painted sol coat is too thin and can not effectively gel the surface of the face coat.

The second method (Figure 6-5(b)) seems more likely to be used with the dipping process without considering contamination. In this method the face coat was first painted on the wax patterns similar to the traditional shell making process, when it dried, sol was then painted on the top of the face coat and allowed to interact with face coat. However, in real industrial processing, after painting with the sol, the wetted face coat was easily slumping down after few minutes. Therefore, a new improvement to the backup sol penetration method was developed to overcome this problem, which is shown in Figure 6-6. This new improvement added an extra backup coat layer before the sol was applied, and the rest of production process was the same as the traditional shell making process. The details of this new method are shown in Table 6-1.

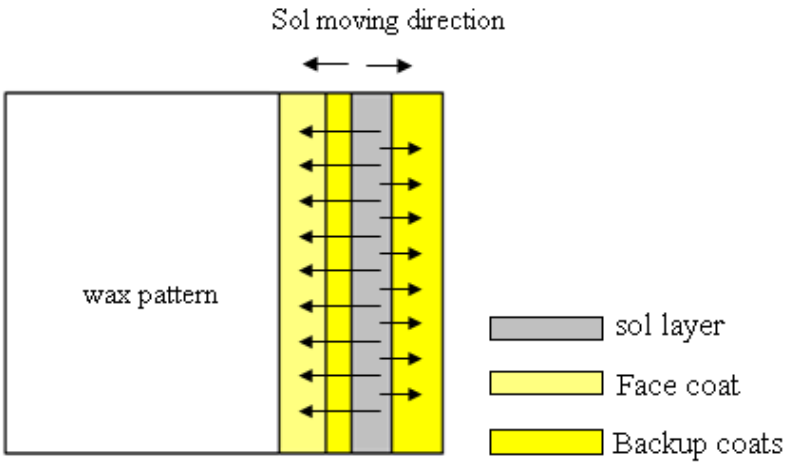

Figure 6-6. The new design of backup sol penetration method

Table 6-1.The coats making procedural.

Coats ID	Drying time
Face coat	Over night
Backup coat (1 layer)	1.5 hours
Sol	2 hours
Backup coat (7 layers)	1.5 hours

This method can be used for a variety of sols (e.g. yttria sol, Ti-coat sol, even Si-sol) without causing a gelation problem of the slurry. The more reactive the sol, the better the strengthening effect on the face coat. Sol can be applied by this new method by any method such as painting, spraying or dipping (preferably painting and spraying to prevent degradation of the sol). In this experiment, the high strength Ti-coat sol (Ammonium Zirconium Carbonate) was used to test the efficiency of the sol ‗back penetration' method, and the shell surface after de-wax and burn out wax at around 800 °C is shown in Figure 6-7. As can be seen, the mould internal surface showed a black/grey colour, and these colours come from the colour of ZrO_2 (from Ti-coat sol) at low firing temperatures, which means the sol has already penetrated from the backup coat into the front of the face coat. No peeling off and de-lamination of the face coat has been observed in this process.

(a)

(b)

(c)

Figure 6-7.The surface inside of the ⎽T‘ shape mould after sintering at 800 °C, (a) the cylindrical hole, (b) the right hand side of the mould, and (c) the left hand side of the mould.

After firing at 1000 °C for 3 hours, the mould internal surface is shown in Figure 6-8. As can be seen, the mould face coat surface was very uniform and smooth, no peeling off and

de-laminating of the face coat was observed.

(a)

(b)

(c)

Figure 6-8.The surface inside of the ‗T' shape mould after sintered at 1000 °C, (a) the cylindrical hole, (b) the right hand side of the mould, and (c) the left hand side of the mould.

As can be seen from the test results, by using the sol back penetration method, the mould shows a very good surface finish, which can be used as an investment casting mould to produce TiAl alloy components.

6.2.4 The friability of the shell

The friability of the face coat after using the sol ‗back penetration' method was tested and shown in Table 6-3 compared to the reference slurry face coat friability (reported in Chapter 4), in Table 6-2

Table 6-2. The friability of the shell sintered at different temperatures.

Sample ID	Friability (g/m^2) at different temperatures		
	1000 °C	1200 °C	1400 °C
Yttria+Sol (Y+S)	**48.2** ± 5.7	**12.91** ± 2.6	**3.12** ±0.7
Yttria+Sol+Polymer(Y+S+P)	**25.81** ±5.5	**11.29** ±2.1	**3.06** ±1.7
Yttria+Water+Polymer (Y+W+P)	**54.42** ±32.3	**19.58** ±19.6	**3.16** ±2.11

Table 6-3. The friability test results of different sol using sol ‗back penetration' method at different temperatures.

Sample ID	Friability (g/m^2) at different temperatures		
	1000 °C	1200 °C	1400 °C
Y+W+P (Ti-coat backup penetrate)	**15.42** ±3.70	**15.99**± 10.4	**8.43**±2.58
Y+W+P (Yttria sol back penetrate)	**41.15**±17.44	**18.27**±5.88	**6.5**±0.88

From Table 6-3 it can be seen that, by using the sol backup penetration method, the friability of the pure yttria water based binder slurry improved a lot without adding any sintering aids. The enhanced sintering properties from the Ti-coat and yttria sol may be due to the strengthening effect of the sol. The ‗sol back penetration' method separated the face coat slurry process and strengthening process, and the resulting face coat exhibits a reasonable strength without influence the slurry life.

Part II, Si penetration from the backup coat

6.3 Si Penetration

This is based on the results reported in Chapter 5, and developed the understanding of the Si penetration mechanism from the backup coat to the face coat and subsequent interaction with the molten TiAl during the sessile drop casting process. The research in this part will mainly focus on the background introduction of the Si backup penetration problems, the analysis of Si penetration mechanisms and the influence on the new designed slurry and production methods.

6.3.1 Background introductions

Due to the heavy interaction between TiAl and the face coat material during the high temperature casting process, mould face coats based on SiO_2 have been restricted to the backup coat slurries for many years due to the low chemical inertness of this oxide. But considering the material cost, silica based filler and stucco have still been used in the secondary or backup coats. High temperature shell sintering will cause the reactive Si from the backup coat to penetrate to the face coat and react with the TiAl alloy during the casting process [198]. The penetrated Si also increases the oxygen absorption of the TiAl alloys and causes huge damage at the metal/shell interface areas [181].

This problem was first observed when abnormal wetting behaviour of one sessile drop sample was observed. By studying the cross section of this sample, some high Si containing

interaction products were found forming along the (α_2+γ) grain boundary using YAZ face coat, see Figure 6-9 and Figure 6-10.

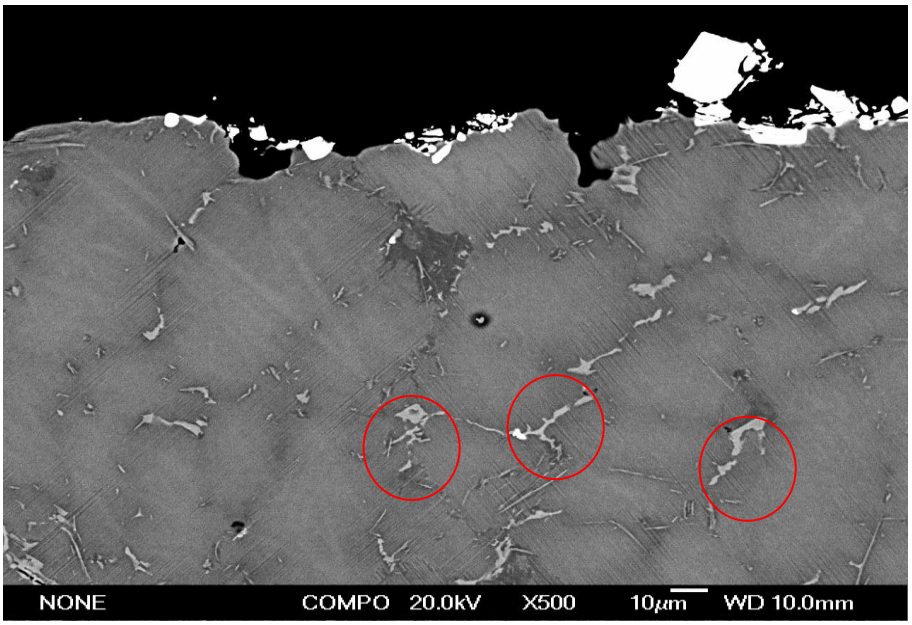

Figure 6-9. High Si containing interaction products forming along the grain boundaries of sample which used YAZ face coat reacted at 1650 °C in 50 s (from sessile drop test).

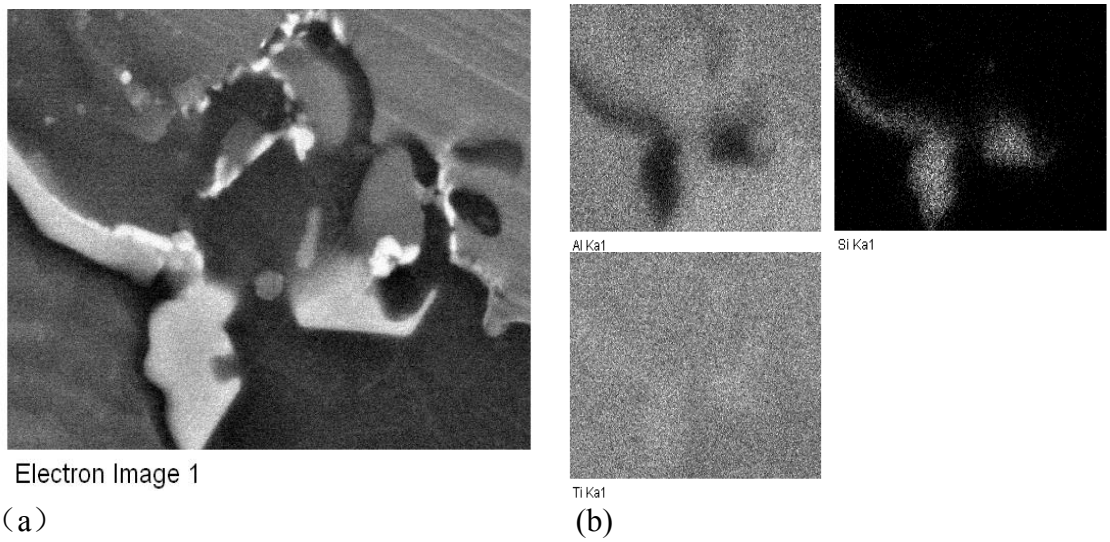

（a） (b)

Figure 6-10. EDX mapping analysis of the inter-metallic phase (a) Backscatter of the intermetallic phase, and (b) the composition distribution of elements

The EDX shows that these light phases contain around 45.92 at% of titanium, 12.78 at% of aluminum, and 16.73 at% of silicon. These high Si containing phases have also been observed by Q. Jia [47] using a CaO stabilized ZrO_2 mould. By using transmission electron microscopy (TEM) to analyze the crystal structure of these phases, it was found that the light phases were Ti_5Si_3.

Not only was very high silicon concentration detected in the reaction layer, but also high amounts of oxygen were found along with the Si-rich precipitates. Because oxygen is the alpha phase stabilizer, it influences TiAl solidification behaviour, therefore, the solidification of TiAl alloy changes from the β phase region to α, and shows a very strong dendritic microstructure at the cross section area [182]. Therefore, the Si diffusion problem should be carefully considered during the casting and mould making process to avoid this extra interaction between the molten TiAl alloys and the mould.

6.3.2 Shell surface microstructure

The face coat surface morphologies using different face coats were detected at different sintering temperatures and are shown in Figure 6-11.

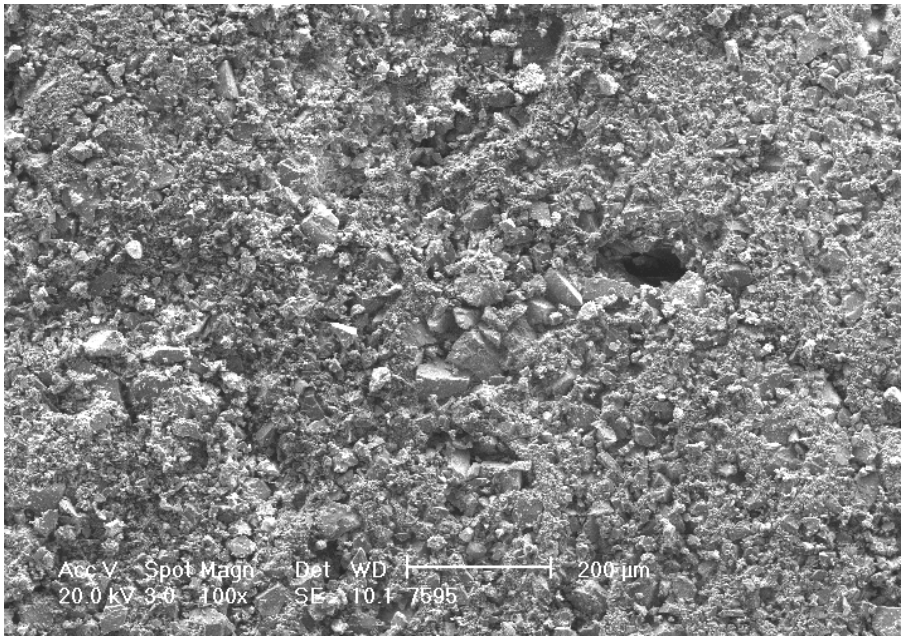
Acc.V Spot Magn Det WD 200 µm
20.0 kV 3.0 100x SE 10.1 7595

(a)

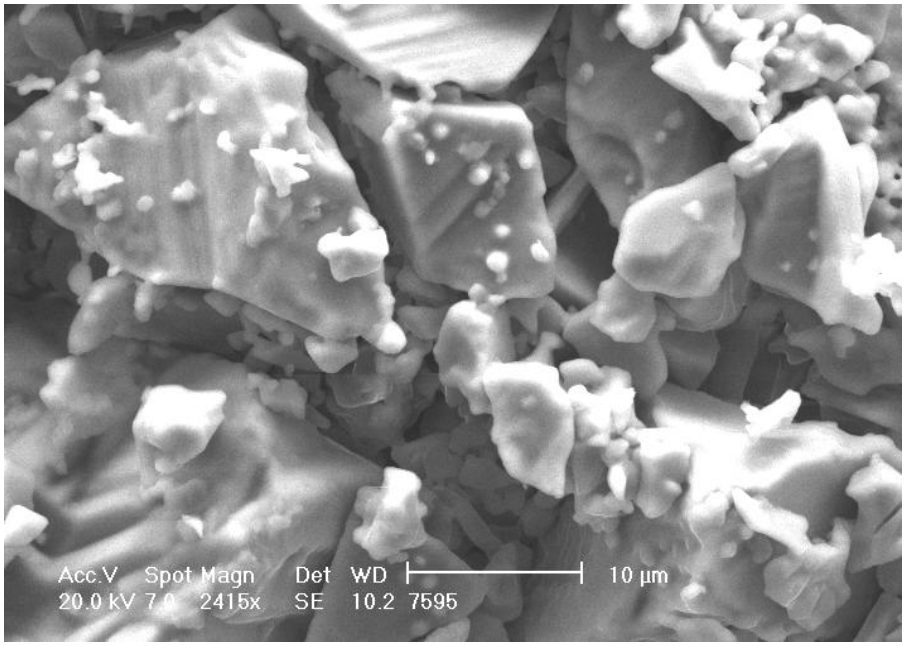
Acc.V Spot Magn Det WD 10 µm
20.0 kV 7.0 2415x SE 10.2 7595

(b)

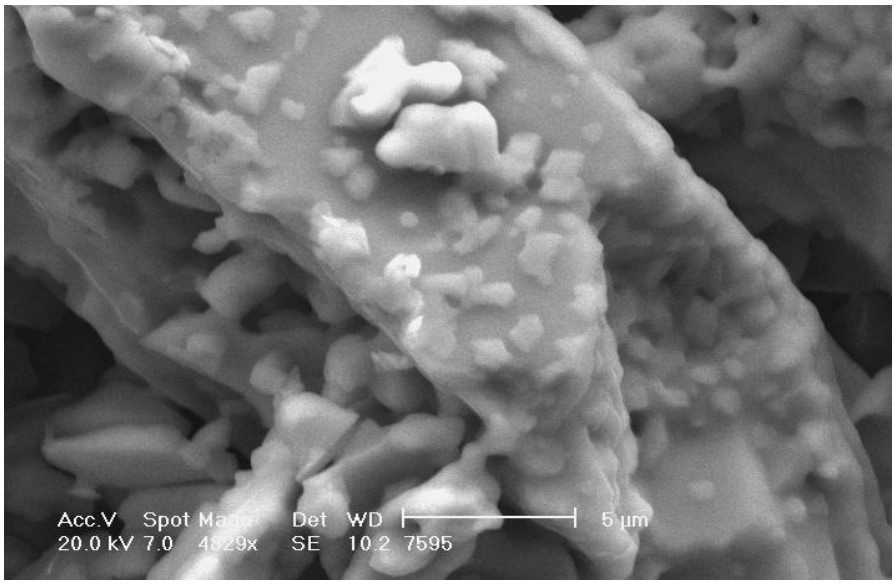

(c)

Figure 6-11. The secondary electron image of the face coat surface of the YF 0.15 shell surface sintered at 1550 ºC for one hour (a) ×400, (b) ×2415, and (c) ×4829.

It can be seen from Figure 6-11 that the mould face coat surface microstructure looks very similar to the face coat slip casting sample in Chapter 4. The powder particles are distributed uniformly with the small particles filling the gaps between large particles. Even after sintering at 1550 °C for one hour, the shell face coat structure was still very open. The gaps between particles may provide the diffusion channel for Si to penetrate from the backup coat to the face coat.

6.3.3 The Si concentration on the different shell surfaces

Table 6-4 and Figure 6-12 show the influence of the sintering aids on Si penetration at different sintering temperatures. As can be seen, the sample surface Si concentrations are different for different face coats at the same sintering temperatures. Except for the yttria +sol system, all the ceramic shells have the highest Si concentration at sintering temperatures

around 1200 °C and 1400 °C, and the smallest Si concentrations were detected after moulds were sintered at 1550 °C for one hour.

Table 6-4: The surface Si (wt%) concentration of different face coat system.

Sample ID	1200 °C	1400 °C	1550 °C
Yttria + sol	**0.70±0.06**	**0.85±0.18**	**0.95±0.21**
Industry used F-doped slurry	**2.69±0.61**	**2.55±0.61**	**0.81±0.15**
YB 0.15	1.04±0.29	1.63±0.54	0.97±0.15
YAZ	1.92±0.27	2.15±0.68	2.04±0.35
YF 0.15	1.97±0.21	2.36±0.36	1.77±0.25
YT 2.0	2.20± 0.41	2.70 ± 0.71	1.03 ± 0.23

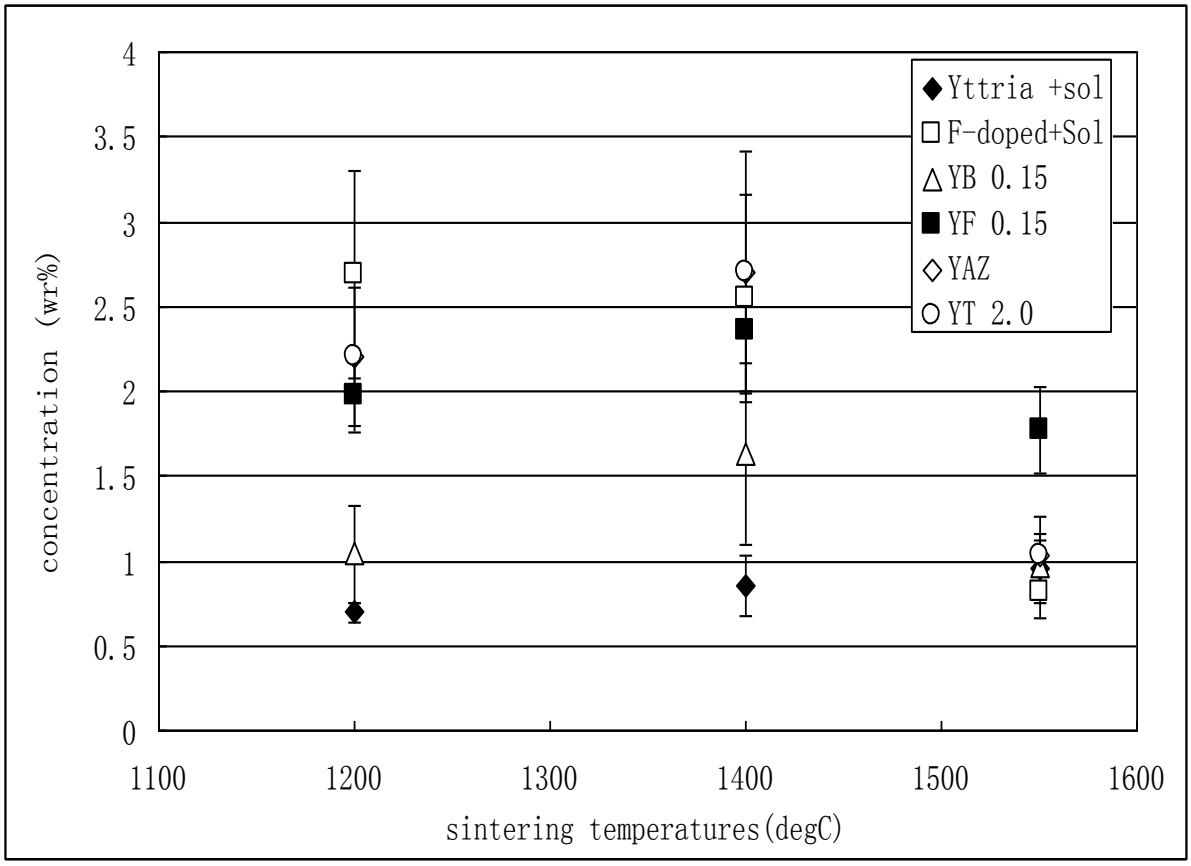

Figure 6-12. Si concentration on different face coat surfaces sintered at different temperatures.

The Yttria +sol system has the smallest Si concentration detected at all temperatures followed by the YB 0.15 system. Using YAZ face coat, very high Si concentrations were detected at a temperature of 1550 °C. The industry standard F-doped face coat shell had around 2.69 wt% Si detected on the surface when sintered at 1200 °C, which means that this small amount of Si on the shell surface does not influence the cast component properties. From the data, it seems that the sintering aids in the face coat will promote Si diffusion into the face coat layer. But the entirely new designed face coat samples have lower surface Si concentration than the industry standard sample, therefore, the new developed slurries can be used as the face coat for investment moulds to cast TiAl alloy.

The Si penetration amount on each face coat surface seems related to both the type of sintering additives and sintering temperatures. As can be seen from the yttria face coat system (Yttria + sol), increasing the sintering temperature caused more Si to diffuse into the face coat. If the silicon penetration is a thermally activated diffusion process, by plotting silicon concentration Log (C) against 1/T, and from the intercept of the Arrhenius relationship, the diffusion activation energy of Si ions in the yttria face coat can be calculated, see Figure 6-13.

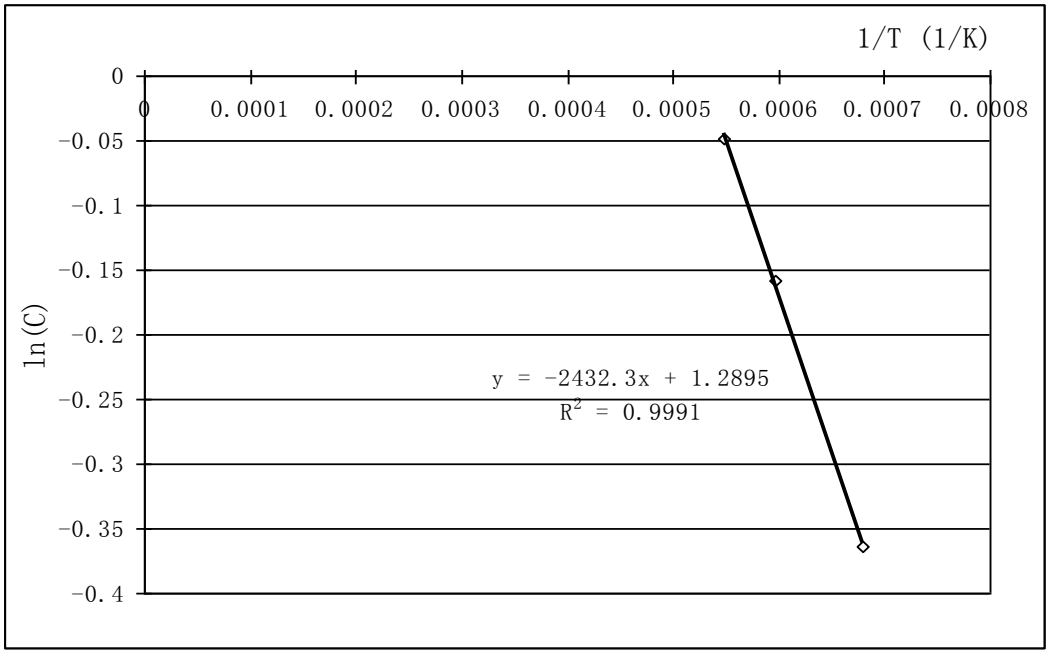

Figure 6-13. The Arrhenius Relationship of the Si concentrations on the Yttria +sol mould surface at different sintering temperatures.

The Si diffusion activation energy in the yttria +sol face coat surface calculated from this experiment is around 20 kJ/mol. Unfortunately, there is no published data to confirm the activation energy of silica in yttria.

By adding sintering additives into the slurry, the detected Si concentration is varying with different face coat systems at the same sintering temperature. This phenomenon may be explained by the sintering additives increasing the diffusivity of Si in the face coat. But at high temperatures around 1550 °C, the face coat with sintering additives will undergo a very quick densification, which may retard the Si penetration and result in a decrease in the Si concentration on the mould surface.

6.3.4 XRD of the shell surface

The Si in the face coat also can be detected by using XRD. Figure 6-14 shows different shells with only one layer of face coat sintered at temperatures of 1200, 1400 and 1550 °C. As can be seen from the standard Yttria+sol and YB 0.15 sample, by increasing the sintering temperature, the Y_2SiO_4 peak intensities increase. But for sample YT 2.0, a very strong Si peak was detected using YT 2.0 face coat after sintering at a temperature of 1200 °C, similar to the EDX analysis results in Table 6-4.

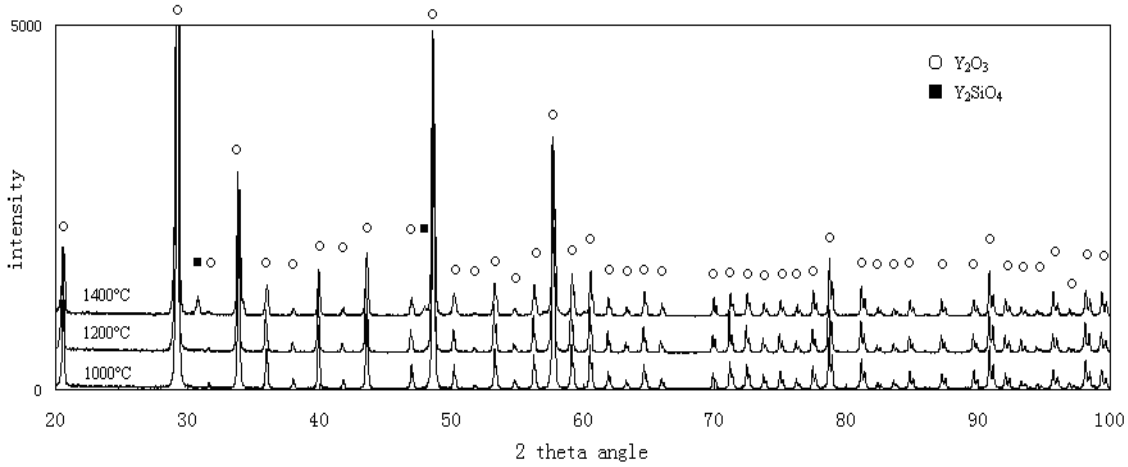

(a)

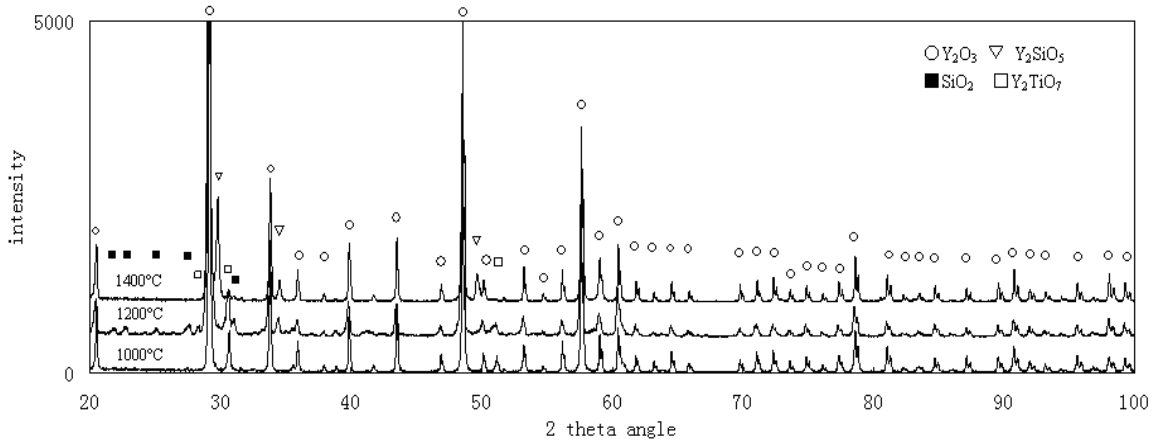

(b)

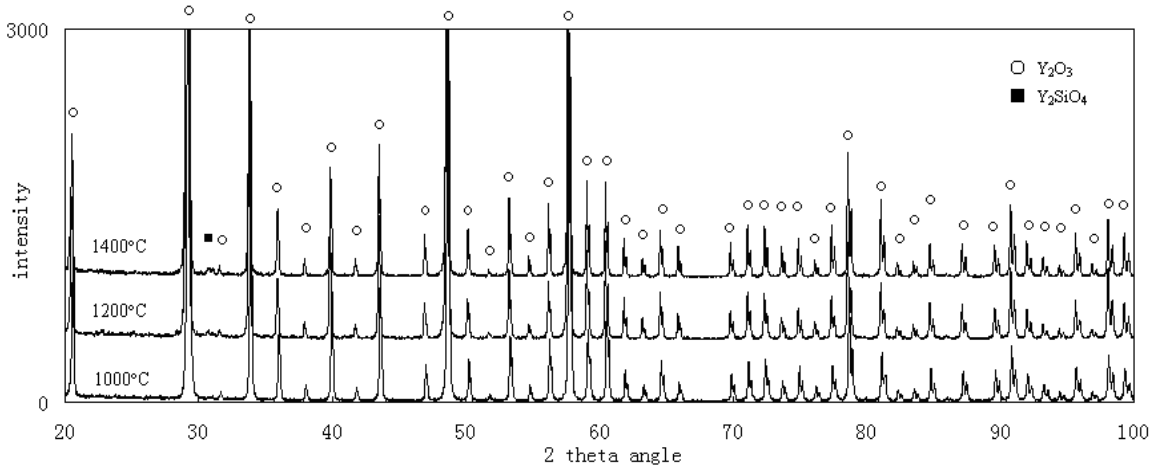

*because only 0.15wt% B_2O_3 in this face coat, it is very difficult to detect Y_xBO_y phase peaks

(c)

Figure 6-14. The surface composition of the different face coats: (a) Yttria +sol, (b) YT 2.0 face coat, and (c) YB 0.15 face coat.

6.3.5 Si penetration problems by using sol 'back penetration' method

The new developed mould production methods used sol back penetration from the backup coat to the face coat. The gelation will cause strengthening in the face coat during the de-wax process. However, this new method may cause Si ions to penetrate from the backup coat to the face coat before shell sintering.

Sample moulds were made by the sol back penetration methods. These moulds were then cut through the cross section of the shell pieces, and the Si penetration distances were tested by selecting a rectangular area using EDX. Figure 6-15 below shows an example of the shell cross section and the selected rectangular areas from the face coat surface to the backup coat.

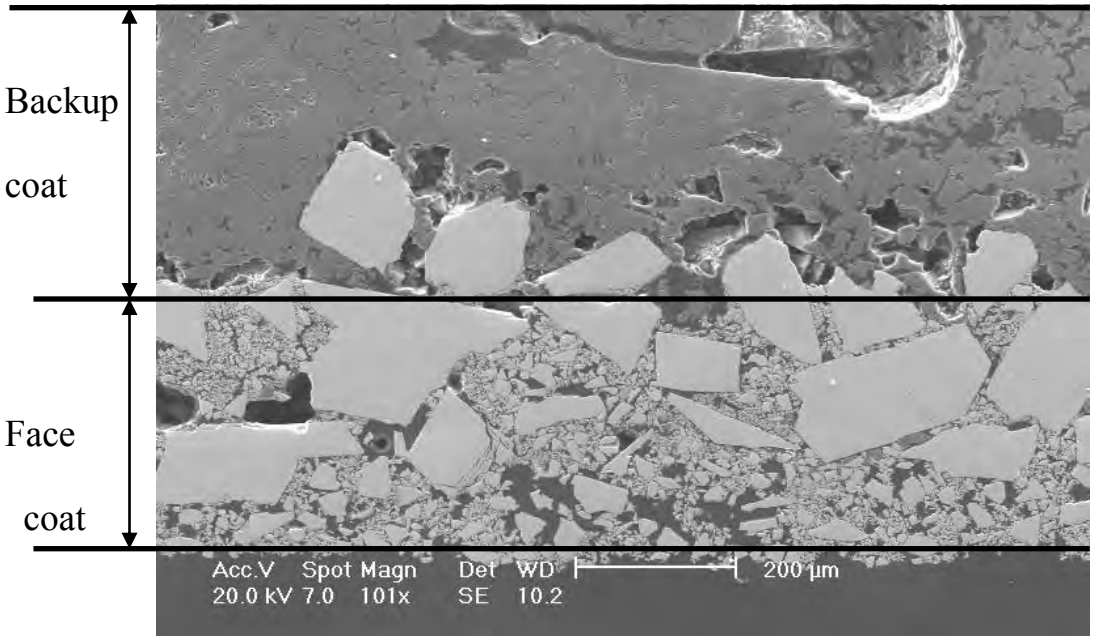

(a)

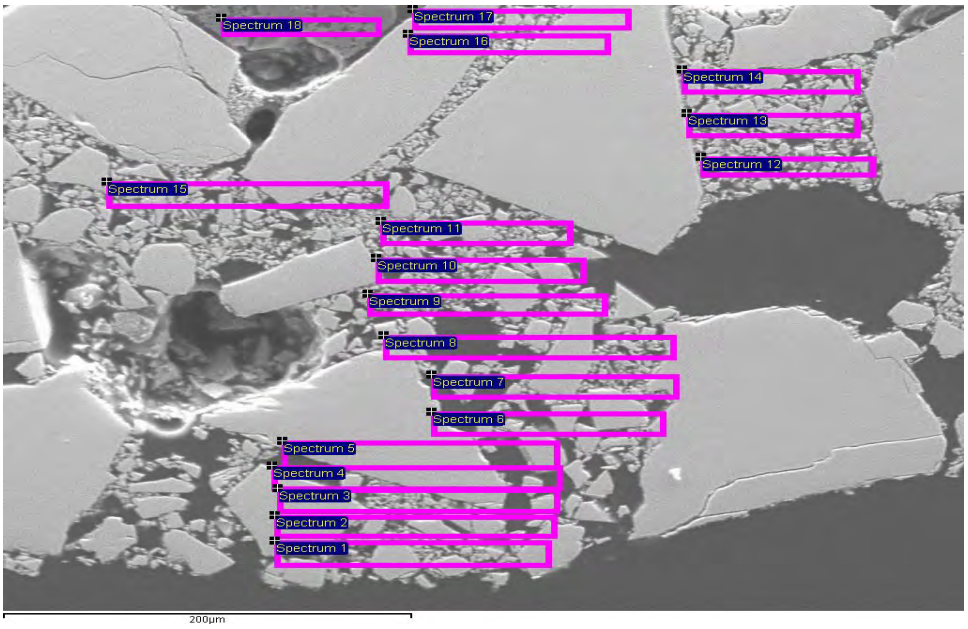

(b)

Figure 6-15. Image of the cross section of the shell: (a) the cross sectional microstructure of the shell, and (b) the selected area of analysis.

The interfacial Si distribution and penetration distance using the yttria and Ti-coat sol back penetration methods compared to the face coat using Ti-coat sol as the binder are shown in Figure 6-16 after sintering at different isothermal temperatures for one hour.

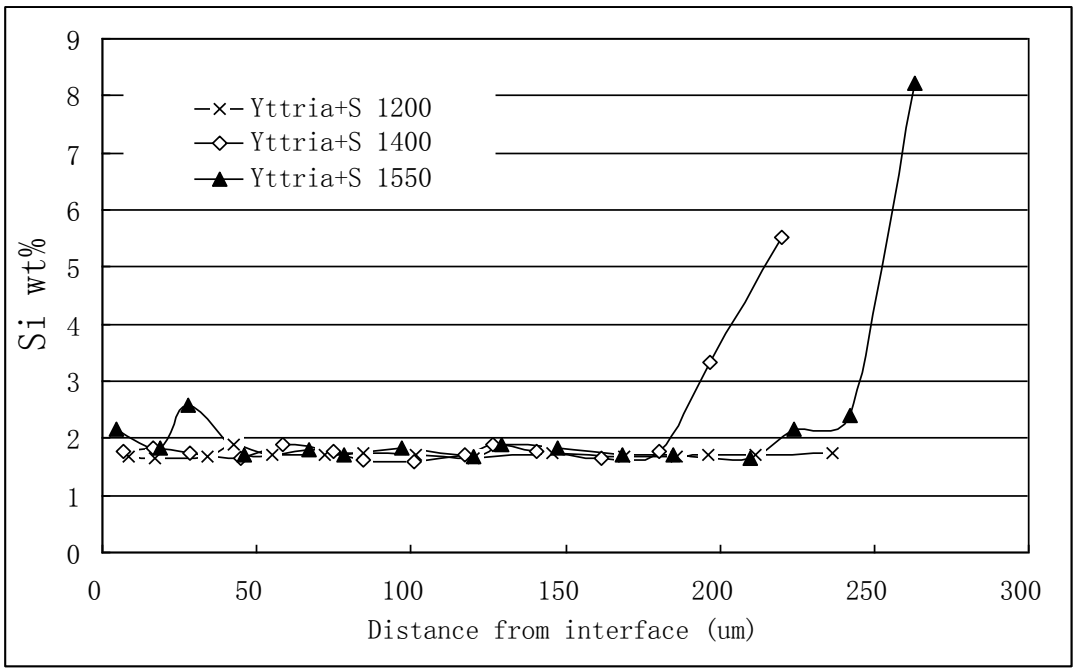
Yttria+S 1200
Yttria+S 1400
Yttria+S 1550
Si wt%
Distance from interface (um)
0
1
2
3
4
5
6
7
8
9
0
50
100
150
200
250
300

(a)

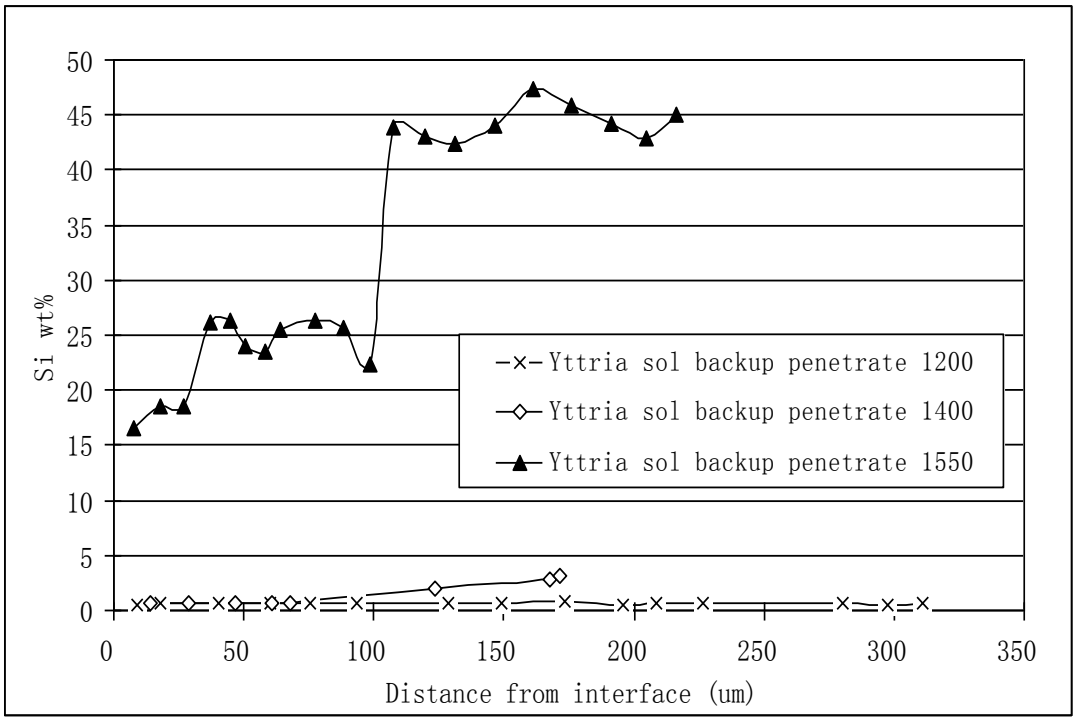
Yttria sol backup penetrate 1200
Yttria sol backup penetrate 1400
Yttria sol backup penetrate 1550
Si wt%
Distance from interface (um)
0
5
10
15
20
25
30
35
40
45
50
0
50
100
150
200
250
300
350

(b)

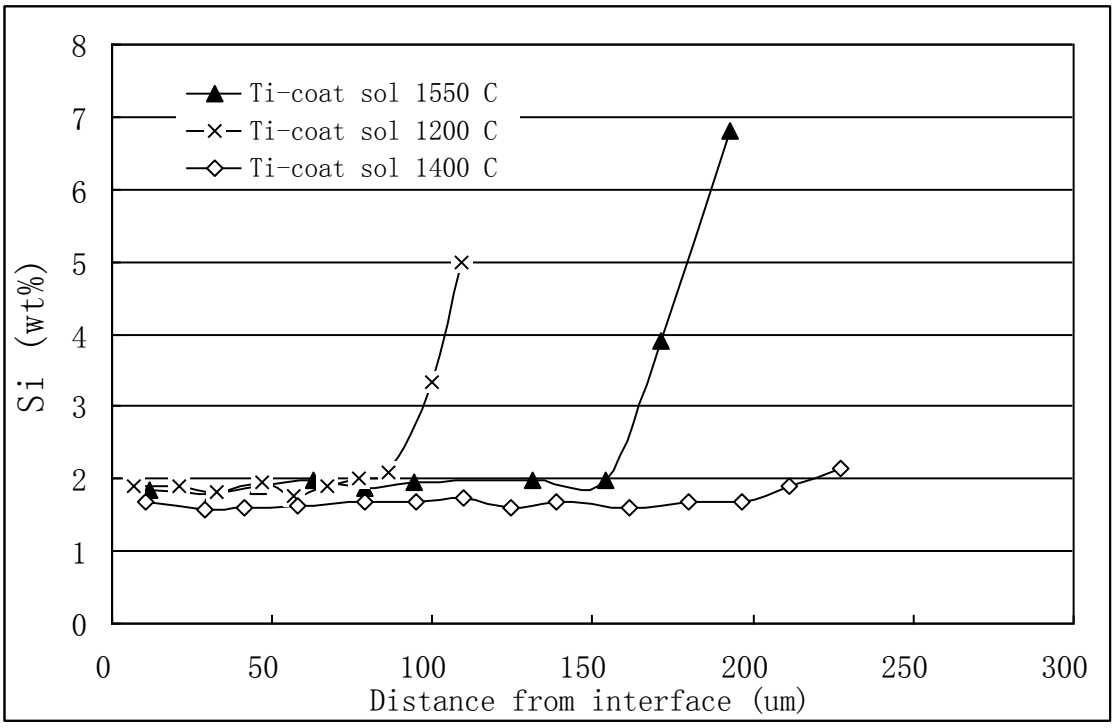

(c)

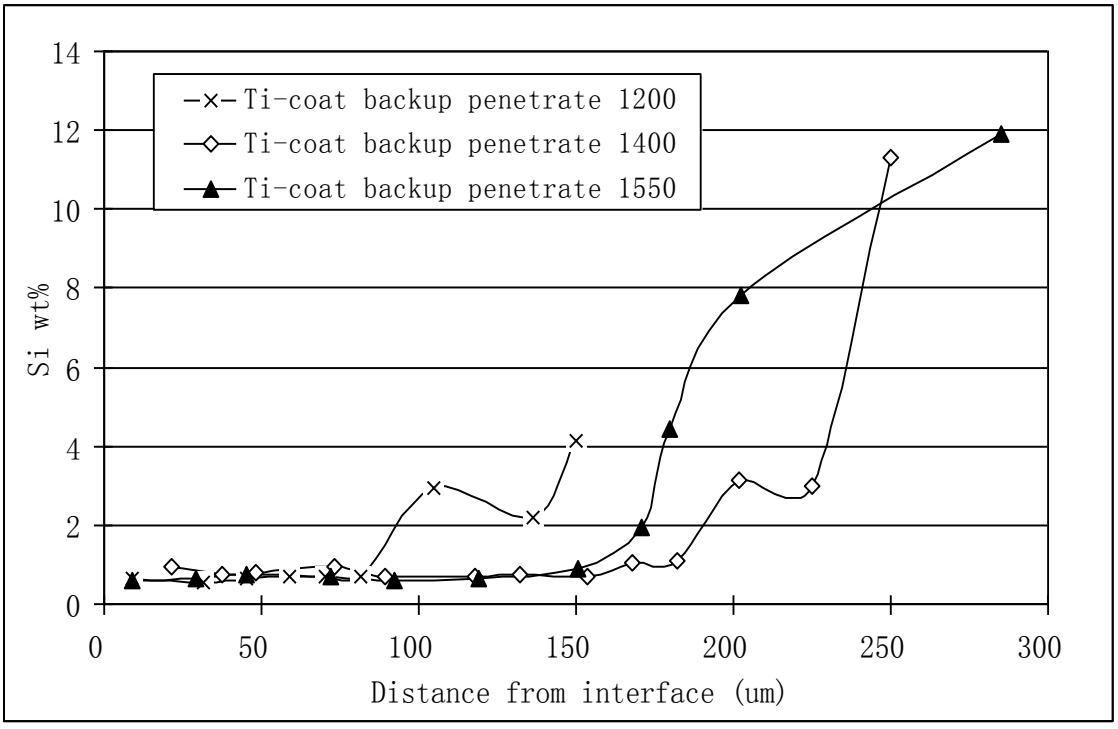

(d)

Figure 6-16. The Si penetration distance across the face coat at different temperatures.(a) yttria sol based binder face coat, (b) the water based binder based slurry with yttria sol backup penetrate, (c) Ti-coat sol based binder face coat, and (d) the water based binder slurry with Ti-coat sol backup penetrated.

As can be seen from Figure 6-16, the silica penetration distance from the backup coat into the face coat increased with increasing sintering temperature due to the high activity of the Si ions at higher temperatures. Compared to the sol based face coat slurry, using backup penetration method, an increased Si concentration was detected on the face coat surface at the same sintering temperatures. The largest diffusion distances of Si have been found in samples with Yttria sol back penetration after firing at 1550 °C for one hour. Therefore, in order to avoid Si penetration, the shell using yttria sol back penetration methods can only be used for sintering at temperatures below 1400 °C in order to avoid too much Si diffusing into the face coat. Using Ti-coat sol in the backup penetration method seems to have a shorter Si penetration distance, and high temperature sintering only causes a slight increase of Si. The percentage Si penetration distances calculated from Figure 6-16 for the different moulds are shown in Table 6-5 and calculated using equation 6-1:

$$\%\text{Si penetration distance} = \frac{d_{Si}}{d_{facecoat}} \times 100\% \qquad 6\text{-}1$$

where, d_{Si} is the Si penetration distance (μm), $d_{facecoat}$ is the total thickness of the face coat (μm).

Table 6-5.The %Si penetration distance of the Sol based back penetrate mould at different firing temperatures.

Sample ID	1000 °C	1200 °C	1400 °C	1550 °C
Yttra sol back penetrate	58.66 %	59.2 %	60.2 %	All react
Yttria sol based slurry	not observed	not observed	18.2 %	20.2 %
Ti-Coat sol back penetrate	34.2 %	45.3 %	38.4 %	47.1 %
Ti-coat sol based slurry	not observed	21.1 %	13.6 %	20.2 %

Therefore, comparing the backup penetration methods, there is not too much difference in

the Si penetration distance using Ti-coat and yttria sol in the slurry (~20% at 1550 °C). But when using back up penetration method (after sintering at 1550 °C), Si penetrated into nearly half of the face coat thickness (around 125 μm if the face coat is 250 μm thick) using Ti-coat sol, and fully penetrated into the face coat using yttria sol. Using yttria sol, even sintered at very low temperatures around 1000 °C, the Si can still penetrate more than half way through the face coat (58.66 % of the face coat thickness). Therefore, this kind of shell should be used carefully even at low sintering temperatures.

6.3.6 Shell cross section images

According to the Si concentration and microstructures, the cross section of the ceramic shell can be generally divided into three different regions from the shell surface down to the backup coats. They are: the un-reacted region, the reacted region and the backup coat, see Figure 6-17 (a). The layer in light colour is the face coat, and the layer in grey colour is the backup coat. As can be seen, the face coat cross sectional microstructure is different for different mould types and sintering temperatures. High sintering temperatures cause an increase in the reaction region thickness. Moulds using yttria sol back penetration show more obvious interaction taking place than moulds using Ti-coat sol. (e.g. Figure 6-17 (b)).

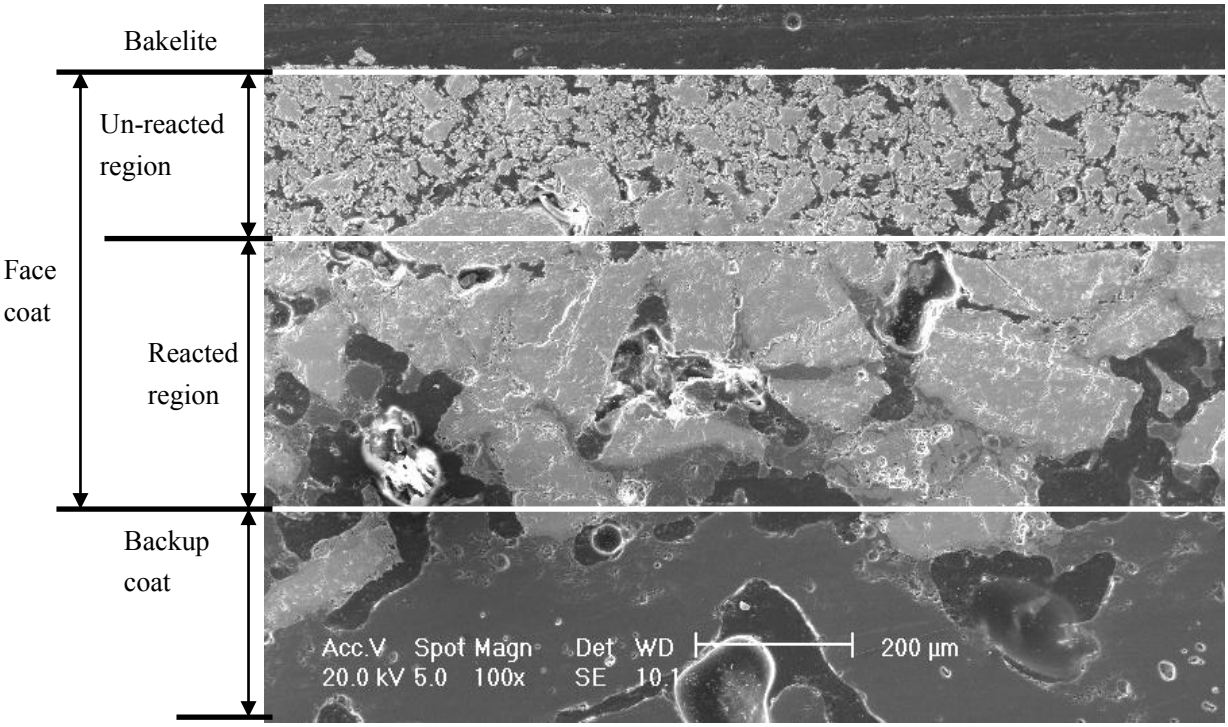
Bakelite
Un-reacted region
Face coat
Reacted region
Backup coat
Acc.V Spot Magn Det WD 200 µm
20.0 kV 5.0 100x SE 10.1

(a)

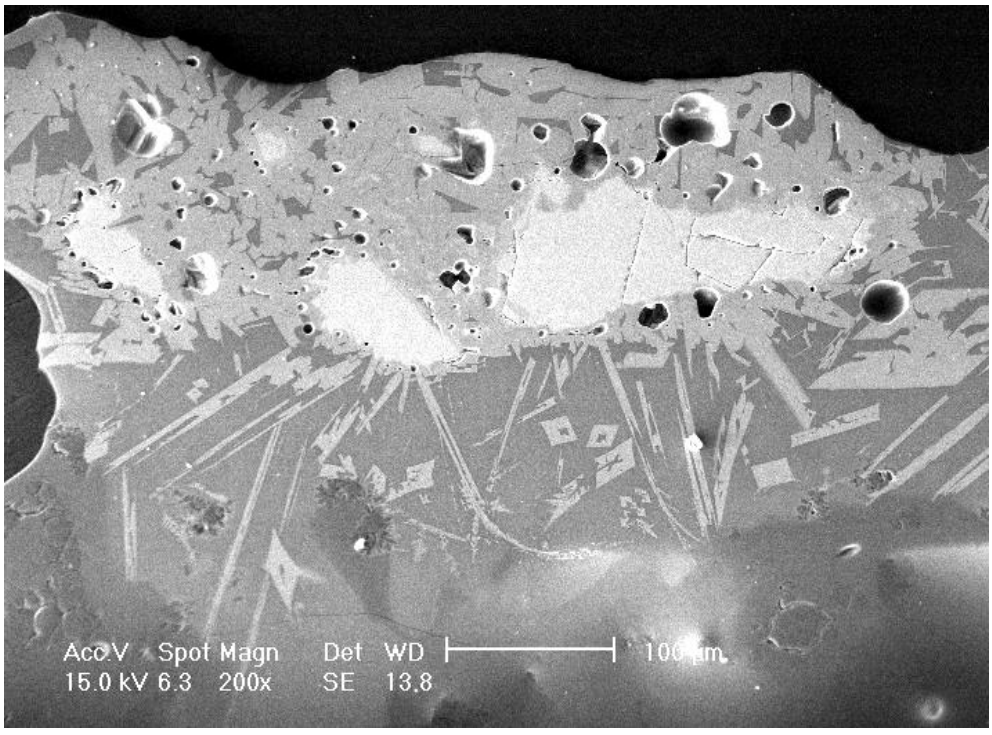
Acc.V Spot Magn Det WD 100 µm
15.0 kV 6.3 200x SE 13.8

(b)

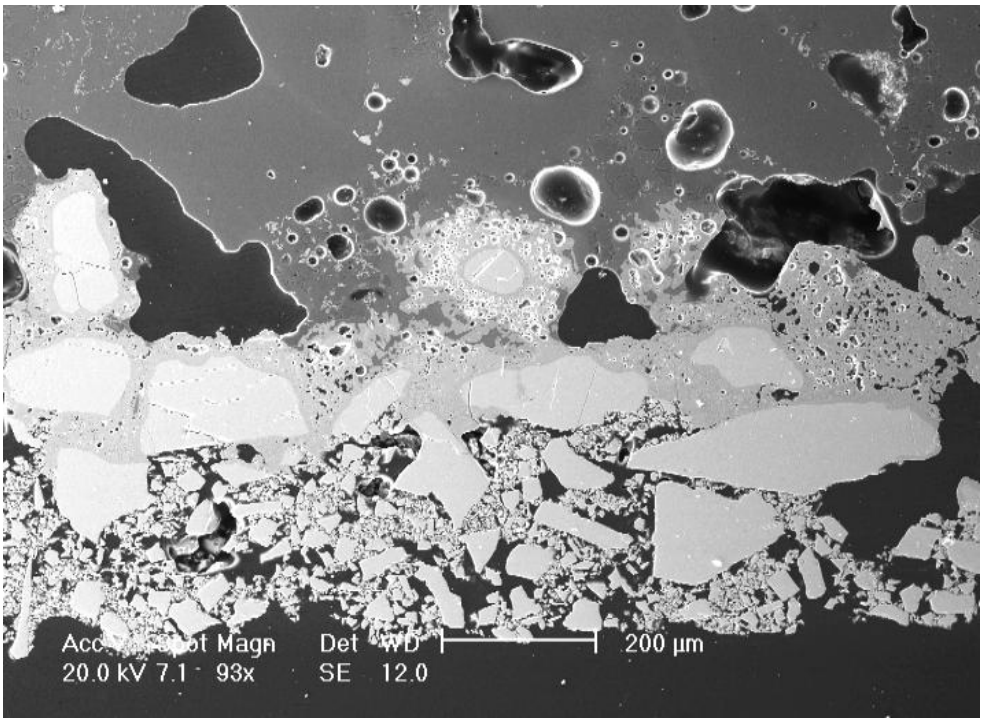

(c)

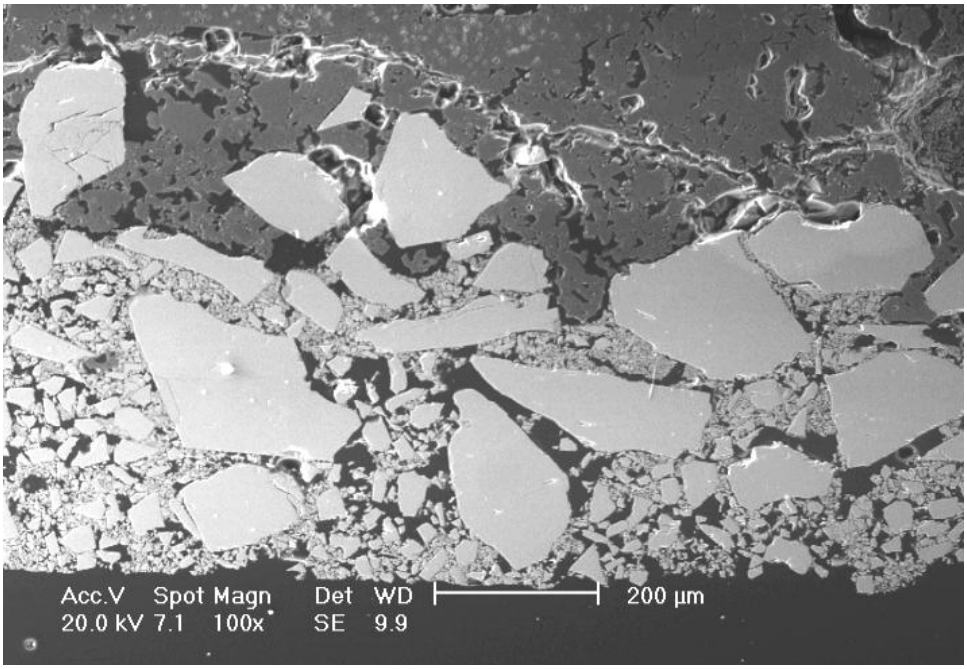

(d)

Figure 6-17.The cross sectional microstructure of the shell, (a) Ti-coat sol back penetration shell sintered at 1550 °C for one hour, (b) yttria sol back penetration sintered at 1550 °C for one hour, (c) Ti-coat back up penetrate shell sintered at 1550 °C for one hour and (d) Ti-coat sol backup penetration shell sintering at 1200 °C for one hour.

The EDX analysis showed that there was very high Si detected at the reacted region between the face coat and the backup coat in Figure 6-17(b), and the detected area and element concentrations are shown in Figure 6-18 and Table 6-6. The thickness of this reaction region depended on the sintering temperatures.

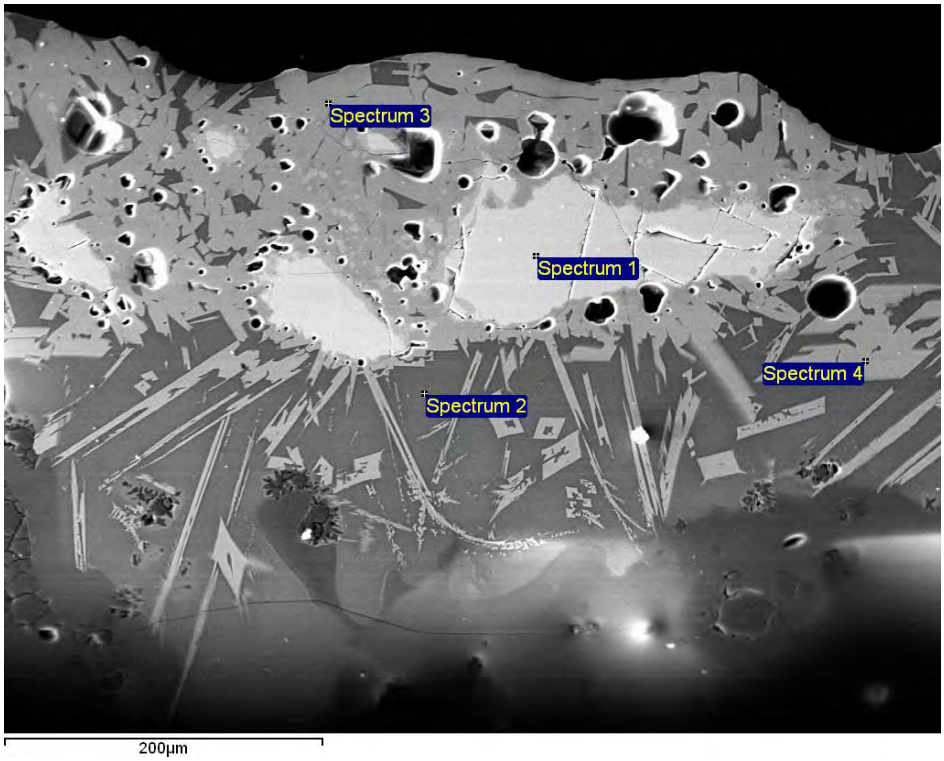

Figure 6-18. The EDX Spectrum of the reacted layer of a sample using yttria sol back penetration sintered at temperature 1550 °C.

Table 6-6. The composition of the fused yttria area (wt%).

Elements	Si	O	Y	Al
Spectrum 1		20.82	79.18	-
Spectrum 2	25.16	43.09	21.86	9.89
Spectrum 3	**17.03**	**29.78**	**52.94**	0.25
Spectrum 4	**52.51**	**30.74**	**16.75**	-

From the EDX composition, the new phase formed at this area is likely to be an Y_2SiO_5

phase detected in XRD results in Figure 6-14 (a).

6.4 Conclusions

1. After firing at different temperatures, Si was found on the shell face coat surface. By considering the composition of the face coat and firing conditions, the only source of this Si is from the backup coats. The amount of Si penetration from the backup coat to the face coat is dependent on three factors; firing temperature, sintering additives and production process.

2. Sintering additives such as ZrO_2, Al_2O_3, etc may enhance the diffusivity of Si in the face coat during the firing process, and the Si concentration found at different face coat surfaces decreased as: YAZ>YF 0.15>YB 0,15>pure yttria.

3. By using the sol back penetration methods to strengthen the face coat, the Si concentration on the shell surface was found to increase with increasing firing temperatures. Compared to yttria sol, using Ti-coat sol had a shorter Si penetration distance and it is possible to use it in industrial applications.

Chapter 7 Investment casting of Titanium aluminide alloys

This section focus on using the new water based slurry and the 'sol back penetration' method to make investment casting shells. The interaction between the new face coat and molten metal has been indentified and compared with the predictions based on the sessile drop test results in Chapter 5.

7.1 Sample preparation

7.1.1 Wax mould preparations

In order to cast the TiAl alloy and compare the interaction between different face coats, an investment casting mould was designed, see Figure 7-1. The mould consisted of a large cylindrical downsprue and four vertical test bars (1.5 cm diameter and 20 cm height) connected via a bottom gating system.

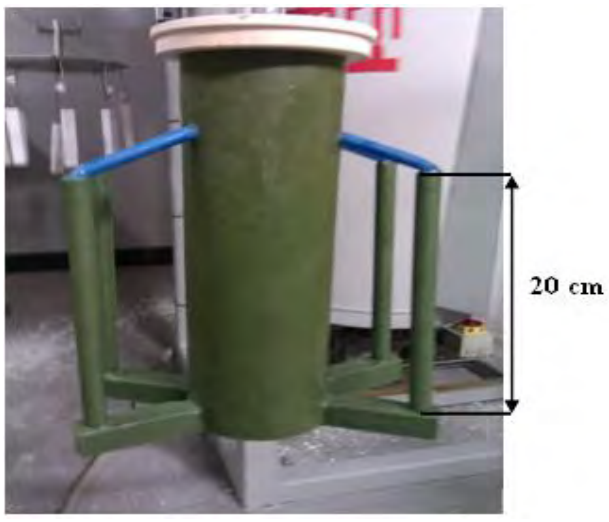

Figure 7-1. The test mould wax assembly

7.1.2 Face coat slurry preparations and mould manufacture

The face coat slurry and mould making process are described in Chapter 6, and the face coat slurry formulations are shown in Table 7-1. All the slurries were blended for at least 2 days to ensure a uniform composition before use. During shelling, different face coat formulations were applied to each test bar and then backed up with the Al_2O_3-SiO_2 based slurry.

Table 7-1. The face coat slurry compositions.

Sample ID	Filler	Binder	Wetting agent	Anti-foam
Wt% in slurry	80 wt%	19.8wt%	0.15 wt%	0.05 wt%
YB	Yttria+ 0.15wt%B_2O_3	Cellulose water solution	Victawet 12	Burst RSD-10
YF 2.0	Yttria + 2.0wt% YF_3	PV alcohol water solution	Victawet 12	Burst RSD-10
YAZ	Commercial YAZ	PV alcohol water solution	Victawet 12	Burst RSD-10
Yttria +sol	-200 mesh pure yttria powder	PV alchol + yttria sol	Victawet 12	Burst RSD-10
F-doped	F-doped powder (Tribachelaer TM)	Ti-coat sol	Victawet 12	Burst RSD-10

* Yttria+ sol is the industry standard shell for casting TiAl alloys
F-doped is a recent industry shell system.

After de-waxing in a Boilerclave, shells were fired at 1200 °C for 3 hours. Vents introduced into the base of the downsprue to assist de-waxing were sealed using fireclay and allowed to dry for at least one day prior to casting, see Figure 7-2. A total of three moulds were invested examples of which are shown in Table 7-2.

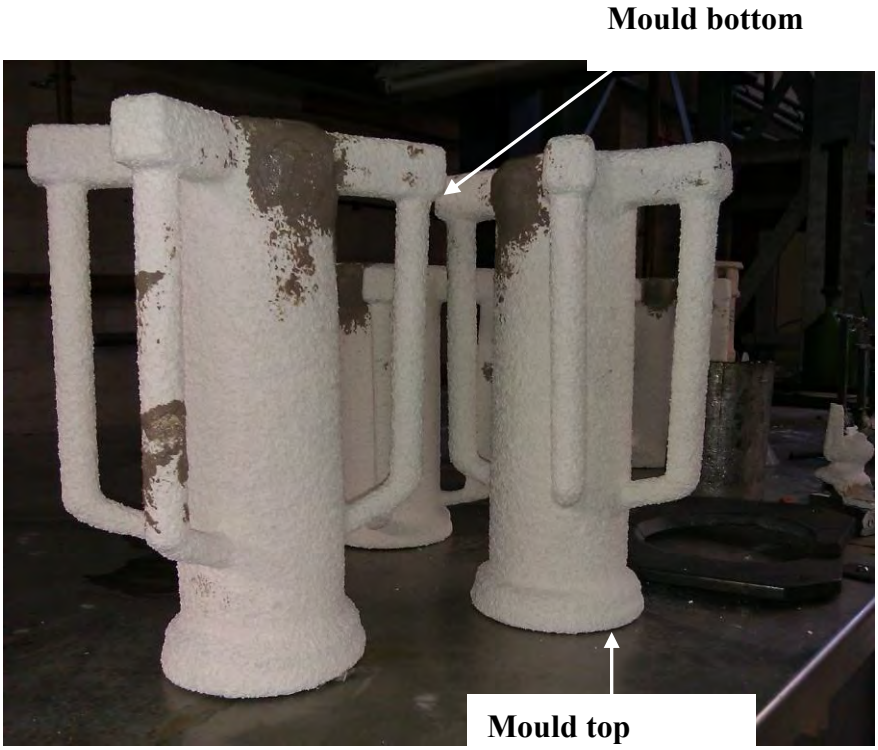

Figure 7-2. Test moulds after firing and sealing

Table 7-2. Face coat compositions used in the three test moulds

Mould ID	Bars number with the face coat composition			
	No. 1	No. 2	No. 3	No. 4
Mould 1	Yttria+ sol	YF 0.15	YAZ	YB 0.15
Mould 2	Yttria+ sol	YF 0.15	YAZ	YB 0.15
Mould 3	Yttria +sol	F-doped	YAZ	YF 0.15

*Mould 1 and 3 had two layers of the face coat
Mould 2 had a single layer of the face coat

7.1.3 Centrifugal casting and mould knockout

The ceramic shells were pre-heated to around 1000 °C. The alloy used in this experiment had the same composition as the sessile drop test, and it was melted using an Induction Skull Melting (ISM) furnace at temperature around 1600 °C as shown in Figure 7-3(a). The metal was gravity poured into a mould, which rotating at 400 rpm on a rotating platform. After

moulds had cooled down, the ceramic shell was mechanically removed as shown in Figure 7-3 (b).

(a)

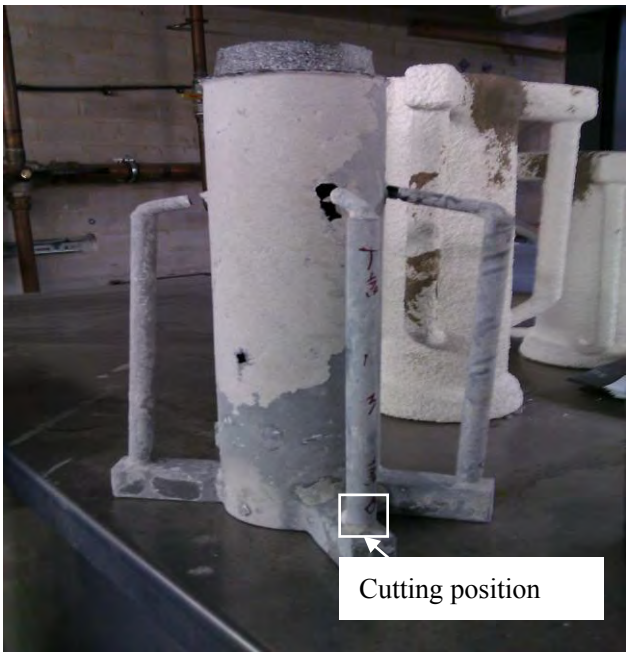

(b)

Figure 7-3. (a) Investment casting ISM furnace, (b) the mould after removal of the ceramic shell.

7.2 Results and discussion

7.2.1Images of the bars bottom

The bars, after removal of the outside shells, are shown in Figure 7-4.

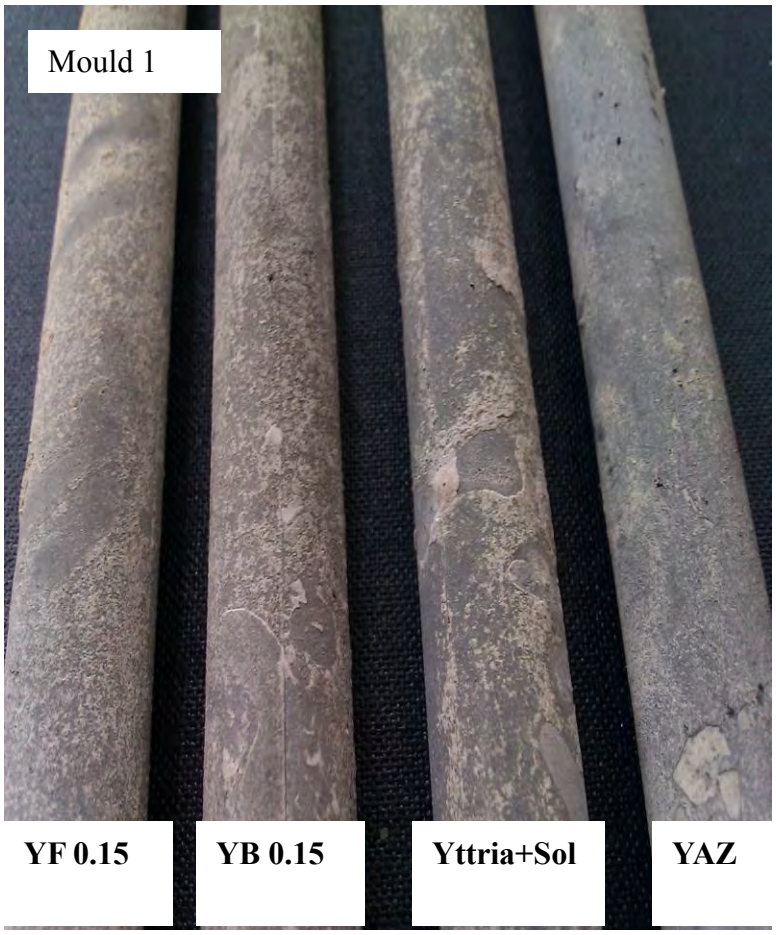

(a)

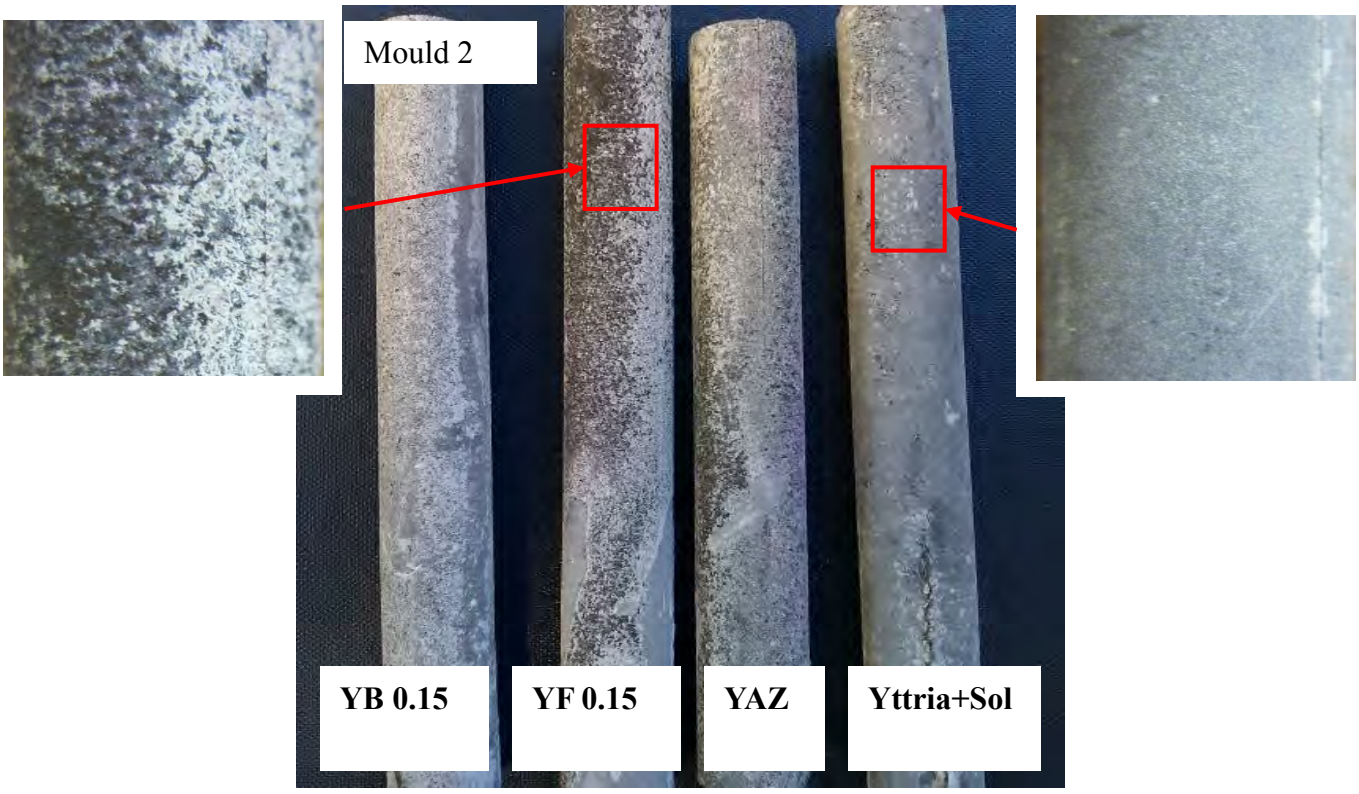

(b)

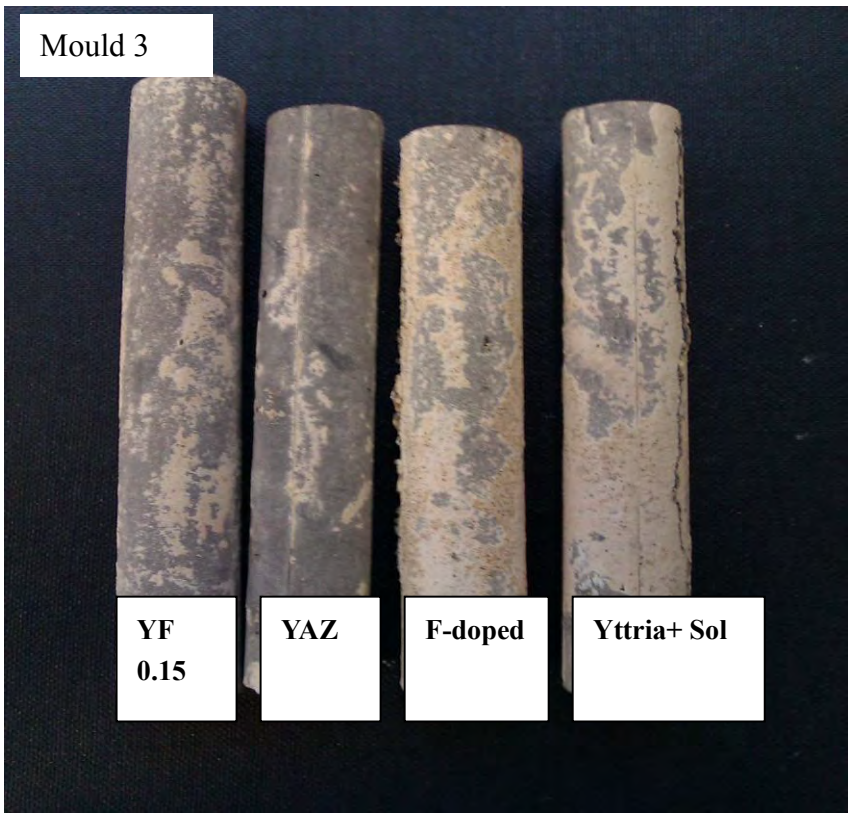

(c)

Figure 7-4. The cast bars after remove of the outer shell of each mould (a) mould 1, (b) mould 2, and (c) mould 3.

The attached ceramic layers on test bars where the moulds have two layers of face coat applied were thicker. The attached face coat for the water based slurry systems were thinner than the standard F-doped and yttria + sol face coat in mould 3, and easily removed. Closer examination revealed some dark spots on those bars which had had a single coating of both YAZ and YF 0.15 in Figure 7-4 (b). Those dark spots appeared as either an isolated feature or clustered together in a small region.

7.2.2 Bar surface microstructure and composition analysis

The microstructures and composition of the bar surface were evaluated using an SEM with EDX analysis. Figure 7-5 shows the microstructure of one of the black spots shown in Figure 7-4 (b) and EDX analysis as shown in Table 7-3 revealed the complex nature of the features.

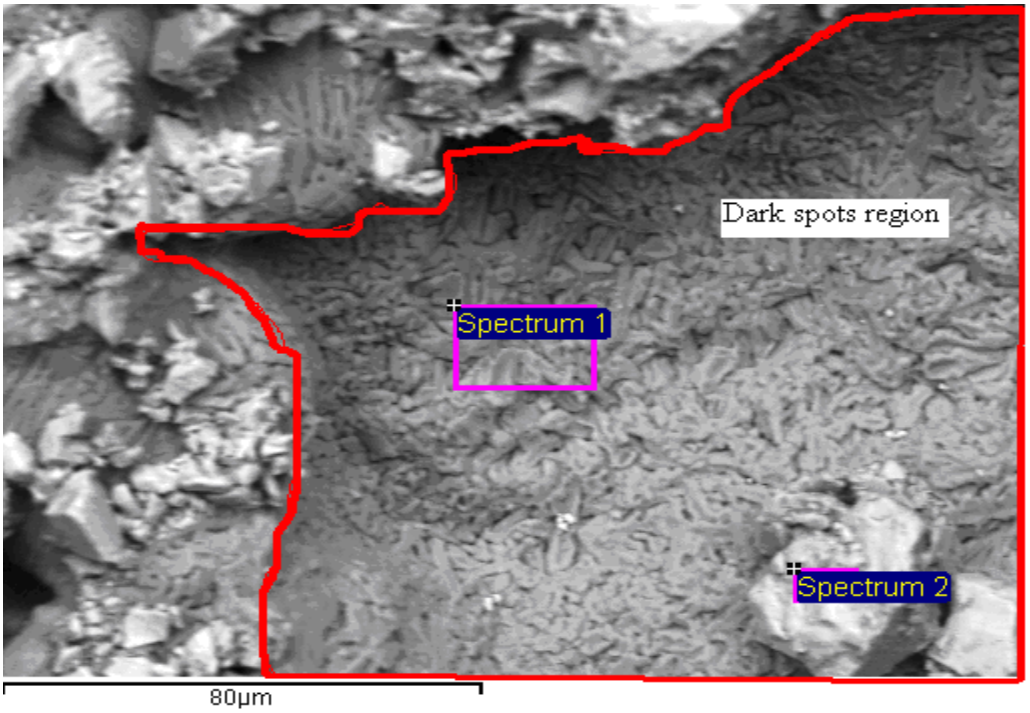

(a)

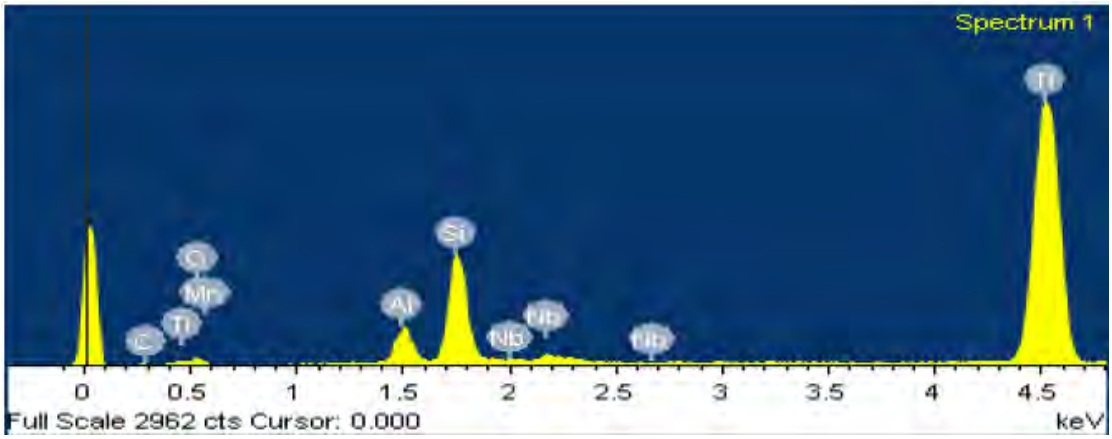

(b)

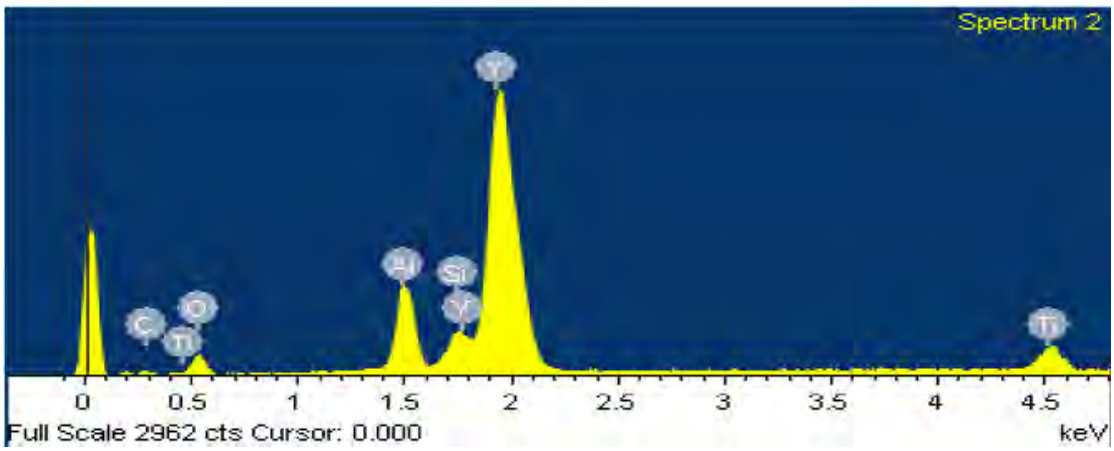

(c)

Figure 7-5. The secondary electron image of the dark spots,(a) the selecting area, (b) elements peaks at spectrum 1, and (c) elements peaks at spectrum 2.

Table 7-3. The compositions of the spectrum in Figure 7-5. (wt%)

Elements	C	O	Ti	Al	Si	Mn	Nb	Y
Spectrum 1	1.3	9.93	**69.7**	3.77	**12.45**	0.54	2.3	0
Spectrum 2	4.4	**13.86**	5.6	6.99	2.92	0	0	**66.22**

From the elemental peaks shown in Figure 7-5 and the selected area compositions in Table 7-3, the difference between those dark spots and the surrounding regions was the high levels of Si (white phases are yttria filler particles). Such concentrations of Si could only be present in the secondary coats as silica.

7.2.3 Interfacial microstructure of cast bars (two face coats)

All the bars were cut at the bottom position (Figure 7-3 (b)) where the metal have the longest time to cool down.

7.2.3.1 yttria + sol face coat

Figure 7-6 shows that the metal had a fully lamellar $\alpha_2+\gamma$ microstructure, which is typical for the TiAl in the cast condition. An interaction layer was observed at the metal/shell interface with the average thickness around 4 μm, and it consists of a bright and dark phase.

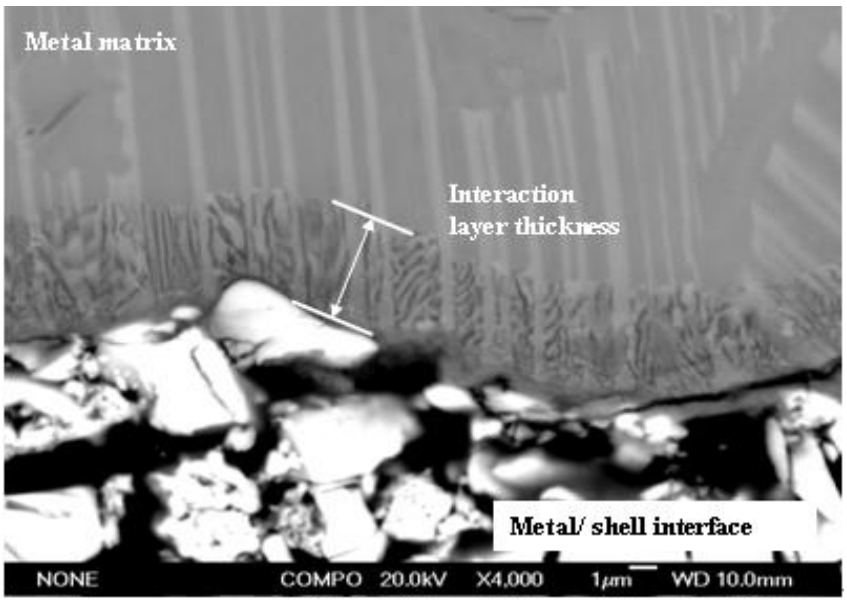

Figure 7-6.The backscattered image of the cast bar interface using yttria+sol face coat slurry.

The EDX elemental mapping analysis results in Figure 7-7 showed this interaction layer contained high amount of oxygen. Comparing to the oxygen penetration distance and the interaction layer thickness in Figure 7-7 (a) & (b), it can be seen that the oxygen penetration distances were similar to the interaction layer thickness at the metal/shell interface. The dark

phases appeared to contain higher oxygen concentration than the surrounding regions.

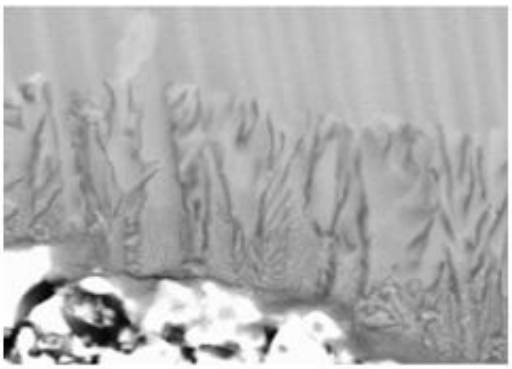

(a)

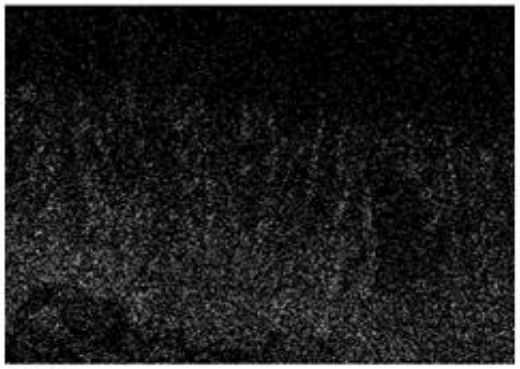

(b)

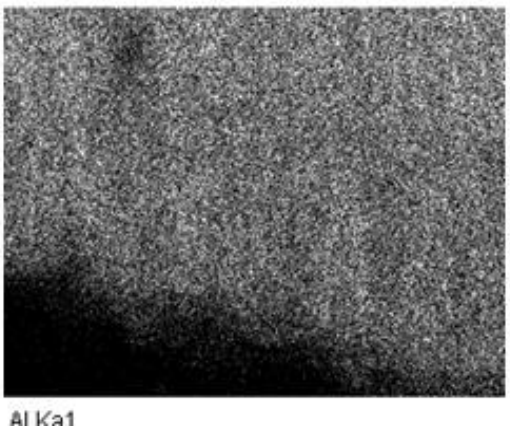

(c)

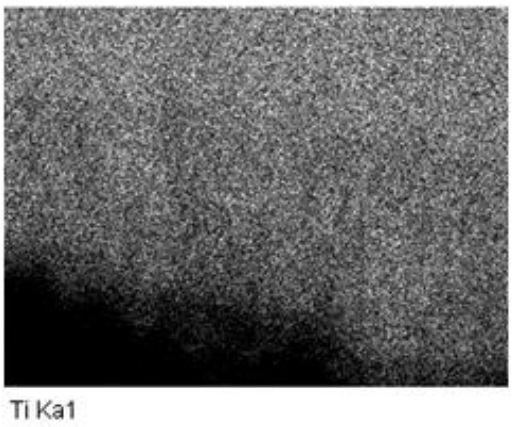

(d)

(e)

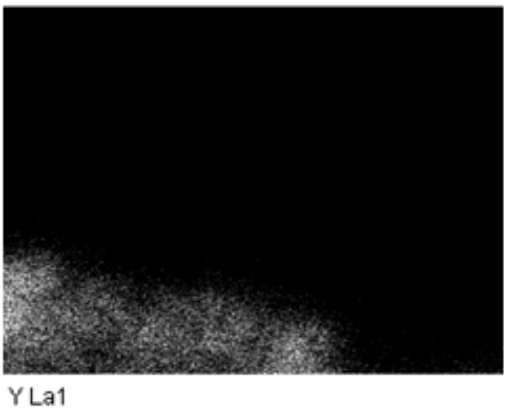

(f)

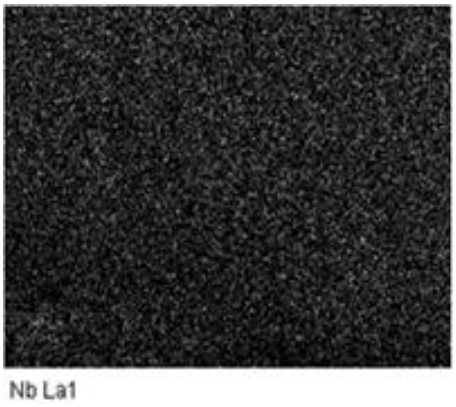

(g)

Figure 7-7.The EDX element mapping of cast bar of sample F-doped at the metal/mould interface. (a) the backscatter images of the interface, (b) oxygen, (c) Aluminum, (d) Titanium, (e) Manganese, (f) yttrium, and (g) Niobium.

7.2.3.2 YF 0.15 face coat

The microstructure of the interface between the YF 0.15 face coat and the metal is shown in Figure 7-8. In a similar way to the yttria +sol face coat, the metal had a fully lamellar $\alpha_2+\gamma$ microstructures and the attached face coat particles appeared at the surface of the metal. But different from using the yttria +sol face coat, the average interaction layer thickness at the interface is around 5 μm.

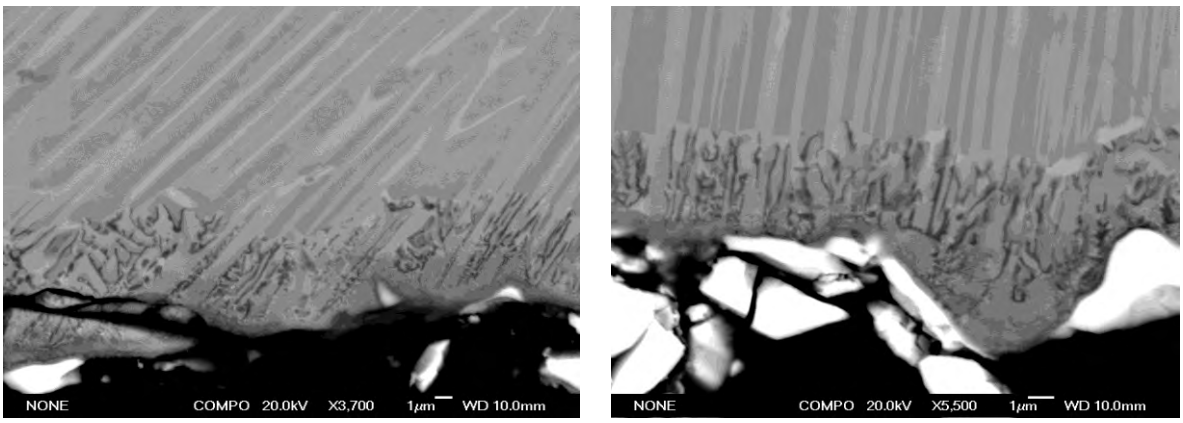

(a) (b)

Figure 7-8.The backscattered images of the cast bar metal/shell interface (two layers of face coat) of sample using YF 0.15 face coat slurry.

7.2.3.3 YAZ face coat

Figure 7-9 shows the SEM micrograph taken from the interface between the mould using YAZ face coat and the metal. In comparison with other crucibles, there is no significant different between the YAZ face coat and the molten metal. The average interaction layer thickness observed at the interface is around 4.1 μm.

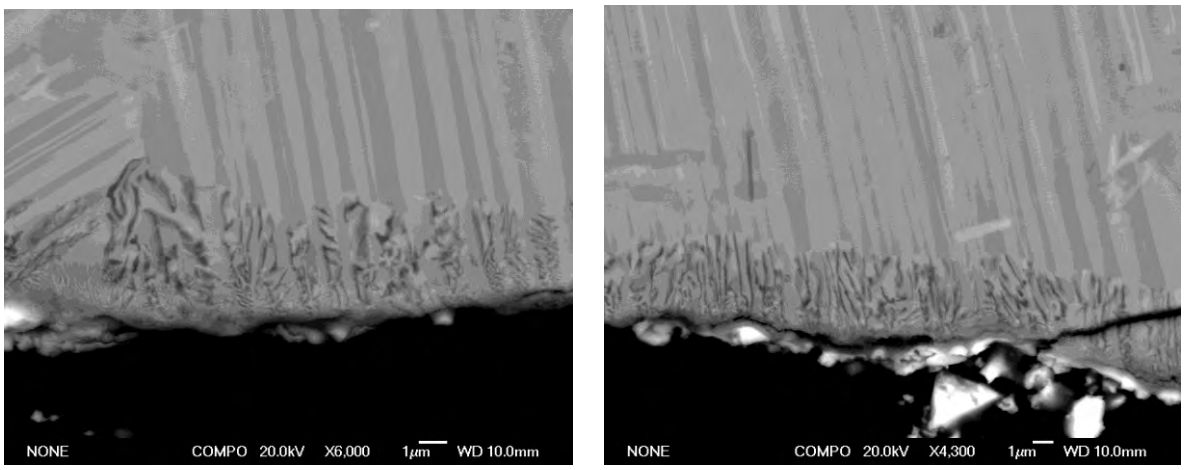

(a) (b)

Figure 7-9.The backscattered images of the cast bar metal/shell interface (two layers of face coat) of using YAZ face coat slurry.

7.2.3.4 F-doped face coat

The microstructure of the interface between the mould using F-doped face coat and the TiAl alloys are shown in Figure 7-10. The metal also had a fully lamellar structure typical of an as cast TiAl alloy. But, it can be noted that the attached face coat layer in the sample surface is thicker than using other face coat with the average thickness around 5 μm. By using the F-doped face coat, the interaction layer observed at the interface is around 7 μm.

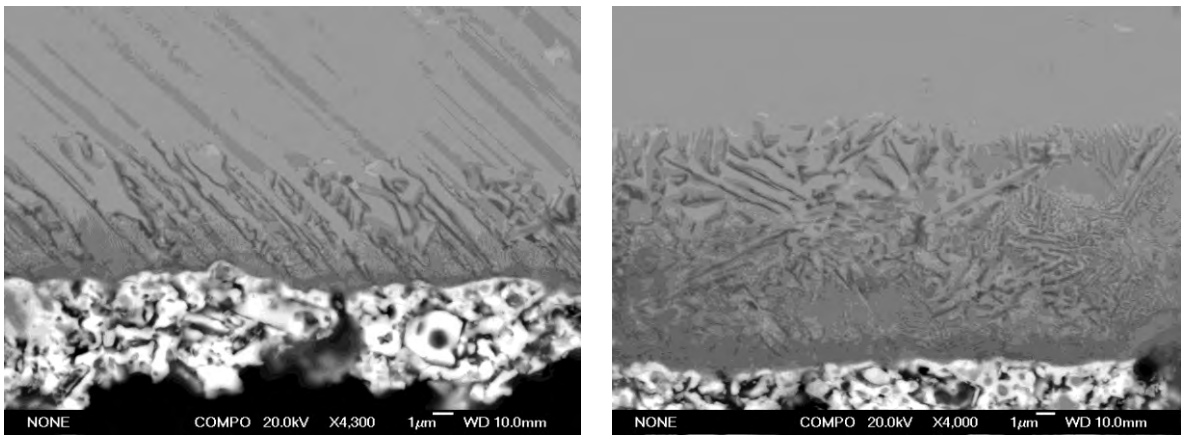

(a) (b)

Figure 7-10.The backscattered images of the cast bar metal/shell interface (two layers of face coat) of using F-doped face coat slurry.

7.2.3.5 YB 0.15 face coat

Compared to the microstructure observed at the interface of using other crucible, the microstructure found at mould using YB 0.15 face coat was different from other face coats. The interaction layer at the metal using YB 0.15 face coat shows a uniform layer at the metal interface and the dark phases only observed at the interface between the interaction layer and the metal matrix. The average interaction layer thickness is around 6 μm.

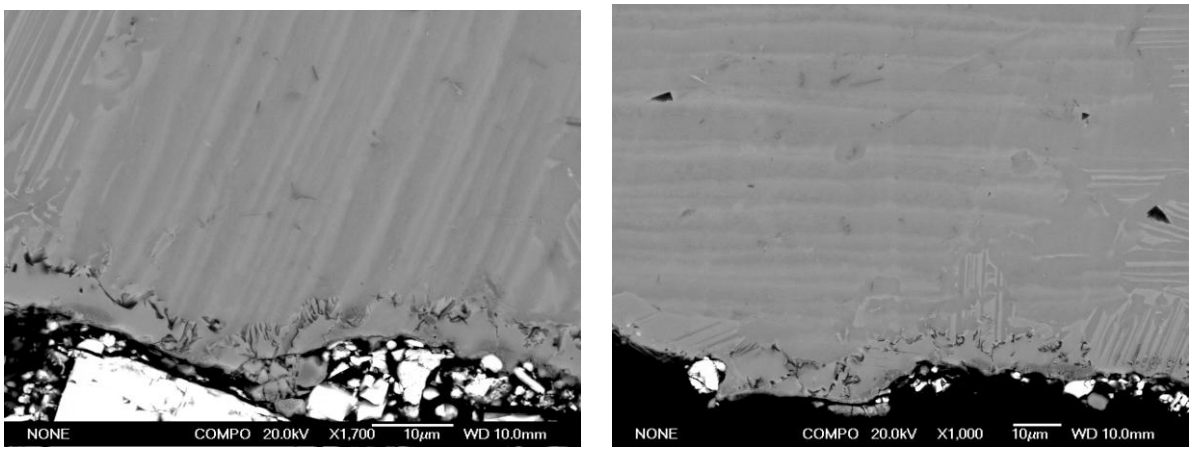

(a) (b)

Figure 7-11.The backscattered images of the cast bar metal/shell interface (two layers of face coat) of using YB 0.15 face coat slurry.

7.2.3.6 Interaction layer thickness

The average interaction layer thickness, with the standard deviations, for different face coat bars was summarized in Figure 7-12.

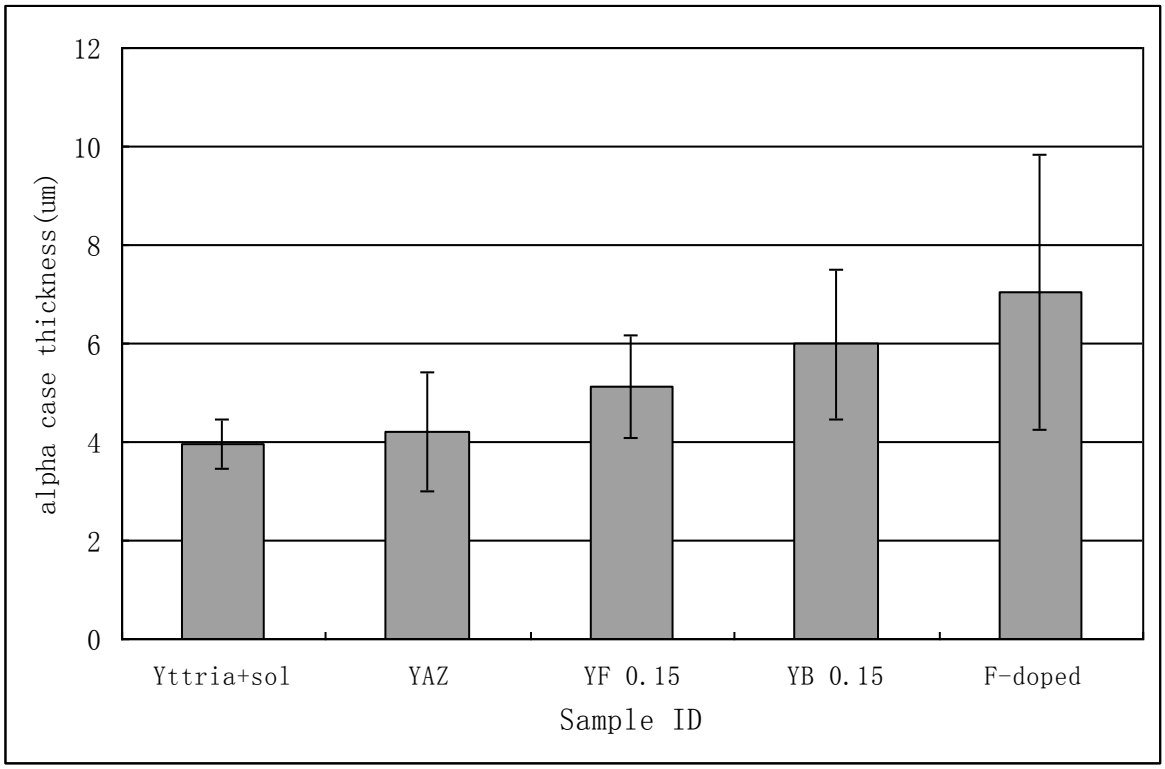

Figure 7-12. The interaction layer thickness of different face coats (double layer face coat).

Figure 7-12 shows that the interaction layer thickness differed for different face coats. For a standard Yttria+ Sol face coat, the interaction layer thickness is only around 4 μm, and hence this kind of face coat has a very high thermodynamic inertness. The superior chemical inertness of yttria face coat when in contact with molten TiAl has also reported by many researchers [42, 45, and 80]. By adding different sintering additives into the slurry, an increased interaction layer thickness was observed. The F-doped slurry face coat had the largest interaction layer thickness of around 7 μm, twice the thickness of that for the pure

yttria face coat even after applying two layers of face coat. Although the presence of sintering additives reduced the thermodynamic inertness of the yttria based face coat, all the slurries had a very limited interaction layer thickness of less than 8 μm, which could be removed after chemical milling or shot blasting.

7.2.4 Si and oxygen penetration distance at the sample interface

No Si was detected at the interface region for those bars with two layers of face coats (Mould 1 and 3). However, those with only one layer of face coat, weak Si peaks were detected at the metal/shell interface. Figure 7-13 shows the oxygen and Si concentrations within the immediate metal surface after the interface for bars that had only one layer of face coat (mould 2).

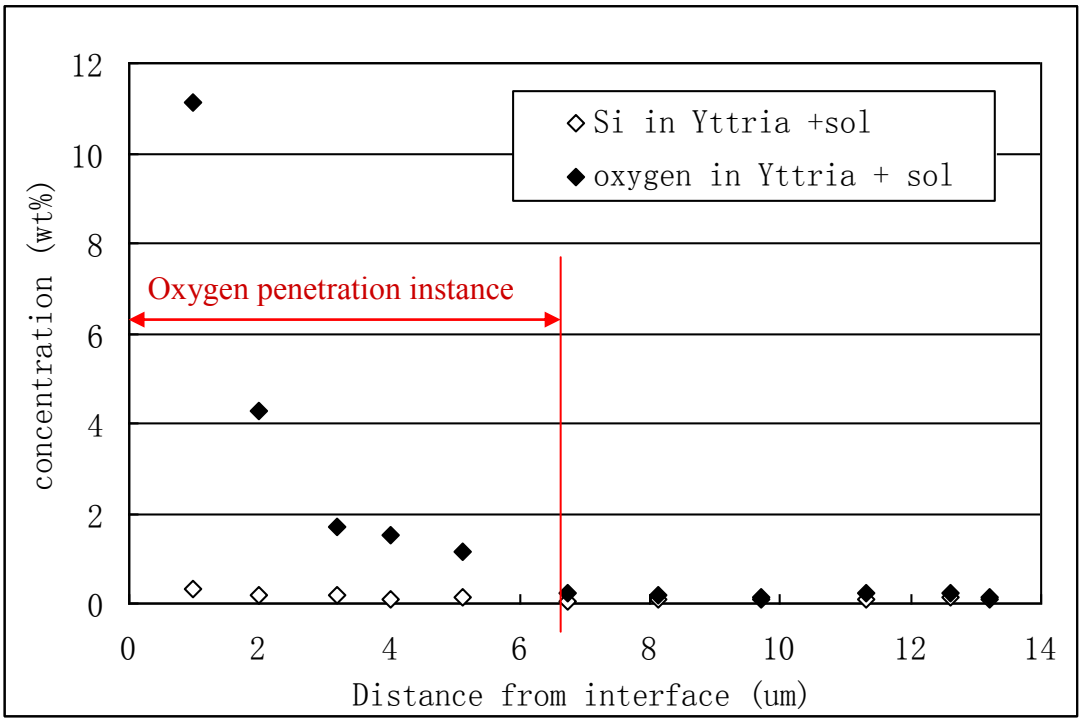

(a)

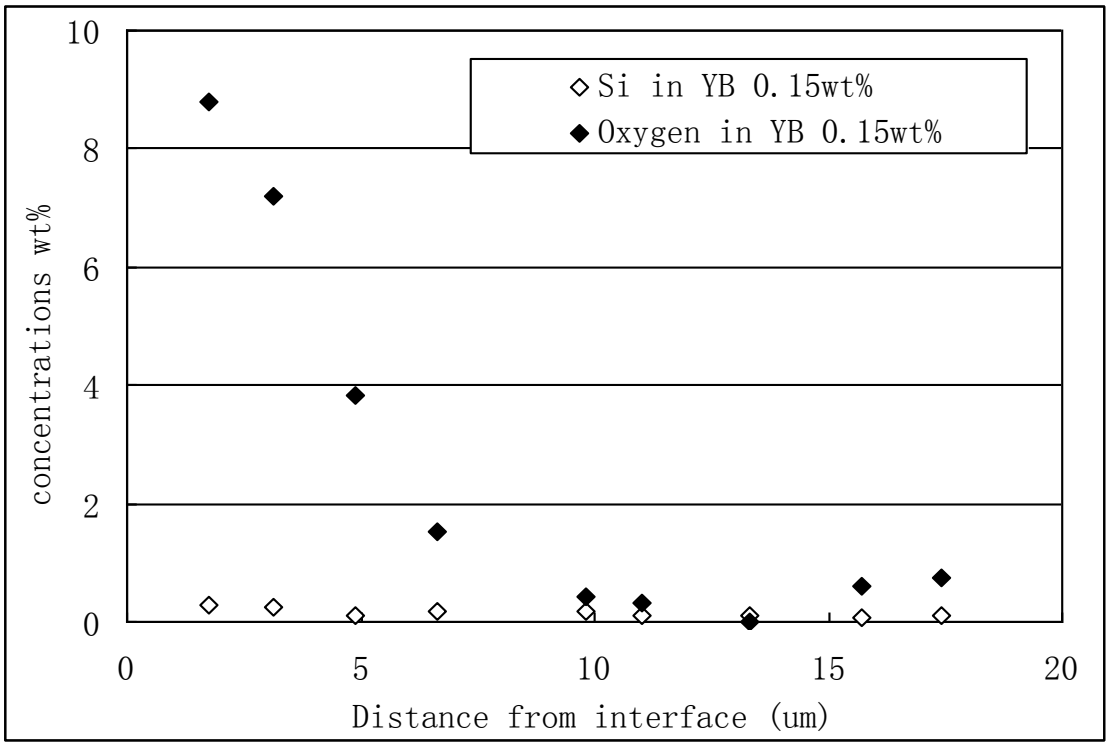
Si in YB 0.15wt%
Oxygen in YB 0.15wt%
concentrations wt%
Distance from interface (um)
0
2
4
6
8
10
0
5
10
15
20

(b)

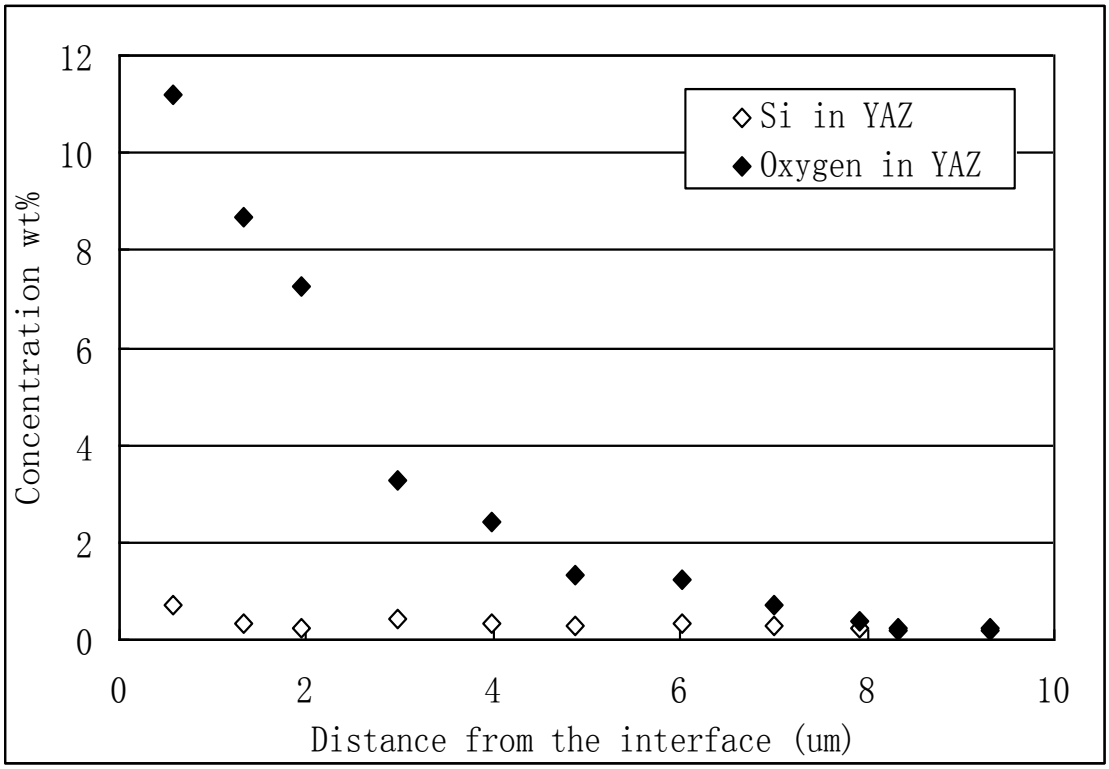
Si in YAZ
Oxygen in YAZ
Concentration wt%
Distance from the interface (um)
0
2
4
6
8
10
12
0
2
4
6
8
10

(c)

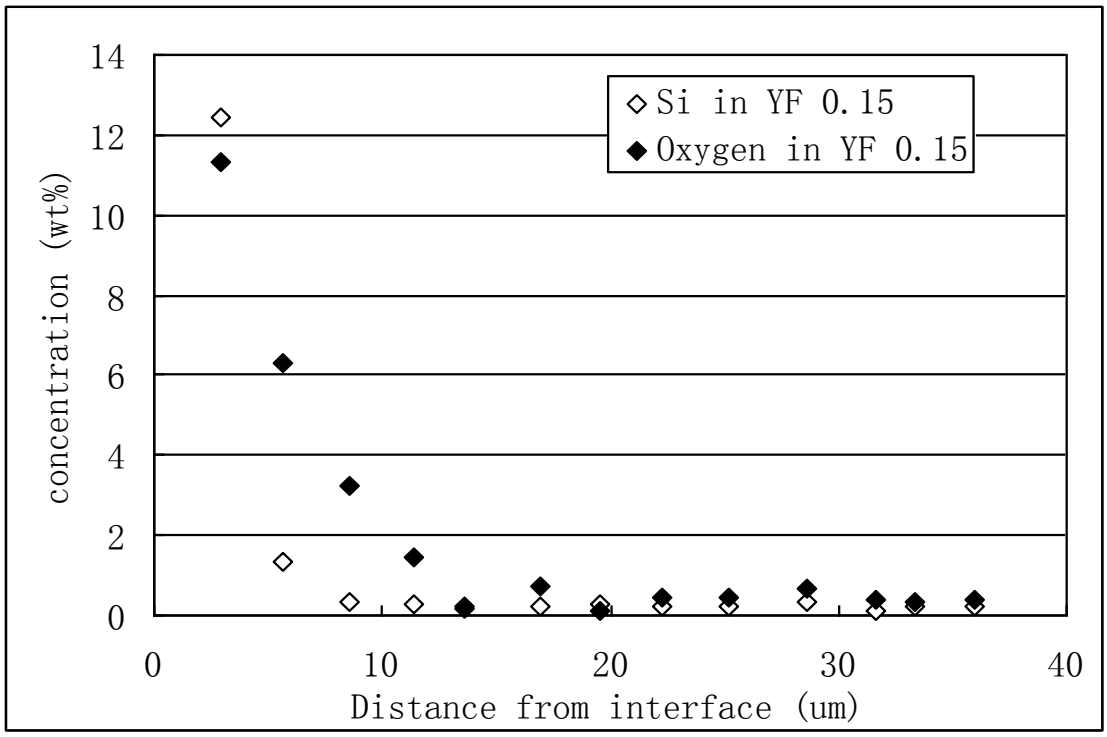

(d)

Figure 7-13.The oxygen and Si concentration change from the metal/shell interface into the metal matrix using one layer of face coat. (a) Yttria + Sol, (b) YB 0.15 wt%, and (c) YAZ shell, and (d) YF 0.15 wt% shell.

From Figure 7-12, Si was detected at the cast interface and decreased with increasing depth into the TiAl. The greatest penetration of Si occurred with the YAZ system followed in decreasing order by coatings based on YF 0.15, YB 0.15 and finally the yttria +sol face coat. However in all cases there was no Si-rich phase observed at the interface regions, since all the Si is in solid solution within the TiAl matrix. The oxygen concentration in samples have same trend as Si, but with deeper penetration depth to the metal matrix. Sample using YB 0.15 has the thickest oxygen penetration distance and the the corresponding oxygen penetration distances decreased as follows YB 0.15>YF 0.15> YAZ> Yttria +sol.

7.2.5 Hardness at the metal/shell interface (two coats of the face coat)

Metal hardness measurements at increasing depths from the surface are presented graphically in Figure 7-14 for the two layers of face coat systems.

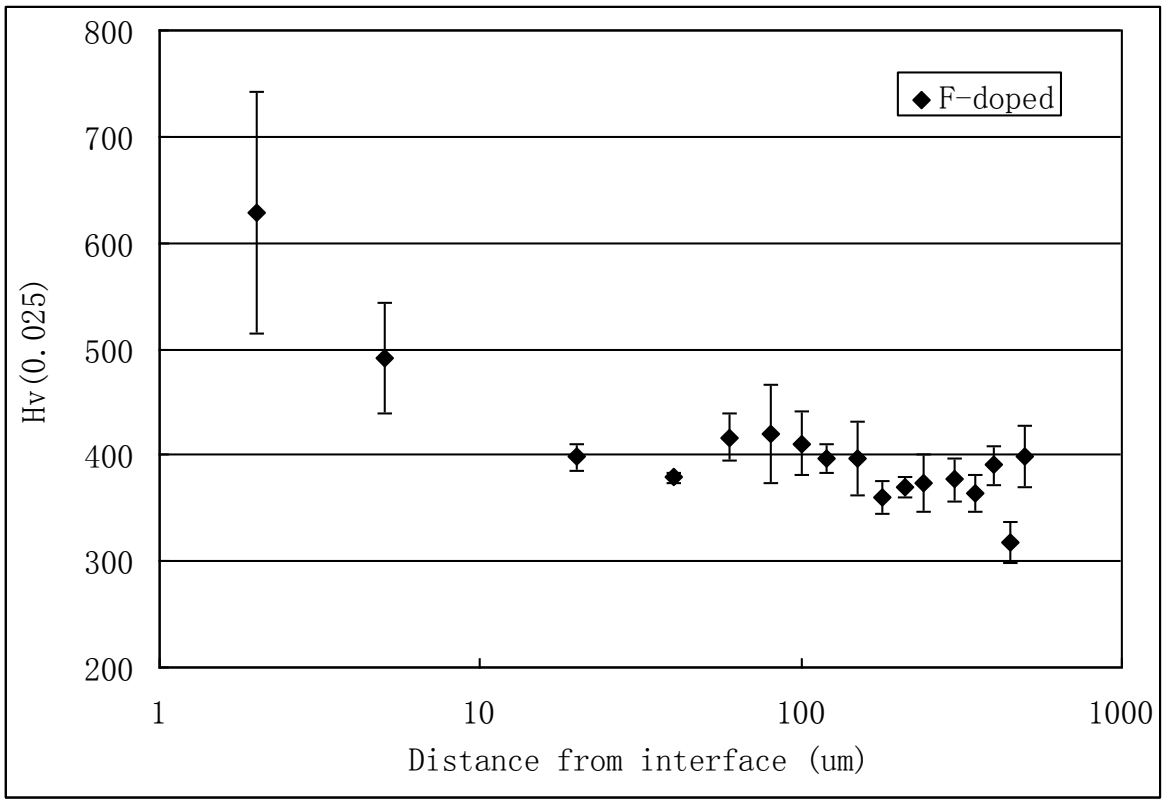

(a)

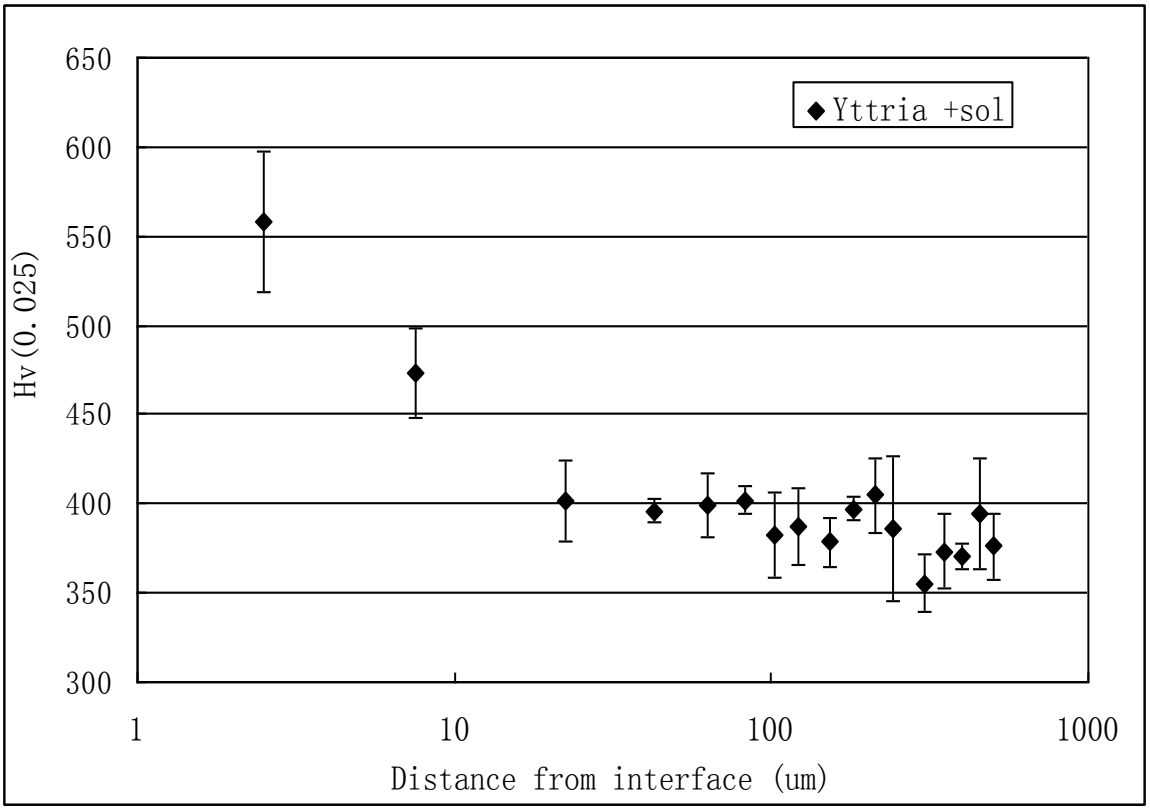
650
600
550
500
450
400
350
300
Hv(0.025)
Yttria +sol
1
10
100
1000
Distance from interface (um)

(b)

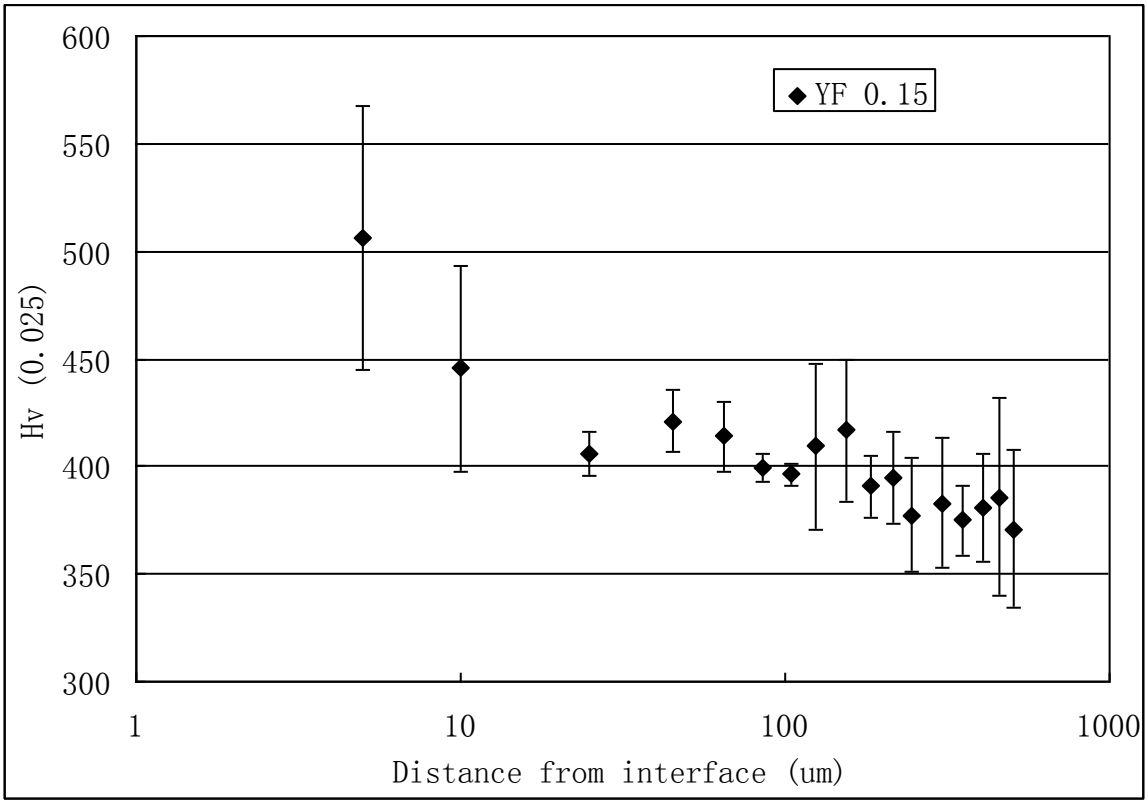
600
550
500
450
400
350
300
Hv (0.025)
YF 0.15
1
10
100
1000
Distance from interface (um)

(c)

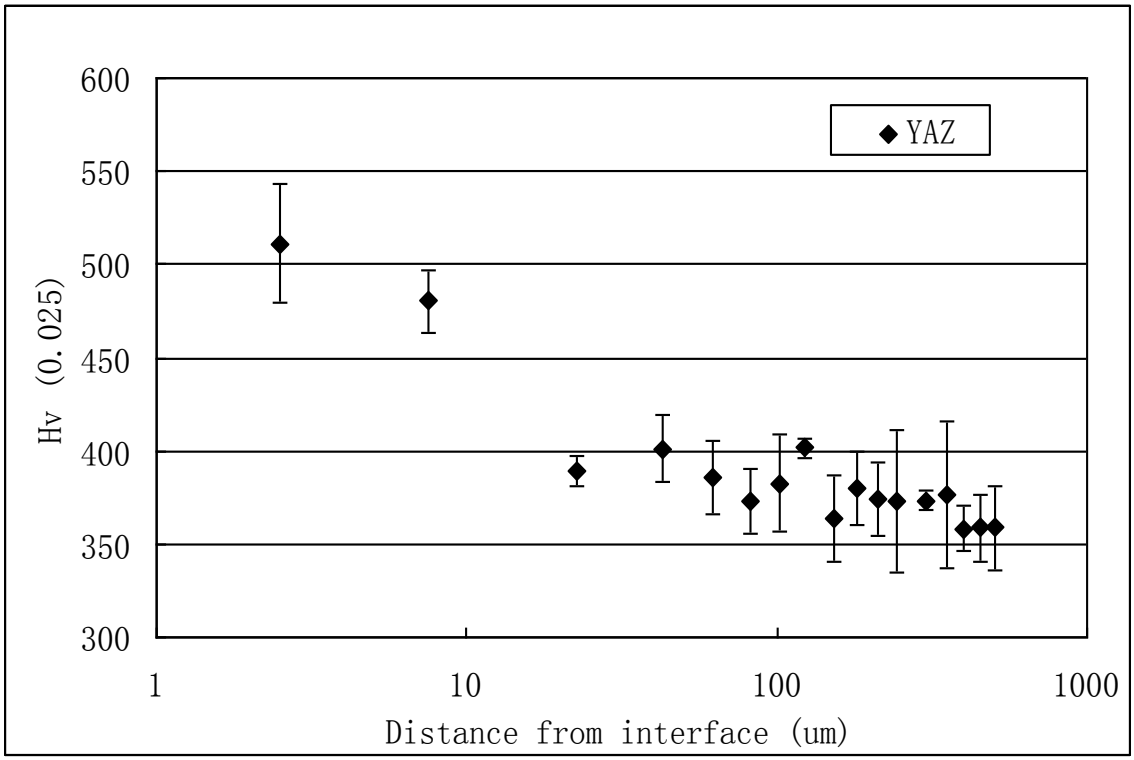

(d)

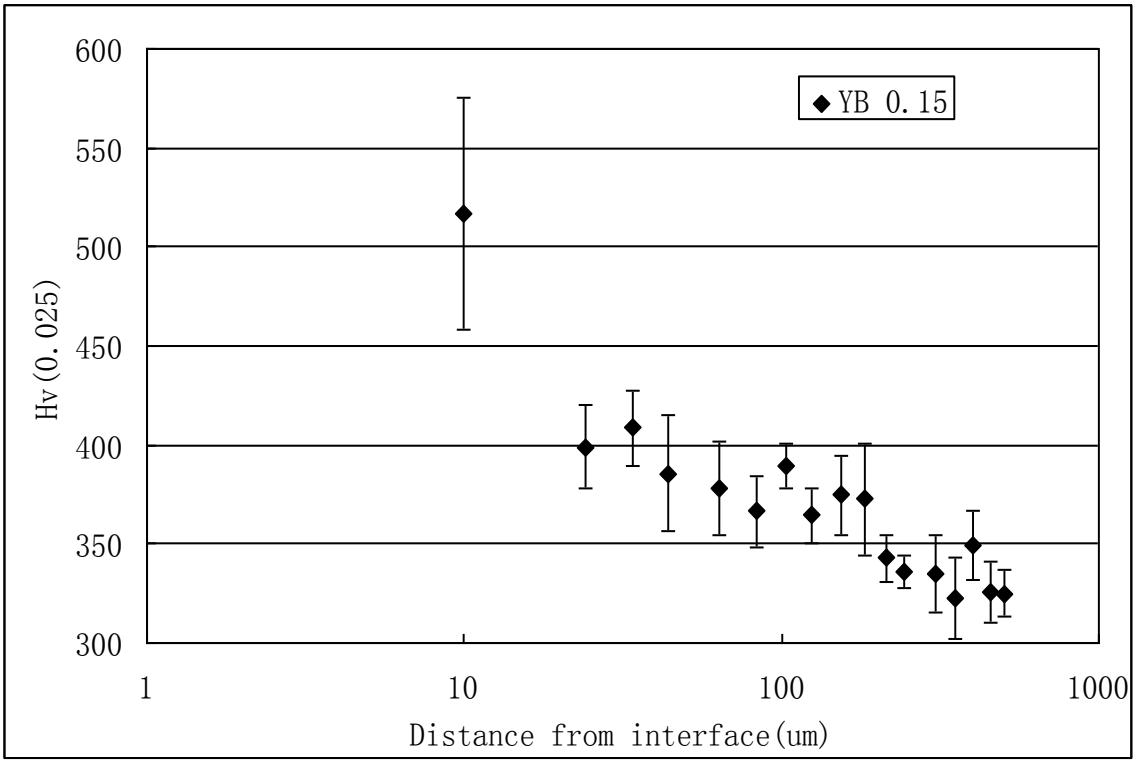

(e)

Figure 7-14. The hardness traces of the casting at the interface areas of samples using two layers of face coat. (a) F-doped sample, (b) Yttria +sol face coat slurry, (c) YF 0.15 face coat slurry, (d)YAZ face coat slurry, and (e) YB 0.15 face coat slurry.

Figure 7-14 highlights that with all coating systems the highest hardnesses were recorded at the interface and gradually decreased at increasing depths. The hardened layer thickness using the two layers of yttria + sol face coat was less than 15 μm. Compared to face coat using pure yttria, all the cast bar hardened layer thickness using new slurry is very similar. The hardened layer thickness was less than 25 μm when using YF 0.15 face coat, and for using YAZ and YB 0.15 shells was less than 23 μm and 24 μm respectively. Using commercial F-doped face coat, the hardened layer thickness was 25 μm.

By considering the solid solute Si in the metal interface area may influence the hardness, the hardness of the metal using a single face coat layer are also detected and presented in Figure 7-15.

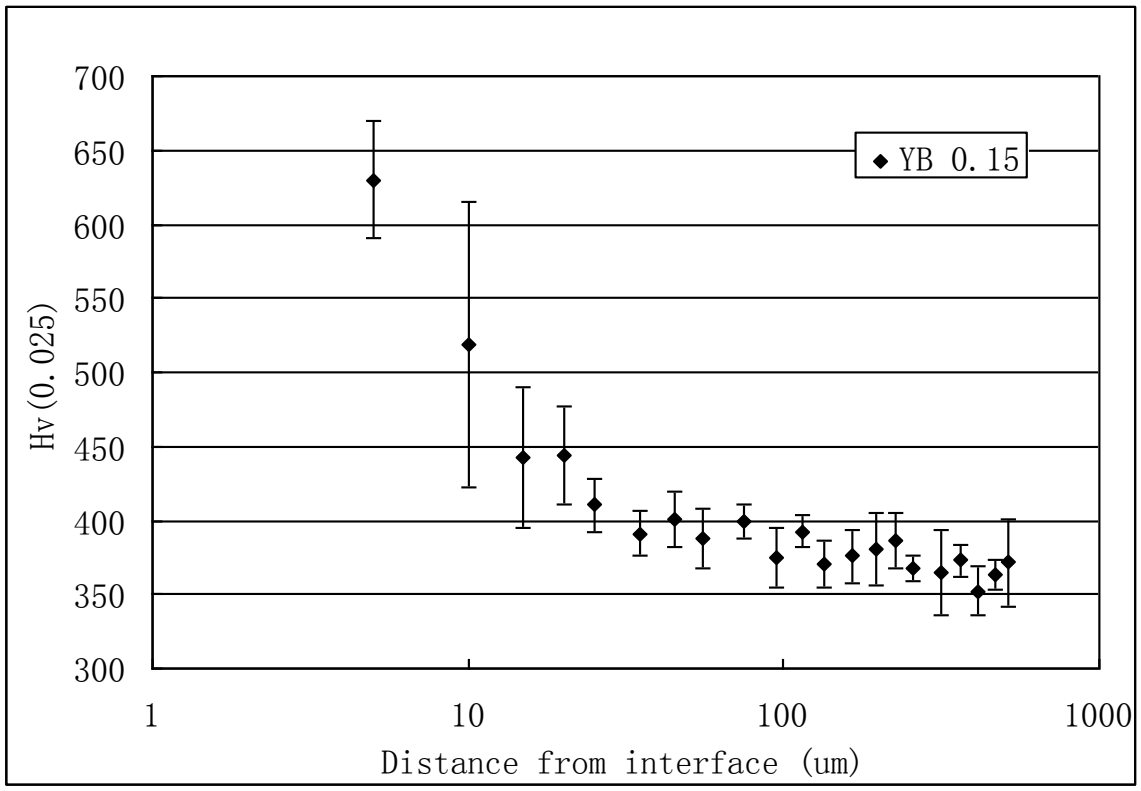

(a)

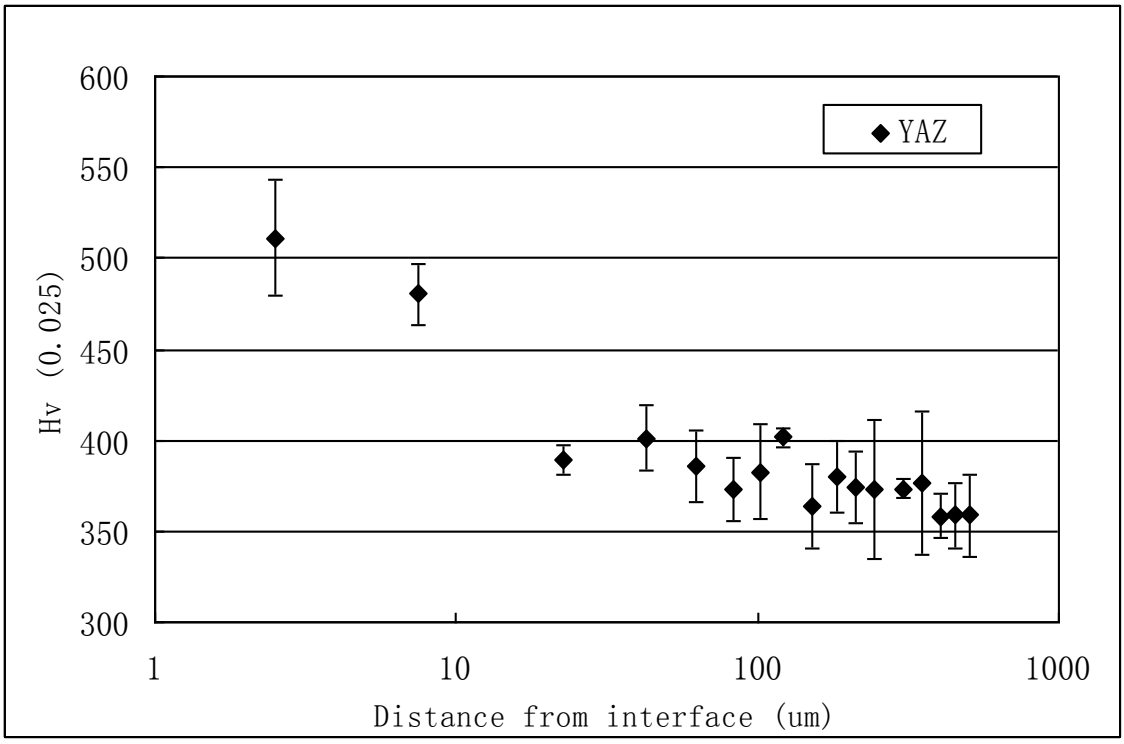
600
550
500
450
400
350
300
Hv (0.025)
YAZ
1
10
100
1000
Distance from interface (um)

(b).

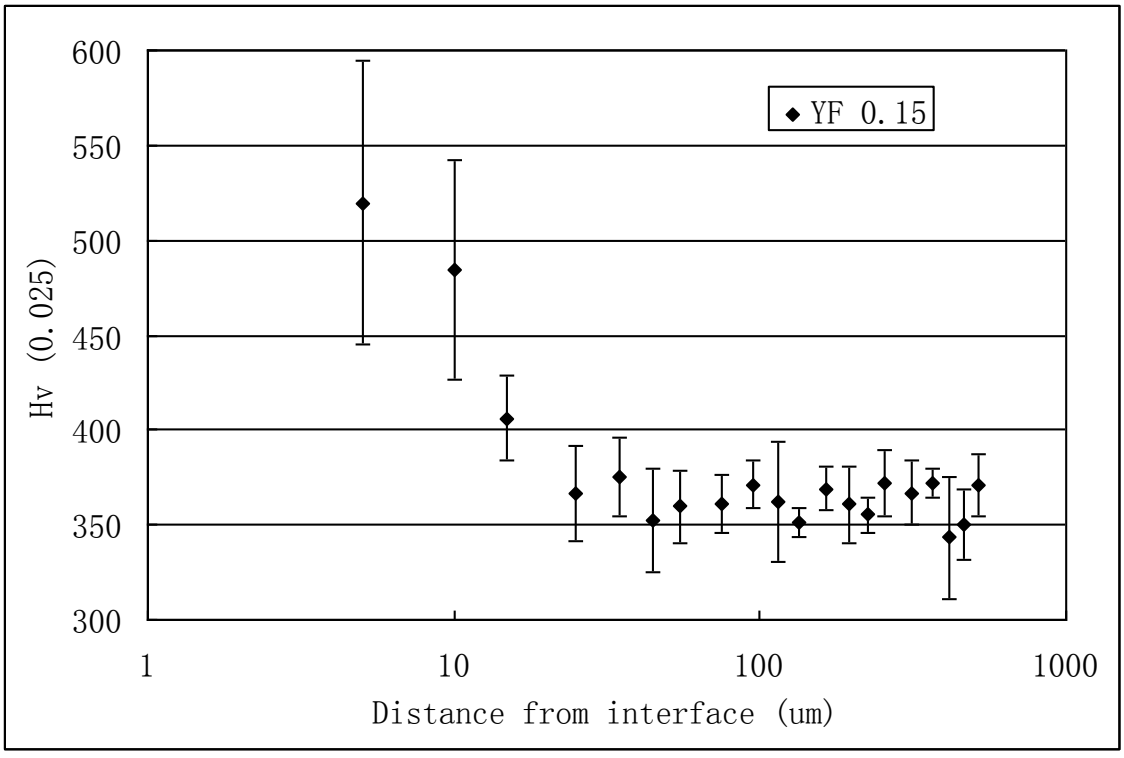
600
550
500
450
400
350
300
Hv (0.025)
YF 0.15
1
10
100
1000
Distance from interface (um)

(c)

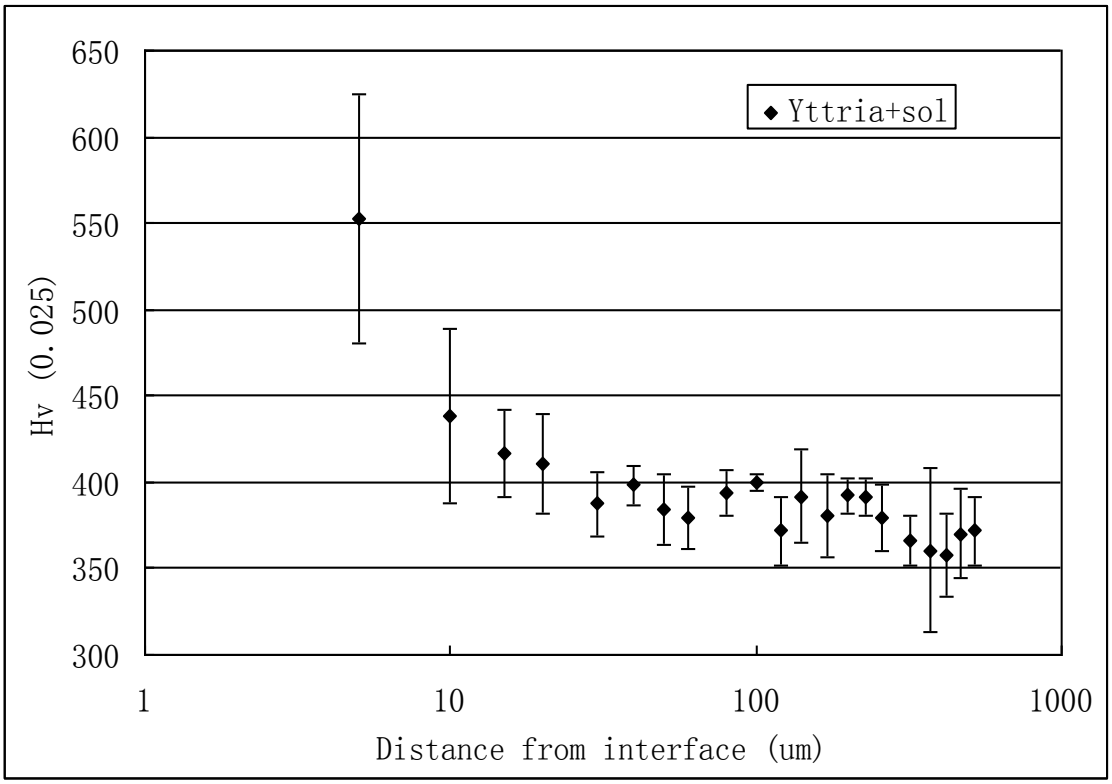

(d)

Figure 7-15. The hardness of the bar interface using one layer of face coat. (a) YB 0.15, (b) YAZ, (c)YF 0.15 and (d) Yttria + sol.

As can be seen from the Figure 7-15, high hardness was found at the metal surface and gradually decrease into the metal matrix. The hardened layer thickness of yttria +sol was around 20 μm, and the hardened layer thickness of YB 0.15, YAZ and YF 0.15 were 25, 30, and 20 μm respectively. The hardened layer thicknesses were nearly the same irrespective if one and two layers of face coat had been applied to the mould.

7.4 Conclusions

In this section, the newly developed face coat slurries were used to make real investment castings. The purpose of this experimental work was to establish both the thermochemical

inertness of the face coat and the Si penetration problems that can develop as a result of their application to moulds which are to be exposed to TiAl. The conclusions have been generated.

1. The newly designed face coat slurries have very good chemical inertness against molten TiAl alloys compared to the industrial used yttria and F-doped face coat. The inertness of the face coat decreased as: Yttria +sol > YAZ > YF 0.15 > YB 0.15 > F-doped face coat slurry. This result was the same as that predicted by the face coat inertness results in the sessile drop test by calculating the liquid metal spreading activation energy on the different face coats.

2. Si penetration from backup coat was found at the interface if only one layer of the face coat was applied. The Si penetration thickness in the TiAl metal interface reduced in the order of F-doped>YAZ> YF 0.15=YB 0.15> Yttria +sol, the same sequence as the detected Si amount on the face coat surface results in Chapter 6.

Chapter 8. Discussion

8.1 Filler powder development

8.1.1 Filler powder sintering properties

There are many factors that affect the sintering properties of face coat filler powder such as particle size and distribution, particle shape, particle structure, particle green density as well as the quantity of sintering additives [181-185].

8.1.1.1 Particle size and distribution

The particle size and distribution of the powder compacts will influence the powder sintering properties [181]. The experiment result in Figure 3-12 and 3-13 for 2.0 wt% TiO_2 with average powder size around 14.8 μm added into yttria. Smaller particles have a large surface area and greater likelihood of neck formation at contact points between two particles. Unfortunately, finer particles are more prone to agglomeration, as shown in Figure 3-11, so the green density is often reduced. The extent of neck growth can be calculated from the measured dimensional changes of pellets and powder particle size. The prediction of neck growth distance of powders after sintering at 1550 °C for one hour calculated from equation 8-1 [105] is listed in Table 8-1. (Assuming particles are spherical, see Figure 8-1).

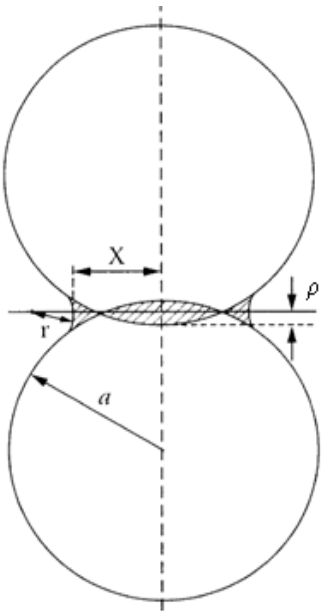

Figure 8-1. A schematic two sphere model of neck growth.

$$\left(\frac{\rho}{a}\right)=\frac{\Delta L}{L_0} \qquad 8\text{-}1$$

where: ρ is the necking distance (m)

a is the particle diameter (m)

ΔL is the pellet diameter (m) after sintering.

L_0 is the pellet original diameter.

Table 8-1. Calculated necking distance ρ, after sintering at 1550°C for 1 hour.

Samples ID		($\Delta L/Lo$)%	mean D(μm)	distance ρ (μm)
B_2O_3	2.0 %	7.3	15.025	0.55
B_2O_3	0.15 %	6.2	20.53	0.64
Yttrium acetate	2.0 %	3.75	14	0.26
Sol	**2.0 %**	**2.55**	**12.06**	**0.15**
TiO_2	0.15 %	2.8	14.64	0.2
YF_3	0.15 %	4	21.49	0.42
TiO_2	2.0 %	2.2	14.8	0.16
Yttrium carbonate	2.0 %	2.1	14.27	0.15
YAZ		1.75	13.78	0.12
Yttrium acetate	0.15%	2.7	21.66	0.29
CeO_2	0.15%	2.1	19.5	0.2
YF_3	2.0%	1.2	12.95	0.08
La_2O_3	0.15%	1.2	13.22	0.08
CeO_2	2.0%	1.5	17.48	0.13
pure yttria		**1.2**	**14.88**	**0.09**
Yttrium carbonate	0.15%	1	19.325	0.1
La_2O_3	2.0%	0.8	17.44	0.07

It is known that neck growth between particles is dependent on the added amount of the sintering additive, the particle size and distributions etc. Table 8-1 shows the calculated neck growth distance between two particles by considering those factors. In this table the additive boron oxide has the largest neck growth distance, followed by yttrium acetate, yttria sol, TiO_2, YF_3 and YAZ. Sintering additives La_2O_3 and CeO_2 do not show very obvious effects in enhancing powder sintering, and the neck growth distance is similar to pure yttria. Sintering precursors like yttrium acetate and carbonate have some benefits in promoting powder

sintering and densification due to the local decomposition interaction of the sintering precursor, but these compounds have limited effects on the entire sintered body (Figure 3-18). Adding high concentrations of sintering precursor seems more beneficial but this may cause the decrease of the final density due to the large shrinkage pores generated with poor surface finish. However, this simplified neck growth distance in equation 8-1 and the calculated values in Table 8-1 only assumed that the sintering mechanisms of all the formulations are solid-state sintering, and the real sintering process is much more complicated.

8.1.1.2 Particle shape and microstructures

Particle shape influences primarily the green density of the powder compact. Mohamed N [184] illustrated that deviation from a spherical or equiax shape leads to a reduction in the packing density and densification. Compacts of acicular (elongated) particles can be sintered to high density only if the powder particles are aligned during packing. In this experiment, yttria based powders (Figure 3-11) have irregular shapes with very poor green packing density. Poor compact density leads to slower sintering and longer diffusion distances for elements to diffuse between particles to achieve high density. The density change after sintering at different isothermal temperatures for one hour in Table 3-4, shows that the higher green compact density, the higher final density after sintering.

8.1.1.3 Sintering temperature and heating rate

The effect of sintering temperature on the densification and coarsening process can be

presented by using the linear densification rate $\dot{\varepsilon}_\rho$ as shown in below equation from 8-2 to 8-10 [185]:

$$\dot{\varepsilon}_\rho = \frac{H_1 D(T)\phi^{(m+1)/2}\sum}{G^m(T,t)kT} \quad 8\text{-}2$$

Where $\dot{\varepsilon}_\rho$ is now a function of both temperature and time, H_1 is a constant, the diffusion coefficient D is now a function of temperature, ϕ is the stress intensity factor, $\sum$ is the sintering stress, k is the Boltzmann constant, and m is a constant that depends on different sintering mechanisms. $G^m(T,t)$ represents a coarsening function that depends on temperature and time and is presented in equation 8-3.

$$G^m(t) = G_0^m + A\exp(-\frac{Q_c}{RT})t \quad 8\text{-}3$$

where G_0 is the initial grain size, A is a constant, and Q_C is the activation energy for the coarsening process. For constant rate sintering, the equation above will be written as:

$$G^m(T,t) = G_o^m + A\int_{t_0}^{t}\exp\left(-\frac{Q_c}{RT}\right)dt \quad 8\text{-}4$$

In constant heating rate sintering, the sintering temperature T and the sintering time t are related by the heating rate α , Therefore

$$T = \alpha t + T_0 \quad 8\text{-}5$$

$$dT = \alpha dt \quad 8\text{-}6$$

Putting equation 8-6 into 8-4, equation 8-4 becomes

$$G^m(T,t) = G_o^m + \frac{A}{\alpha}\int_{t_0}^{t}\exp\left(-\frac{Q_c}{RT}\right)dT \approx \frac{1}{\alpha}F_1(T) \quad 8\text{-}7$$

where $F_1(T)$ is a function of temperature. Put equation 8-7 into equation 8-2:

$$\dot{\varepsilon}_\rho \approx \alpha F_2(T) \quad 8\text{-}8$$

where $F_2(T)$ is also a function of temperature only, by converting the linear densification rate to the volume densification rate $(1/\rho)d\rho/dt$, so:

$$\frac{1}{3}\int_{\rho_0}^{\rho}\frac{d\rho}{\rho}=\alpha\int_{t_0}^{t}F_2(T)dt \qquad 8\text{-}9$$

Substituting for dt from equation 8-9

$$\frac{1}{3}\ln\left(\frac{\rho}{\rho_0}\right)=\alpha\int_{T_0}^{T}F_2(T)dT \qquad 8\text{-}10$$

According to these equations, for compacts with same green density, the density at any temperature is only a function of temperature.

The sintering behavior is also dependent on the heating rate α of different types of powders [186]. For amorphous ceramics, viscous flow is the dominant densification mechanism with no powder/grain coarsening taking place. When increasing the heating rate, the shrinkage curve is shifted to higher temperatures [186]. But for a polycrystalline gel, the behavior is different, with the shrinkage curve shifting to lower temperature with increasing heating rate.

The sintering and microstructure evolution of ZnO_2 powder compacts was studied by Chu *et al* [187] over a wide range of constant heating rates (0.5-12 °C/min). This study shows that the densification rate increases with increasing heating rate. But the densification will not infinitely increase with the increasing heating rate. Lange *et al* [188] studied the sintering behavior of Al_2O_3 powder at constant heating rates of 2.5 to 20 °C/min from room temperature up to 1550 °C. This study found that there is a limit on the heating rate, and further increasing the heating rate will lead to a decreasing density. Fast heating will lead to

powder coarsening rather than densification. In the experimental data reported in this thesis, it is seen that slower heating rates are more beneficial for powder densification, see Figure 3-10.

8.1.1.4 Sintering additives and the sintering mechanisms

8.1.1.4.1 Sintering precursors (yttrium carbonate, yttrium acetate)

The decomposition of sintering precursors can produce nano-sized powder particles, and because of the large surface area, those small particles are very reactive [142]. By using nano-sized yttria particles, the starting temperature for sintering pure yttria can reduce to around 1000 °C [143]. These small particles also increase powder compact density by filling large gaps between particles. The sintering precursor will not influence the yttria thermochemical inertness due to very clean evaporation. This study shows that by using the precursor as the sintering aid, high density can only be achieved in some local areas within the poorly-sintered powder matrix. Therefore, sintering precursors added into yttria powder were not be considered as the face coat filler materials in this study.

8.1.1.4.2 Sintering additives (TiO_2, B_2O_3, La_2O_3. etc)

In order to achieve a high density at low sintering temperatures in ceramics, solid sintering additives are sometimes added into the powder to enhance sintering. The enhanced sintering effects of adding sintering aids are due to the sintering additives interacting with yttria to form new phases which can promote matter diffusion between particles. These new phases

will not only enhance powder sintering but also reduce the sintering temperature.

In this research, in order to attain better sintering properties of the face coat, sintering additives were incorporated selectively into the powder. When heating up to certain temperatures, chemical reactions will take place between sintering additives and the yttria powder based on the phase diagram, e,g B_2O_3-Y_2O_3 binary phase diagram in Figure 8-2 [189].

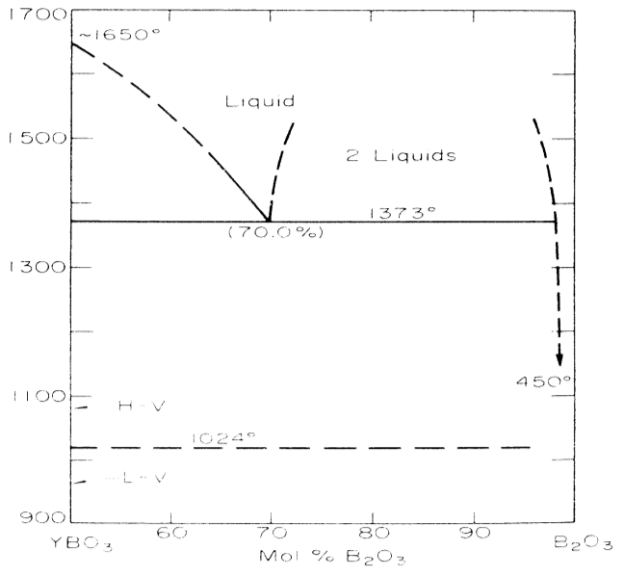

Figure 8-2. B_2O_3-Y_2O_3 phase diagram . L-V and H-V=low and high vaterite –type structures, respectively.

During heating, B_2O_3 will react with yttria to form new phases and this series of new phases will form local pockets of liquid phase around the powder surface (Figure 3-16). As the sintering temperature increases, these liquid phases will cause a very quick densification of the powder compacts (confirmed in the dilatometer test in Figure 3-8 (c)). Because of this

reaction, the powder can achieve a very high density at relatively low sintering temperature when compared to pure yttria. US patent number 2007161499 [127] used these transient liquid phases to achieve high density transparent yttria components at a relatively low sintering temperature of 1300-1500 °C.

8.1.1.5 The prediction of sintering mechanism at different isothermal temperature

By using Koji's methods (described in section 3.3.2 [156, 158]), the powder sintering mechanism at different isothermal temperatures can be predicted. The correction number δL was used (in equation 3-11) to reduce the pre-sintering effect, before isothermal sintering takes place, and this δL is defined as the shrinkage between the largest expansion of the sample and the sample dimension at the start of the isothermal heating stage. However, by studying the shrinkage curves of the powder pellets, the author found that the correction methods of Koji can not fully eliminate the pre-sintered effect during heating. Therefore, new correction methods were used in this experiment to better understand the powder sintering mechanisms. This new method used a corrective length $\Delta L_{(cor)}$ to replace ΔL, a corrected isothermal sintering time (t-t_o) to replace t in equation 3-10, and the equation change to 8-11.

$$\log\left(\frac{\Delta L_{cor}}{L_{ocor}}\right) = n\log\left(\frac{K\gamma\Omega D}{kTa^{p}}\right) + n\log(t - t_0) \qquad 8\text{-}11$$

$$\Delta L_{cor} = L - L_{ocor} \qquad 8\text{-}12$$

Where, ΔL_{cor} is the length change at time t=to which is defined in equation 8-12, and the L_{ocor} , t_o is shown in Figure 8-3.

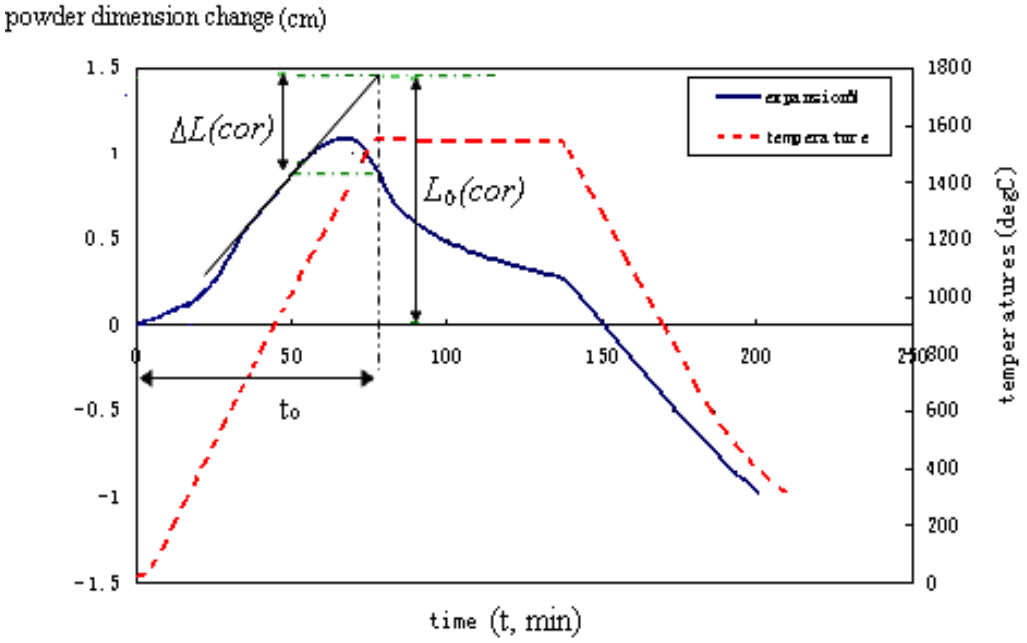

Figure 8-3. A schematic diagram dilatometer test trace of the correction methods with annotations used in this experiment.

Therefore, by using this method some of the corrected isothermal sintering curves of 2.0 wt% of different sintering additives (also including B_2O_3 at 0.15 wt%) added to the basic yttria powder trace are shown in Figure 8-4.

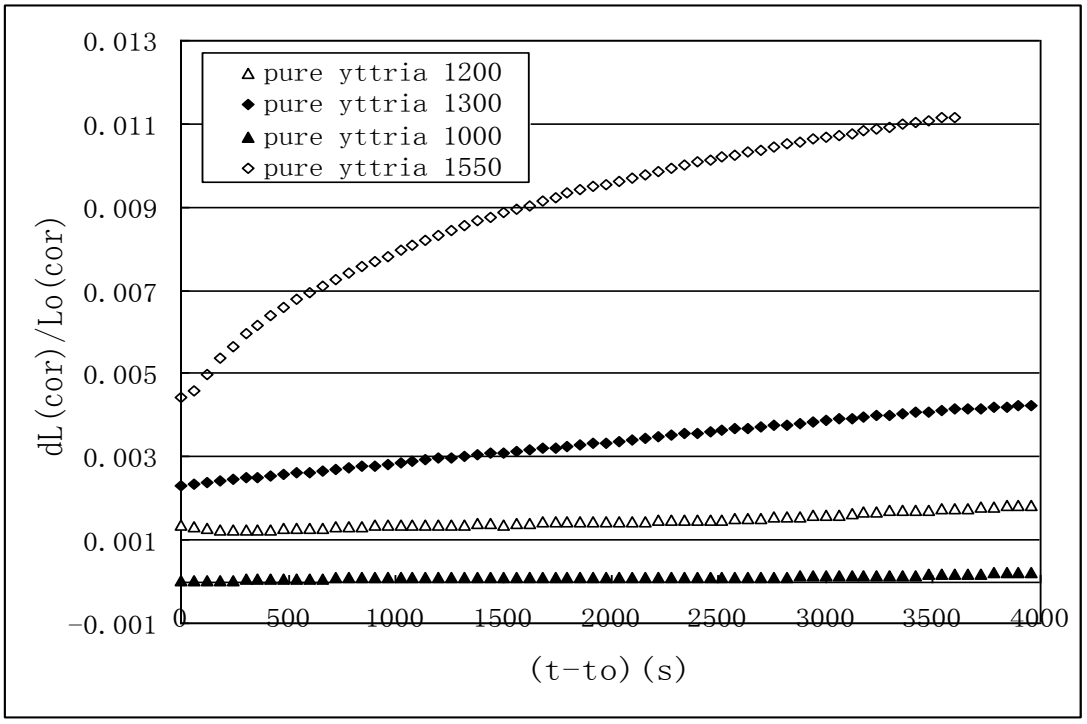
0.013
0.011
0.009
0.007
0.005
0.003
0.001
-0.001
dL(cor)/Lo(cor)
pure yttria 1200
pure yttria 1300
pure yttria 1000
pure yttria 1550
0
500
1000
1500
2000
2500
3000
3500
4000
(t-to)(s)

(a)

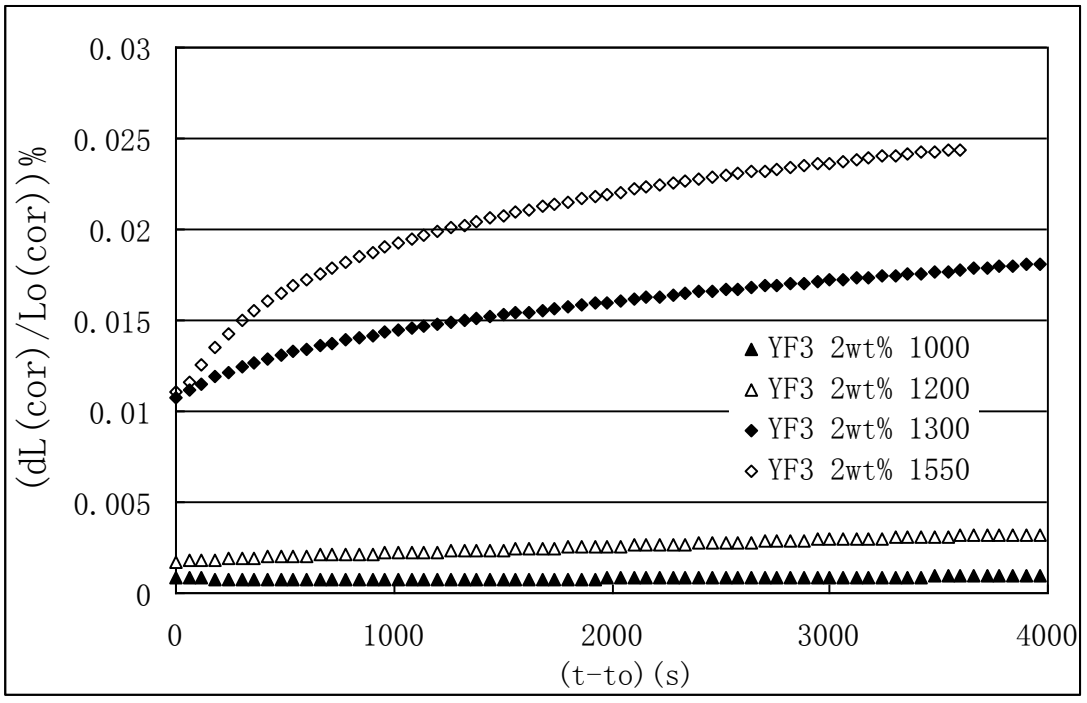
0.03
0.025
0.02
0.015
0.01
0.005
0
(dL(cor)/Lo(cor))%
YF3 2wt% 1000
YF3 2wt% 1200
YF3 2wt% 1300
YF3 2wt% 1550
0
1000
2000
3000
4000
(t-to)(s)

(b)

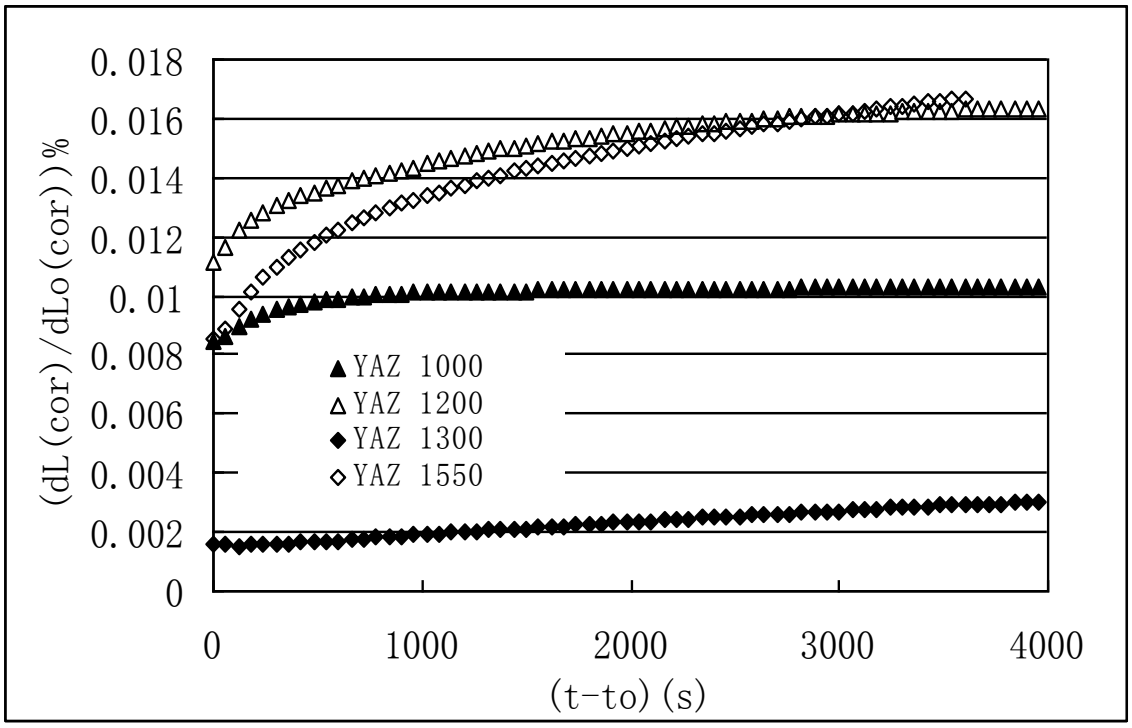
0.018
0.016
0.014
0.012
0.01
0.008
0.006
0.004
0.002
0
(dL(cor)/dLo(cor))%
YAZ 1000
YAZ 1200
YAZ 1300
YAZ 1550
0
1000
2000
3000
4000
(t-to)(s)

(c)

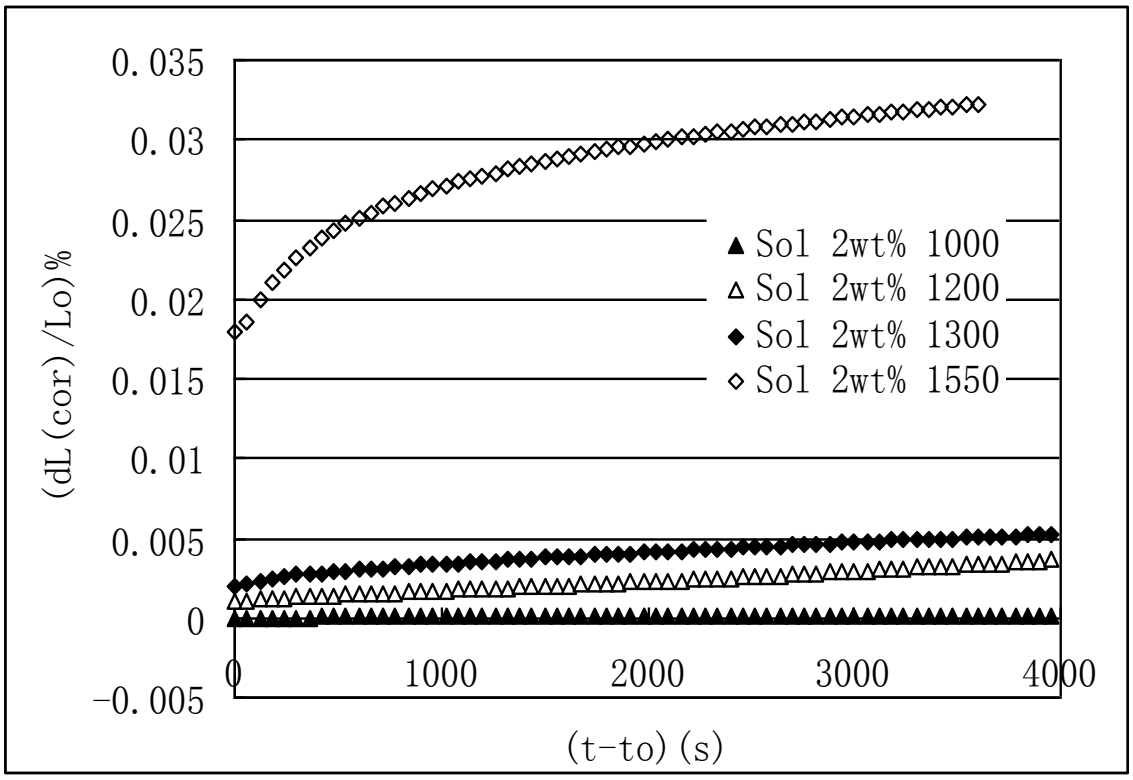
0.035
0.03
0.025
0.02
0.015
0.01
0.005
0
-0.005
(dL(cor)/Lo)%
Sol 2wt% 1000
Sol 2wt% 1200
Sol 2wt% 1300
Sol 2wt% 1550
0
1000
2000
3000
4000
(t-to)(s)

(d)

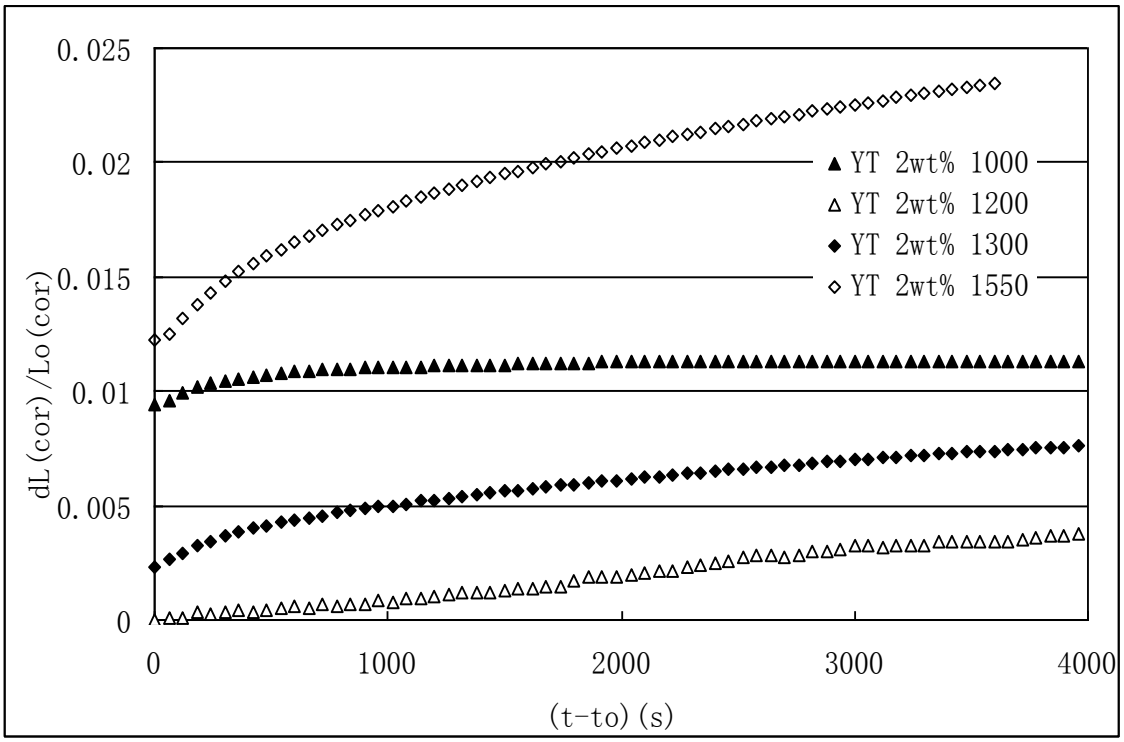
0.025
0.02
0.015
0.01
0.005
0
dL(cor)/Lo(cor)
YT 2wt% 1000
YT 2wt% 1200
YT 2wt% 1300
YT 2wt% 1550
0
1000
2000
3000
4000
(t-to)(s)

(e)

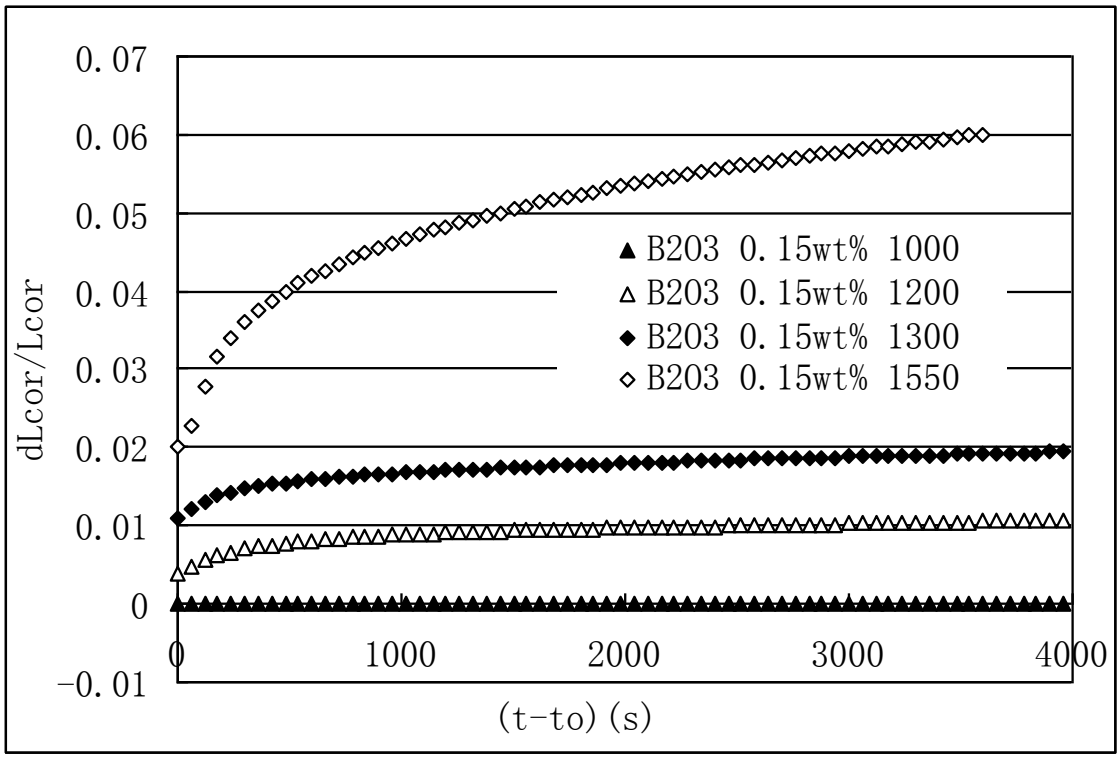
0.07
0.06
0.05
0.04
0.03
0.02
0.01
0
-0.01
dLcor/Lcor
B203 0.15wt% 1000
B203 0.15wt% 1200
B203 0.15wt% 1300
B203 0.15wt% 1550
0
1000
2000
3000
4000
(t-to)(s)

(f)

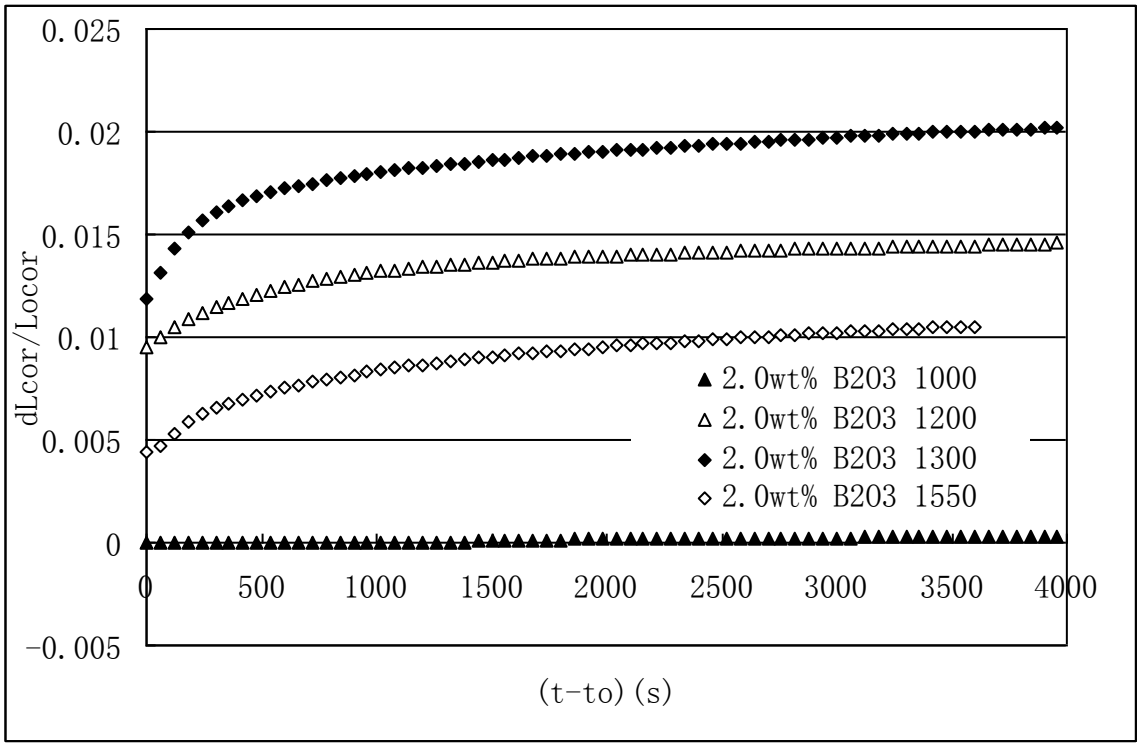

(g)

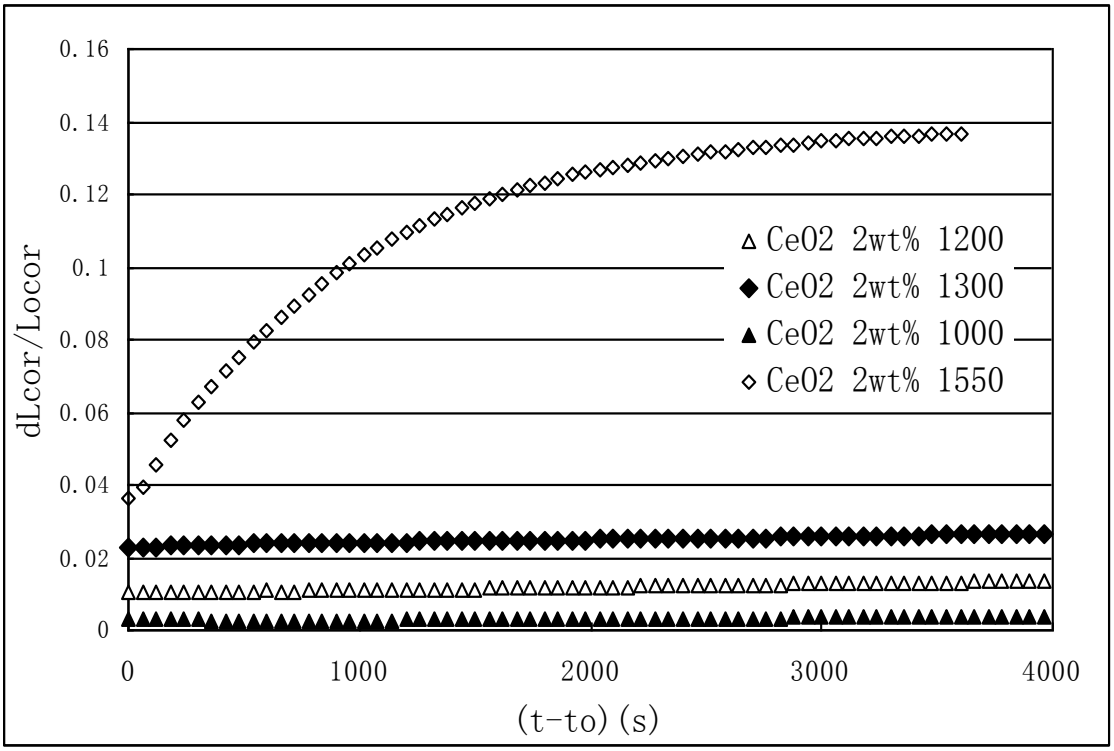

(h)

Figure 8-4. The corrected isothermal trace.(a) pure yttria, (b) 2.0 wt% YF_3, (c) YAZ, (d) Yttria +sol, (e) 2.0 wt% TiO_2, (f) 0.15 wt% B_2O_3, (g) 2.0 wt% B_2O_3, and (h) 2.0 wt% CeO_2.

By taking logarithms of the corrected time and shrinkage in Figure 8-4, a linear relationship of the corrected shrinkage and the corrected time based on equation 8-11 are obtained in Figure 8-5, and the slope value *n* of each line can be measured and shown in Table 8-2.

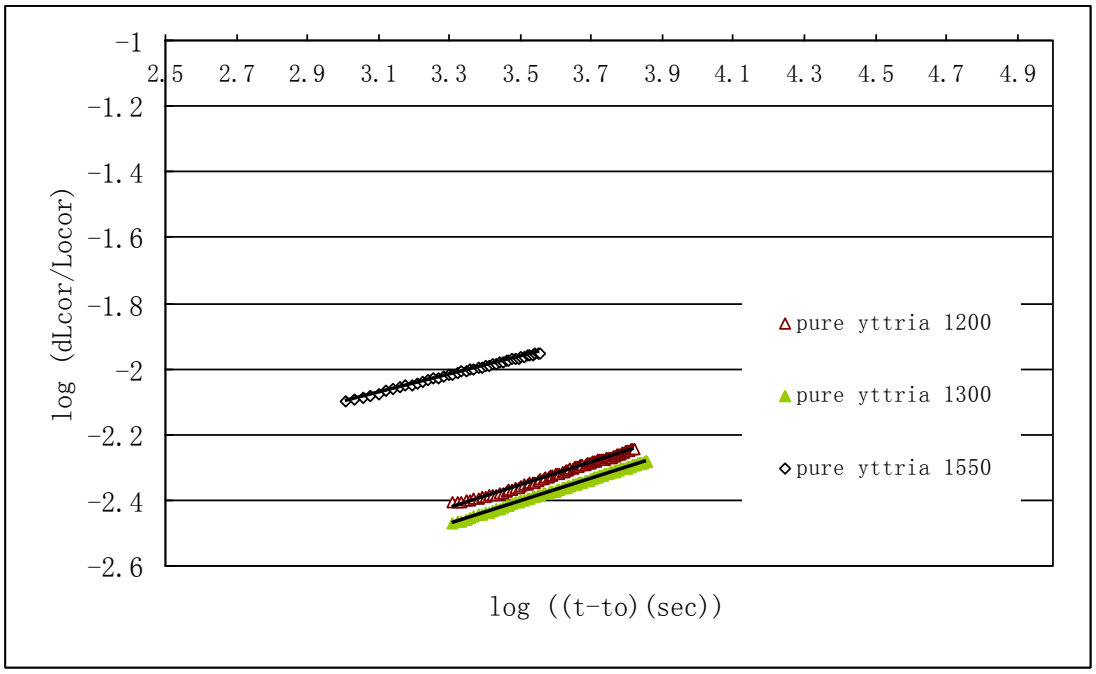

*At 1000°C yttria powder still in expansion

(a)

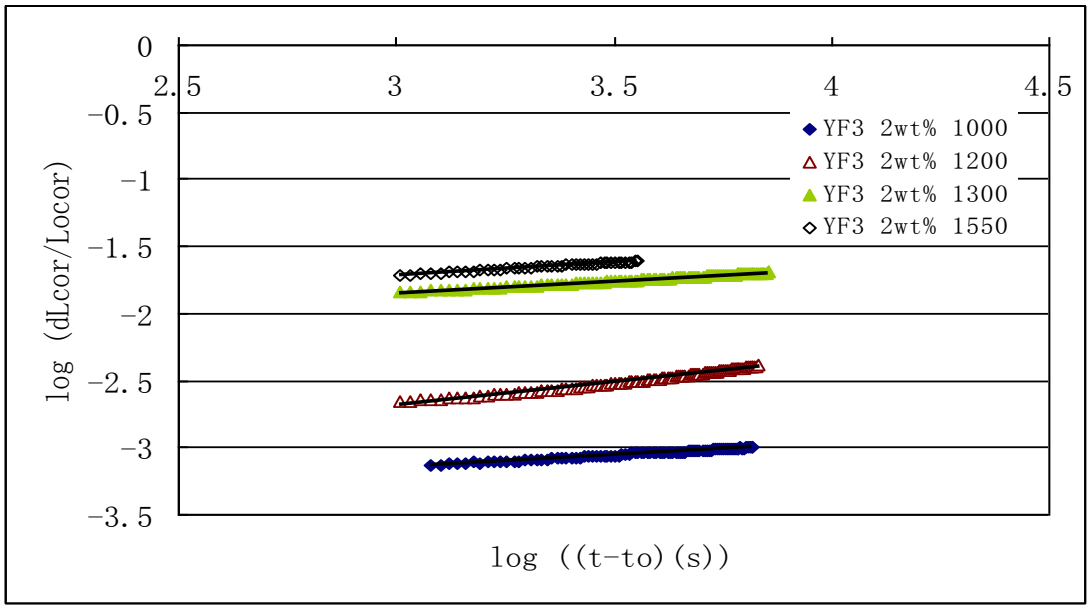

(b)

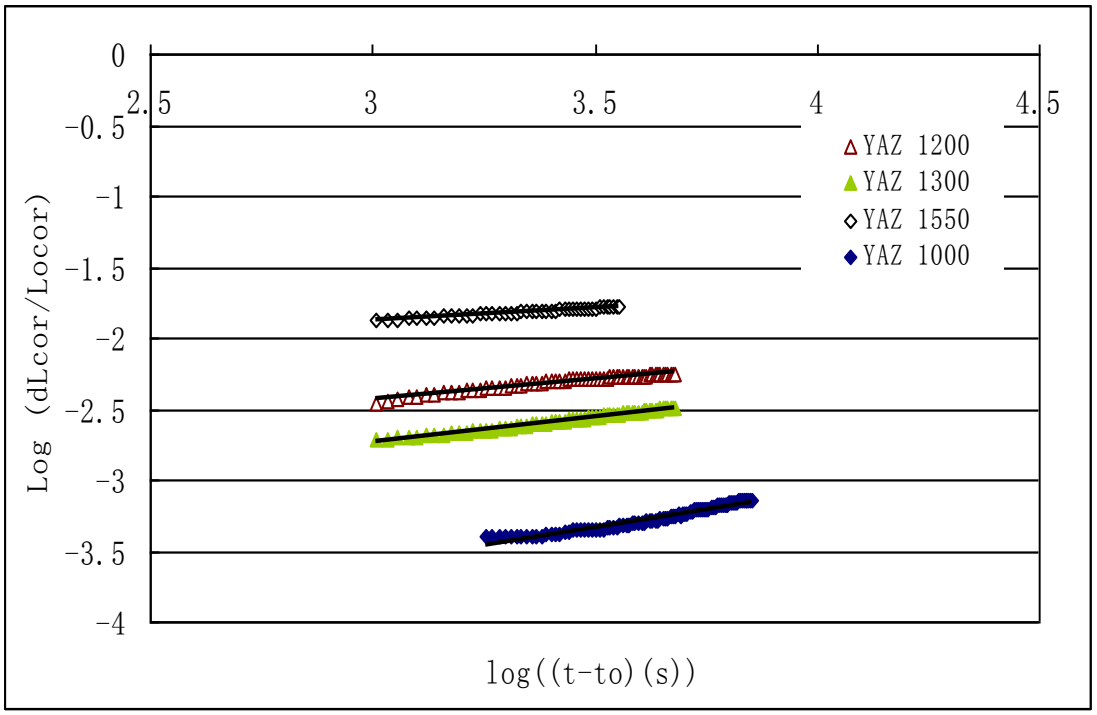
0
-0.5
-1
-1.5
-2
-2.5
-3
-3.5
-4
2.5
3
3.5
4
4.5
Log (dLcor/Locor)
log((t-to)(s))
YAZ 1200
YAZ 1300
YAZ 1550
YAZ 1000

(c)

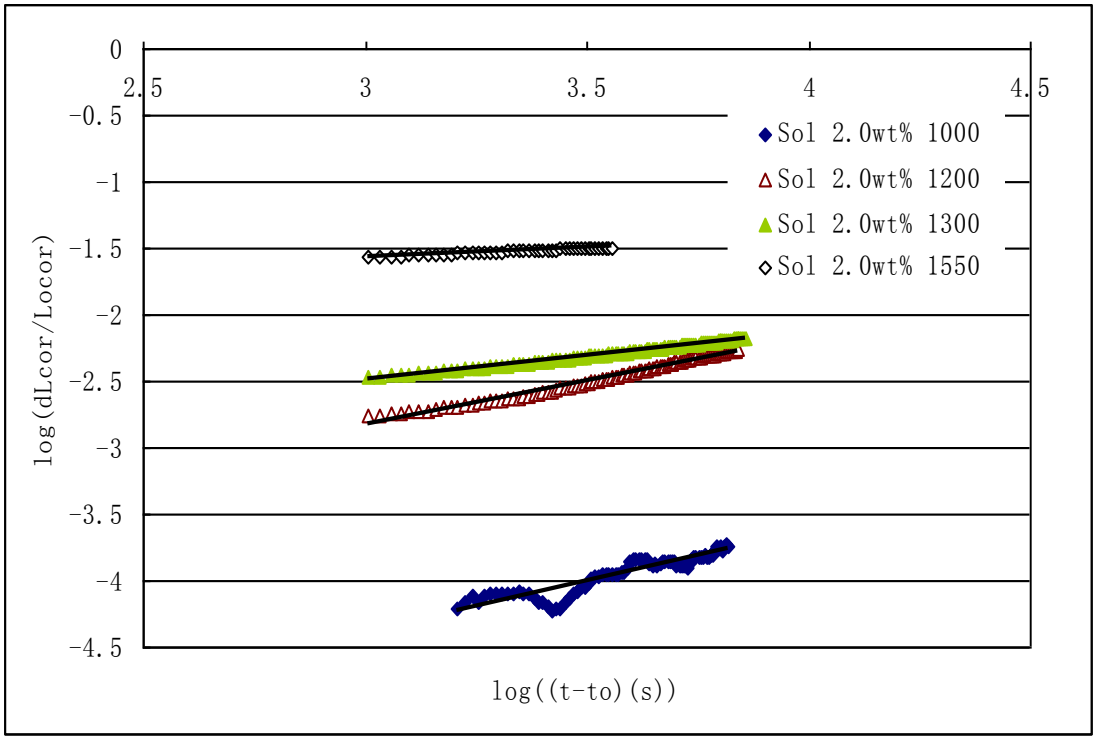
0
-0.5
-1
-1.5
-2
-2.5
-3
-3.5
-4
-4.5
2.5
3
3.5
4
4.5
log(dLcor/Locor)
log((t-to)(s))
Sol 2.0wt% 1000
Sol 2.0wt% 1200
Sol 2.0wt% 1300
Sol 2.0wt% 1550

(d)

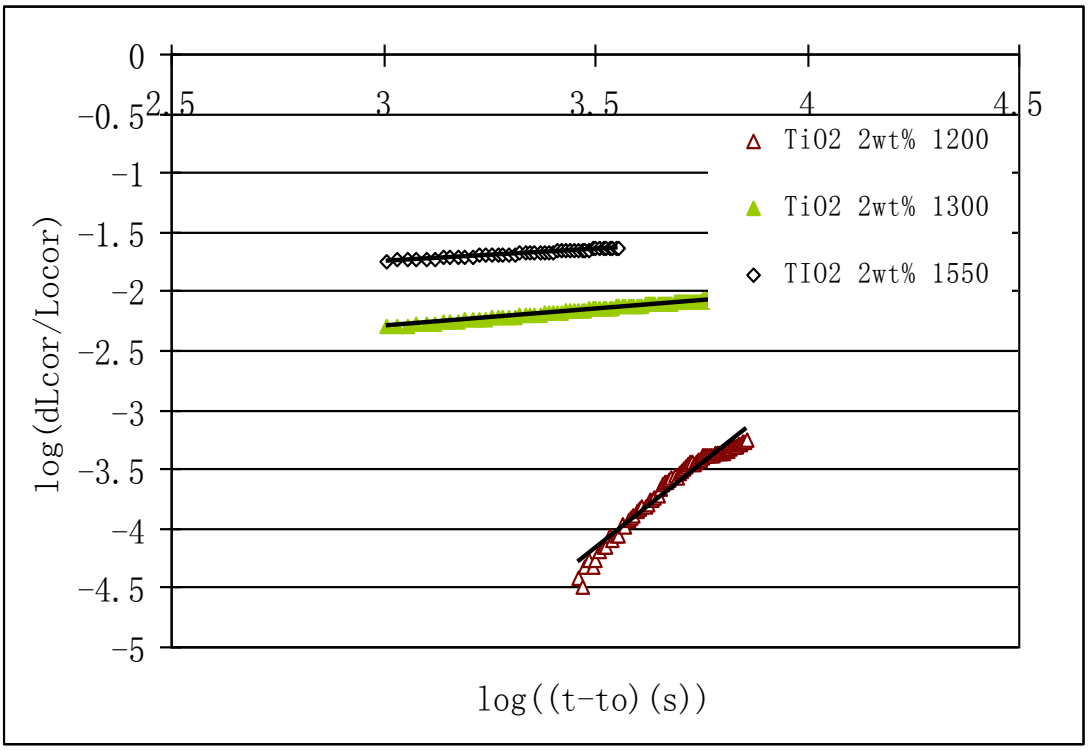

*no 2wt% TiO_2 1000 data available due to powder still in expansion stage.

(e)

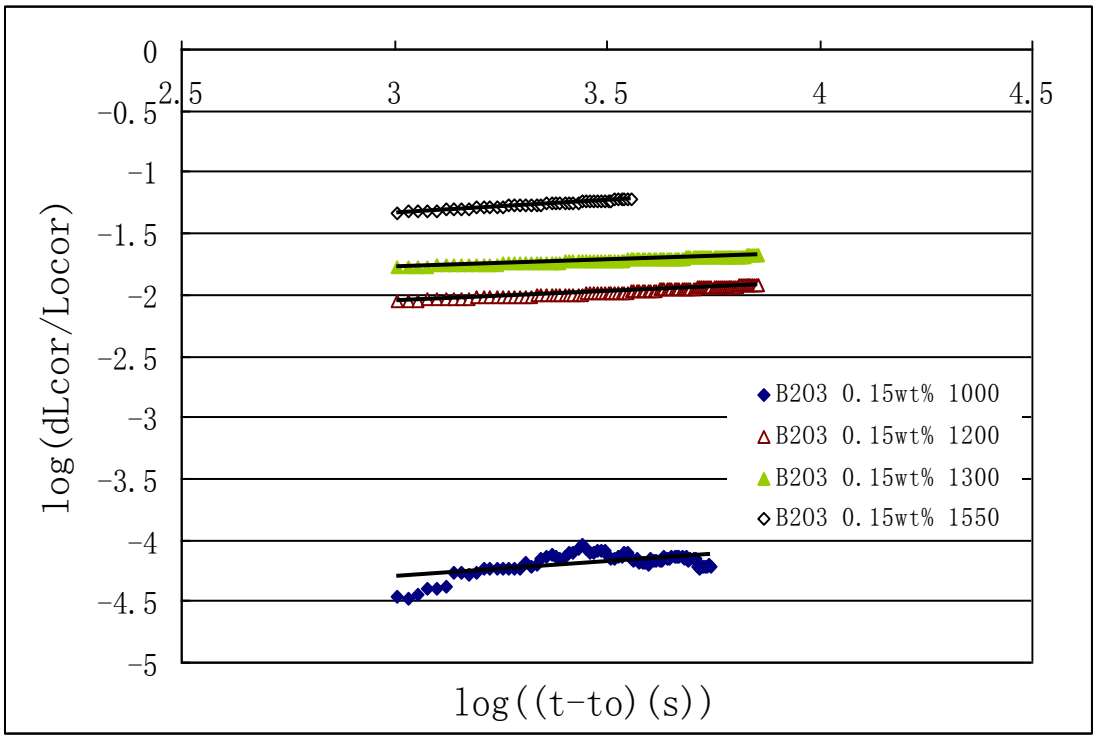

(f)

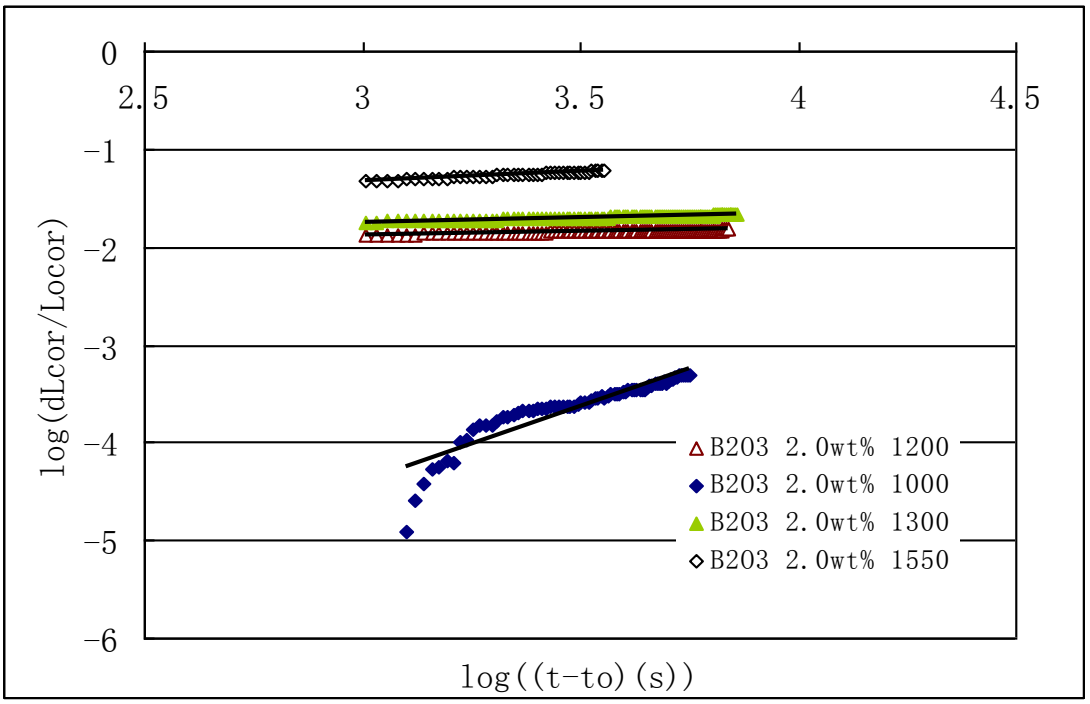

(g)

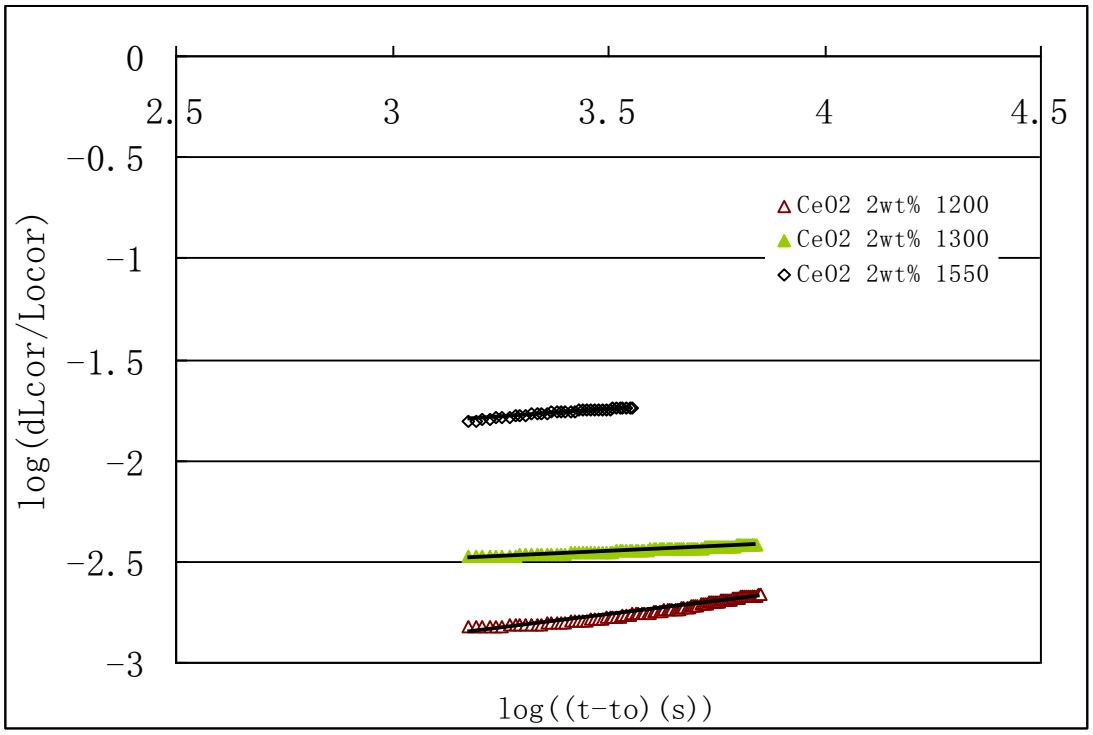

*no CeO_2 2 wt% 1000 data available due to powder being still in the expansion stage.

(h)

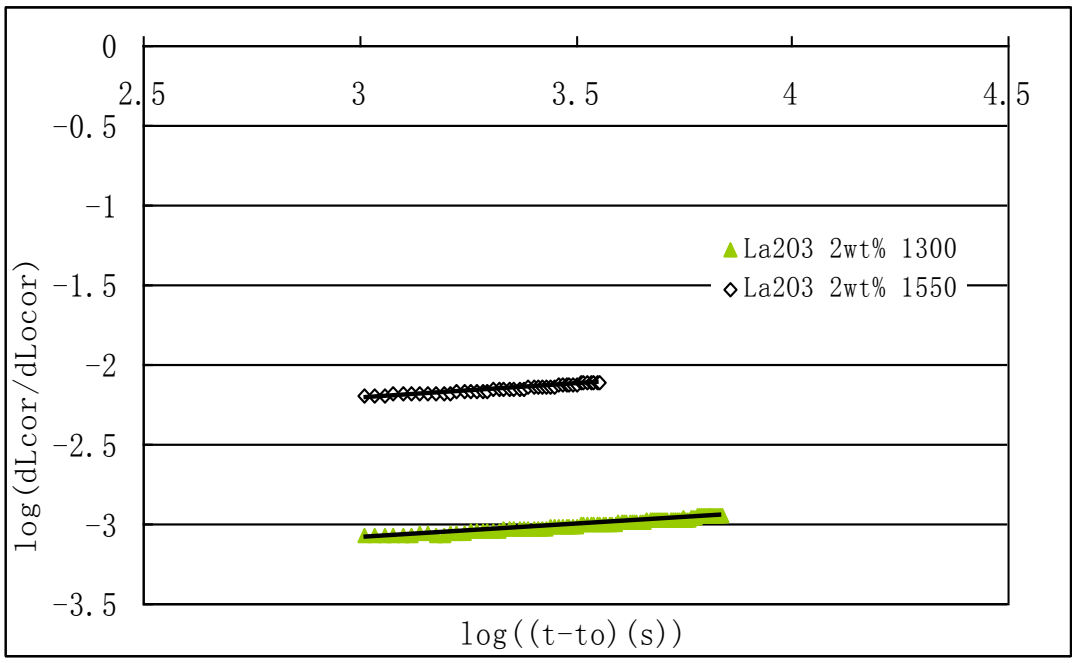

*no 2wt% La_2O_3 1000, 1200 data available due to powder still in expansion stage.

(i)

Figure 8-5. Logarithm-corrected shrinkage-logarithm time plots of (a) pure yttria, (b) 2.0 wt% YF_3, (c) YAZ, (d) Yttria +sol, (e) TiO_2 2.0 wt%, (f) 0.15 wt% B_2O_3, (g) 2.0 wt% B_2O_3, (h) 2.0 wt% CeO_2, and (i) 2.0 wt% La_2O_3.

Table 8-2. Sintering mechanism *n* value of each powder at different sintering temperatures.

Sample ID	1000 °C	1200 °C	1300 °C	1550°C
Yttria	**Expansion**	**0.31**	**0.32**	**0.27**
Sol 2.0wt%	**0.76**	**0.66**	**0.36**	**0.14**
B_2O_3 0.15wt%	0.26	0.20	0.16	0.11
B_2O_3 2.0wt%	Re-solidification after forming new phase 1.56	0.06	0.09	0.20
YF_3 2.0wt%	0.19	0.34	0.18	0.19
TiO_2 2.0 wt%	Expansion (no shrinkage)	2.86	0.30	0.21
YAZ	0.50	0.28	0.36	0.18
CeO_2 2.0wt%	Expansion (no shrinkage)	0.27	0.09	0.32
La_2O_3 2.0wt%	Expansion (no shrinkage)	Expansion	0.17	0.16

Based on each *n* value and published sintering mechanisms in Table 8-2, the powder

sintering mechanism at different sintering temperatures are listed in Table 8-3.

Table 8-3. The different sintering mechanism of different powder at different isothermal heating temperature.

Sample ID	1000°C	1200°C	1300°C	1550°C
Pure yttria	**Expansion**	**Bulk diffusion**	**Bulk diffusion**	**g. b diffusion**
Sol 2.0wt%	**Vapor diffusion**	**Vapor diffusion**	**Bulk diffusion**	**g. b diffusion**
B_2O_3 0.15wt%	g. b diffusion	g. b diffusion	g. b diffusion	Dissolution-precipitation (liquid phase sintering)
B_2O_3 2.0wt%	Re-solidification after forming New phase 1.56	Dissolution-precipitation (liquid phase sintering)	Dissolution-precipitation (liquid phase sintering)	g. b diffusion
YF_3 2.0wt%	g. b diffusion	Bulk diffusion	g. b diffusion	g. b diffusion
TiO_2 2.0 wt%	Expansion (no shrinkage)	Viscous flow	Bulk diffusion	g. b diffusion
YAZ	Vapor diffusion	g. b diffusion	Bulk diffusion	g. b diffusion
CeO_2 2.0wt%	Expansion (no shrinkage)	g. b diffusion	Dissolution-precipitation (liquid phase sintering)	Bulk diffusion
La_2O_3 2.0wt%	Expansion (no shrinkage)	Expansion (no shrinkage)	g. b diffusion	g. b diffusion

As can be seem from the table, B_2O_3 is the most effective additive through the entire experimental groups due to the dissolution-precipitation sintering mechanism which taken place at comparably low temperature around 1200 °C, which largely enhanced powder sintering. The sintering additives YF_3 and YAZ can also enhance material diffusion between

particles with different sintering mechanisms, and no compact expansion took place at sintering temperatures around 1000 °C. Sintering additives such as TiO_2, CeO_2 and La_2O_3 seem to retard yttria powder sintering at temperatures around 1000 to 1200 °C, and proved more beneficial in improving the sintering of the powder at temperatures higher than 1200 °C (confirmed with the published data [138, 141]).

However, the results shown in the table show that the dominant sintering mechanism for the 2.0 wt% B_2O_3 added powder is liquid state sintering at temperatures around 1200 °C. But from the phase diagram, the liquid phase only appeared at temperatures higher than 1373 °C (Figure 8-2) unless the additives segregated to local areas (particle surface, grain boundary) which can cause the liquid to be present below the eutectic temperature [190]. Also, the table also shows that at 1400 °C, the dominating sintering mechanism for powder 2.0 wt% CeO_2 is dissolution-precipitation (liquid phase sintering), but from the XRD data in Figure 3-19 (f), there is no evidence to support this prediction.

By analyzing the experimental observations and the predicted sintering mechanisms, the results shown in Table 8-3 seem to have slightly over estimated the powder sintering temperatures for certain sintering mechanism. But the sintering mechanisms and the correction methods shown above still can give a general idea of powder sintering behaviors and the material diffusion routes.

8.1.1.6 Sintering activation energy calculation (CRH)

By using the constant rate heating method [158, 159], the powder sintering activation energy can be calculated from the slope of the trace by plotting $\ln\left(T\left(dT/dt\right)\left(d\rho/dT\right)\right)$ and *1/T* according to equation 3-6. Because the sintering mechanisms change with temperature, the activation energy for powder sintering also changed. Figure 8-6 gives an example of the different sintering activation changes with temperatures.

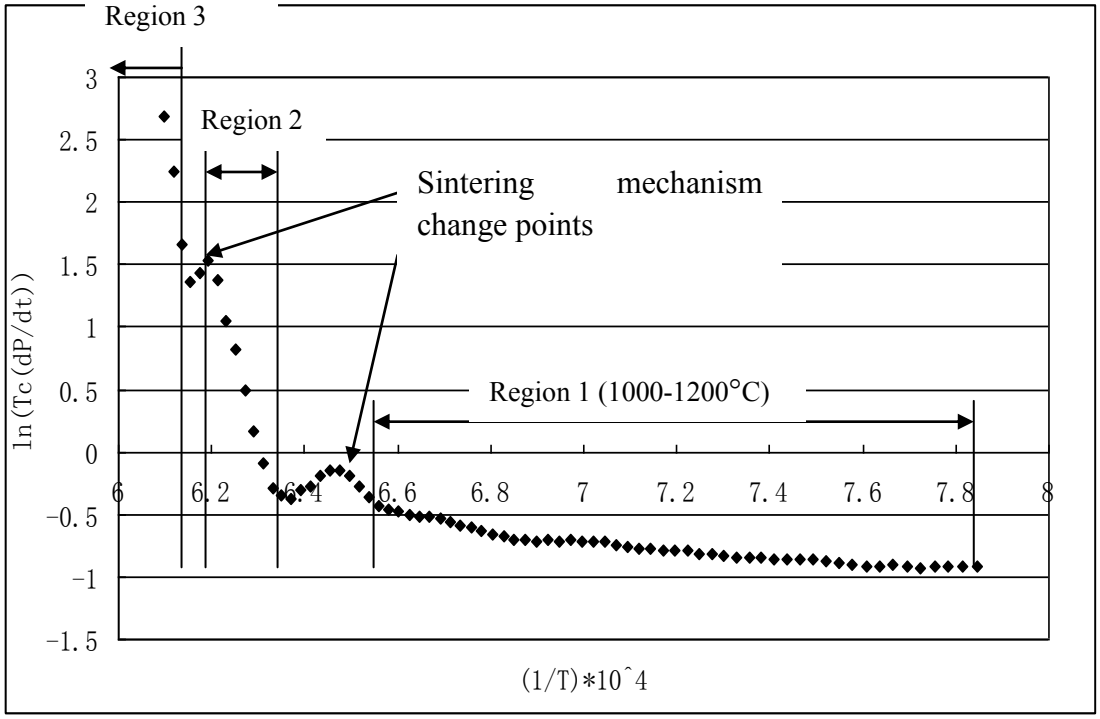

Figure 8-6. The shrinkage curve of pure yttria with annotations.

From this graph it can be seen that, by increasing the sintering temperature, the sintering curve can be divided into three regions, in each region, the plot of value $\ln\left(T\left(dT/dt\right)\left(d\rho/dT\right)\right)$ and *1/T* has a linear relationship. The sintering activation energy changes at different temperature ranges. The detailed trace information at different

temperature regions of pure yttria sintered at 5 °C/min is shown in Figure 8-7.

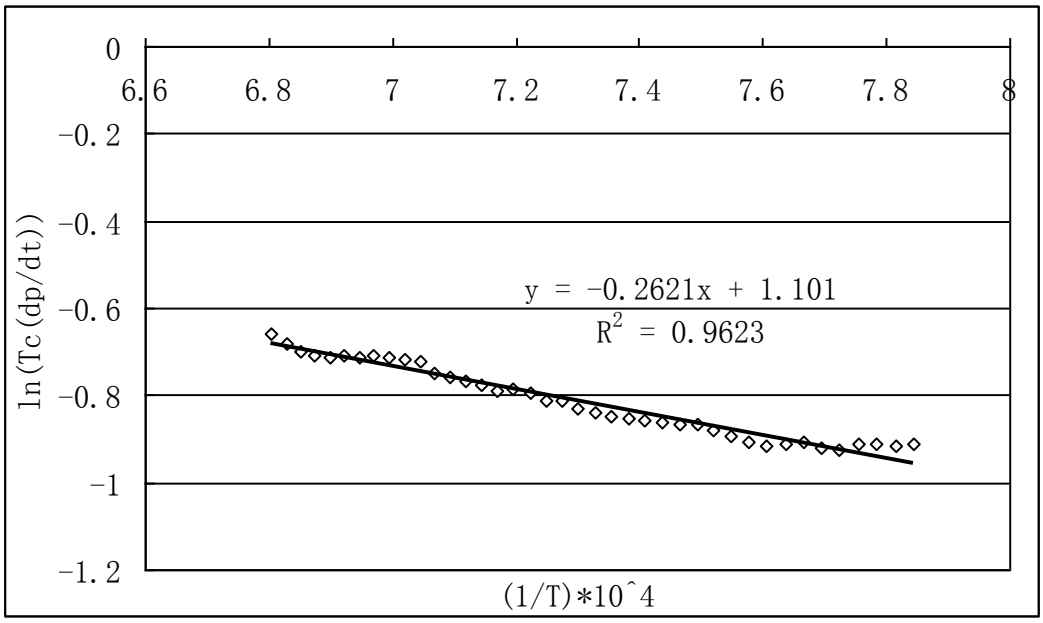

(a)

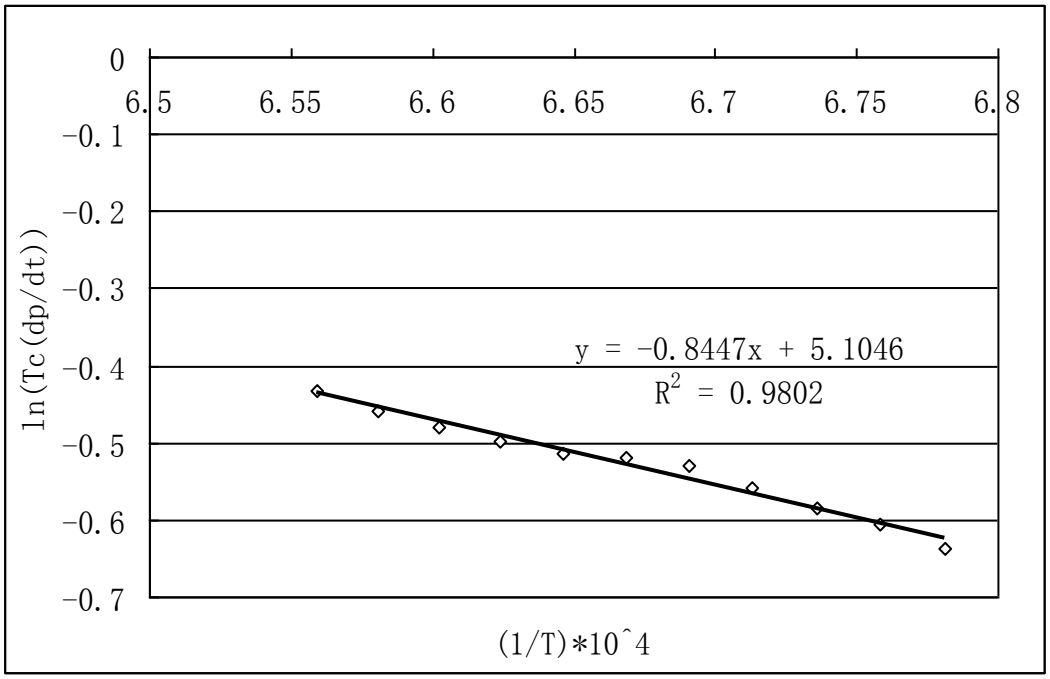

(b)

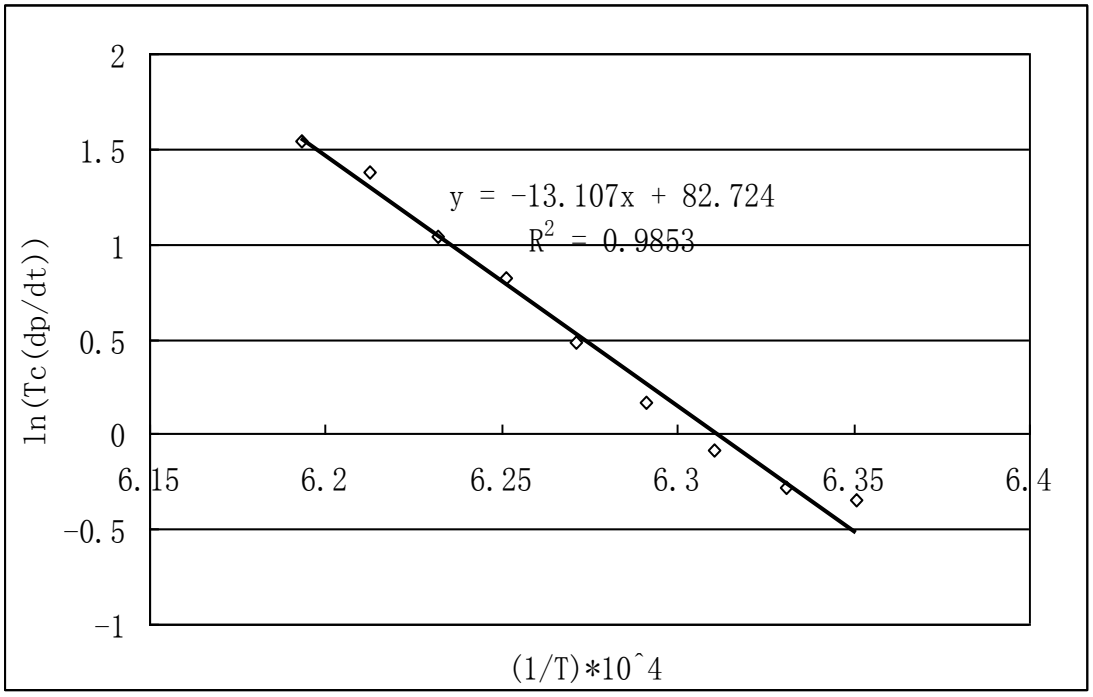

(c)

Figure 8-7. Constant rate heating (CRH) shrinkage trace of pure yttria powder. (a) region 1 (1000-1200°C), (b)region 2 (1200-1250 °C), and (c) region 3 (1250-1400 °C).

The sintering activation energy calculated from equation 3-6 using the data in Figure 8-7 with the predicted sintering mechanism (Table 8-3) is shown in Table 8-4.

Table 8-4. Yttria sintering activation energy at different temperature range.

temperatures	1000-1200°C	1200-1250°C	1250-1400°C	1400-1500°C
energy	78.675 kJ/mol	331.8 kJ/mol	509.56 kJ/mol	324.71 kJ/mol
Sintering mechanisms	Expansion	Bulk diffusion	Bulk diffusion	g. b diffusion

The published data for yttria powder sintering for grain boundary diffusion are 410 kJ/mol [191], 340 kJ/mol [192], 398 kJ/mol [193], 336 kJ/mol [194] and for bulk diffusion is 4.1ev

(equal to 395 kJ/mol) [194]. In this experiment, the grain boundary diffusion activation energy was calculated to be around 324.71 kJ/mol and bulk diffusion activation energy around 331.8 to 509 kJ/mol, very similar to the published data. The similarly between the activation energy value of this experiment and published data means that the methods can successfully be used in this experiment, and the other sintering additive sintering activation energies calculated using this method are listed in Table 8-5.

Table 8-5. The activation energy at different temperature range of different sintering additive added

Sol 2 wt%	1000-1100 °C	1100-1150 °C	1150-1300 °C	1300-1400 °C	1400-1550 °C
energy	33 kJ/mol	126 kJ/mol	566 kJ/mol	382 kJ/mol	319 kJ/mol

$B_2O_3$0.15wt%	1000-1100°C	1100-1150 °C	1150-1200 °C	1200-1350 °C	1350-1550 °C
energy	393kJ/mol	123kJ/mol	-283 kJ/mol	589 kJ/mol	259 kJ/mol

$B_2O_3$2 wt%	1000-1100 °C	1100-1200 °C	1200-1300 °C	1300-1400 °C	1400-1550 °C
energy	274 kJ/mol	170 kJ/mol	-139 kJ/mol	133 kJ/mol	298 kJ/mol

YF_3 2 wt%	1000-1100 °C	1100-1200 °C	1200-1300 °C	1300-1400 °C	1400-1550 °C
energy	-72 kJ/mol	97 kJ/mol	730 kJ/mol	211 kJ/mol	177 kJ/mol

$TiO_2$2wt%	1000-1100 °C	1100-1200 °C	1200-1300 °C	1300-1400 °C	1400-1550 °C
energy	67 kJ/mol	534 kJ/mol	508 kJ/mol	229 kJ/mol	148 kJ/mol

YAZ	1000-1150°C	1150-1200 °C	1200-1300 °C	1300-1400 °C	1400-1550 °C
energy	unsintered	1743 kJ/mol	822 kJ/mol	179 kJ/mol	79 kJ/mol

CeO_2 2 wt%	1000-1150 °C	1150-1250 °C	1250-1300 °C	1300-1500 °C
energy	unsintered	157 kJ/mol	857 kJ/mol	614 kJ/mol

La_2O_3 2 wt%	1000-1250 °C	1250-1300 °C	1300-1500 °C
energy	17 kJ/mol	281 kJ/mol	668 kJ/mol

Therefore, from Table 8-3 and Table 8-5 it can be seen that the sintering activation energy for the solid state sintering is higher than the liquid phase sintering process. By adding different sintering additives, the activation energy for the yttria powder sintering is different for different systems dependent on the different sintering mechanisms. In this experiment, the activation energy for bulk diffusion is around 400 kJ/mol and for gain boundary diffusion is around 300 kJ/mol. But for liquid phase sintering, the activation energies are always less than 250 kJ/mol, and some powder systems such as B_2O_3 have a negative value. The negative calculated activation energy of sintering means that at that temperature range, due to the chemical interaction taking place, the material diffusion between particles can largely enhanced without further increasing sintering temperatures.

8.2 Face coat slurry development

8.2.1 The life of the slurry

The life of the slurry is different for different sintering additive systems. Most aqueous solution of the metal oxides used in this experiment are acidic, e.g. for 0.15 wt% boron oxide dissolved into 100 ml water, the solution had pH value around 3.62. But the polymer water solution (Poly vinyl alcohol) has a pH around 6.27. Therefore, the mis-match in pH of the polymer solutions and the oxide solutions will cause premature gelling problems in the slurry.

The study (Figure 4-8) found that the yttria filler will still undergo a slow gelation process even without adding sol into the slurry. For the water based pure yttria filler binder slurry, the life was around two weeks. The amount of the sintering aids will also influence the yttria particle gelation speed, the more additive the quicker of the slurry gelation, e.g. YF 0.15 wt% had a life time around 10 days while YF 2.0 wt% had a life time only around 5 days (Figure 4-8). However, some of the sintering additives had the opposite effect, which can extend the life of the slurry, e.g. the YB 0.15 and YAZ face coat slurry systems. The increase in the life of the YAZ face coat slurry may due to the addition of ZrO_2 particles. Yasrebi, M, 1997 [86] studied the colloidal stability of zirconia-doped yttria–silica binary aqueous suspensions and found ZrO_2 has higher hydration rate than Y_2O_3, therefore, instead of the hydration reaction taking place between yttria particles, ZrO_2 will first hydrate and slow down the gelation of the slurry. There is no published data available to explain the reduced

hydration effect of the slurry with B_2O_3 as the additive. For industrial purposes, the slurry should have a life time of at least 2 weeks. Therefore, the slurry candidate YB 0.15, YAZ, YF 0.15 may be used in this application.

8.2.2 Face coat surface finish

Shell surface roughness not only influenced the surface finish of the cast metal component but also influenced the wetting or spreading behavior of the metal on the ceramic shell [55]. The smoother the shell surfaces, the easier it is for liquid metal to spread out [54].

From Figure 4-9 can be seen that, after sintering additives were added into the slurry, the shell surface roughness was changed. The yttria + sol and YAZ face coats have the smoothest surface finish, but the maximum roughness difference between the best and the worst face coat is around 3 μm in the test samples, which is acceptable for the industrial use.

8.2.3 Sintering properties of the face coat

Due to the different green density and packing structures, the slip cast and the filler powder compacts showed different sintering behaviors, especially at temperatures exceed 1200 °C. The filler powder compact seems likely to have a lower sintering starting temperature but with a delayed densification speed, see Figure 4-12. At low heating temperatures (25-500 °C), the slip cast samples shows some small shrinkage peaks in the dilatometer traces due to water evaporation, polymer burn out, and yttrium acetate decomposition.

Polymer addition face coats seem to have some benefit in increased face coat strength, which was confirmed by the friability test results shown in Table 4-4 and Table 4-5. At 1000 °C, nearly all the face coats were still undergoing thermal expansion and no densification took place, but after increasing the sintering temperature to around 1200 °C, YB 0.15 wt%, YT 2.0 wt% and YF 2.0 wt% powder had already begun to shrink, with decreasing friability, see Table 4-5 (except for the YT 2.0 wt% sample). One possible explanation of the high friability value of YT 2.0 wt% sample is the large density grains formed (Figure 4-10, (d)), which had very poor bonding with powder matrix and easily brushed off during the friability test.

8.3 Chemical inertness of the face coat

8.3.1 Face coat refractory thermodynamic analysis

It has been observed that the extent of the chemical interaction between the molten metal and ceramic is different for different face coat systems, dependent on the thermodynamic inertness of the oxides when in contact with molten metal. High interaction temperatures make the decomposition of the oxide and the oxidation of the TiAl alloy become an energetically favorable process. The thermodynamic inertness of the face coat is dependent on the Gibbs free energy changes during the decomposition process based on equation 8-13 below [68]:

$$M_xO_y = yO(TiAl) + xM \qquad 8\text{-}13$$

where, x, y, are constants dependent on the oxide. After the interaction, the released oxygen

will penetrate into the metal and oxidize or harden the metal at the metal/shell interface. Yttria, as a rare earth oxide, used in this experiment has a superior inertness against molten TiAl alloys [41, 80] when compared to many oxides.

As is known, the sintering additive YF_3 has a low evaporation temperature, around 1000 °C [155], and no YF_3 peaks have been detected at elevated sintering temperatures, even when 2.0 wt% of YF_3 was added into yttria, by the XRD tests in Figure 3-21(a). Therefore, the influence of the YF_3 in the face coat after sintering at 1200 °C for one hour on the chemical inertness of the yttria face coat is limited. In the sample of YB 0.15, 0.15 wt% B_2O_3 was added into the yttria powder to help sintering. When sintering at 1200 °C, boron oxide will interact with the yttria forming the new phases, YBO_3 or Y_3BO_6. Because of a lack of thermal chemical data having been reported for those compounds, the chemical inertness of this type of shell was previously unknown. However, with only a small amount of boron added into the face coat this would not influence the thermal inertness of the yttria dramatically.

For the face coat with YAZ, in which 0.5 wt% Al_2O_3 and 0.5 wt% ZrO_2 were added into the yttria. From the ternary phase diagram of Y_2O_3-Al_2O_3-ZrO_2 [175], when sintered at 1200 °C, the possible new phases in the YAZ face coat may be $Y_4Zr_3O_{12}$ and $Y_4Al_2O_9$, and these new phases may react with the molten metal and degrade the inertness of the yttria face coat. Some metal oxide formation Gibbs energies are shown in Table 8-6 [68].

Table 8-6. The formation energy (kJ/mol) of ceramic systems at 1873K, 1898K and 1923K. per mol/O_2 [68]

compositions	**1873k**	**1898k**	**1923k**
Y_2O_3	-899.77	-894.66	-864.89
Al_2O_3	-707.11	-701.45	-695.79
ZrO_2	-723.26	-729.33	-724.39
TiO_2	*-568.339*	*-562.77*	*-557.18*

Considering the oxidation properties of TiAl alloys when interacting at 1600 °C, 1625°C, and 1650 °C, as the metal oxide Gibbs reduction energy of yttria and zirconia are much more negative than TiO_2 and Al_2O_3, so the decomposition of yttria in energetically unfavorable.

Based on the above discussion and the amount of sintering additive, all the new developed test face coat systems have reduced thermochemcial inertness compared with the yttria + sol face coat system, and the more sintering additives added into the face coat the greater the chance for the face coat to interact with metal.

8.3.2 Wetting dynamics of molten TiAl on the shell

It has been reported previously that the initial contact angle of a liquid metal on a ceramic substrate is closely related to the substrate roughness, the rougher the shell the larger the contact angle [54]. Due to a similar measured roughness for all the face coats (reported in Chapter 4), so the influence of the surface roughness on the molten metal spreading on the shell surface was small. In the experiments, the behavior of the molten metal drop on the ceramic shell is considered to be an interaction controlled process.

After re-melting, molten metal interacted with face coat spread out on the shell surface. The spreading rate of the molten metal was different for the different face coat systems. From the literature (Chapter 2), the fastest diameter change for the drop is due to the interaction taking place between the shell and molten metal.

By observing the wetting behavior of molten drops on ceramic shells, Lopez and Kennedy [60] indicated that the wetting process is thermally activated, since the process clearly showed temperature dependency, and followed a strong Arrhenius type behavior:

$$\frac{dr}{dt} = k \exp\left[\frac{-E_a}{RT}\right] \qquad 8\text{-}14$$

where, r is diameter of the sessile drop, t the measured time. dr/dt is the speed of sessile drop spreading, k is a numerical constant, E_a is the spreading activation energy, R is the gas constant, and T is the temperature (°C). By taking logarithms of both sides, equation 8-14 is formed:

$$\log\left(\frac{dr}{dt}\right) = \log k - \frac{E_a}{R}\left(\frac{1}{T}\right) \qquad 8\text{-}15$$

Therefore, plotting the logarithm of the sessile drop contact diameter change rate for different systems against 1/T, the activation energy for the metal spreading on each ceramic face coat system can be calculated from the slope of the traces. The Arrhenius type behavior of the drop contact diameter change can be seen in Figure 8-8 (All the samples showed a very good linear Arrhenius relationship, > 90%).

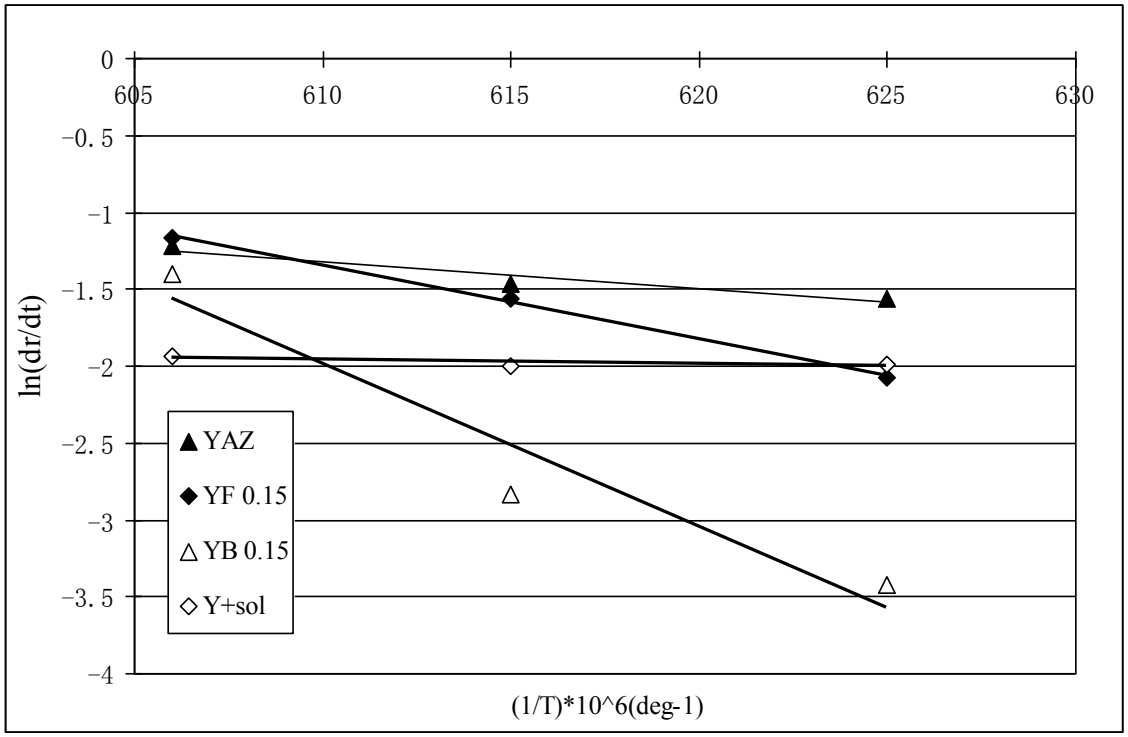

Figure 8-8. Arrhenius plot of the sessile drop diameter change rate at different interaction temperatures.

The spreading activation energy can be calculated from the plot of each line, and is shown in Table 8-7:

Table 8-7. The metal spreading activation energy of each face coat system.

Sample ID	**Activation energy (kJ/mol)**
Yttria +Sol	**24.9**
YAZ	144.7
YF 0.15	397.4
YB 0.15	879.6

The spreading activation free energy of TiAl alloys on the sintering additive systems were all larger than that of the pure yttria face coat system. The high value of the activation energy indicated that the spreading is not only dominated by viscous flow, but also closely

associated with the interaction between metal and ceramic. In this work, the face coats of YF 0.15 and YB 0.15 have very large activation energies, which confirmed that the wetting is driven by the chemical reaction at the interface. It also should be noted that, due to the equipment limitations, the drop flash re-melt detecting reaction time *t* is quite low at each temperature. In order to better understand the interaction between the metal and face coat, improvements in testing conditions should be done in future.

Therefore, from this point the reactivity of the face coat system is decreased in the order YB0.15>YF 0.15>YAZ>Y+sol. This prediction is the same as the experimental observation of centrifugal casting of TiAl bars in Chapter 7.

8.3.3 The prediction of re-melting time

Barbosa, 2006[41] found that the high hardness of the TiAl alloy at the metal/shell interfacial area was due to the oxygen from the face coat penetrating into the metal/shell interface during the casting process and causing solid solution hardening in the interface area. Based on this research, the hardened layer growth rate should be also closely related to the oxygen penetration rate at different interaction temperatures. By increasing the contact time, the hardened layer thickness is also increased. According to the diffusion equation, as distance is a function of the square root of time, therefore, the oxygen diffusion distance should also be a linear relationship with the square root of contact time.

In this experiment, contact time (t) was defined as the elapsed time from the ram beginning to move into the chamber 2 to the withdrawal, and a time t_o is needed for the metal piece to fully melt and react with the shell after entry into chamber 2. In order to find the actual interaction time of the molten metal and ceramic, a linear relationship was established between hardened layer thickness and the square root of the real interaction time (t-t_o). By adjusting 't_o' to best fit the linear relationship, the actual interaction time can be obtained, e.g. the largest R^2 value around 0.98 is obtained when t_0 = 51-52s, which means if the contact time is 60s in 1600 °C, the real interaction time between molten metal and ceramic is around 8s. Figure 8-9 shows the linear relationship of the hardened layer thickness and square root of time at different interaction temperatures.

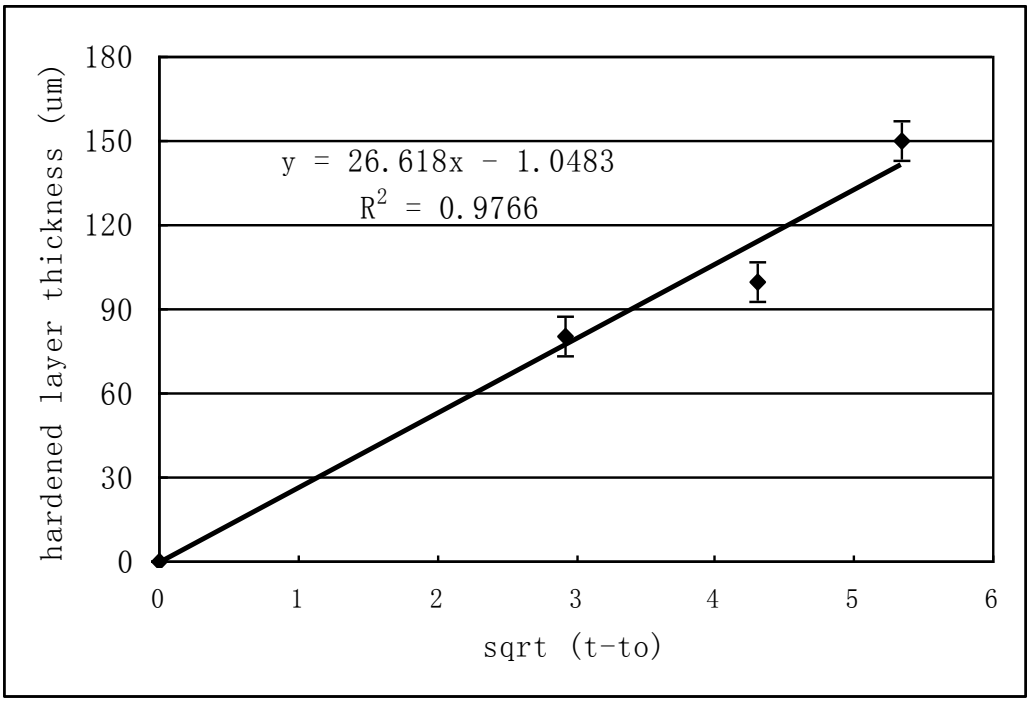

(a)

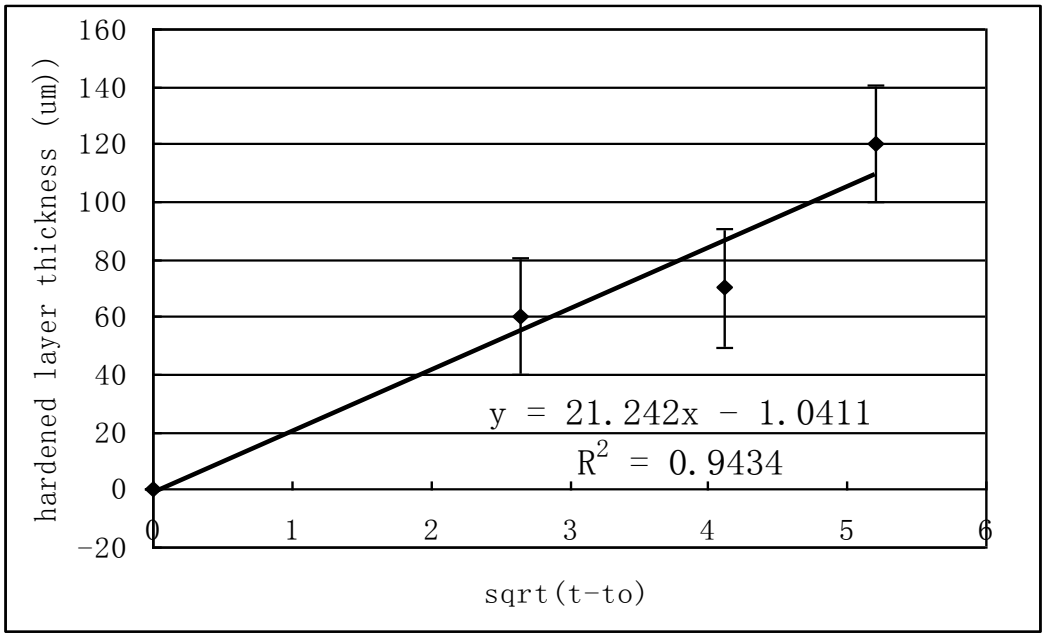

(b)

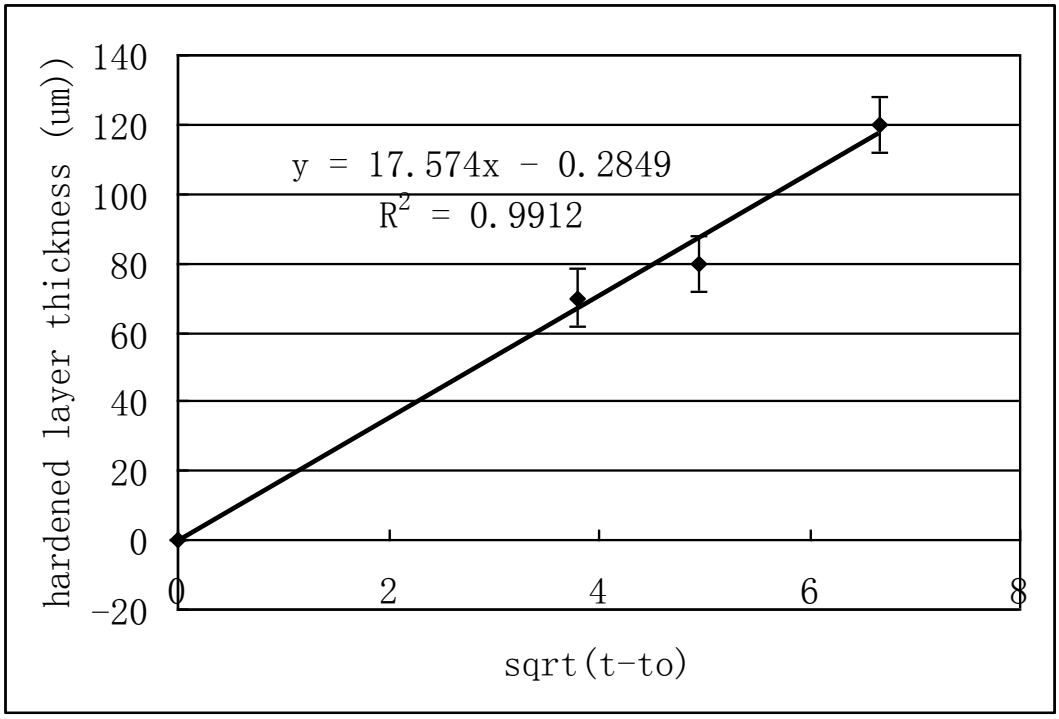

(c)

Figure 8-9. The linear relationship of the hardened layer thickness and square root of time of sample YF 0.15 at different interaction temperature, (a) 1600 °C, (b) 1625 °C, and (c) 1650 °C.

The actual interaction time t_o needed for re-melting the sessile drop at different interaction

temperatures was calculated and shown in Table 8-8. The higher the interaction temperature, the shorter the time needed to fully melt the metal piece on the ceramic shell surface. For interaction at 1600 °C, the calculated real interaction times were 8 s (60 s contact time), 18 s (70 s contact time) and 28 s (80 s contact time). For interaction at 1625 °C, the real interaction times were 5 s, 15 s, 25 s (contact times of 40 s, 50 s, and 60 s). For interaction at 1650 °C, the real interaction times were: 14 s, 24 s, and 34 s (contact times were 30 s, 40 s, and 50 s). Compared to the real interaction time during investment centrifugal casting of around of 2 s for a 10 mm diameter bar, the sessile drop test created a more severe interaction between the ceramic shell and metal.

Table 8-8. The t_o values at different interaction temperatures.

Sample ID	1600 °C	1625 °C	1650 °C
YF 0.15	51-52 s	33-34 s	15-16 s

Due to the limitation of the experimental setting, the metal melting process on the ceramic shells was difficult to observe and control. Therefore, the prediction of the interaction time and the spreading activation energy calculated form this experiment may show some errors.

8.4 The reliability of face coat slurry

8.4.1 The strength of the face coat

The newly developed water based slurry can be successfully used in the small scale plate crucible giving a very smooth surface finish (see Figure 6-2), but when they were used to make the large moulds, after de-wax, the face coat peeled off and de-laminated, see Figure 6-3. The reason for the face coats peeling off during de-wax is the reduced strengthening effect of the polymer in the face coat at temperatures around 180 °C.

In order to improve this behaviour, a new method called the ‗sol back penetration' method was developed. This new method used the gelation reaction which takes place between the face coat and the sol to maintain the face coat strength to very high temperatures. Therefore, by using this method, the face coat can survive in the de-wax process without the face coat pealing off and delaminating. This method offers a new route to produce ceramic shells by separating the slurry manufacture and gelling process.

8.4.2 Si penetration problems by using new methods

The Si penetration problems from the backup coat to the face coat can be influenced by three factors; first is the sintering/firing temperature; second is the face coat additives and the third is the production method.

As it is known, by increasing the sintering temperature, the activity of Si will increase, so

higher Si concentration was detected on the shell surface. The Si diffusion activation energy in the yttria face coat could be calculated according to the Arrhenius relationship in Figure 6-13 and was around 20 kJ/mol.

By adding different sintering additives into the face coat, the Si concentrations on the different face coat surface were different for the same sintering temperatures. These differences were due to the sintering additives enhancing the Si diffusivity in the yttria face coat. At high sintering temperature, the detected Si concentration on the mould surface is decreased, which may due to the higher density of the face coat which made Si diffusion difficult.

By using the ‗sol back penetration' methods, the possibility of Si ions penetrated from the backup layer to the face coat is increased. Two types of sol (yttria sol and Ti-coat sol) were used to test the Si ion penetration distance at different sintering temperatures. From these results, using Ti-coat in the ‗sol back penetration' a much shorter diffusion distance than that using yttria sol was achieved (Figure 6-16, Table 6-5). The different Si penetration distance of those two face coats may due to the different face coat density at different sintering temperatures, and more dense face coat layer seemed to retard Si penetration more, see Figure 8-10 (The Friability test results of the face coat using Ti-coat back penetration methods (Table 6-3) and the %Si penetration distances (Table 6-5)).

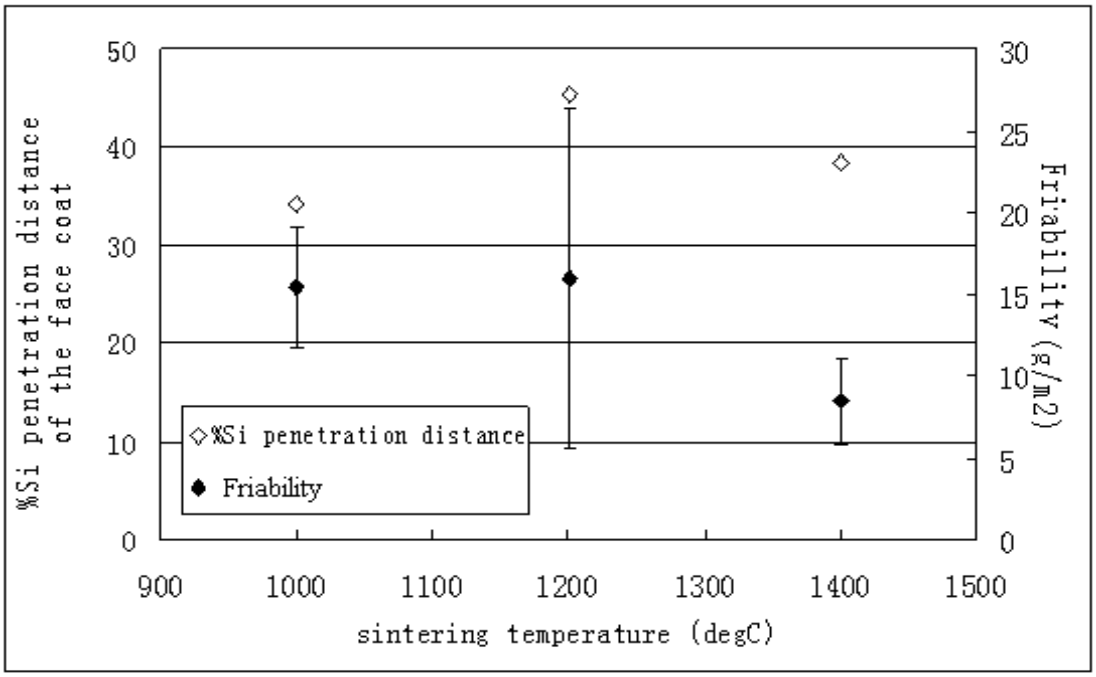

Figure 8-10. The %Si penetration distance with the friability change of the face coat by using Ti-coat back penetrates methods.

When sintering at 1000 and 1200 °C, the friability for the Ti-coat sol back penetrated sample was almost the same, but the %Si penetration distance increased with increasing sintering temperatures. At higher sintering temperatures (1400 °C), the face coat density increased, although at high temperature Si has higher activity, but due to the increased the strength of the face coat, the detected Si amount at the face coat surface was decreased. This maybe explained as at higher temperature, the bonding formation between the particles is stronger than at low temperature due to the powder particle ‗neck' growth. Compared to the slip casting sample at lower temperature around 1000 °C, the sample at high sintering temperature is denser and made the diffusion of Si difficult.

8.5 Investment casting of Titanium aluminide alloy

8.5.1 The inertness of the face coat

The interaction between the metal and the shell will cause the decomposition of the face coat surface releasing oxygen to diffuse into the metal interfacial areas, see Figure 7-7. Although the dissolution of oxygen from yttria is energetically unfavorable, an undoubted high hardness and oxygen enrich layer was observed at the investment casting bar surface. This means that some sort of interaction between TiAl and yttria face coat has taken place. According to the study by Renjie, Cui [195] and Ding [196], one possible cause is the dissolution of yttria, which takes place during casting at high temperatures.

Compared to the massive reaction which took place in the sessile drop test (metal was melted from the cylindrical sample surface), investment casting gives a more stable and uniform interaction at the metal/shell interface, therefore, a very uniform interaction layer was formed. The chemical thermodynamic inertness of the face coat according to the thickness of the interaction layer observed at the metal/shell interface is given as; yttria+ sol> YAZ> YF 0.15> YB 0.15> F-doped face coat shells (Figure 7-11).

The spreading activation energy in the sessile drop test calculated from the Arrhenius relationship between the drop contact diameter changing rate at different interaction temperatures (Table 8-7), gave the predicted face coat inertness as: yttria + sol> YAZ > YF 0.15 > YB 0.15, and this is the same as that observed in the investment casting from the

interaction layer thickness. Therefore, the prediction of inertness of the face coat using the sessile drop test by calculating the metal spreading activation energy was correct. The magnitude of the spreading activation energy correlated to a more severe interaction which took place between the ceramic shell and the metal.

The F-doped face coat slurry, which had the largest interaction layer thickness, had already been used to cast TiAl turbine blades in industrial applications with acceptable inertness and properties. So, all the newly developed face coat slurry systems can be potential face coat slurries for use in casting TiAl alloys in the future, with the benefit of increasing the slurry life time from hours to days. Meanwhile, the attached face coat layer thickness on the cast component surfaces of these water based face coat slurries was thin and easily removed (Figure 7-4).

8.5.2 The interface hardness and element penetration distance (oxygen, Si)

In this experiment, the oxygen penetration distance at the interface was found to be similar to the observed hardened layer thickness at the interface, see Figure 8-11.

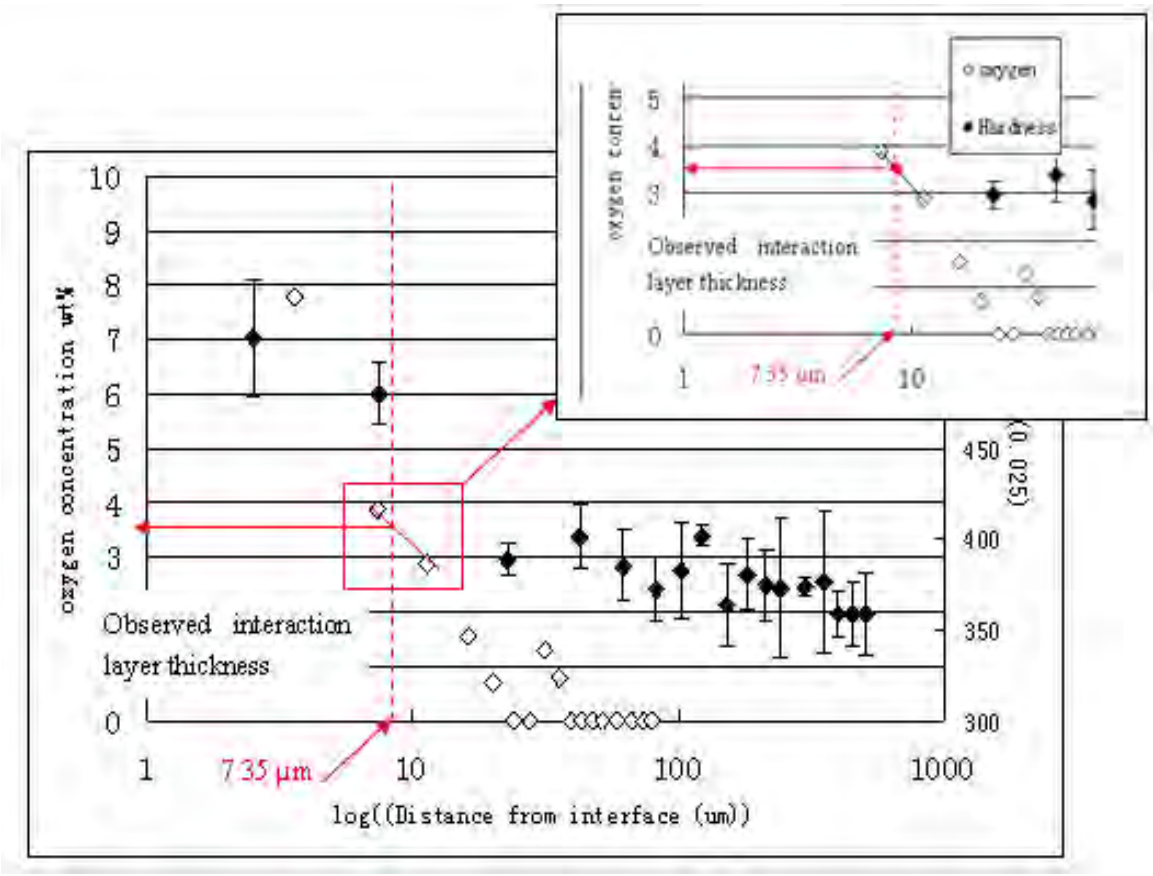
oxygen concentration wt%
Observed interaction layer thickness
7.35 μm
log((Distance from interface (um))
oxygen
Hardness
Hv(0.025)

(a)

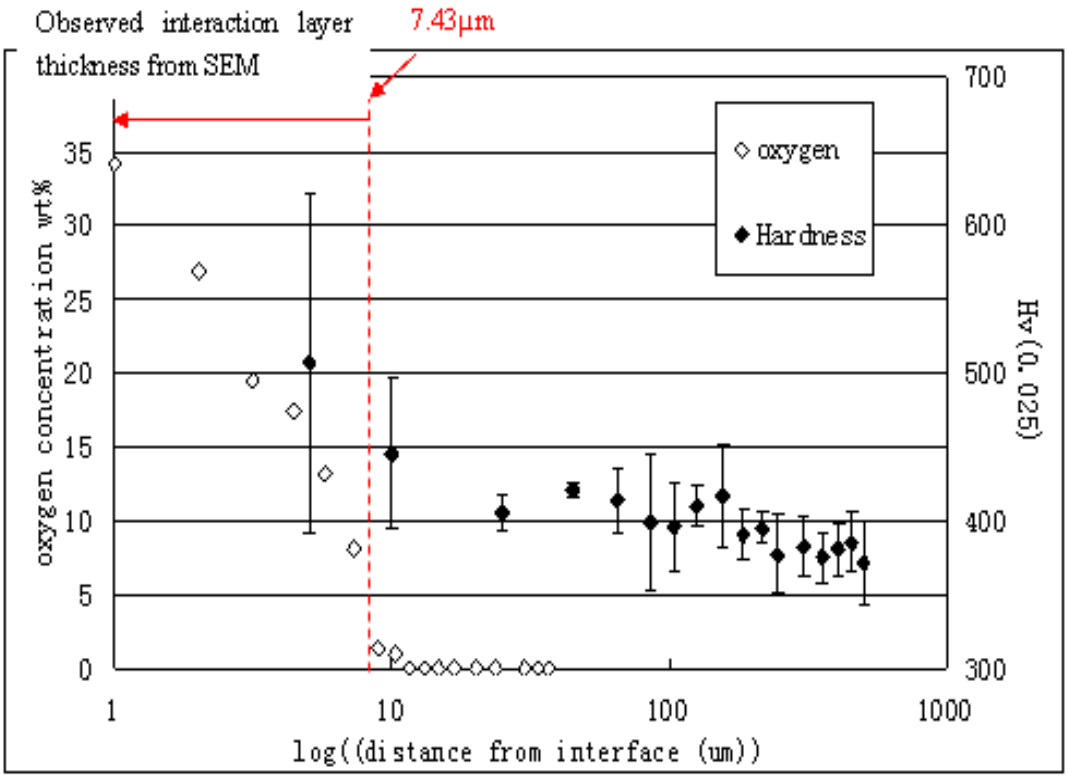
Observed interaction layer thickness from SEM
7.43μm
oxygen
Hardness
oxygen concentration wt%
log((distance from interface (um))
Hv(0.025)

(b)

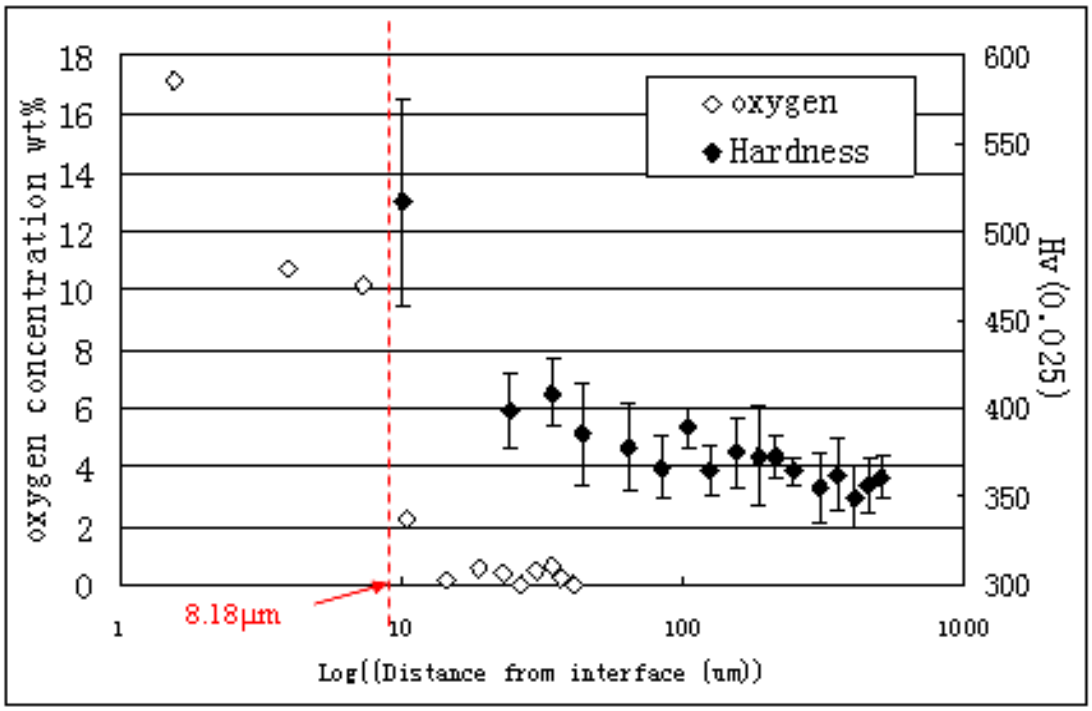

(c)

Figure 8-11. The oxygen penetration distance and metal interface hardness, (a) YAZ face coat, (b) F-doped face coat, (c) YB 0.15 face coat.

It can be seen that, the oxygen penetration distance and hardened layer thickness was larger than the observed interaction layer thickness at the interface. From the intersection point of the interaction layer thickness and the oxygen penetration distance (hardened layer thickness) in Figure 8-11 (a), it illustrated that in the YAZ, F-doped, and YB 0.15 samples, around 3.5 wt% oxygen concentration was required to stabilize the observed interaction layer at the interface. Therefore, the oxygen diffusion distance was greater than the observed interaction layer thickness shown in these SEM images.

Based on the results in Figure 8-12 shown below, compared to the hardness of the cast bars using one and two layers of face coat, the Si contamination at the metal interface seemed not

have had much influence on the hardness of the metal.

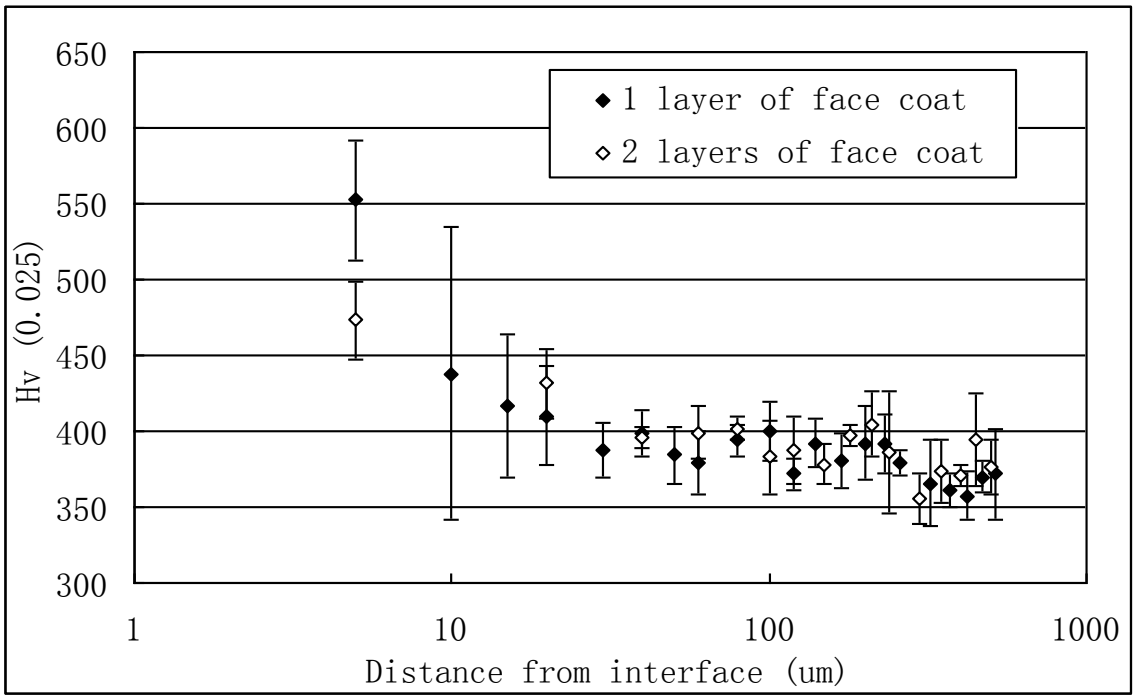

(a)

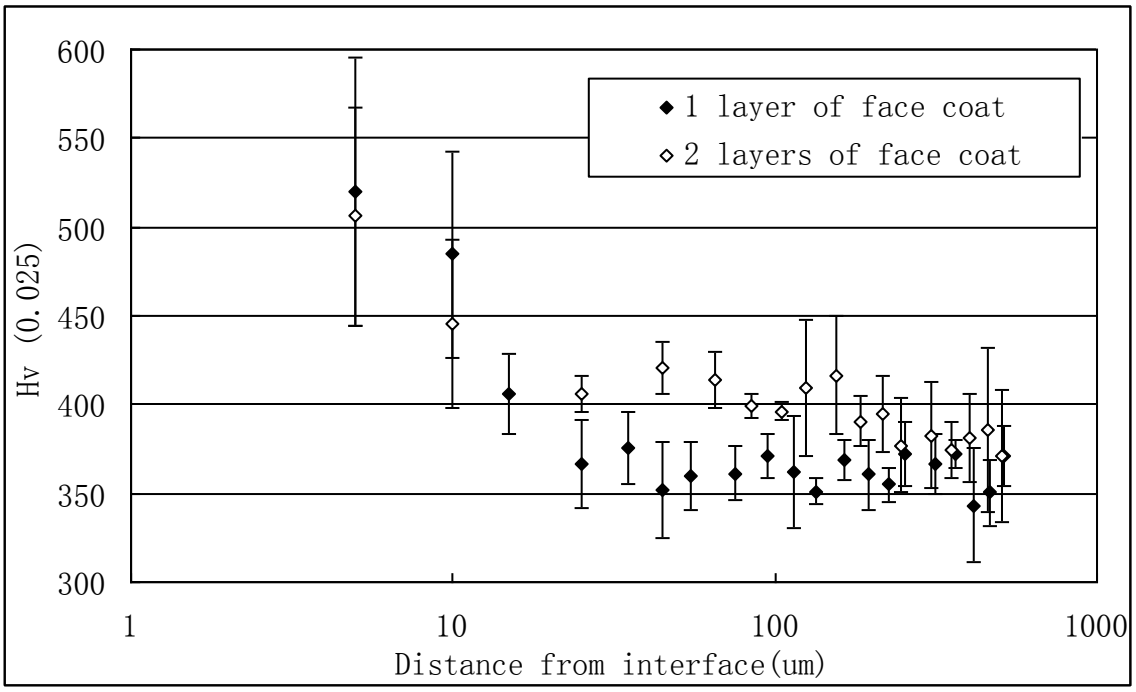

(b)

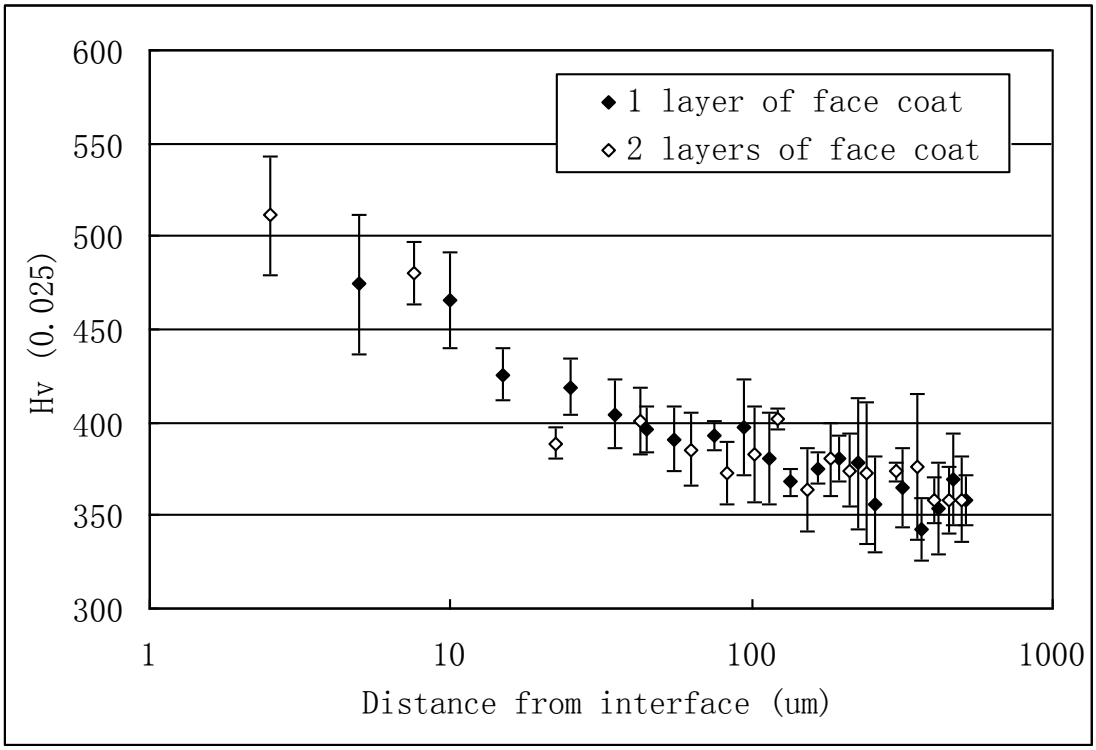

(c)

Figure 8-12. The hardness of the sample interface by using one layer and two layers of face coat for different face coats. (a)Yttria + sol, (b) YF 0.15, and (c) YAZ face coat.

8.5.3 The amount of Si on the face coat surface (mould 2)

As can be seen from Figure 7-4 (b) and Figure 7-5, by using the sol back penetration methods with one layer of face coat, Si was detected at the cast bar surface. During the interaction, reactive Si penetrated into the metal and the concentration of the Si decreased away from the metal/shell into the metal matrix. From the Figure 8-13, it can be seen that the highest Si concentration at the interface was detected by using the YAZ face coat with a penetration distance more than 13 μm, and then YF 0.15 face coat and YB 0.15 had a similar penetration distance around 10 μm, Yttria +sol had the smallest Si penetration distance at around 7 μm. Therefore, the inertness of the face coat for Si penetration decreased as; Yttria

+ sol > YB 0.15 =YF 0.15> YAZ, and this test results also agreed with the detected Si concentration on the different face coat surfaces after firing at 1200 °C for one hour in Table 6-4.

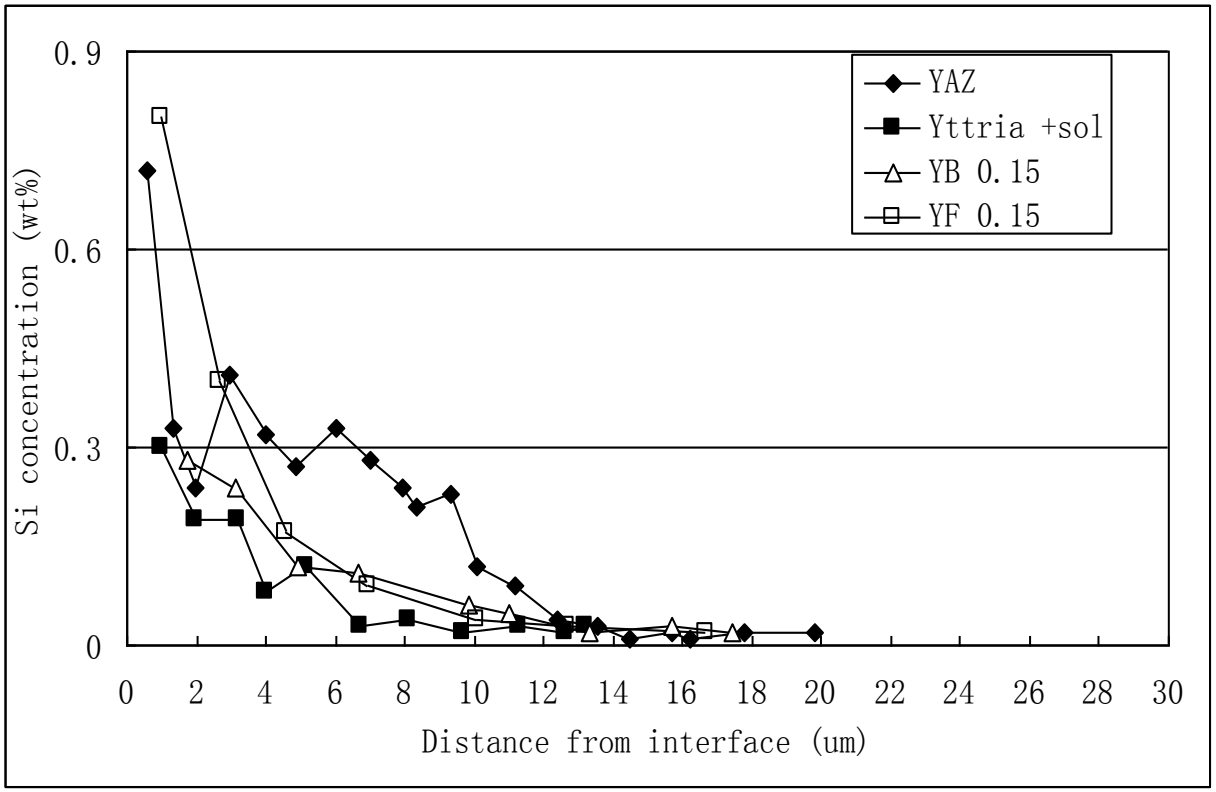

Figure 8-13. Si concentration from the metal/shell interface of all the test bars.

Chapter 9 Conclusions and future work

9.1 Conclusions

The water based binder face coat slurries were developed to be used to make the face coat of moulds for investment cast TiAl alloys. The research mainly consists of two parts; the slurry recipe development (filler powders, polymers) and an assessment of the reliability of the face coat used in the investment casting process. The first part is mostly focus on the improvement of face coat sintering properties and slurry stability through adding different additives into the water based binder slurry. The secondary part is more focused on study of the face coat chemical inertness and the strength. There are some conclusions are made:

The research shows that the industry standard sol used in the face coat slurry can help, by slurry gelation, to increase the face coat strength during drying. It increases the strength by increasing the contact area between the particles, but makes little difference to the overall rate of sintering. Sintering aids such as B_2O_3, YF_3, YAZ, and TiO_2 have good sintering properties at lower sintering temperatures compared to CeO_2 and La_2O_3. According to the dilatometer test results, the sintering aids can effectively promote powder sintering by changing the sintering mechanisms, therefore giving enhanced material diffusion with decreased powder densification temperatures. But, the sintering precursors like yttrium acetate and yttrium carbonate are less effective than the additives, and they retard the powder sintering start temperature. Meanwhile, the decomposition of the precursor will also cause

large holes to be formed and influence the powder compact quality.

The research on the slurry properties show that the water based binder yttria slurry still underwent a very slow gelation process even if no sol was added during slurry preparation, and the average life of most new slurries was limited to two weeks. The presence of sintering additives also can influence the life of the slurry. Sometimes, a high amount caused a shorter slurry life, e.g. YF_3, TiO_2. However, for the additives such as B_2O_3 and YAZ, they retarded the gelling of the slurry and increased the slurry life to in excess of one month. The sintering properties of the face coat is similar to the filler powder, but because of the different green density of the test sample, the face coat slip casting sample showed a rapid densification speed at temperatures higher than 1000 °C.

The face coat surface roughness using the new slurries was quite similar, with a maximum roughness variation of around 3 μm for the test samples, and therefore all could be used as the face coat slurry for alloy casting. However, due to the low softening temperature of the polymer, the strength of the new face coats were comparably poorer than the commercial face coat slurry, therefore, in order to improve the green strength of the face coat, a new production method called the ‗sol back penetration' method was used to make the shell, especially for the manufacture of large shells (‗T' shape).

The thermochemical inertness of the water based binder face coats was tested by first using

the sessile drop flash re-melt test, and then investment casting. The experimental results showed that, by adding sintering aids, the chemical inertness of the face coat was decreased, and this depended on the thermochemical properties of the additives and added amount. The interaction between the face coat and the metal can be observed in three different ways: The quickly reducing contact angle of the sessile drop; the high hardness at the metal/shell interface; the thickness of the interaction layer observed at the metal/shell interface.

The decreased contact angle of the sessile drop was caused by the metal/shell interfacial energy changing due to the chemical interaction. The high spreading activation energy at the interface indicated that the most severe interaction took place between the shell and the metal. The face coat chemical inertness, according to the activation energy results, decreased as the sequence: Yttrai+sol> YAZ>YF 0.15> YB 0.15.

The penetrated oxygen from the dissolved face coat caused an increased hardness at the metal surface. The high hardness layer thickness at the metal surface is different from sample to samples according to the amount of chemical reaction between the metal and different face coats at variety temperatures with different contact times. The research shows that the hardened layer thickness of the investment casting sample bars surface using new face coat is less than 25 μm, and is acceptable for industrial use.

The observed interaction layer at the metal/shell interface contains very high amounts of

oxygen, and more than 3.5 wt% oxygen was found to establish this layer at the metal surface. The interaction layer thickness observed in this research is increased as: Yttria +sol > YAZ > YF 0.15 > YB 0.15 > F-doped face coat. The chemical inertness of the new face coats are the same as the predicted face coat inertness from the sessile drop test giving the liquid metal activation energy.

After firing at different sintering temperatures, Si from the backup coat was found to penetrate into the face coat surface during sintering. The amount of Si penetration from the backup coat to the face coat was dependent on three factors; the firing temperature, sintering additives and production process. The higher the firing temperature, the more reactive the Si and the easier for the Si to diffuse into the face coat. But higher sintering temperatures also caused higher densification of the face coat, retarding the Si penetration. Sintering additives such as ZrO_2, Al_2O_3, etc seemed to enhance the Si diffusivity in yttria and increase the Si amount in the shell face coat. The Si concentration found at the different face coat surfaces decreased as: YAZ>YF 0.15>YB 0.15> Yttria + Sol. Using the sol back penetration method increased the chance of Si penetration from the backup coat to the face coat. But there was no evidence that the penetrated Si in the metal surface influenced the micro-hardness of the alloy.

9.2 Future works

The water based binder face coat slurry obviously increased the slurry life but the green

strength of this slurry was poor, therefore there are two main aspects of the improvements of the slurry in future: one focuses on the use of polymer, the other uses sol for a ‗back penetrate' process.

The investigation of the polymer mostly focused on the high temperature polymers (softening temperature up to 300 °C). Different from the traditional production methods, these high temperatures polymers do not necessarily have to dissolve in water, they can be painted on the wax pattern surface to protect the face coat during the de-wax process, then, this thin polymer layer will be evaporated or pyrolysed and disappear when mould was fired. Some high temperature polymers such as the tri-beta-aminoborazoles, which have a working temperature around 600 °C, can be used in this application.

The second improvement is using a more reactive sol for the back penetration method, which can quickly gel the face coat. The benefit of this methods is it separates the slurry making and geling processes, therefore it does not impact the viscosity management of the slurry by adding different types of polymer and the matching of the pH values of the polymer and sintering aids.

Reference:

[1] Xinhua, W. (2006). "Review of alloy and process development of TiAl alloys." Intermetallics **14**(10–11): 1114-1122.

[2] Ramanujan, R. V. (2000). "Phase transformations in c based titanium aluminides." International Materials Reviews **45**(6): 217-240.

[3] Edward A, L. (2000). "Gamma titanium aluminides as prospective structural materials." Intermetallics **8**(9–11): 1339-1345.

[4] Kovács, K., I. V. Perczel, V. K. Josepovits, G. Kiss, F. Réti and P. Deák (2002). "In situ surface analytical investigation of the thermal oxidation of Ti–Al intermetallics up to 1000 °C." Applied Surface Science **200**(1–4): 185-195.

[5] http://www.nasa.gov/centers/glenn/news/AF/2008/July08_GEnx.html

[6] Roger C. Reed. The Superalloys: Foundamentals and Applications. Cambridge Univeristy Press, 2006.

[7] Imayev, R. M., V. M. Imayev, M. Oehring and F. Appel (2007). "Alloy design concepts for refined gamma titanium aluminide based alloys." Intermetallics **15**(4): 451-460.

[8] N.Saunders (February 28 - March 4, 1999). "Phase equilibria in multi-component gamma-TiAl based alloys. Symposium on Gamma Titanium Aluminides 1999 and 1999 TMS Annual Meeting". Y-W.Kim. San Diego, California, USA, TMS Warrendale, PA**:** 183.

[9] Lamirand, M., J. Bonnentien, S. Guérin, G. Ferrière and J. Chevalier (2006). "Effects of interstitial oxygen on microstructure and mechanical properties of Ti-48Al-2Cr-2Nb with fully lamellar and duplex microstructures." Metallurgical and Materials Transactions A **37**(8): 2369-2378.

[10] Leyens.C, P. M. (2003). Titanium and titanium alloys - Fundamentals and applications, editedby WILEY-VCH Verlag GmbH & Co. KGaA, Weinheim。

[11] Kawabata, T., T. Tamura and O. Izumi (1993). "Effect of Ti/Al ratio and Cr, Nb, and Hf additions on material factors and mechanical properties in TiAl." Metallurgical and Materials Transactions A **24**(1): 141-150.

[12] Shida, Y. and H. Anada (1993). "The influence of ternary element addition on the oxidation behaviour of TiAl intermetallic compound in high temperature air." Corrosion Science **35**(5–8): 945-953.

[13] Liu, Q. and P. Nash (2011). "The effect of Ruthenium addition on the microstructure and mechanical properties of TiAl alloys." Intermetallics **19**(9): 1282-1290.

[14] Hecht, U., V. Witusiewicz, A. Drevermann and J. Zollinger (2008). "Grain refinement by low boron additions in niobium-rich TiAl-based alloys." Intermetallics **16**(8): 969-978.

[15] Wang, W. D., Y. C. Ma, B. Chen, M. Gao, K. Liu and Y. Y. Li (2010). "Effects of Boron Addition on Grain Refinement in TiAl-based Alloys." Journal of Materials Science & Technology **26**(7): 639-647.

[16] Cheng.T.T (2000). "The mechanism of grain refinement in TiAl alloys by boron addition — an alternative hypothesis." Intermetallics **8**(1): 29-37.

[17] Gosslar, D., R. Günther, U. Hecht, C. Hartig and R. Bormann (2010). "Grain refinement of TiAl-based alloys: The role of TiB2 crystallography and growth." Acta Materialia **58**(20): 6744-6751.

[18] Hu, D. and R. R. Botten (2002). "Phase transformations in some TiAl-based alloys." Intermetallics **10**(7): 701-715.

[19] Lasalmonie, A. (2006). "Intermetallics: Why is it so difficult to introduce them in gas turbine engines?" Intermetallics **14**(10–11): 1123-1129.

[20] Gomes, F., Barbosa.Joaquim. and C. S. Ribeiro (2008). "Induction melting of gama-TiAl in CaO crucibles." Intermetallics **16**: 1292-1297.

[21] Prihar, R.I. (2001) Structural Intermetallics TMS, Warrendale, PA, Bamberg, Germany.

[22] kuang, J. P., R. A. Harding and J. Campbell (2001). "A study of refractories as crucible and moulf materials for melting and casting gamma- TiAl alloys." International journal of cast metal research **13**(5): 277-292.

[23] Sung, S.-Y. and Y.-J. Kim (2005). "Alpha-case formation mechanism on titanium investment castings." Materials Science and Engineering: A **405**(1–2): 173-177.

[24] T, N. (1998). "Application of cast gamma TiAl for automobiles." Intermetallics **6**(7–8): 709-713.

[25] Eylon, D., M. M. Keller and P. E. Jones (1998). "Development of permanent-mold cast

TiAl automotive valves." Intermetallics **6**(7–8): 703-708.

[26] Reed, D. S. and M. L. Jones (May 1991). Investment Casting of Induction Skull-Melted Titanium and Reactive Alloys. Ninety-Fifth Annual Meeting American Foundrymen's Society. Birmingham, Alabama, USA**:** 697-700.

[27] Harding, R. A. (2004). Recent developments in the induction skull melting and investment casting of titanium aluminides. International conference of advanced metallic materials Bratislava, Slovak Republic. **42:** 225 - 241.

[28] Fu, P. X., X. H. Kang, Y. C. Ma, K. Liu, D. Z. Li and Y. Y. Li (2008). "Centrifugal casting of TiAl exhaust valves." Intermetallics **16**(2): 130-138.

[29] http://www.castingreps.com/casting/investment-castings.aspx

[30] Yuan, C., S. Jones, P. A. Withey and P. M. Marquis (2002). "Development of alumina primary coat for single crystal investment casting ceramic mould." British Ceramic Transactions **101**(2): 59-64.

[31] Beeley, P. R. and R. F. Smart (1995). Investment casting. The Institute of Materials. The University Press Cambridge.

[32] Jovanović, M. T., B. Dimčić, I. Bobić, S. Zec and V. Maksimović (2005). "Microstructure and mechanical properties of precision cast TiAl turbocharger wheel." Journal of Materials Processing Technology **167**(1): 14-21.

[33] Cao, G., L. Fu, J. Lin, Y. Zhang and C. Chen (2000). "The relationships of microstructure and properties of a fully lamellar TiAl alloy." Intermetallics **8**(5–6): 647-653.

[34] Hu, D., J. F. Mei, M. Wickins and R. A. Harding (2002). "Microstructure and tensile properties of investment cast Ti–46Al–8Nb–1B alloy." Scripta Materialia **47**(4): 273-278.

[35] Harding.R.A, W. M and Li.Y.G (2001). "Progress towards the production of high quality-TiAlcastings" K.J. Hemker (Ed.) et al., Structural intermetallics 2001, TMS: 181-189.

[36] Harding, R. A. and M. Wickins (2007). The effect of some process variables on defects in titanium aluminide castings. The 11th World Conference on Titanium. Kyoto, Japan**:** 1157-1160.

[37] Harding, R. A., M. Wickins, H. Wang, G. Djambazov and K. A. Pericleous (2011). "Development of a turbulence-free casting technique for titanium aluminides." Intermetallics **19**(6): 805-813.

[38] Mi, J., R. A. Harding, M. Wickins and J. Campbell (2003). "Entrained oxide films in TiAl castings." Intermetallics **11**(4): 377-385.

[39] Wang, H., G. Djambazov, K. A. Pericleous, R. A. Harding and M. Wickins (2011). "Modelling the dynamics of the tilt-casting process and the effect of the mould design on the casting quality." Computers & Fluids **42**(1): 92-101.

[40] Guilin, Y., L. Nan, L. Yousheng and W. Yining (2007). "The effects of different types of investments on the alpha-case layer of titanium castings." The Journal of Prosthetic Dentistry **97**(3): 157-164.

[41] Barbosa, J., H. Puga, C. S. Ribeiro, O. M. N. D. Teodoro and A. C. Monteiro (2006). "Characterisation of metal/mould interface on investment casting of gamma-TiAl." International Journal of Cast Metals Research **19**(6): 331-338.

[42] Barbosa, J., C. S. Ribeiro and A. C. Monteiro (2003). "Processing of gamma-TiAl, by ceramic crucible induction melting, and pouring in ceramic shells." Materials Science Forum **426 - 432**: 1933-1938.

[43] Barbosa, J., C. S. Ribeiro and A. C. Monteiro (2007). "Influence of superheating on casting of γ-TiAl." Intermetallics **15**(7): 945-955.

[44] Jia.Qin, Y. Y. Cui and Y. Rui (2002). "Effects of two oxide face coating materials on the surface quality of titanium alloys casts." Acta Metallurgica Sinaca **38**: 348-350.

[45] Kuang, J. P., R. A. Harding and J. Campbell (2000). "Investigation into refractories as crucible and mould materials for melting and casting γ-TiAl alloys." Materials Science and Technology **16**(9): 1007-1016.

[46] Li, B.-s., A.-h. Liu, H. Nan, W.-s. Bi, J.-j. Guo and H.-z. Fu (2008). "Wettability of TiAl alloy melt on ceramic moulds in electromagnetic field." Transactions of Nonferrous Metals Society of China **18**(3): 518-522.

[47] Jia, Q., Y. Y. Cui and R. Yang (2004). "Intensified interfacial reactions between gamma titanium aluminide and CaO stabilised ZrO_2." International Journal of Cast Metals Research **17**(1): 23-28.

[48] Eustathopoulos, N., D. Chatain and L. Coudurier (1991). "Wetting and interfacial chemistry in liquid metal-ceramic systems." Materials Science and Engineering: A **135**(0): 83-88.

[49] Liu, G., Valenza, F., Muolo, M., Qiao, G. ,Passerone, A.(2009)."Wetting and interfacial

behavior of Ni–Si alloy on different substrates".Journal of Materials Science, 2009, vol.44, pp 5990-5997.

[50] Eustathopoulos.N (1998). "Dynamics of wetting in reactive metal/ ceramic systems." Acta Materialia **46**(7): 2319-2327.

[51] Yu, D. Q., H. P. Xie and L. Wang (2004). "Investigation of interfacial microstructure and wetting property of newly developed Sn–Zn–Cu solders with Cu substrate." Journal of Alloys and Compounds **385**(1–2): 119-125.

[52] Yost, F. G., F. R. Michael and E. T. Eisenmann (1995). "Extensive wetting due to roughness." Acta Metallurgica et Materialia **43**(1): 299-305.

[53] Zhou, X. B. and J. T. M. De Hosson (1996). "Reactive wetting of liquid metals on ceramic substrates." Acta Materialia **44**(2): 421-426.

[54] Landry, K. and N. Eustathopoulos (1996). "Dynamics of wetting in reactive metal/ceramic systems: linear spreading." Acta Materialia **44**(10): 3923-3932.

[55] Kumar, G. and K. N. Prabhu (2007). "Review of non-reactive and reactive wetting of liquids on surfaces." Advances in Colloid and Interface Science **133**(2): 61-89.

[56] Mortensen, A., B. Drevet and N. Eustathopoulos (1997). "Kinetics of diffusion-limited spreading of sessile drops in reactive wetting." Scripta Materialia **36**(6): 645-651.

[57] Eustathopoulos, N. (1998). "Dynamics of wetting in reactive metal/ ceramic systems." Acta Materialia **46**(7): 2319-2327.

[58] Dezellus, O., F. Hodaj and N. Eustathopoulos (2002). "Chemical reaction-limited spreading: the triple line velocity versus contact angle relation." Acta Materialia **50**(19): 4741-4753.

[59]Contreras, A. (2007). "Wetting of TiC by Al–Cu alloys and interfacial characterization." Journal of Colloid and Interface Science **311**(1): 159-170.

[60] López, V. H. and A. R. Kennedy (2006). "Flux-assisted wetting and spreading of Al on TiC." Journal of Colloid and Interface Science **298**(1): 356-362.

[61] Contreras, A., E. Bedolla and R. Pérez (2004). "Interfacial phenomena in wettability of TiC by Al–Mg alloys." Acta Materialia **52**(4): 985-994.

[62] Toy., C. and W. D. Scott. (1997). "Wetting and spreading of molten aluminum against AlN surfaces." Journal of Materials Science. **32**: 3243-3248.

[63] Dezellus, O., F. Hodaj and N. Eustathopoulos (2002). "Chemical reaction-limited spreading: the triple line velocity versus contact angle relation." Acta Materialia **50**(19): 4741-4753.

[64] Contreras, A., V. H. López and E. Bedolla (2004). "Mg/TiC composites manufactured by pressureless melt infiltration." Scripta Materialia **51**(3): 249-253.

[65]Barbosa, J. and M. Caetano.A (2001). Controlled Residual Surface Contamination of gTiAl, Induction Melted in Ceramic Crucibles. Guimarães, Portugal, Universidade do Minho**:** 1-8.

[66] Saha, R., T. Nandy, R. Misra and K. Jacob (1989). "Evaluation of the reactivity of titanium with mould materials during casting." Bulletin of Materials Science **12**(5): 481-493.

[67] Saha, R., T. Nandy, R. Misra and K. Jacob (1990). "On the evaluation of stability of rare earth oxides as face coats for investment casting of titanium." Metallurgical and Materials Transactions B **21**(3): 559-566.

[68] Kostov, A. and B. Friedrich (2006). "Predicting thermodynamic stability of crucible oxides in molten titanium and titanium alloys." Computational Materials Science **38**(2): 374-385.

[69] Bale, C. W., E. Bélisle, P. Chartrand, S. A. Decterov, G. Eriksson, K. Hack, I. H. Jung, Y. B. Kang, J. Melançon, A. D. Pelton, C. Robelin and S. Petersen (2009). "FactSage thermochemical software and databases — recent developments." Calphad **33**(2): 295-311.

[70] G, L. N. (Mar. 1966). Precious mould and method of fabrication. USA. **No. 3241200**.

[71] G, L. N. (Jan. 1967). Method of preparing an investment mould for use in precious casting. USA. **No.3296666**.

[72] G, L. N. (Jan. 1967). Method of preparing an investment mould for use in precious casting. USA. **No. 3256574**.

[73] Lirones, N. G. (Aug, 1966). Graphite mould the fabrication method. USA. **No.3266106**.

[74] Lirones, N. G. (May, 1967). Method of making shell moulds for casting reactive metals. USA. **No.3321005**.

[75] Brown, R. A. and C. A. Brown (Jan. 1969). Methods of making investment shell moulds for the high intensity precious casting of reactive and refractory metals. USA. **No.3422880**.

[76] Brown, R. A. and C. A. Brown (Nov 1970). Investment shell moulds for the high intensity precision casting of reactive and refractory metals and methods for their manufacture. **No.3537949**.

[77] Brown, R. A. (Nov. 1976). Investment shell mould for use in casting of reactive and refractory metals. USA. **No.3994346**.

[78] Abbas, H. A., F. F. Hamad, A. K. Mohamad, Z. M. Hanafi and M. Kilo (2008). "Structural Properties of Zirconia Doped with Some Oxides." Diffusion Fundamentals **7.1-7.8**(1862-4138).

[79] Manicone, P. F., P. Rossi Iommetti and L. Raffaelli (2007). "An overview of Zirconia ceramics: Basic properties and clinical applications." Journal of Dentistry **35**(11): 819-826.

[80] Renjie Cui, Ming Gao, Hu Zhang and Shengkai Gong (2010). "Interactions between TiAl alloys and yttria refractory material in casting process." Journal of Materials Processing Technology **210**(9): 1190-1196.

[81] Zhang, L., N. Cao and L. Liu (2007). Theory and practice of near net shape investment casting. BeiJing, Chinese academy ministry

[82] Lassow, E. S. and P. R. Johnson (Nov 1987). Ceramic shell mould face coat and core coating systems for investment casting of reactive metals. USA. **No. 4703806**.

[83] Horton, R. (Aug. 1990). Method of casting a reactive metal against a surface formed from an improved slurry containing yttria. USA. **No. 4947927**.

[84] Yasrebi. M, Kemp. W. W, and Sturegis. D. H (1998), –Aging of Aqueous Investment Casting Slurries, Causes and Solutions," in proceeding of the 46th annual technical meeting and exhibition of the Investment Casting Institute.

[85] Yasrebi, M., Ziomek-Moroz, M., Kemp, W. ,Sturgis, D.H.(1996)."Role of Particle Dissolution in the Stability of Binary Yttria-Silica Colloidal Suspensions". Journal of the American Ceramic Society , vol.79, pp.1223-1227.

[86] Yasrebi, M., Springgate, M.E., Nikolas, D.G., Kemp, W., Sturgis, D.H. ,McCarthy, J.M.(1997)." Colloidal Stability of Zirconia-Doped Yttria–Silica Binary Aqueous Suspensions". Journal of the American Ceramic Society, vol.80, pp.1615-1618.

[87] D. C. Bradley, R. C. Mehrotra and D. P. Gaur: Metal Alkoxide . Academic Press Inc.,

London, 1978.

[88] Frueh, C., D. Poirier and M. Maguire (1997). "The effect of silica-containing binders on the titanium/face coat reaction." Metallurgical and Materials Transactions B **28**(5): 919-926.

[89] Dieter, B. and N. Heinz (Mar. 25, 1986). Binding agents containing titanic acid esters for the preparation of coating compositions and refractory bodies, and a method for the preoaration of these binding agents. USA. **No. 4578487**.

[90] Yasrebi, M. and W. Kemp (Apr, 1997). Method for stabilizing ceramic suspensions. USA. **No.5,624,604**.

[91] Yasrebi, M. and K. M. Taft (May. 2002). Method for processing materials to increase slurry lifetime. USA. **No. 6,390,179**.

[92] Yasrebi, M. and W. Kemp (Nov, 1995). Yttria-zirconia slurries and mould facecoats for casting reactive metals. USA. **No.5,464,797**.

[93] Pauliny, T. A. and R. K. Mattson (Oct. 1998). Face coat ceramic slurry and materials for use thereof in mould fabrication and casting. USA. **No. 5,827,791**.

[94] Feagin, R. C. (Apr. 1988). Casting of reactive metals into ceramic moulds. USA. **No.4,740,246**.

[95] Cesarano, J., I. A. Aksay and A. Bleier (1988). "Stability of Aqueous α-Al2O3 Suspensions with Poly (methacrylic acid) Polyelectrolyte." Journal of the American Ceramic Society **71**(4): 250-255.

[96] Janz, P. and S. Tauber (Nov. 2008). Yttria Based refractory composition. EP. No. **19992430 (A)**

[97] Janz, P. and S. Tauber (2010). Yttria-based refractory composition. USA. **No.2,010,043,999**.

[98] Tauber, S. and P. Janz (Dec. 2010). Yttria-based slurry compsotion. **WO 2010141971 (A1)**

[99] Kartavykh, A. V., V. V. Tcherdyntsev and J. Zollinger (2009). "TiAl–Nb melt interaction with AlN refractory crucibles." Materials Chemistry and Physics **116**(1): 300-304.

[100] Kartavykh, A. V., V. V. Tcherdyntsev and J. Zollinger (2010). "TiAl–Nb melt interaction with pyrolytic boron nitride crucibles." Materials Chemistry and Physics **119**(3): 347-350.

[101] Shen, B. and H. Liu, Kong, Bo, Mao, Xiemin, Li, Chonghe, Zhou Xing, Zhu, Ming, Jiang, Liuquan, (2008). "Trial test of processing of boron nitride-based shell mould used for titanium alloy investment casting." Journal of Chinese ceramic society(S1). Vol 36. pp.124-127.

[102] Rahaman, M. N. (2008). Sintering of ceramics. New York, CRC Press, Taylor & Francis Group**:** pp 46.

[103] Rahaman, M. N. (2008). Sintering of ceramics. New York, CRC Press, Taylor & Francis Group**:** pp 48.

[104] Coble, R. I. (1961). "Sintering crystalline solids. I. Intermediate and final state diffusion models." Journal of Applied Physics **32**: 787.

[105] Rahaman, M. N. (2007). Ceramic processing, CRC Press. Taylor&Francis Group**:** pp 381

[106] Colenz, W. S., J. M. Dynys and R. I. Coble (1980). "Initial stage solid state sintering models. A critical analysis and assessment." Materials Science Research **13**: 141-157.

[107] Exner, H. E. (1979). " Principle of single-phase sintering." Reviews on powder metallurgy and physical ceramics. Vol 1. Freund Publishing House Ltd

[108] Rahaman, M. N. (2008). Sintering of ceramics. New York, CRC Press, Taylor & Francis Group**:** pp.177.

[109] Rahaman, M. N. (2008). Sintering of ceramics. New York, CRC Press, Taylor & Francis Group**:** pp. 178.

[110] German, R. M. (1985). Liquid phase sintering. New York, Plenum Press.

[111] German, R. M. (1996). Sintering Theory and Practice. New York, Wiley.

[112] Kingery, W. D. (Mar 1959). "Densification during Sintering in the Presence of a Liquid Phase. I. Theory." Journal of Applied Physics **30**(3): 301 - 306.

[113] Yoon, D. N. and W. J. Huppmann (1979). "Grain growth and densification during liquid phase sintering of W-Ni." Acta Metallurgica **27**(4): 693-698.

[114] Rahaman, M. N. (2008). Sintering of ceramics. New York, CRC Press, Taylor & Francis Group**:** pp. 203-205.

[115] Rahaman, M. N. (2008). Sintering of ceramics. New York, CRC Press, Taylor & Francis Group**:** pp. 285.

[116] Yu, P. C., Q. F. Li, J. Y. H. Fuh, T. Li and L. Lu (2007). "Two-stage sintering of nano-sized yttria stabilized zirconia process by powder injection moulding." Journal of Materials Processing Technology. Vol.192–193. pp 312-318.

[117] Li, X., J.-G. Li, Z. Xiu, D. Huo and X. Sun (2009). "Transparent Nd: YAG Ceramics Fabricated Using Nanosized γ-Alumina and Yttria Powders." Journal of the American Ceramic Society. Vol **92**(1): pp 241-244.

[118] Rahaman, M. N. (2008). Sintering of ceramics. New York, CRC Press, Taylor & Francis Group.

[119] Lee, Y. I., J.-H. Lee, S.-H. Hong and D.-Y. Kim (2003). "Preparation of nanostructured TiO_2 ceramics by spark plasma sintering." Materials Research Bulletin **38**(6): 925-930.

[120] T.B, S. (2003). "On the sintering of uncompacted, pre-alloyed Al powder alloys." Materials Science and Engineering: A **341**(1–2): 163-168.

[121] Saurabh.Anand and N. Verma (2006). Effect of Sintering Temperature, Heat Treatment and Tempering on Hardness of Sintered Hardened Grade Steels (SH737-2Cu-0.9C), Indian Institute of Technology**:** 27-31.

[122] Samsonov, G. V, (1973). The oxide handbook. IFI/Plenum, New York ; London.

[123] Gasgnier, G., J. F. Baumard, et al. (1994). "Enhanced densification of yttria by addition of titanium oxide." Journal of the European Ceramic Society **13**(1): 67-72.

[124] Baumard, J.-F. and M. Boncoeur (May, 1994). Transparent ceramics and production process for the same. USA. **No. 5308809**.

[125] Baumard, J.-F. and M. Boncoeur (Apr. 1996). Yttrium oxide/titanium oxide ceramic compositions. USA. **No.5508242(A)**.

[126] Paine, R.T. ,Narula, C.K.(1990)."Synthetic routes to boron nitride". Chemical Reviews, vol.90, pp.73-91

[127] Takayuki, I. and K. Masakatsu (Aug. 2008). Yttriia sintered body and corrosion-resistant material, and manufacturing method. USA. **No 2,007,161,499 (A1)**.

[128] Wei, G. (Mar, 2005.). Transparent sintered ceramic material. Japan. **No.2005075726**.

[129] Granger, B. and G. Sinet (Dec. 2007). A sintered and doped yttrium oxide product. **WO 2,007,107,954**.

[130] Chen, P.-L. and I. W. Chen (1996). "Grain Boundary Mobility in Y2O3: Defect Mechanism and Dopant Effects." Journal of the American Ceramic Society **79**(7): 1801-1809.

[131] Stubican, V. S., R. C. Hink and S. P. Ray (1978). "Phase Equilibria and Ordering in the System ZrO2-Y2O3." Journal of the American Ceramic Society **61**(1-2): 17-21.

[132] B, Cockayne. (1985). "The uses and enigmas of the Al_2O_3-Y_2O_3 phase system." Journal of the Less Common Metals **114**(1): 199-206.

[133] Hess, N. J., G. D. Maupin, L. A. Chick, D. S. Sunberg, D. E. McCreedy and T. R. Armstrong (1994). "Synthesis and crystallization of yttrium-aluminium garnet and related compounds." Journal of Materials Science **29**(7): 1873-1878.

[134] Bertaut, F. and J. Mareschal (1963). "Un nouveau type de structure hexagonale: $AlTO_3$ (T= Y, Eu, Gd, Tb, Dy, Ho, Er)." (in French) Comptes Rendus hebdomadaires des Séances de l'Académie des Sciences. **257**: 867-870.

[135] Warshaw, C. M. and R. Roy (1961). "Classification and a Scheme for the Identification of Layer Silicates." Geological Society of America Bulletin **72**(10): 1455-1492.

[136]Joseph, R. F. and R. W. H (Sep. 1979). Transparent yttria ceramics and method for producing same. USA. **No.4,166,831**.

[137] Rhodes, W. H. (1981). "Controlled Transient Solid Second-Phase Sintering of Yttria." Journal of the American Ceramic Society **64**(1): 13-19.

[138] Akio, I. (Nov. 1993). A method to produce transparent YAG. Japan. **No.5294722**.

[139] Huang, Y. H., D. Jiang, J. Zhang and Q. Lin (2009). "Fabrication of Transparent Lanthanum-Doped Yttria Ceramics by Combination of Two-Step Sintering and Vacuum Sintering." Journal of the American Ceramic Society **92**(12): 2883-2887.

[140] H, R. W. (Sep. 1978). Transparent yttria ceramics and method for producing same. USA. **No. 4,115,134**.

[141] Zeng, R. and C. Lin (Dec. 2010). Method for preparing cerium-activated yttrium

alumium granet fluorescent powder. China. **CN.10111333 3(A)**.

[142] Rasmussen, M. D., M. Akinc and O. Hunter Jr (1985). "Processing of Yttria powders derived from hydroxide precursors." Ceramics International **11**(2): 51-55.

[143] Ikegami, T., J.-G. Li, et al. (2002). "Fabrication of Transparent Yttria Ceramics by the Low-Temperature Synthesis of Yttrium Hydroxide." Journal of the American Ceramic Society **85**(7): 1725-1729.

[144] Gong, H., D. Tang, H. Huang and J. Ma (2009). "Fabrication of yttrium aluminum garnet transparent ceramics from yttria nanopowders synthesized by carbonate precipitation." Journal of Electroceramics **23**(1): 89-93.

[145] Venkatachalam, N., Y. Saito and K. Soga (2009). "Synthesis of Er^{3+} Doped Y_2O_3 Nanophosphors." Journal of American Ceramic Society **92** (5): 1006-1010.

[146] Kopylov, Y. L., V. B. Kravchenko, A. A. Komarov, Z. M. Lebedeva and V. V. Shemet (2007). "Nd:Y_2O_3 nanopowders for laser ceramics." Optical Materials **29**(10): 1236-1239.

[147]Li, Y. C. (2007). The slurry for casting and applications. Bei Jing, China Machine Press

[148] C. A. Finch , (1973) Polyvinyl alcohol. Properties and applications. John Wiley, Chichester.

[149] Wan, W.K., Campbell, G., Zhang, Z.F., Hui, A.J., Boughner, D.R. (2002)."Optimizing the tensile properties of polyvinyl alcohol hydrogel for the construction of a bioprosthetic heart valve stent". Journal of Biomedical Materials Research, **63**:854-861.

[150] Brydson, J. (1999). Plastics Materials (7th Edition), Elsevier**.**

[151] Fischer, S., Thümmler, K., Volkert, B., Hettrich, K., Schmidt, I. ,Fischer, K.(2008)."Properties and Applications of Cellulose Acetate". Macromolecular Symposia, **262**:89-96.

[152] http://www.nyacol.com/yttria-data.htm

[153] http://www.remet.com/pic_support_anti-foams.php

[154] http://www.remet.com/pic_support_wetting_agents.php

[155] Rüssel, C. (1993). "A pyrolytic route to fluoride glasses. I. Preparation and thermal decomposition of metal trifluoroacetates." Journal of Non-Crystalline Solids **152**(2-3): 161-166.

[156] Matsui, K., A. Matsumoto, M. Uehara, N. Enomoto and J. Hojo (2007). "Sintering Kinetics at Isothermal Shrinkage: II, Effect of Y_2O_3 Concentration on the Initial Sintering Stage of Fine Zirconia Powder." Journal of the American Ceramic Society **90**(2): 443-447.

[157]Wang, J. and R. Raj (1990). "Estimate of the Activation Energies for Boundary Diffusion from Rate-Controlled Sintering of Pure Alumina, and Alumina Doped with Zirconia or Titania." Journal of the American Ceramic Society **73**(5): 1172-1175.

[158] Matsui, K., N. Ohmichi, M. Ohgai, N. Enomoto and J. Hojo. (2006). "Sintering Kinetics at Constant Rates of Heating: Effect of Al_2O_3 on the Initial Sintering Stage of Yttria-Stabilized Cubic Zirconia Powder." Journal of the Ceramic Society of Japan **114**: 763-768.

[159] Matsui, K. and J. Hojo (2008). "Sintering kinetics at constant rates of heating: effect of GeO_2 addition on the initial sintering stage of 3 mol% Y_2O_3-doped zirconia powder." Journal of Materials Science **43**(3): 852-859.

[160] Lukin, E. and N. Makarov (2000). "Sintering kinetics of aluminum oxide ceramics with an additive of eutectic composition." Glass and Ceramics **57**(1): 23-25.

[161] Johnson, D. L. and I. B. Cutler (1963). "Diffusion Sintering: I, Initial Stage Sintering Models and Their Application to Shrinkage of Powder Compacts." Journal of the American Ceramic Society **46**(11): 541-545.

[162] Colenz, W. S., J. M. Dynys and R. I. Coble (1980). "Initial Stage Solid State Sintering Models. A Critical Analysis and Assessment " Materials Science Research **13**: 141-157.

[163] Johnson, D. L. (1969). "New Method of Obtaining Volume, Grain-Boundary, and Surface Diffusion Coefficients from Sintering Data." Journal of Applied Physics **40**: 192-200.

[164] Johnson, D. L. and I. B. Cutler (1963). "Diffusion Sintering: II, Initial Sintering Kinetics of Alumina." Journal of the American Ceramic Society **46**(11): 545-550.

[165] Madarász, J., E. Beregi, J. Sztatisz, I. Földvári and G. Pokol (2001). "Combined DTA and XRD Study of Sintering Steps Towards $YAl_3(BO_3)_4$." Journal of Thermal Analysis and Calorimetry **64**(3): 1059-1065.

[166] J. Mosiadz, M., K. L. Juda, S. C. Hopinks, J. Soloducho, B. A. Glowacki (2011). "An in-depth in situ IR study of the thermal decomposition of yttrium trifluoroacetate hydrate." Journal of Thermal Analysis and Calorimetry **107**(2): 681-691.

[167] Boyer, D., G. Bertrand-Chadeyron, R. Mahiou, A. Brioude and J. Mugnier (2003).

"Synthesis and characterization of sol–gel derived $Y_3BO_6:Eu^{3+}$ powders and films." Optical Materials **24**(1–2): 35-41.

[168] Lin, J. H., S. Zhou, et al. (1997). "Structure and Luminescent Properties of $Y_{17.33}(BO_3)_4(B_2O_5)_2O_{16}$." Journal of Solid State Chemistry **134**(1): 158-163.

[169] Hosokawa, S., Y. Tanaka, S. Iwamoto and M. Inoue (2008). "Morphology and structure of rare earth borate ($REBO_3$) synthesized by glycothermal reaction." Journal of Materials Science **43**(7): 2276-2285.

[170] Fagg, D. P., J. R. Frade, M. Mogensen and J. T. S. Irvine (2007). "Effects of firing schedule on solubility limits and transport properties of ZrO_2–TiO_2–Y_2O_3 fluorites." Journal of Solid State Chemistry **180**(8): 2371-2376.

[171] Mizutani, N., A. Kitazawa, Nobuyuki. O, Kato. M (1974). "Phase equilibrium of Y_2O_3-TiO_2." Journal of The Chemical Society Japan .**9**: pp. 1623-1628.

[172] Mizutani, N., Y. O. Tajima, and M. Kato. (1976). "Phase Relations in the System Y_2O_3-TiO_2." Journal of the American Ceramic Society **59**(3-4): 168-168.

[173] Scott, H. G. (1975). "Phase relationships in the zirconia-yttria system." Journal of Materials Science **10**(9): 1527-1535.

[174] S, S. V. and J. R. Hellmann (1980). Phase equilibira in some zirconia systems. Proc. 1st. Int. Conf. . A. H. H. a. L. W. Hobbs. Cleveland, Ohio, American Ceram. Soc**:** 25.

[175] Tuohig, W. D. and T. Y. Tien (1980). "Subsolidus phase equilibria in the system ZrOz-YzO3-A1203." journal of American Ceramic society **63**(9/10): 595-596

[176] M. Mizuno, A. Rouanet, Yamada. T, and Noguchi. T (1976). "Phase diagram of the system La_2O_3 - Y_2O_3 at high temperature." journal of ceramic society Japan **87**(7): 342-347.

[177] S. Jones, R. A. Harding, and G. S. Holt. (19th-22nd October 2008). Development of a friability Test for the Quantitative Measurement of Primary Coat ntergrity of Investment Casting Moulds. 12th World Conference On Investment Casting and Equipment Expo. Dallas, USA.

[178] Chen, C.Y., Tseng, T.K., Tsai, S.C., Lin, C.K. ,Lin, H.M.(2008)."Effect of precursor characteristics on zirconia and ceria particle morphology in spray pyrolysis".Ceramics International, **34**:409-416.

[179] Rahaman, M. N., L. C. De Jonghe and M.-Y. Chu (1991). "Effect of Green Density on Densification and Creep During Sintering." Journal of the American Ceramic Society **74**(3):

514-519.

[180] Bruch, C. A. (1962). "Sintering Kinetics for the High Density Alumina Process." Journal of American Ceramic Society Bulletin, 41(12), 799-860.

[181] Liu, S.-Y., J.-X. Shang, Fu-HeWang and Y. Zhan (2009). "Surface segregation of Si and its effect on oxygen adsorption on a γ -TiAl(111) surface from first principles." Journal of physics: condensed matter **21**: 7.

[182] Zollinger, J., J. Lapin, D. Daloz and H. Combeau (2007). "Influence of oxygen on solidification behaviour of cast TiAl-based alloys." Intermetallics **15**(10): 1343-1350.

[183] Rahaman, M. N. (2007). Ceramic processing, CRC Press. Taylor &Francis Group**:** pp.310.

[184] Rahaman, M. N. (2007). Ceramic processing, CRC Press. Taylor&Francis Group**:** pp.311.

[185] Rahaman, M. N. (2007). Ceramic processing, CRC Press. Taylor&Francis Group: pp. 328.

[186] Brinker, C. J., E. P. Roth, G. W. Scherer and D. R. Tallant (1985). "Structural evolution during the gel to glass conversion." Journal of Non-Crystalline Solids **71**(1–3): 171-185.

[187] Chu, M.-Y., M. N. Rahaman, L. C. De Jonghe and R. J. Brook (1991). "Effect of Heating Rate on Sintering and Coarsening." Journal of American Ceramic Society **74**(6): 1217-1225.

[188] Lange, F. F. (1988). "Approach to reliable powder processing." Ceramic Powder Science II. **1**: 1069-1083 The American Ceramic Society, Inc., Westerville, Ohio.

[189] In, M. L. and A. M. Alper (1970). B_2O_3-Y_2O_3 phase diagram. Phase digram. New York. **3:** 180.

[190] German, R.M., "A quantitative theory of diffusional activated sintering", Science of Sintering, 15, 27, 1983.

[191] Wang, X.-H., P.-L. Chen and I. W. Chen (2006). "Two-Step Sintering of Ceramics with Constant Grain-Size, I. Y_2O_3." Journal of the American Ceramic Society **89**(2): 431-437.

[192] Chen, I.-W. and P.-L.Chen (1996). Sintering characteristics of fine oxide powders. Korean-Japen-US Workshop On micro-structural development in materials, Centre for interface science and engineering of materials. , Kaist. Teajon, Korea.

[193] Zhao, J. and M. P. Harmer. (1987). "Sintering of Ultra-High-Purity Alumina Doped Simultaneously with MgO and FeO." Journal of the American Ceramic Society **70**(12): 860-866.

[194] Chen, P.-L. and I. W. Chen.(1997). "Sintering of Fine Oxide Powders: II, Sintering Mechanisms." Journal of the American Ceramic Society **80**(3): 637-645.

[195] Cui, R.J., Tang, X.X., Gao, M., Zhang, H. ,Gong, S.K.(2012)."Microstructure and composition of cast Ti–47Al–2Cr–2Nb alloys produced by yttria crucibles".Materials Science and Engineering: A, vol.541,pp. 14-21

[196] Ding, X.F., Lin, J.P., Zhang, L.Q., Su, Y.Q. ,Chen, G.L.(2012)."Microstructural control of TiAl–Nb alloys by directional solidification".Acta Materialia, vol.60, pp.498-506

[197] F. Gomes, H. Puga, Joaquim Barbosa, C. Silva Ribeiro. (2011). "Effect of melting pressure and superheating on chemical composition and contamination of yttria-coated ceramic crucible induction melted titanium alloys. " Journal of Materials Science. Vol. 46, pp. 4922–4936.

[198] Yuan, C., Compton, D., Cheng, X., Green, N. ,Withey, P.:*Journal of the European Ceramic Society,* http://dx.doi.org/10.1016/j.jeurceramsoc.2012.06.010.